REFLOW SOLDERING

APPARATUS AND HEAT TRANSFER PROCESSES

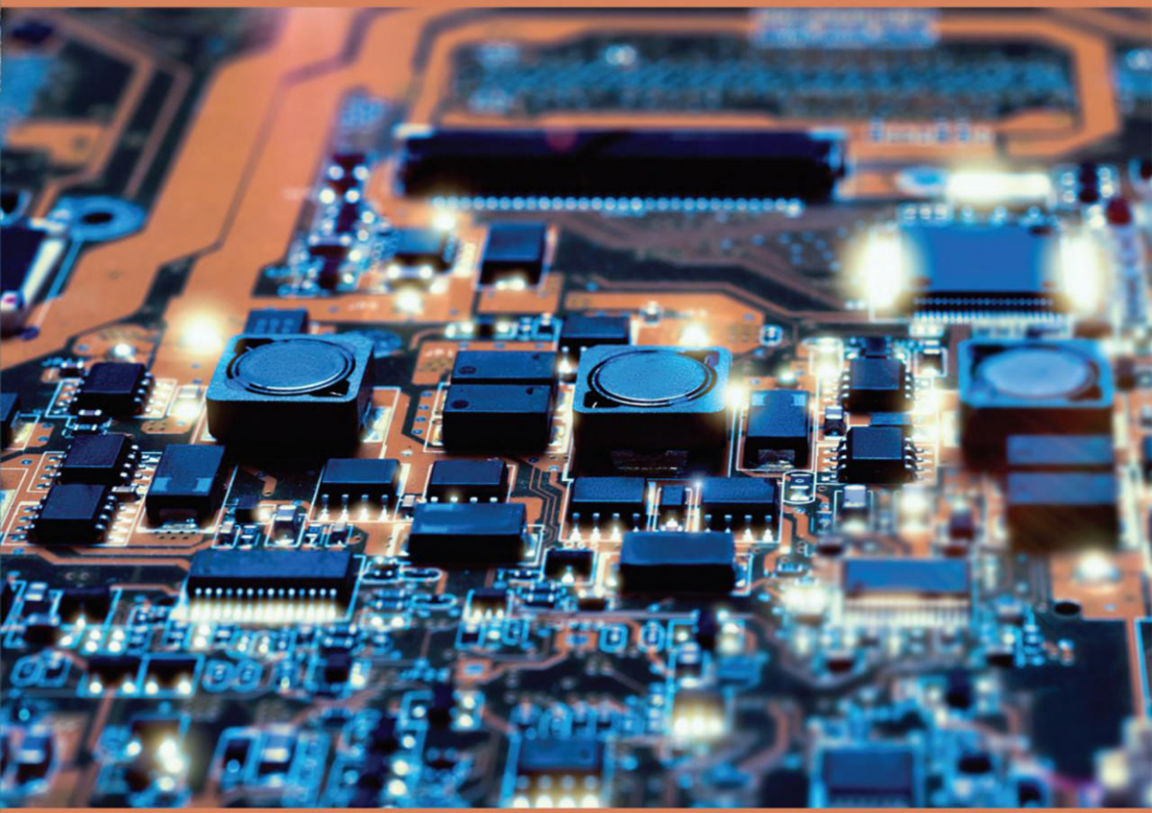

Balázs Illés
Olivér Krammer
Attila Géczy

ELSEVIER

Reflow Soldering

Apparatus and Heat Transfer Processes

Reflow Soldering

Apparatus and Heat Transfer Processes

Balázs Illés
Department of Electronics Technology, Budapest University of Technology and Economics, Budapest, Hungary

Olivér Krammer
Department of Electronics Technology, Budapest University of Technology and Economics, Budapest, Hungary

Attila Géczy
Department of Electronics Technology, Budapest University of Technology and Economics, Budapest, Hungary

ELSEVIER

Elsevier
Radarweg 29, PO Box 211, 1000 AE Amsterdam, Netherlands
The Boulevard, Langford Lane, Kidlington, Oxford OX5 1GB, United Kingdom
50 Hampshire Street, 5th Floor, Cambridge, MA 02139, United States

Notices
Knowledge and best practice in this field are constantly changing. As new research and experience broaden our understanding, changes in research methods, professional practices, or medical treatment may become necessary.

Practitioners and researchers must always rely on their own experience and knowledge in evaluating and using any information, methods, compounds, or experiments described herein. In using such information or methods they should be mindful of their own safety and the safety of others, including parties for whom they have a professional responsibility.

To the fullest extent of the law, neither the Publisher nor the authors, contributors, or editors, assume any liability for any injury and/or damage to persons or property as a matter of products liability, negligence or otherwise, or from any use or operation of any methods, products, instructions, or ideas contained in the material herein.

British Library Cataloguing-in-Publication Data
A catalogue record for this book is available from the British Library

Library of Congress Cataloging-in-Publication Data
A catalog record for this book is available from the Library of Congress

ISBN: 978-0-12-818505-6

Publisher: Matthew Deans
Acquisitions Editor: Christina Gifford
Editorial Project Manager: Mariana L. Kuhl
Production Project Manager: Nirmala Arumugam
Cover Designer: Miles Hitchen

Typeset by MPS Limited, Chennai, India

Contents

Chapter 1

Introduction to surface-mount technology

1.1 Electronic components

Today electronic circuits consist of almost solely surface-mounted components (~90%) and potentially only some through-hole components for realizing plug connectors or high power devices. Surface-mounted components and surface-mount technology are evolving since the mid-1960s [1]. Nowadays, the pitch dimensions reduced down to 0.3 mm or to even lower by the interest of portable device manufacturers, for example. Nevertheless, surface-mounted components never can supersede the through-hole devices entirely; therefore the assembly of both types of components should be done by the comprehensive soldering technology, which is reflow soldering.

The electronic components can be classified from many points of view, for example, they can be passive or active components or electromechanical components like switches, connectors, or relays. From the assembly point of view, the components can be through-hole (Fig. 1.1) or surface-mounted (Fig. 1.2). From the packaging point of view, they can be discrete components (one function is realized by one component—e.g., a resistor), they can be packaged as series of alike components (e.g., resistor array), or can be integrated components, in which many functions are realized by one component.

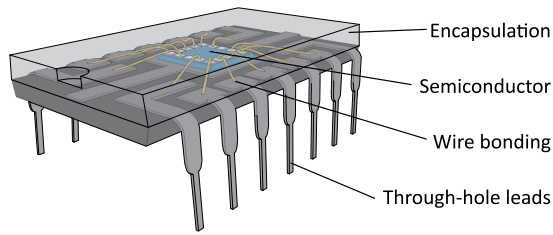

FIGURE 1.1 Through-hole integrated circuit—dual inline package (DIP). *Reproduced with permission from G. Harsányi, Elektronikai Technológia és Anyagismeret, University lecture notes, BME-ETT, 2019, ISBN: 978-963-421-791-6 [2].*

Reflow Soldering. DOI: https://doi.org/10.1016/B978-0-12-818505-6.00001-7

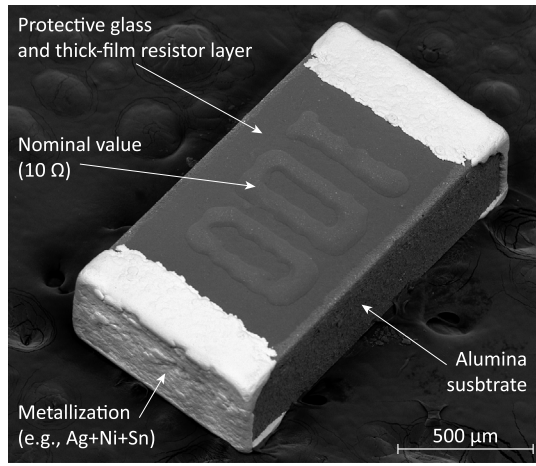

FIGURE 1.2 Scanning electron microscopy image of a surface-mounted resistor.

In this chapter, the different types of electronic components will be detailed. Classification possibilities will be elaborated for both through-hole and surface-mounted components. Finally, the advantages and disadvantages of both through-hole and surface-mount technology will be given and compared to each other.

1.1.1 Through-hole components

The through-hole (TH) components can have flexible or rigid/fixed leads. The flexible leads are bent according to the position of the holes in the printed wiring board (PWB) and cut to the proper size. In the case of TH components with rigid leads, the through-holes in the PWB are designed according to the position of the leads in a given raster. In through-hole technology (THT), component leads are inserted through the holes of the PWB, and they soldered to the lands (solder ring) on the other side of the PWB. Therefore a TH assembly has a "component side" and a "soldering side" (Fig. 1.3).

The arrangement of the component leads can be axial (resistors, capacitors), radial (transistors, LEDs—light-emitting diodes), or the leads can be in the so-called perimeter style, where the leads are located in the perimeter of the components along its edges (integrated circuit packages). Further, special through-hole components are the high lead-count, PGA (pin grid array) packages (e.g., CPUs in personal computers in the 1990s), and the electromechanical components, like USB connectors. In PGA packages, the leads are located in a so-called grid array style, where a grid is projected onto the bottom side of a package, and the leads are at points of intersections. The advantage of these types of components is that they can be placed into

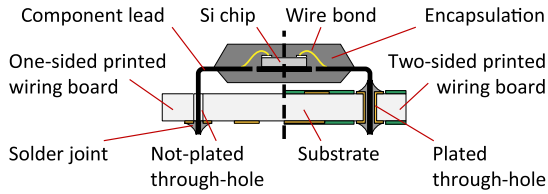

FIGURE 1.3 Schematic of a soldered through-hole component; formation of solder joint in the case of not-plated through-holes (left side) and plated through-holes (right side). *Reproduced with permission from G. Harsányi, Elektronikai Technológia és Anyagismeret, University lecture notes, BME-ETT, 2019, ISBN: 978-963-421-791-6 [2].*

sockets with detachable mechanical joining, which makes it possible to change the components easily.

The through-hole components are stored according to the type of component as follows: axial lead components are stored in two-sided straps; radial lead components are stored in single-sided straps; whereas integrated circuit packages are stored in tube/stick magazines. All of them aid the automated placement of components, which includes the following steps for axial- and radial lead components:

- Cutting out the component from the strap, in which it is placed in the proper order
- Picking the component up, bending its leads for the right shape, then positioning both the component and the bending unit
- Inserting the component into the holes of the PWB, cutting the leads of the component
- Fixing the components by bending back its leads on the bottom side of the PWB

High current capacity and high mechanical strength of the connections are the advantages of THT. Disadvantages include the large area occupied on both sides of the PWB by the components, and the automated insertion becomes problematic if the lead count of the component is large (>40). Furthermore, the package shapes of through-hole components are not standardized exhaustively.

1.1.2 Surface-mounted components

The surface-mounted components are placed and joined (e.g., soldered) directly to the surface of the PWB. They have short leads, which are inappropriate for through-hole mounting, or they have no leads at all, just solderable, metalized terminals on the sides or the bottom of the package. The copper pattern (footprint) on the PWB is designed according to the geometrical layout of components' terminals. Regularly, the components are placed onto the soldering pads, and they are soldered on the same side (Fig. 1.4).

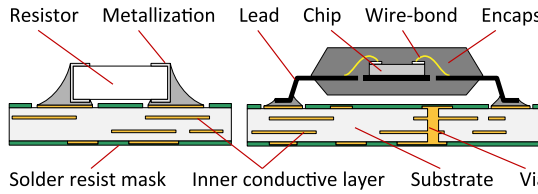

FIGURE 1.4 Schematic of soldered surface-mounted components. *Reproduced with permission from G. Harsányi, Elektronikai Technológia és Anyagismeret, University lecture notes, BME-ETT, 2019, ISBN: 978-963-421-791-6 [2].*

The most widely used passive components are the thick-film surface-mounted resistors and the ceramic (layer) capacitors. A size code describes the size of the components—designation, for example, 1206—which indicates the length and the width of the component by the following rule (down to 0402): $12 \times 10 = 120$ mil; $06 \times 10 = 60$ mil, where the mil is milliinch, the thousandth of an inch (0.001″, 25.4 μm). Regular size codes are collected in Table 1.1. The surface-mounted passive components are stored in paper- or plastic tapes.

The active and integrated surface-mounted components can be classified according to the arrangement of the leads similar to the through-hole components. Integrated component packages with perimeter style leads include SOT (small outline transistor), SOIC (small outline integrated circuit—Fig. 1.5), QFP (quad flat pack), and PLCC (plastic leaded chip carrier) packages. Both the QFP and PLCC packages have leads on all four sides of the component.

The difference between them is that QFP packages have gull-wing-shaped lead (Fig. 1.6), while the leads of PLCC packages are bent back in "J" shape. Similarly to these package types, the QFN (quad flat no-lead) packages do not have leads, but terminals in the form of solderable metallization on the four sides of the package.

In surface-mounted components, the lead arrangement of grid array style materializes in BGA (ball grid array) and LGA (land grid array) packages. The leads of BGA type packages have a ball shape (Fig. 1.7—Bump), whereas there are no leads in LGA type packages, but metalized terminals on the bottom side of the package.

The small size, surface-mounted integrated package types are stored in plastic tapes or plastic sticks. The QFP, PLCC, QFN, BGA, and LGA type packages are stored in plastic trays for the automatic placement of the components.

The surface-mount technology has many advantages over the THT. The size of the surface-mounted components is smaller than that of the through-hole ones while having the same function. Therefore higher integration, more functions per area unit can be achieved, resulting in smaller parasitic effects on the interconnection lines (e.g., leads, traces on the PWB) and in

TABLE 1.1 Regular size codes of surface-mounted passives.

Designation	$L \times W$ (mil)	$L \times W$ (mm)
1206	120×60	3.2×1.6
0805	80×50	2×1.2
0603	60×30	1.6×0.8
0402	40×20	1×0.5
0201	24×12	0.6×0.3
01005	16×08	0.4×0.2
0201 m	10×5	0.25×0.12
0201 mm	8×4	0.2×0.1

Source: Data from G. Harsányi, Elektronikai Technológia és Anyagismeret, University lecture notes, BME-ETT, 2019, ISBN: 978-963-421-791-6 [2].

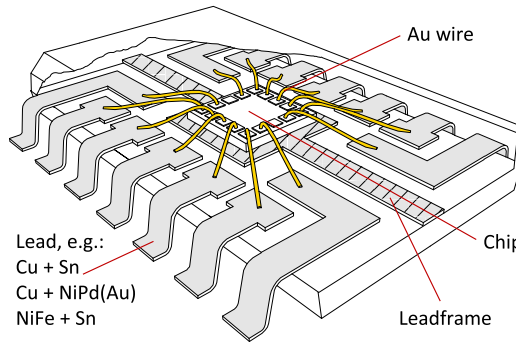

FIGURE 1.5 Schematic of a small outline (SO-type) integrated circuit. *Reproduced with permission from G. Harsányi, Elektronikai Technológia és Anyagismeret, University lecture notes, BME-ETT, 2019, ISBN: 978-963-421-791-6 [2].*

higher operating frequencies. Furthermore, the surface-mounted components are almost entirely standardized allowing the easy automation of component placement by placement machines.

1.2 Reflow soldering technology

Reflow soldering technology is the most popular and generally applied method for fastening electronic components mechanically to the PWB and connecting them electrically to the electronic circuit [3]. The solder material for this technology is the so-called solder paste, which is a dense suspension of solder particles and flux. The flux is responsible for the cleaning,

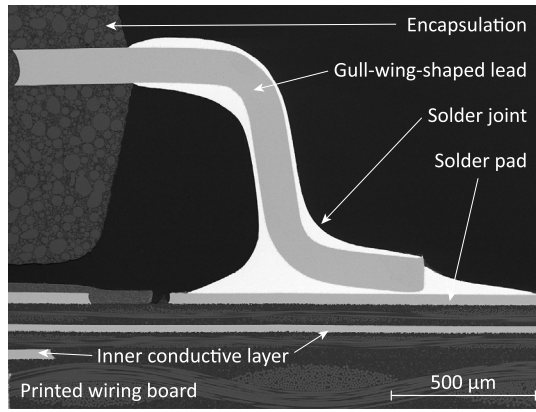

FIGURE 1.6 Scanning electron microscopy image of a gull-wing-shaped lead in a QFP package.

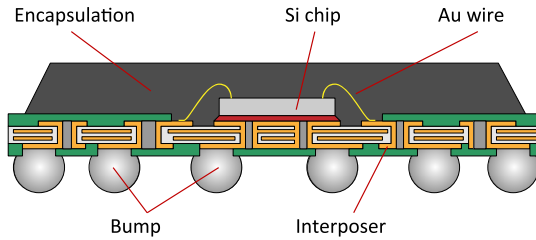

FIGURE 1.7 Schematic of a ball grid array package. *Reproduced with permission from G. Harsányi, Elektronikai Technológia és Anyagismeret, University lecture notes, BME-ETT, 2019, ISBN: 978-963-421-791-6 [2].*

removing oxides and contaminants from the metalized terminals to be soldered. The solder particles are made from solder alloys by ultrasonic or centrifugal atomization with a diameter of a couple of micrometers ($\sim 5-45$ µm depending on the type of solder paste) [4]. The solder alloys were mostly lead-bearing till the beginning of the 2000s; for example, the eutectic tin-lead, Sn_{63}/Pb_{37} alloy with a melting point of 183°C was especially popular. Since the restriction of hazardous substances in the EU (RoHS directive), the electronic industry was urged to introduce the lead-free solder alloys. Nowadays, the most commonly used, second-generation lead-free alloys are Sn-Ag-Cu (SAC)-based alloys. The SAC305 ($Sn/Ag_3/Cu_{0.5}$) alloy with a melting point of 217°C−219°C is a universal favorite.

A huge number of research works are investigating the properties of SAC alloys. Based on these works, the wetting and the mechanical behaviors of some SAC alloys are more superior compared to the traditional Sn/Pb alloys. However for certain applications, for example, under extreme operation, for

example, overpressure [5] or mechanical vibration, the pure SAC alloys might not perform sufficiently; therefore the development of third-generation lead-free solder alloys, even doped with microalloys (additives with less than 0.2 wt.%), or with nanoparticles is still a current topic. Some common alloys and their melting- and solidification temperatures are listed in Table 1.2.

In this chapter, the elementary steps of reflow soldering technology will be overviewed. The rheological properties of the solder paste, which is one of the essential materials in this technology, will be detailed. Finally, a new measurement method will be presented for addressing not just the rheological properties but also the thixotropic behavior of solder pastes.

1.2.1 Overview of the reflow soldering technology steps

The reflow soldering technology consists of three basic steps. First, the solder paste is deposited onto the pads of the PWB by stencil printing technology. A squeegee is moved with a predefined velocity and force over the stencil and pushes the solder paste into the apertures (Fig. 1.8). After separating the PWB from the stencil, the solder paste remains on the solder pads.

Next, the components are placed into the deposited solder paste by automatic placement machines. The machines pick up the component from the storage (e.g., paper tapes, plastic trays) with a vacuum nozzle, measure its location and orientation on the nozzle, and place the component by automatically adjusting positional and rotational offsets according to the prior measurements (Fig. 1.9).

Two types of placement machines are distinguished from the placement head point of view: pick&place and collect&place heads. The pick&place

TABLE 1.2 Solder alloys commonly used in electronics technology (composition is in wt.%).

Solder alloy	Liquidus point (°C)	Solidus point (°C)
Sn_{63}/Pb_{37}	183	
Sn_{60}/Pb_{40}	183	188
$Sn_{60}/Pb_{38}/Ag_{2}$	176	189
$Sn_{95.5}/Ag_{3.8}/Cu_{0.7}$	217	218
$Sn_{96.5}/Ag_{3}/Cu_{0.5}$	217	220
$Sn_{98.4}/Ag_{0.8}/Cu_{0.7}/Bi_{0.1}$	217	225
$Sn_{98.9}/Ag_{0.3}/Cu_{0.7}/Bi_{0.1}$	217	228
$Sn_{91}/Ag_{3.8}/Cu_{0.7}/Bi_{3}/Sb_{1.5}/Ni_{0.15}$	206	218
Sn_{42}/Bi_{58}	139	141

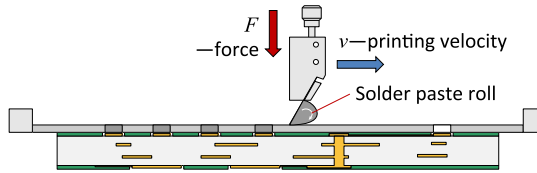

FIGURE 1.8 Schematic of stencil printing. *Reproduced with permission from O. Krammer, K. Dušek, Numerical investigation on the effect of the printing force and squeegee geometry on stencil printing, J. Manuf. Process. 45 (2019) 188–193 [6].*

heads pick up one component and then place it to the respective location. Contrary, collect&place heads pick up, collect several components (4, 8–32), and then place them onto the particular locations. The collect&place machines are faster than pick&place machines. The placement speed can reach several 10,000 components per hour, but the positional error, offset is also larger (up to 20–40 μm) in the case of collect&place machines.

Lastly, the assembly travels through an oven, where the solder alloy in the solder paste is remelted, reflowed employing infrared radiation (Chapter 2: Infrared Reflow Soldering), forced convection (Chapter 3: Convection Reflow Ovens), or by a phase-changing material in vapor phase soldering (Chapter 4: Vapor Phase Soldering (VPS) Ovens). The molten, liquid state solder wets the metalized terminals and forms the solder joints (fillet shape). After the solder melting, the assembly cools down, the solder solidifies and establishes the mechanical and electrical connection between the components and the PWB. From the quality and reliability point of views, the most important factors are the rheological properties of the solder paste [7], the process of stencil printing [8], and the physical processes take place during the reflow phase of the soldering when the solder alloy is in molten form.

1.2.2 Rheology of solder pastes

The solder pastes are dense suspensions of solder particles and flux, as aforementioned. The typical solid content is 50 vol.% and 85–90 wt.%. The particle sizes in the solder pastes vary according to the type of the paste as defined by the IPC J-STD-005 standard [9] (Table 1.3).

The generally known law describes the viscosity of Newtonian fluids, presented in (1.1) [10].

$$\tau = \mu \frac{\partial u}{\partial y} \tag{1.1}$$

where τ (Pa) is the shear stress, $\partial u/\partial y$ (second^{-1}) is the rate of shear, and the proportionality factor μ is the viscosity (Pa s). The solder pastes exhibit

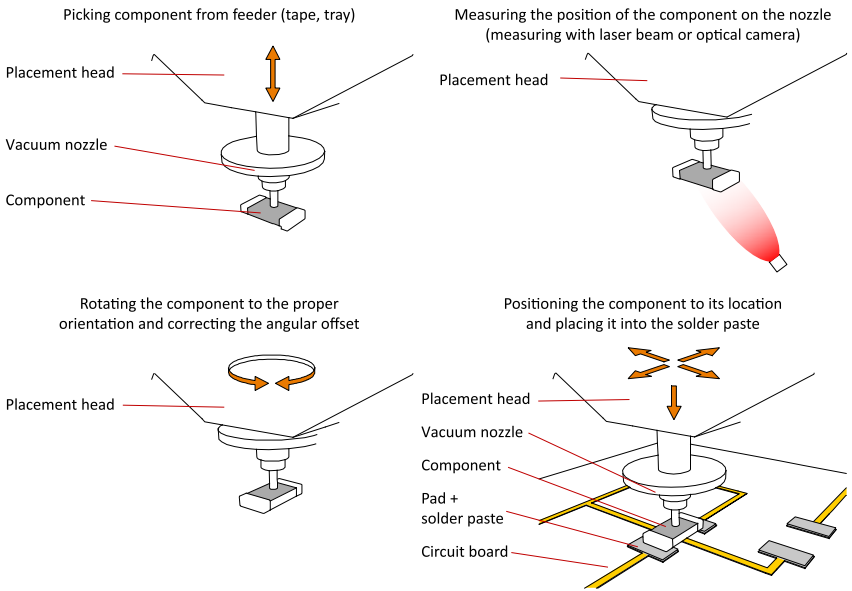

FIGURE 1.9 Steps of automatic component placement. *Reproduced with permission from G. Harsányi, Elektronikai Technológia és Anyagismeret, University lecture notes, BME-ETT, 2019, ISBN: 978-963-421-791-6 [2].*

TABLE 1.3 Particle sizes in solder pastes.

Solder paste	None larger than (μm)	Less than 1% larger than (μm)	Minimum 80% between (μm)	Maximum 10% less than (μm)
Type-1	160	150	150–75	20
Type-2	80	75	75–45	20
Type-3	50	45	45–25	20
Type-4	40	38	38–20	20
Type-5	30	25	25–15	15
Type-6	20	15	15–5	5

Source: Data from IPC J-STD-005, Requirements for Soldering Pastes, Solder Paste Task Group (5-22b) of IPC, Bannockburn, Illinois, USA, 1995 [9].

non-Newtonian fluid properties (1.2); the apparent viscosity of solder pastes decreases with the rate of shear ($0 \leq n \leq 1$ in expression (1.2)).

$$\tau = \mu \left(\frac{\partial u}{\partial y} \right)^n \tag{1.2}$$

The rheological properties, the apparent viscosity of solder pastes are usually measured by a rotational rheometer in a plate–plate arrangement (Fig. 1.10).

The solder paste is placed between the upper, rotating plate, and the lower, Peltier temperature controlled standing plate. Serrated plates (e.g., with *Ra*: 4–7 μm) can be used with the view to reduce the wall-slip effect [12]. A hood is also used to enhance temperature control and avoid evaporation of the flux. The distance between the plates should be chosen according to the particle size in the paste. As recommended by Barnes [13], the gap to particle size ratio should be at least 10, that is, 500 μm for Type-3 solder paste and 400 μm for Type-4 solder pastes as examples. After setting the measuring gap, the rotation or oscillation of the upper plate is started. The instrument controls the strain and the strain rate (strain-controlled method) and records the torque needed for the movement as a function of time. By using the geometric parameters of the measuring system, viscosity and dynamic moduli are calculated by the software of the instrument for rotational and oscillatory mode, respectively.

Many research works investigated the rheological properties of the solder pastes. Pietriková and Kravčík [14] and Nguty and Ekere [15] investigated the viscosity of solder pastes by sweeping the rate of shear during the measurements, in order to present the non-Newtonian, shear-thinning properties

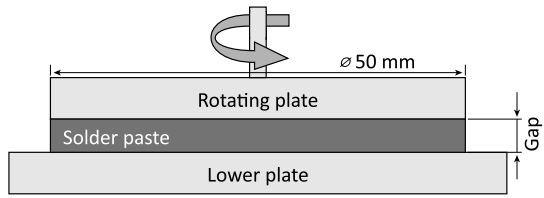

FIGURE 1.10 Schematic of the rheological measurement with a rotational rheometer. *Reproduced with permission from O. Krammer, B. Gyarmati, A. Szilágyi, B. Illés, D. Bušek, K. Dušek, The effect of solder paste particle size on the thixotropic behaviour during stencil printing, J. Mater. Process. Technol. 262 (2018) 571–576 [11].*

of the pastes. They found that the apparent viscosity of solder pastes can decrease three to four orders of magnitude over the rate of shear from 10^{-3} to 10^{2} second^{-1}. Durairaj et al. [16] characterized the viscosity of solder paste for future modeling of the stencil printing process with numerical methods. Glinski et al. [17] suggested implementing non-Newtonian viscosity parameters in the numerical modeling of stencil printing instead of using Newtonian fluid properties. Durairaj et al. [18] highlighted the differences between the two approaches (Newtonian or non-Newtonian fluid properties) with calculations for different printing speeds. They suggested using the Cross material model (1.3) [10] for describing the viscosity decrease with an increasing rate of shear.

$$\eta_{Cross} = \eta_{\infty} + \frac{\eta_0 - \eta_{\infty}}{1 + (\lambda\dot{\gamma})^n} \tag{1.3}$$

where η_0 is the zero-shear viscosity, η_{∞} is the infinite-shear viscosity, λ is the time constant, $\dot{\gamma}$ is the rate of shear, and n is a power-law index.

However, Al-Ma'aiteh and Krammer [19] found that the viscosity curve of solder pastes has a plateau region at low rates of shear, approximately from 10^{-3} to 10^{-2} second^{-1} in their work (Fig. 1.11). This nature of the viscosity curve can be captured with the Carreau–Yasuda material model (1.4) [20].

$$\eta_{C-Y} = \eta_{\infty} + \frac{\eta_0 - \eta_{\infty}}{[1 + (\lambda\dot{\gamma})^a]^{(1-n)/a}} \tag{1.4}$$

where a is the Yasuda exponent.

Goodwin [21] showed that the rheological parameters did not depend on the size distribution of metal particles in the paste, but on their volume fraction. He presented that the effect becomes apparent at volume fractions higher than 30 vol.%. Solder pastes usually have 50 vol.% of metal particles in the total volume, so Goodwin's results suggest that the viscosity does not depend on the particle size. Nevertheless, according to empirical and industrial experiences, solder pastes exhibit thixotropic behavior (time-dependent

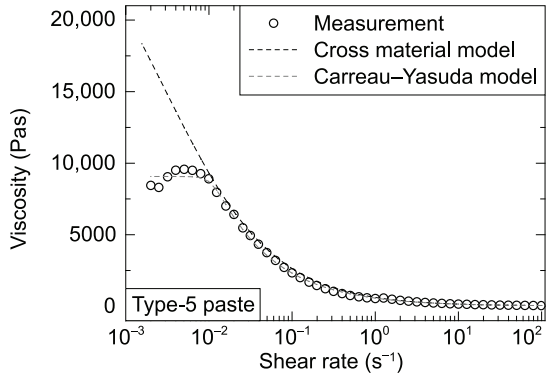

FIGURE 1.11 Viscosity curve of a Type-5 solder paste.

shear thinning) on the one hand, and their viscosity depends on the particle size on the other hand. Goodwin et al. could not show this phenomenon possibly because they measured suspensions only in their initial state, and the thixotropic behavior was not considered.

Dynamic, time-dependent characteristics were also investigated in the literature. Nevertheless, only constant rates of shear were applied in the measurements for revealing the viscosity change over time, and the lowest rates of shear were relatively high, from 0.1 [22] to 2 second^{-1} [23]. These works also did not take into account the thixotropic behavior of solder pastes and the idle time between individual stencil printings, which is generally between 15 and 60 seconds [24]. One particular research dealt with the thixotropic behavior where a sequence of measurements was used for addressing this property of solder pastes [12]. However, only a narrow shear rate sweep (from 0.01 to 0.2 second^{-1}) was applied and no idle time between the measurements was set. The effect of idle time was investigated based on structure kinetics in the work of Vachaparambil et al. [25], but only a longer duration of idle time ($\sim$100 seconds) was used, which is not common in stencil printing.

These shortcomings were addressed by the research wok of Krammer et al. recently [11]. They focused on improving the characterization of viscosity for enhanced numerical modeling of the stencil-printing and better process optimization. Three solder pastes (Type-3, Type-4, and Type-5) were investigated and compared in that work. Special attention was paid on the choice of identical flux for all tested pastes so that the flux did not alter the results. The rate of shear varied from 1.5×10^{-4} to 10^{2} second^{-1} within their measurement. The idle time of stencil printing was addressed by letting the samples rest for a given time frame between individual measurement cycles. This "rest-period" was matched with the idle time of stencil printing since its length affects the thixotropic behavior of solder pastes significantly.

Therefore the samples were allowed to rest in the experiment for 15, 30, and 60 seconds (length of "*b*" in Fig. 1.12), and eight measurement series were carried out automatically in all of the cases. The schematic of the test run (rate of shear over time) and the theoretical change in viscosity are illustrated in Fig. 1.12.

Krammer et al. [11], Pabst [26], and also Zhang et al. [27] found that no difference in viscosity can be shown between the different types of solder pastes in the initial state, after the first measurement cycle. The difference in the viscosities between the solder pastes was below 10% (Fig. 1.13), which is in the order of magnitude of the measurement uncertainties.

Contrary to these findings, Krammer et al. [11] showed that there is a significant decrease in the viscosity of solder pastes over the measurement cycles on the one hand (Fig. 1.14).

On the other hand, noteworthy differences can be shown in the zero-shear and infinite-shear viscosity values between the different types of solder pastes in the stabilized state, that is, after eight measurement cycles. The difference in zero-shear viscosity could even be 30% (Fig. 1.15), whereas the infinite-shear viscosity can vary for the different solder pastes by 20%−30% (Fig. 1.16). These differences imply that for the numerical modeling of stencil printing, that viscosity curve of solder pastes should be utilized, which were measured in their stabilized state.

Oscillatory stress sweep tests were also performed in the research work of Krammer et al. [11] in the stabilized state (after eight measurement cycles) of the solder pastes. An important parameter of the oscillatory measurement results is the so-called cross-over stress, where the values of storage (G') and loss modulus (G'') are equal to each other. Bao et al.

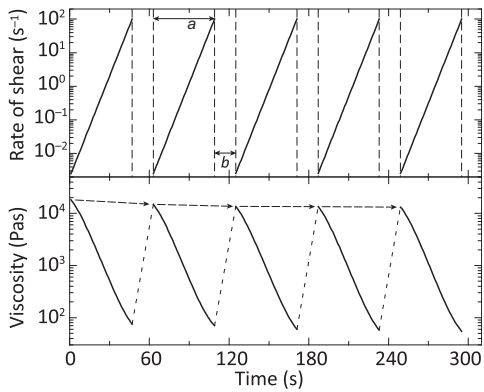

FIGURE 1.12 Viscosity curve of a Type-5 solder paste. *Reproduced with permission from O. Krammer, B. Gyarmati, A. Szilágyi, B. Illés, D. Bušek, K. Dušek, The effect of solder paste particle size on the thixotropic behaviour during stencil printing, J. Mater. Process. Technol. 262 (2018) 571−576 [11].*

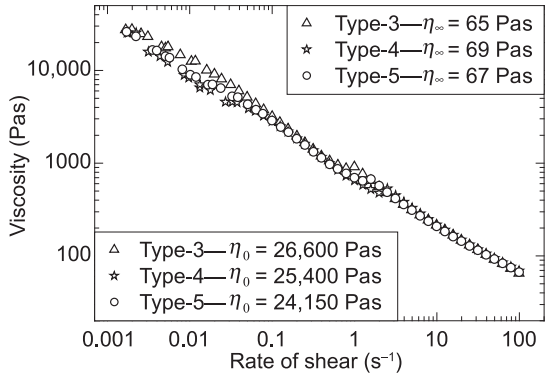

FIGURE 1.13 The viscosity curves of solder pastes in the initial state. *Reproduced with permission from O. Krammer, B. Gyarmati, A. Szilágyi, B. Illés, D. Bušek, K. Dušek, The effect of solder paste particle size on the thixotropic behaviour during stencil printing, J. Mater. Process. Technol. 262 (2018) 571–576 [11].*

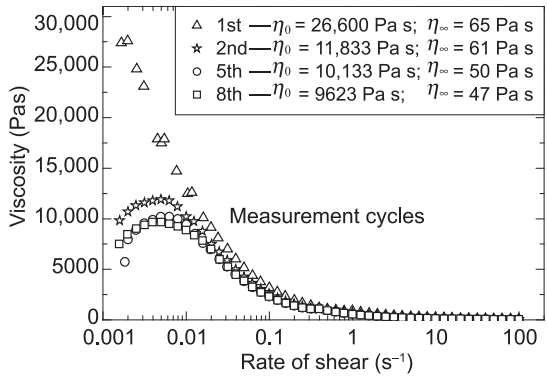

FIGURE 1.14 The viscosity curve of a Type-3 solder paste over the measurement cycles. *Reproduced with permission from O. Krammer, B. Gyarmati, A. Szilágyi, B. Illés, D. Bušek, K. Dušek, The effect of solder paste particle size on the thixotropic behaviour during stencil printing, J. Mater. Process. Technol. 262 (2018) 571–576 [11].*

demonstrated that the lower the stress at $G' = G''$, the more liquid-like the solder paste is, which could result in paste fracture in stencil printing during the stencil separation process [28]. Furthermore, slump defects after the printing can occur more frequently with solder pastes exhibiting lower values of cross-over stress. Krammer et al. presented in Ref. [11] that their Type-3 solder paste showed significantly lower cross-over stress compared to that presented by the Type-5 solder paste (Fig. 1.17). This result also proved that more precisely defined deposits in stencil printing can be achieved by using solder pastes with smaller particle sizes.

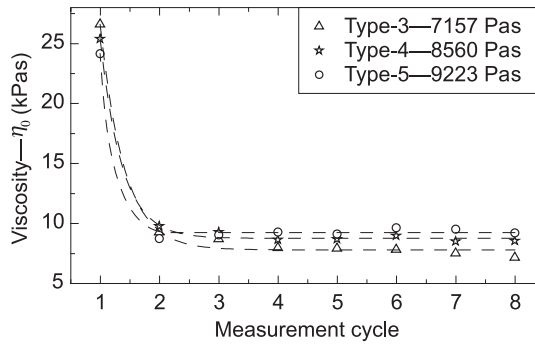

FIGURE 1.15 Zero-shear viscosities of solder pastes in their stabilized state. *Reproduced with permission from O. Krammer, B. Gyarmati, A. Szilágyi, B. Illés, D. Bušek, K. Dušek, The effect of solder paste particle size on the thixotropic behaviour during stencil printing, J. Mater. Process. Technol. 262 (2018) 571–576 [11].*

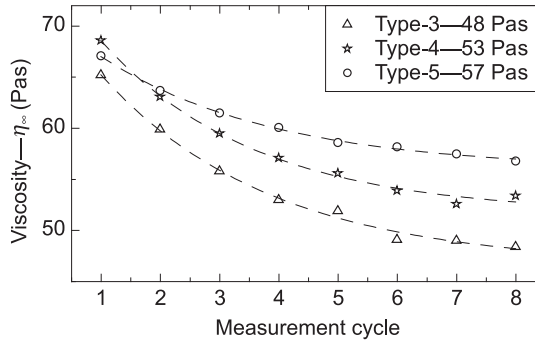

FIGURE 1.16 Infinite-shear viscosities of solder pastes in their stabilized state. *Reproduced with permission from O. Krammer, B. Gyarmati, A. Szilágyi, B. Illés, D. Bušek, K. Dušek, The effect of solder paste particle size on the thixotropic behaviour during stencil printing, J. Mater. Process. Technol. 262 (2018) 571–576 [11].*

1.3 Stencil printing

Stencil printing might be the most crucial step in reflow soldering technology. Even 60%–70% of the soldering failures can be traced back to this process; principally the formation of solder bridges and open joints. In this chapter, the process of stencil printing will be discussed both from the process parameters and from the related assembly defects point of view. Structure of traditional stencils and the so-called Vectorguard frame system will be given. The numerical modeling aspects of the stencil printing process will be discussed. Detailed description about the modeling of reflow ovens is presented in Chapter 6, Numerical Simulation of Reflow Ovens. This

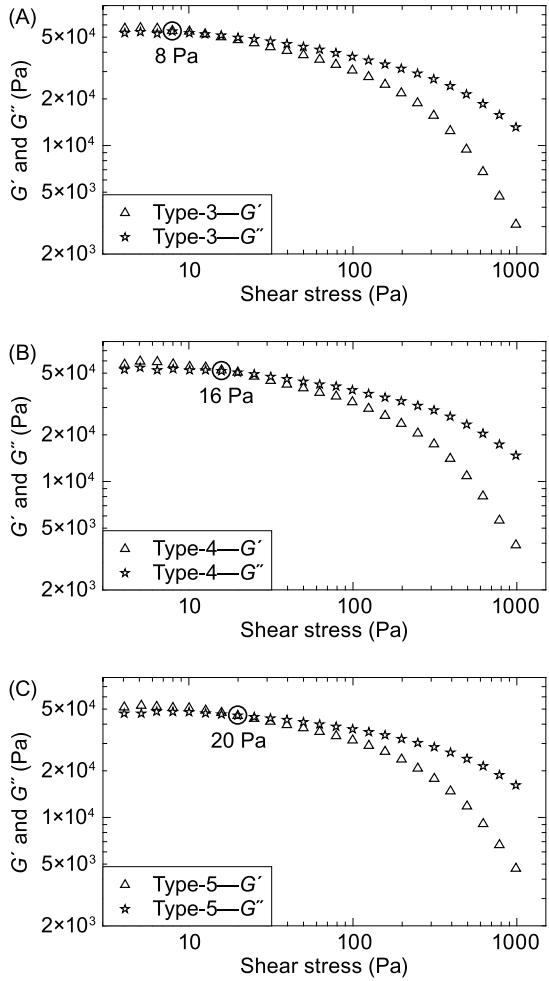

FIGURE 1.17 Oscillatory stress sweep test: (A) solder paste Type-3; (B) solder paste Type-4; (C) solder paste Type-5. *Reproduced with permission from O. Krammer, B. Gyarmati, A. Szilágyi, B. Illés, D. Bušek, K. Dušek, The effect of solder paste particle size on the thixotropic behaviour during stencil printing, J. Mater. Process. Technol. 262 (2018) 571–576 [11].*

subchapter is confined exclusively to present some modeling aspects only in connection with the process of stencil printing.

1.3.1 The process of stencil printing

As mentioned above, the process of stencil printing is responsible for providing the solder paste onto the soldering pads by a fast, mass deposition process. The process of stencil printing can be divided into three substeps. First, the stencil,

which is a 50−200 μm thick metal foil, is perfectly aligned to the PWB. The apertures in the stencil are formed according to the solder pads on the substrate. Next, the solder paste is forced into the apertures by a squeegee stroke with predefined pressure and velocity. Lastly, the PWB is separated from the stencil with a predefined speed (6−8 mm/s); the solder paste is released from the apertures and remains on the solder pads (Fig. 1.18).

The stencil, which is a key tool in stencil printing, is usually made from stainless steel or nickel. Its thickness ranges typically from 50 to 200 μm. The apertures (openings) are designed precisely according to the soldering pads on the PWB. There are three techniques for forming the apertures within the stencil, namely, chemical etching, laser cutting, and electroforming. All of them have advantages and disadvantages. Chemical etching is the cheapest method, the price of the stencil depends on the foil size, but it provides the worst quality stencils, which are appropriate for pitch sizes above 0.63 mm. Laser cutting is the most widespread technique for preparing stencils. Their price is moderate depending on the number of apertures, and they are appropriate for pitch sizes down to 0.4 mm and for passive discrete components down the size code of

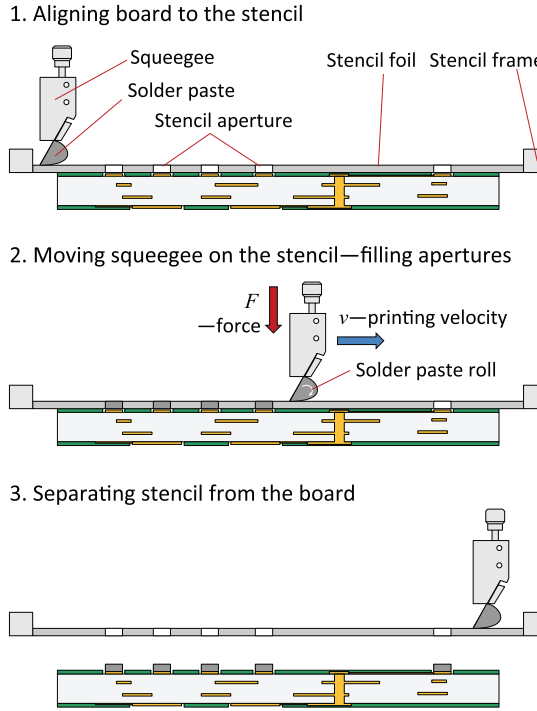

FIGURE 1.18 The substeps of stencil printing. *Reproduced with permission from G. Harsányi, Elektronikai Technológia és Anyagismeret, University lecture notes, BME-ETT, 2019, ISBN: 978-963-421-791-6 [2].*

0201. Both of these technologies are subtractive ones; the preparation of the stencil is started from a full sheet of foil and, the material is removed from the places where apertures should be formed. The best quality stencils can be prepared by electroforming for a relatively high price. They are perfect for ultra-fine pitch integrated circuit packages and the smallest passives. The price of electroformed stencils depends on the thickness of the foil, but note that the fine-pitch components require thinner stencils ($\sim$50–75 μm). The traditional structure of stencils as a tool is illustrated in Fig. 1.19. It is consisting of the stencil foil itself, an aluminum frame for handling, and a metal mesh for tensioning the foil by approximately 50 N/cm. As aforementioned, the layout of the apertures is designed appropriately to soldering pads. Furthermore, alignment marks (fiducial points) are engraved on the bottom side of the stencil for aiding its positioning to the PWB. The fiducial points are filled with black epoxy yielding better contrast by the automatic optical inspection of them.

Besides the traditional stencils, the so-called Vectorguard stencils (stencil frames) are also used. In this stencil frame, the foils are interchangeable. During operation, springs tighten aluminum profiles, which cling into the grooves formed along the edges of the stencil foil. Ahead of the springs, there is a silicone tube. By blowing up the tube with compressed air, the profiles open, and the stencil foil can be inserted into the frame. By deflating the tube, the profiles close and the stencil foil becomes tight (Fig. 1.20). The advantage of this system is that the stencil itself can be thinner allowing easier transport and storage. Slight disadvantage by industrial experiences is the somewhat lower reliability of the tensioning system.

1.3.2 Process parameters and related printing failures

The main process parameters of stencil printing include the printing speed (velocity of stroke), specific printing force, attack angle of the squeegee, stencil

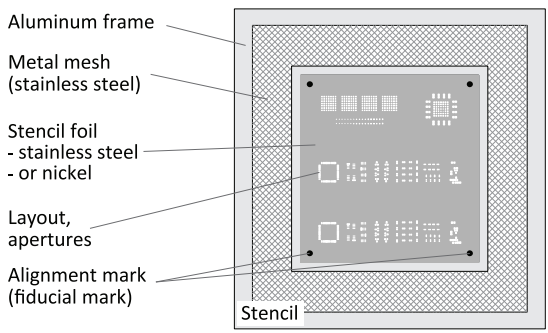

FIGURE 1.19 Structure of a traditional stencil. *Reproduced with permission from G. Harsányi, Elektronikai Technológia és Anyagismeret, University lecture notes, BME-ETT, 2019, ISBN: 978-963-421-791-6 [2].*

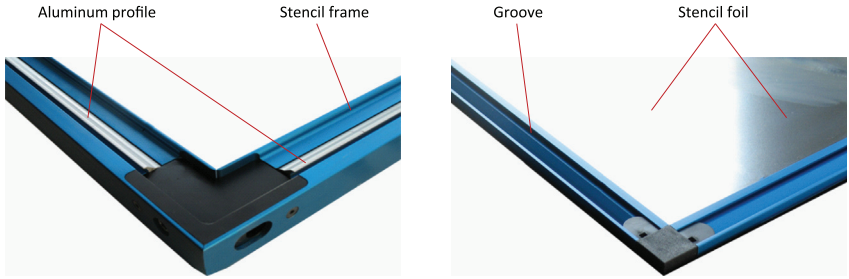

FIGURE 1.20 Vectorguard stencil frame.

separation speed, intervals between stencil cleaning, and ambient conditions in the printer. The main characteristic of the stencil printing process is the so-called transfer efficiency (1.5), which is the ratio of the deposited solder paste volume to the volume of stencil aperture. Deviance of $\pm 25\%$ is allowed usually in the industry for this parameter. The transfer efficiency depends not only on the process parameters but on the manufacturing technology of the stencil and on the size of stencil aperture as well. The size of the stencil aperture is usually characterized by two ratios, by the aspect ratio (AS) and the area ratio (AR), which is the ratio of the stencil aperture area to the wall surface of the stencil aperture (1.6). For expecting a transfer efficiency over 75%, the aspect ratio should be larger than 1.5, and the area ratio should be larger than 0.66 by empirical findings for each and every aperture in the stencil.

$$TE = \frac{V_{paste}}{V_{aperture}} \tag{1.5}$$

$$AS = \frac{w}{t} \geq 1.5; \quad AR = \frac{w \cdot l}{2(w + l)t} \geq 0.66 \tag{1.6}$$

where w and l are the shorter and longer sides of a rectangular aperture, respectively, and t is the thickness of stencil foil. Typically the rule regarding area ratio is used for determining the proper foil thickness for a given assembly, by analyzing its value for critical apertures (mostly at fine-pitch components), and ensuring that to be larger than 0.66 by reducing the foil thickness. A theoretical curve of transfer efficiency (as a function of area ratio) fitted to a measurement of a Type-3 solder paste is illustrated in Fig. 1.21.

The printing speed is usually can be set between 10 and 300 mm/s in stencil printers, but typical values are from 30 to 70 mm/s. If the printing speed is set to a too high value, rolling of the solder paste ahead of the squeegee can cease, and aperture skipping (no solder paste is deposited into) might occur, resulting in open joints after soldering. Too slow printing speed does not affect the printing quality significantly but reduces the throughput of the process itself.

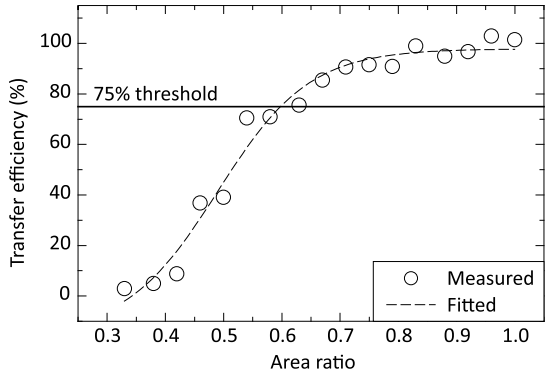

FIGURE 1.21 Transfer efficiency over the area ratio of stencil apertures.

The usual value for the specific printing force is 0.3 N/mm. It should be noted that giving the value of the printing force instead of the specific force (e.g., in datasheets) can be misleading, since there are several lengths of squeegees (20, 30, and 40 mm), which are used in the industry for stencil printing. By the optimization of this parameter, the value of the specific printing force can be reduced until the value, when the stencil is completely wiped during the stroke, and its surface is free from solder paste residues. Since the pressure over a stencil and similarly over a squeegee due to the roll of solder paste depends on the printing speed (see Section 1.3.3), lower specific printing force can be enough for lower printing speeds, and larger force values are optimal for faster strokes. If the printing force is too large, the squeegee and the stencil can wear out rapidly. If the printing force is too low, a layer of solder paste is left on the surface of the stencil after printing (Fig. 1.22), which can result in higher solder paste deposits on the PWB than the thickness of the stencil, yielding solder bridges after soldering. It should be noted that in industrial stencil printers, there are two squeegees, one for the forward direction for printing the nth assembly and one for the backward direction for printing the $n + 1$ assembly.

The stencil separation speed can be set approximately between 1 and 10 mm/s. The rheological properties of today solder pastes are designed for allowing faster stencil separation speeds like 6−8 mm/s. If the separation speed is set to a too low value, edge of the solder paste deposit can be lifted ("dog-ears" effect) while separating the PWB from the stencil, resulting in an uneven deposit surface and height (Fig. 1.23). If the stencil separation speed is set to a too high value, the viscosity of the deposited solder paste can also remain high (thixotropic behavior). As a consequence, the deposited solder paste cannot keep its shape; it can slump and can form bridges between adjacent component leads.

The automatic cleaning interval of the stencil is also an essential parameter. During the printings, the solder paste sticks in a given extent to the walls

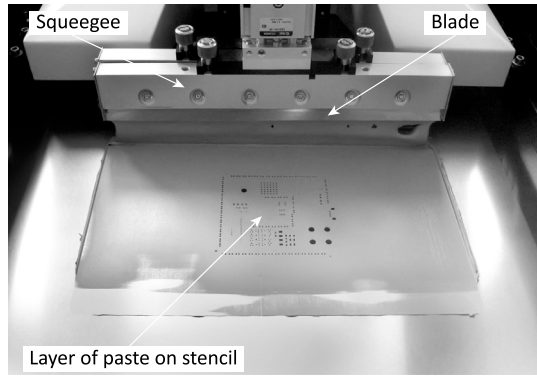

FIGURE 1.22 A layer of paste remains on the stencil because of too low printing force.

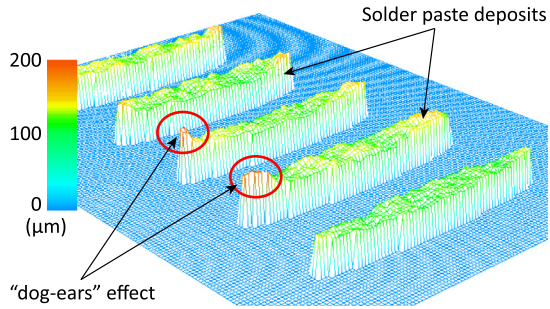

FIGURE 1.23 SPI (solder paste inspection) image of deposits for QFP component; edge of solder paste is lifted (dog-ears) because of inappropriate stencil separation speed.

of the stencil aperture, and a layer of solder paste continuously build up there, resulting in lower transfer efficiency. In the end, the solder paste can completely block the aperture, yielding open joints after soldering. Cleaning of the stencil can be performed by a dry cloth, by a wet cloth (impregnated by the solvent of solder paste) and by those together with vacuum aiding. The stencil is cleaned automatically within around 5−10 printings, and the optimal interval is usually determined with an experiment, where the transfer efficiency is measured over the printings without stencil cleaning. A typical result of this experiment is illustrated in Fig. 1.24.

The recommended interval between stencil cleanings is the number where the transfer efficiency decreases below 75%. A slight oscillation can be observed in the results between the onward and backward traveling squeegees if the given stencil printer lacks a closed-loop squeegee force control system. In newer systems, the stencil cleaning interval can be optimized continuously over time by the machine-to-machine communication between the stencil printer and the SPI (solder paste inspection), in the concept of Industry 4.0.

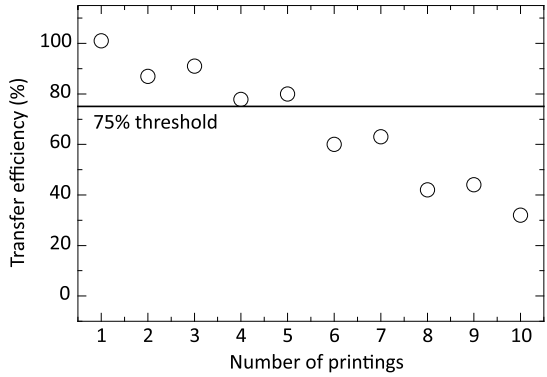

FIGURE 1.24 Transfer efficiency over the number of printings without stencil cleaning.

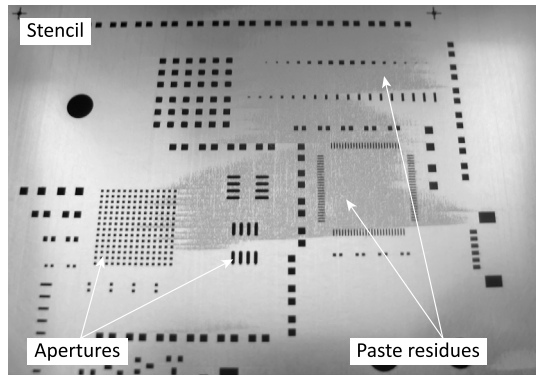

FIGURE 1.25 Solder paste residues on the surface of the stencil because of inappropriate support.

Last but not least, the support system of PWBs also affects the quality of stencil printing. In modern stencil printers, either the support pins are placed automatically by the printer, or the support system itself includes pneumatically operated pins that automatically adapt to the board surface (note that there are components on the bottom side in double-sided assemblies). Nevertheless, if the support pins are set inappropriately, the solder paste can remain on the surface of the stencil (Fig. 1.25) at specific locations (where the PWB can bend away from the stencil), indicating that the deposited solder paste will be too high on the PWB according to those places on the stencil. Furthermore, the solder paste can dry onto the bottom surface of the stencil (bleeding of the solder paste between the stencil and board). Considering the particle size of approximately 40 μm and the stencil thickness of approximately 120 μm, "bleeding" can cause even a 30% increase in the deposited volume of solder paste. Both printing defects can results in solder bridges after the soldering.

1.3.3 Numerical modeling of stencil printing

Since stencil printing is considered to be the critical step in eliminating soldering failures—~60% of soldering failures can be traced back to this process [8]—exhaustive optimizations of the process are continuously carried out using numerical modeling, and recently even utilizing methods based on machine learning. The flow of the solder paste can be described by beginning with the Navier–Stokes equation (1.7) [29]:

$$-\frac{1}{\rho}\nabla p = \frac{\partial \mathbf{u}}{\partial t} + \mathbf{u}\cdot\nabla\mathbf{u} - \frac{\mu}{\rho}\nabla^2\mathbf{u} - \mathbf{f} \tag{1.7}$$

where ρ is the density of the fluid, p is the pressure, $\mathbf{u}$ is the flow velocity, μ is the dynamic viscosity, and $\mathbf{f}$ represents body accelerations acting on the continuum. The solder paste can be considered as an incompressible fluid (ρ is constant). Hence the equation of mass continuity reduces to the equation of volume continuity (1.8) [30]:

$$\nabla\cdot\mathbf{u} = 0 \tag{1.8}$$

In the case of stencil printing, the flow velocity is relatively low, and the viscosity of solder pastes is relatively high. The term of the convective acceleration ($\mathbf{u}\cdot\nabla\mathbf{u}$) is insignificant compared to the term of diffusion ($\mu\cdot\rho^{-1}\nabla^2\mathbf{u}$) in the Navier–Stokes equation (1.7). Furthermore, the Reynolds number (1.9) is much lower than 1 ($\mathrm{Re} < 10^{-2}$) based on the work of Durairaj et al. [18]), which implies a laminar flow.

$$\mathrm{Re} = \frac{\rho\cdot u\cdot L}{\mu} \tag{1.9}$$

where u is the magnitude of the flow velocity, and L is the characteristic length. As a consequence, the flow field of the solder paste can be described by the Stokes flow (1.10) in steady-state, as shown by Constantinscu [31]:

$$\nabla p = \mu\nabla^2\mathbf{u} + \mathbf{f} \tag{1.10}$$

where $\mathbf{f} = 0$ in this case.

The finite volume method is used typically for approximating the fluid flow equations numerically. Furthermore, the solder paste is usually considered as a homogenous liquid, utilizing single-phase calculations. The geometry of the model usually consists of the stencil and the squeegee as solid walls and the solder paste as the fluid. The system is generally represented in an opposite frame of reference, which means that the squeegee is a static wall, whereas the stencil moves by the printing speed in the opposite direction to the printing. Both the stencil and the squeegee have a no-slip boundary condition, meaning that the velocity of the first fluid layer next to the respective wall is equal to the velocity of that wall. The remaining fluid interface (paste–air interface) has a free-slip boundary condition, meaning

that the tangential velocity of the first fluid layer and the shear stress along the interface is zero. Finally, the system can be modeled to be isothermal (1.11), since Mannan et al. [32] have found that the heat generated inside the solder paste roll during the printing is conducted away so that temperature does not rise noticeably.

$$\frac{\mathrm{d}T}{\mathrm{d}t} = 0 \tag{1.11}$$

where T is the absolute temperature. The geometry with the various boundary conditions is illustrated in Fig. 1.26.

The material property for the fluid should be set to describe the non-Newtonian behavior of the solder paste, using either the Cross or the Carreau−Yasuda model (see Section 1.2.2). Many researchers proposed using the Cross material model to define the apparent viscosity over the rate of shear. However, Krammer et al. [11] showed that there is a plateau range in the viscosity curve of pastes at low rates of shear (from 10^{-2} to 10^{-3} second^{-1}). This suggests that the Carreau−Yasuda model (described by Boyd and Buick in Ref. [20]), which is similar to an inverted S-curve can be a better approach for determining the apparent viscosity of solder pastes.

The validation of the numerical model regarding stencil printing can be performed based on the work of Riemer. He started the numerical modeling of printing processes at the end of the 1980s by developing an analytical model (based on the Navier−Stokes equation) to predict the pressure distribution along the surface of a mask in printing processes (screen printing or stencil printing) [33]. He found that the pressure distribution (which is commonly used for subsequent calculations) depends on three parameters: the squeegee angle, the printing velocity, and the viscosity of the solder paste (1.12) [34]. These parameters are the most

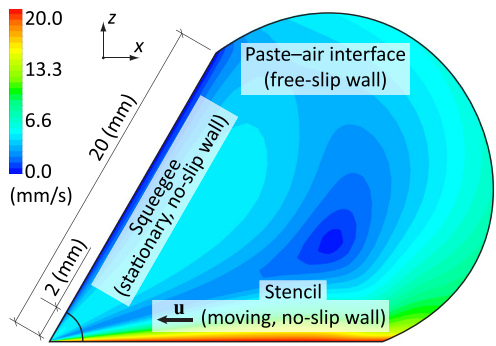

FIGURE 1.26 Finite volume model of stencil printing. *Reproduced with permission from O. Krammer, K. Dušek, Numerical investigation on the effect of the printing force and squeegee geometry on stencil printing, J. Manuf. Process. 45 (2019) 188−193 [6].*

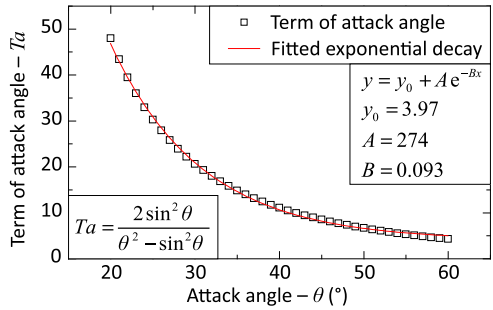

FIGURE 1.27 Finite volume model of stencil printing. *Reproduced with permission from O. Krammer, K. Dušek, Numerical investigation on the effect of the printing force and squeegee geometry on stencil printing, J. Manuf. Process. 45 (2019) 188–193.*

significant, which are affecting the aperture filling of solder pastes, or paste release during stencil separation.

$$P = \frac{1}{r}\left(\frac{2\sin^2\theta}{\theta^2 - \sin^2\theta}\right)\mu \cdot u \tag{1.12}$$

where P is the pressure at a distance r from the squeegee (x-direction in Fig. 1.26 at $z = 0$), θ is the attack angle of the squeegee, μ is the dynamic viscosity, and u is the printing velocity. The pressure depends on the velocity and on the viscosity linearly. Note that Riemer solved the Navier–Stokes equation considering Newtonian fluid properties, so the validation of the numerical model regarding stencil printing should begin with setting Newtonian properties to the solder paste, for example, a viscosity of 200 Pa s.

The pressure during printing depends on the squeegee angle by a decaying exponential function (Fig. 1.27), resulting in that the squeegee attack angle (45 or 60 degrees in the unloaded state) has a major influence on the results of stencil printing, especially in pin-in-paste (PIP) technology (Section 1.6). The pressure along the surface of the stencil is two times higher for squeegees with a 45-degree angle than those with a 60-degree attack angle during the printing.

Both Seo and Kim [35] and Glinski et al. [17] analyzed the pressure distribution along the surface of the stencil for different squeegee angles by numerical models. Though, they have applied nominal, unloaded squeegee angles, not the real attack angles. The real attack angle is always lower than the unloaded one due to the actual printing force. Krammer et al. [36] investigated the decrease in attack angle both empirically and utilizing a finite element method. They built custom equipment to measure the deformation of the printing squeegee. The load arm was chosen to be long enough to span the whole width of the stencil (50×50 cm), and to be able to produce a load close to industrial standards (e.g., 0.3 N/mm) using precision weight calibers ($\sim$500 g each). The printing squeegee consists of two main parts, a holder to

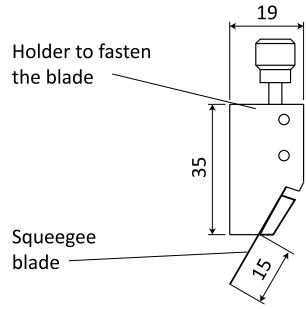

FIGURE 1.28 The geometry of a squeegee tool (all dimensions are in mm). *Reproduced with permission from O. Krammer, L.M. Molnár, L. Jakab, A. Szabó, Modelling the effect of uneven PWB surface on stencil bending during stencil printing process, Microelectron. Reliab. 52(1) (2012) 235–240.*

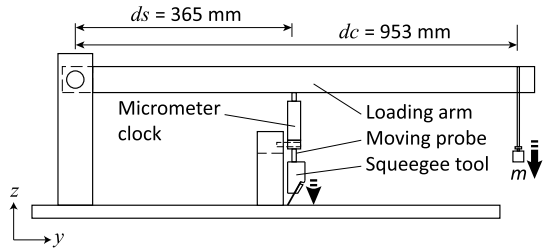

FIGURE 1.29 Custom equipment for measuring squeegee deformation for different loads. *Reproduced with permission from O. Krammer, L.M. Molnár, L. Jakab, A. Szabó, Modelling the effect of uneven PWB surface on stencil bending during stencil printing process, Microelectron. Reliab. 52(1) (2012) 235–240.*

fasten the blade and the blade to transfer the paste through the stencil, as it is illustrated in Fig. 1.28. The overhang size of the blade was 15 mm, its thickness was 200 μm, and its unloaded angle was 60 degrees.

With the constructed measuring equipment, different loads were applied to the squeegee tool through the measuring probe of a fixed dial indicator; and the vertical displacement of the tool was measured by the dial indicator itself. The measuring range of the indicator was 0–10 mm, while its resolution was 1 μm. The loads were applied through a loading arm (Fig. 1.29), and the load force was varied from 22 to 131 N.

The resolution of the load force was 1.9 mN obtained by (1.13):

$$Res = al \cdot \left(\frac{ds}{dc}\right) = 5 \cdot \left(\frac{365}{953}\right) = 1.9 \text{ mN} \tag{1.13}$$

where *al* is the accuracy of applied load weights (5 mN), *ds* is the distance of squeegee from the lever pivot point (365 mm), and *dc* is the distance of load weights from the lever pivot point (953 mm).

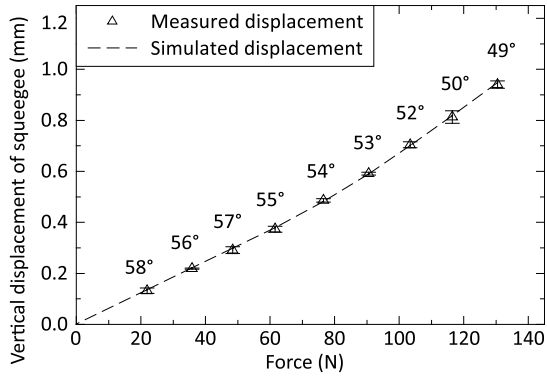

FIGURE 1.30 Measured and calculated displacement of a 200 μm thick, stainless steel squeegee for various loads. *Reproduced with permission from O. Krammer, L.M. Molnár, L. Jakab, A. Szabó, Modelling the effect of uneven PWB surface on stencil bending during stencil printing process, Microelectron. Reliab. 52(1) (2012) 235–240.*

TABLE 1.4 Loaded squeegee angles for a specific printing force of 0.3 N/mm.

Unloaded angle (°)	Overhang sizes			
	6 mm	15 mm	20 mm	25 mm
60	58.9	53.4	48.4	42.1
45	43.5	35.7	28.8	20.5

Source: Data from O. Krammer, L. Jakab, B. Illes, D. Bušek, I.B. Pelikánová, Investigating the attack angle of squeegees with different geometries, Solder. Surf. Mt. Technol. 30(2) (2018) 112–117.

After measuring the deformation of the squeegee, its FEM model was created using a 3D elastic-plastic material model of steel. The movement of this squeegee was not constrained; it was free to move, rotate, and bend in all directions. The measured and simulated results can be seen in Fig. 1.30 and simulated blade angles are indicated along the graph. It can be seen that a squeegee with these initial parameters can bend such an extent that its attack angle decreases to 53 degrees from the initial value of 60 degrees.

In their next work, Krammer et al. investigated further the decrease in attack angle of squeegees, for various overhang sizes (6, 15, 20, and 25 mm) and for the two initial angles of 45 and 60 degrees [37]. They highlighted that in the case of large overhang sizes (e.g., 25 mm) the unloaded squeegee angles of 60 and 45 degrees can decrease to even 42 and 21 degrees, respectively. The changes in the attack angle for the various parameters are listed in Table 1.4.

The expressions for the loaded squeegee angles with the mentioned conditions are given in (1.14) and (1.15) [37]:

$$\alpha_{a|\alpha_u=60^\circ} = 60 - 0.026 \cdot S_O - 0.0276 \cdot S_O^2 \tag{1.14}$$

$$\alpha_{a|\alpha_u=45^\circ} = 45 - 0.0789 \cdot S_O - 0.0363 \cdot S_O^2 \tag{1.15}$$

where α_a is the attack angle, α_u is the unloaded angle, and S_O is the overhang size.

Besides, they found that the deformation of the squeegee is quite similar along its length, denoting that a two-dimensional numerical model can be a correct approach in the investigation of stencil printing [37].

In the numerical modeling of stencil printing, many research works (e.g., in 1.17 and 1.36) utilized the unloaded angle of the squeegee; they analyzed the differences between the unloaded angles of 45 and 60 degrees, for example. Nevertheless, Krammer et al. showed the difference in the numerical results of these models as a function of a decrease in the squeegee attack angle [6]. The change in attack angle and consequently, the increase in the pressure was negligible for the loaded squeegee with an overhang size of 6 mm. Contrary, the differences were noteworthy for longer overhang sizes. In the case of the commonly used overhang size of 15 mm, the decrease in attack angle from 60 to 53.5 degrees resulted in a pressure increment of approximately 22%. The pressure increment was even larger for longer overhang sizes; 45% and even 90% for overhang sizes of 20 and 25 mm, respectively. These changes in pressure indicated that the printing force, the geometry of the squeegee, and eventually, the resultant attack angle should absolutely be taken into account during the numerical modeling of the stencil printing process (Fig. 1.31).

The changes in pressure are illustrated in Fig. 1.32 for the unloaded squeegee angle of 45 degrees. The results were similar to the case of the unloaded squeegee angle of 60 degrees, but the increase in pressure was

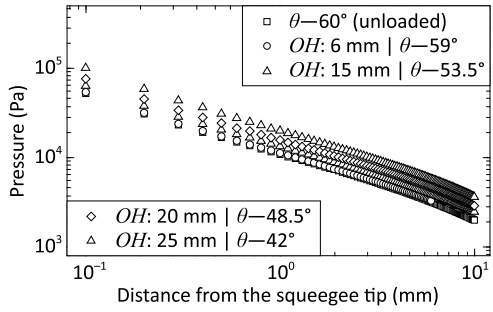

FIGURE 1.31 Pressure values over the stencil (unloaded squeegee angle is 60 degrees). *Reproduced with permission from O. Krammer, K. Dušek, Numerical investigation on the effect of the printing force and squeegee geometry on stencil printing, J. Manuf. Process. 45 (2019) 188–193.*

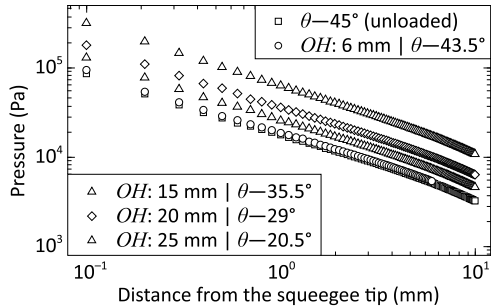

FIGURE 1.32 Pressure values over the stencil (unloaded squeegee angle is 45 degrees). *Reproduced with permission from O. Krammer, K. Dušek, Numerical investigation on the effect of the printing force and squeegee geometry on stencil printing, J. Manuf. Process. 45 (2019) 188–193.*

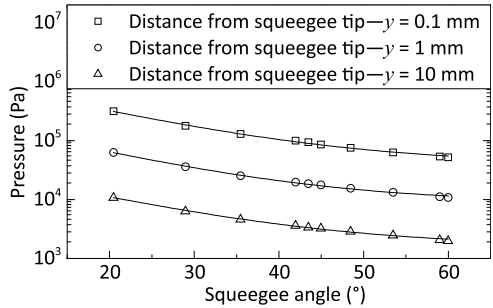

FIGURE 1.33 Pressure as a function of squeegee angle (valid for the investigated fluid properties). *Reproduced with permission from O. Krammer, K. Dušek, Numerical investigation on the effect of the printing force and squeegee geometry on stencil printing, J. Manuf. Process. 45 (2019) 188–193.*

even more pronounced; ~45%, ~102%, and ~250% for the overhang sizes of 15, 20, and 25 mm, respectively [6].

The exponential change in pressure over the attack angle has been presented in Fig. 1.27 for Newtonian fluid properties, and also analyzed for the non-Newtonian case. The pressure values were evaluated at three locations: at a distance from the squeegee tip of 0.1, 1, and 10 mm, and illustrated in Fig. 1.33 [6]. The parameters of the exponential fit (collected in Table 1.5) were also determined for these cases, and the average of the exponential decay coefficient was found to be 0.075. This value of the decay coefficient indicates even a slightly higher increase in pressure for decreasing attack angles in the case of non-Newtonian fluid properties compared to that by Newtonian fluid properties.

As a summary, it was proven that neglecting the squeegee force and/or the exact geometry of the squeegee in the modeling of stencil printing, and thus utilizing inappropriate attack angle, leads to significant calculation

TABLE 1.5 Parameters of the exponential fit to the pressure change over the squeegee angle (Fig. 1.33).

Parameter	$y = 0.1$ mm	$y = 1$ mm	$y = 10$ mm
y_0	40,493 Pa	9002 Pa	1615 Pa
A	1,248,320 Pa	260,551 Pa	40,920 Pa
B	0.074	0.077	0.073

Source: Data from O. Krammer, K. Dušek, Numerical investigation on the effect of the printing force and squeegee geometry on stencil printing, J. Manuf. Process. 45 (2019) 188–193.

errors. In the case of the unloaded squeegee angle of 60 degrees, the error can reach up to 90%, whereas at the 45-degree unloaded angle, the error can reach even 250%. Taking these geometrical parameters into account is therefore strongly recommended for appropriate and valid calculation results in this field. By obtaining more precise and reliable calculation results, the optimization of the stencil printing process could be more productive also for critical assembly methods, like the PIP technology (see Section 1.6).

1.4 Component placement

By the continuous decrease in the size of the surface-mounted components, the accuracy of placement machines is getting more critical, even if the surface-mounted components can self-align during the soldering (see Section 1.5). As mentioned in Section 1.2.1, two types of placement machines are distinguished from the placement head point of view; the pick&place and collect&place heads. From these, collect&place machines (which place typically passive components) are the faster but, the less accurate ones. However, the size of the passive discrete components reduced to 200×100 μm recently. Therefore both the machine capability itself, and the accurate measurement of this parameter are getting attention. Prior to the determination of machine capability, qualifying the measurement system is necessary by a Gage R&R (repeatability and reproducibility) study to decide if the system is appropriate for measuring the particular parameter. This qualification should not be confused with the calibration procedure of that equipment. In this chapter, the procedure of a Gage R&R study will be overviewed. Then, the measurement possibility of placement machine accuracy and the calculation of the machine capability index will be detailed.

1.4.1 Gage R&R study

Gage R&R (repeatability and reproducibility) study is intended for analyzing a measurement system, whether or not it suits measuring a given parameter.

The repeatability characterizes the measurement equipment, that is, estimates variation in measurements taken by a single person. Reproducibility describes the persons, who perform measurements, that is, estimates the variation induced when different operators measure the same items. The study uses more than one person/operator (typically 3), several items owning the parameter to be measured (usually up to 20), and some repeats of the measurements (typically 2−3). The study should be performed randomly in a single-blind experiment, meaning that the operators are blinded, that is, they do not know which part/which repeat actually they measure. After the experiment, the value of *R&R* can be calculated by analyzing variances with the following expression (1.16):

$$R\&R = \frac{\sigma^2{}_{measurement}}{\sigma^2{}_{total}} = \frac{\sigma^2{}_{repeatability} + \sigma^2{}_{reproducibility}}{\sigma^2{}_{repeatability} + \sigma^2{}_{reproducibility} + \sigma^2{}_{item}} \tag{1.16}$$

If the value of *R&R* is below 10%−15%, then the measurement system is qualified for measuring the given parameter. If the *R&R* is higher than 30%, the measurement system is not appropriate for the specific measurement. In between, further actions should be taken, like analyzing if the variance between operators was significant, then training of the operators or upgrading the measurement system.

If the parameter to be measured follows a normal distribution with high certainty, then the variances in (1.16) can be estimated as follows. Consider an R&R study with o operators, p repeats of measurements, and q items. Determine the repeatability first. The range of measurement repeats (*Rmr*) should be calculated for each operator and for each item (1.17).

$$Rmr_{i,k} = \max(mes_{i,1,k}; \ldots; mes_{i,p,k}) - \min(mes_{i,1,k}; \ldots; mes_{i,p,k}) \tag{1.17}$$

where $mes_{i,j,k}$ is the jth measurement result by a given operator (i) for a given item (k) within the repeats (p). Then, the average of *Rmr* values is calculated for each operator separately, resulting in $\overline{Rmr_i}$ for the ith operator (1.18).

$$\overline{Rmr_i} = \frac{\sum_{k=1}^{q} Rmr_{i,k}}{q} \tag{1.18}$$

Next, the average of $\overline{Rmr_i}$ values is determined (1.19).

$$\overline{\overline{Rmr}} = \frac{\sum_{i=1}^{o} \overline{Rmr_i}}{o} \tag{1.19}$$

Note that Eqs. (1.18) and (1.19) could be contracted to one expression, but usually, they are calculated separately because of illustration purposes. The standard deviation and thus the variance of repeatability can be estimated then by dividing (1.19) with a so-called coefficient d_2, resulting in (1.20). The respective coefficient can be obtained from the Table of Control Chart Constants (Table 1.6) [38]. The value of d_2 depends on the subgroup

TABLE 1.6 The d_2 values for estimating the standard deviation.

n	2	3	4	5	6	7	8	9	10	11	12	13
d_2	1.128	1.693	2.059	2.326	2.534	2.704	2.847	2.970	3.078	3.173	3.258	3.336
n	14	15	16	17	18	19	20	21	22	23	24	25
d_2	3.407	3.472	3.532	3.588	3.640	3.689	3.735	3.778	3.819	3.858	3.895	3.931

Source: Data from A.M. Joglekar, Statistical Methods for Six Sigma, John Wiley & Sons, Hoboken, NJ, 2003, ISBN: 0-471-20342-4.

size (n), which is equal to the number of measurement repeats (p) in this case; for example, $d_2 = 1.128$ if the value of measurement repeats is 2.

$$\sigma_{repeatability} = \frac{\overline{\overline{Rmr}}}{d_{2|n=p}} \tag{1.20}$$

For determining the reproducibility, the average of measurement repeats (Xmr) should be calculated for each operator and for each item (1.21).

$$\overline{Xmr_{i,k}} = \frac{\sum_{j=1}^{p} mes_{i,j,k}}{p} \tag{1.21}$$

where $mes_{i,j,k}$ is the jth measurement result by a given operator (i) for a given item (k) within the repeats (p). Then, the average of $\overline{Xmr_{i,k}}$ values is calculated for each operator separately, resulting in $\overline{\overline{Xmr_i}}$ for the ith operator (1.22).

$$\overline{\overline{Xmr_i}} = \frac{\sum_{k=1}^{q} \overline{Xmr_{i,k}}}{q} \tag{1.22}$$

Next, the range of $\overline{\overline{Xmr_i}}$ values is determined (1.23).

$$R_{\overline{\overline{Xmr}}} = \max\left(\overline{\overline{Xmr_1}}; \ldots; \overline{\overline{Xmr_o}}\right) - \min\left(\overline{\overline{Xmr_1}}; \ldots; \overline{\overline{Xmr_o}}\right) \tag{1.23}$$

The standard deviation and thus the variance of reproducibility can be estimated then by dividing (1.23) with the respective coefficient d_2, resulting in (1.24). The subgroup size (n) is equal to the number of operators (o) in this case, for example, $d_2 = 1.693$ if the number of operators is 3.

$$\sigma_{reproducibility} = \frac{R_{\overline{\overline{Xmr}}}}{d_{2|n=o}} \tag{1.24}$$

Finally, the standard deviation of the measured item parameter should be calculated. The average of each and every measurement (all measurement repeats and all operators) for a particular item should be averaged first. Since the average of measurement repeats has already been calculated, it is enough averaging the values of $\overline{Xmr_{i,k}}$ for each item separately, resulting in $\overline{\overline{Xim_k}}$ for the kth item (1.25).

$$\overline{\overline{Xim_k}} = \frac{\sum_{i=1}^{o} \overline{Xmr_{i,k}}}{o} \tag{1.25}$$

Next, the range of $\overline{\overline{Xim_k}}$ values is determined (1.23).

$$R_{\overline{\overline{Xim}}} = \max\left(\overline{\overline{Xim_1}}; \ldots; \overline{\overline{Xim_q}}\right) - \min\left(\overline{\overline{Xim_1}}; \ldots; \overline{\overline{Xim_q}}\right) \tag{1.26}$$

The standard deviation and thus the variance of the items' parameter can be estimated then by dividing (1.26) with the respective coefficient d_2,

resulting in (1.27). The subgroup size (n) is equal to the number of items (q) in this case, for example, $d_2 = 3.078$ if the number of measured items is 10.

$$\sigma_{item} = \frac{R_{\overline{\overline{Xim}}}}{d_{2|n=q}} \tag{1.27}$$

Finally, the variances should be determined for obtaining the *R&R* value (1.16) by calculating the squares of the respective standard deviations ($\sigma_{repeatability}$,$\sigma_{reproducibility}$,σ_{item}).

1.4.2 Measuring component placement position

For determining the machine capability index of component placement machines, an experiment should be carried out. In this, many components (e.g., 1000 pcs. of passive discrete resistors) are placed onto a test board. There are several parameters, which can be varied in the experiment—for example, size of component (e.g., 0603 or 0201), type of placement nozzle (or the sequential number of nozzles on a collect&place head), orientation of a nozzle (0, 90, 180, and 270 degrees)—and the machine capability index can be determined for each variant.

A specific test board should be used, which allows the measurement of component positions after placement. The test board includes reference marks (fiducial points), and the corners of passive components are measured to the marks for determining the component positions (Fig. 1.34). The positional- and rotational offset of a particular component can be calculated then by using Eqs. (1.28)−(1.30) [39].

There are two kinds of measurement principles, namely, absolute measurement and relative measurement. In the case of absolute measurement, the corners of all components are measured to the same reference marks at the corners of the PWB (global fiducial points). Contrary, in the case of the relative measurement method, reference marks are designed onto the test board around each component locations (local fiducial points), and the corners of components are always measured to the respective (closest) reference marks. At the absolute measurement method, the accuracy of measuring equipment (e.g., coordinate measuring machine) plays a key role in the measurement error since usually large distances should be measured between the component corners and the reference marks. In the case of the relative measurement method, much shorter distances should be measured; the primary cause of the measurement error is the accuracy/inaccuracy of the test pattern. For example, if a footprint for a given component has a slight positional offset, a placement offset will be measured even then if the respective component is placed into an absolutely proper position. Test boards, which are designed for the relative measurement method, are prepared, therefore with vacuum technology using a glass substrate. After measuring the components position, the average and the standard deviation can be

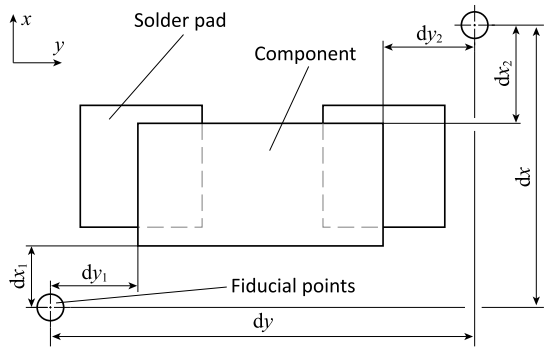

FIGURE 1.34 Test pattern for measuring the component location after placement.

$$x_{offset} = \frac{dx_1 - dx_2}{2} \tag{1.28}$$

$$y_{offset} = \frac{dy_1 - dy_2}{2} \tag{1.29}$$

$$\theta_{offset} = \arctan\left(\frac{dx}{dy}\right) - \arctan\left(\frac{dx - dx_1 - dx_2}{dy - dy_1 - dy_2}\right) \tag{1.30}$$

calculated for the lateral and rotational offsets assuming that the process of component placement follows a normal distribution.

1.4.3 Machine and process capability index

Machine and process capability indices are the quantitative measures regarding how those can perform against specifications. The process or machine output parameter, which is described by the capability index, is assumed following a normal distribution. The capability index actually merges the two parameters of the normal distribution (mean: $\hat{\mu}$ and standard deviation: $\hat{\sigma}$) into one single parameter by comparing the measured process parameters to a theoretical three sigma process. The limits of that theoretical process are the upper and lower specification limits (*USL* and *LSL*), and *T* is the target value (Fig. 1.35).

The process capability ($\hat{C}_p$) and machine capability ($\hat{C}_m$) indices can be calculated by (1.31) for processes and machines where the mean of measured parameter equals to the value of a target ($\hat{\mu} = T$):

$$\hat{C}_{p,m} = \frac{USL - LSL}{2 \cdot k \cdot \hat{\sigma}} \tag{1.31}$$

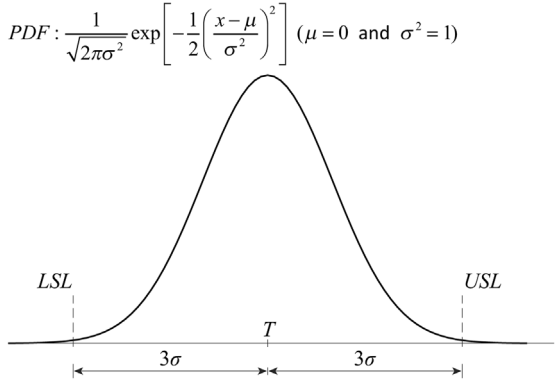

FIGURE 1.35 The probability density function of normal distribution.

where *USL* and *LSL* are the specification limits, k is 3 for process capability, and 4 for machine capability, and $\hat{\sigma}$ is the standard deviation of the measured process parameter. The typical specification limits for component placement are the one-quarter of the component shorter side. For example, the shorter side of a 0603 size resistor is 750 μm; the *USL* and *LSL* are then +187 μm and −187 μm, respectively. In some cases (e.g., high-quality electronics), stricter rules can also be applied like ±100 μm for this component size. Usually, a $\hat{C}_{p,m}$ value larger than 1 (±3σ process) is accepted, whereas a too large value of $\hat{C}_{p,m}$ may indicate unnecessary precision that might be expensive.

If the mean of measured parameter is not equal to the value of a target ($\hat{\mu} \neq T$), that is, the mean is not centered between the specification limits, then the corrected capability index ($\hat{C}_{pk,mk}$) is calculated by (1.32). Note that $\hat{C}_{pk,mk} \leq \hat{C}_{p,m}$.

$$\hat{C}_{pk,mk} = \min\left[\frac{\frac{USL-\hat{\mu}}{k\cdot\hat{\sigma}}; \hat{\mu} - LSL}{k\cdot\hat{\sigma}}\right] \tag{1.32}$$

where $\hat{\mu}$ is the mean of the measured parameter.

By knowing the capability index of a parameter, the fallout or defect rate of that parameter can be estimated. Multiplying the capability index by 3, the interval width regarding the variation of that parameter can be obtained; for example, if the capability index is 1.33, then the interval width is ±4σ. The coverage by this interval (area under the PDF—probability density function), or more precisely, the probability that a parameter lies between $\mu - n\sigma$ and $\mu + n\sigma$ is given by (1.33) [38]:

$$p = P(\mu + n\sigma) - P(\mu - n\sigma) = \Phi(n) - \Phi(-n) = \text{erf}\left(\frac{n}{\sqrt{2}}\right) \tag{1.33}$$

TABLE 1.7 Defect rate in ppm for specific capability indices.

$\hat{C}_{p,m}$	Interval width	Area under PDF	Defect rate in PPM
		$p = \Phi(n) - \Phi(-n)$	$(1-p)\cdot 10^6$
0.33	$\pm 1\sigma$	0.682689492137086	317,311
0.66	$\pm 2\sigma$	0.954499736103642	45,500
1.00	$\pm 3\sigma$	0.997300203936740	2700
1.33	$\pm 4\sigma$	0.999936657516334	63
1.66	$\pm 5\sigma$	0.999999426696856	0.6
2.00	$\pm 6\sigma$	0.999999998026825	0.002

where erf is the Gauss error function (1.34) [38]:

$$\mathrm{erf}(x) = \frac{2}{\sqrt{\pi}} \int_{\xi=0}^{\xi=x} e^{-\xi^2} \mathrm{d}\xi \tag{1.34}$$

The process fallout, defect rate is usually represented in part per million (ppm); typical ppm values for capability indices are collected in Table 1.7.

In the long term, parameters can shift significantly; therefore these defect rates are usually estimated also for a maximum allowed 1.5σ shift (Table 1.8) to take the real-life increase in parameter variation into account. Note that a $\pm 6\sigma$ process shifted by 1.5σ is not equal to a $\pm 4.5\sigma$ process, because the mean is not centered within the specification limits. Therefore the ppm is calculated in this case slightly differently (1.35); defects beyond the far specification limit (opposite to the direction of shift) are omitted:

$$\frac{(1-p)\cdot 10^6}{2} \tag{1.35}$$

1.5 Reflow soldering

As mentioned in Section 1.2, after populating the PWB with components, the assembly travels through an oven, where the solder alloy in the solder paste is reflowed. The methods for heating the assembly include infrared radiation (Chapter 2: Infrared Reflow Soldering), forced convection (Chapter 3: Convection Reflow Ovens), or vapor phase soldering (Chapter 4: Vapor Phase Soldering (VPS) Ovens). The molten, liquid state solder wets the metalized terminals and forms the solder joints (fillet shape). Then, the assembly is cooled down, the solder solidifies and establishes the mechanical and electrical connection between the components and the PWB. The most

TABLE 1.8 Defect rate in ppm in the case of a 1.5σ shift in the parameter.

$\hat{C}_{p,m}$	Sigma levels (1.5σ shift)	Area under PDF	Defect rate in PPM
		$p = \Phi(n) - \Phi(-n)$	$(1-p)\cdot 10^6/2$
1.00	1.5σ	0.866385597462284	66,807
1.33	2.5σ	0.987580669348448	6210
1.66	3.5σ	0.999534741841929	233
2.00	4.5σ	0.999993204653751	3.4

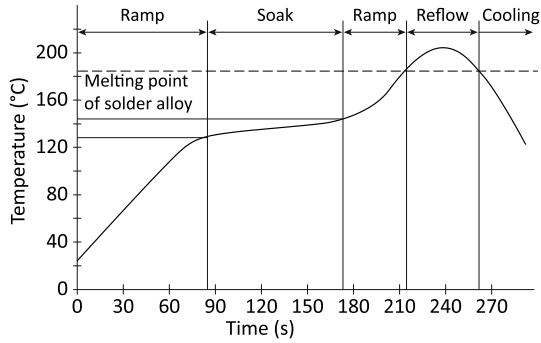

FIGURE 1.36 Typical soak reflow profile.

critical factor in this step from the assembly quality and reliability point of view, the heating profile (reflow profile) will be presented. Besides, phenomena happening during the soldering like component shift or intermetallic layer (IML) formation will be discussed in this chapter. Finally, some reflow failures, soldering defects will be presented briefly.

1.5.1 Reflow soldering profile

The reflow soldering profile is the temperature curve over the duration of assembly soldering. It influences not just the quality of the assembly (whether or not soldering defects will occur), but the reliability as well through influencing the intermetallic compound (IMC) formation within the joint. There are two types of reflow soldering profiles, linear profile (delta type) and soak profile (trapezoidal type). Acquiring temperature profiles by thermocouples is detailed in Chapter 2, Infrared Reflow Soldering. The soak profile can be divided into four to five sections (phases), as illustrated in Fig. 1.36.

TABLE 1.9 Typical reflow parameters.

Phase in reflow profile	SnPb	SnAgCu
Ramp	Temperature range: 0°C–150°C	Temperature range: 0°C–150°C
	Rate of heating: <2°C/s	Rate of heating: <2°C/s
	Duration: 60–150 s	Duration: 60–150 s
Soak	Temperature range: 150°C–183°C	Temperature range: 150°C–183°C
	Duration: 60–90 s	Duration: 60–90 s
Reflow	Peak temperature: 208°C–220°C	Peak temperature: 208°C–220°C
	Duration: 45–90 s	Duration: 45–90 s
Cooling	Down to 130°C	Down to 130°C
	Rate of cooling: 3–4°C/s	Rate of cooling: 3–4°C/s

The first phase of the profile (ramp) is a rapid heating up to 120°C–150°C. This is followed by a soak phase, where the flux in the solder paste is activated, and the temperature distribution over the assembly is homogenized. The ramp and the soak phases together are also called as pre-heating. Then, the next main phase is the reflow of the solder, where the optimal peak temperature depends on the melting point of the alloy. For example, the melting point of the Sn_{63}/Pb_{37} alloy is 183°C, whereas that of the lead-free $Sn_{96.5}/Ag_3/Cu_{0.5}$ alloy is 217°C–219°C. The peak temperature of the profile is set to 20°C–30°C higher than these melting points. The reflow phase can follow the soak phase immediately, or a separate ramp phase can be inserted in between. Lastly, the assembly is cooled down with a predefined rate (cooling phase). The typical parameters of the phases in reflow profiles are collected in Table 1.9 with indicative values. Note that all the solder paste manufacturers have specific recommendations regarding these parameters for their pastes and alloys.

The reflow phase in the temperature profiles is characterized regularly by two parameters. Since components with different heat capacities can heat up with different rates, a difference in temperature (ΔT) might exist in the peak temperature (Fig. 1.37). The ΔT should be below 5°C based on industrial standards, and its value is much more critical for lead-free assemblies, where the peak temperature should be above ~240°C and should not be higher than ~255°C at each and every component. A ΔT too large can cause the

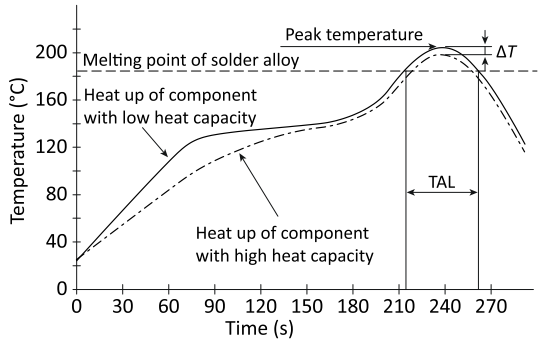

FIGURE 1.37 Parameters for characterizing the reflow phase of the thermal profile.

damage of the components and/or the substrate (including conductive traces) and also can contribute to the excessive warpage of the PWB.

An inappropriate set of the reflow profile parameters can cause various reflow soldering failures. A too low rate of temperature change in the phase of the ramp can cause the slump of the solder paste (paste viscosity would decrease), resulting in the formation of solder bridges. Contrary, a too fast rate of heating would cause the boiling of flux, and particles in the solder paste can be ejected due to excessive outgassing. These solder balls can form short circuits between the leads of fine-pitch components.

The incorrect parameter set of the soak phase can result in a temperature difference too large between low and high heat capacity components, thus increasing the ΔT also. A soak too short can cause insufficient activation of the flux, resulting in excessive oxidation on the metallization and yielding solder wetting problems. A soak too long can also cause excessive oxidation and reduces the throughput of the manufacturing line.

A peak temperature too low would result in brittle "cold" joints, whereas a peak temperature too high would damage the temperature-sensitive components. The other parameter is the time above liquidus (TAL). An appropriate length of this time is necessary for the solder joint formation, but a TAL too long would cause excessive oxidation during the soldering, resulting in quality and reliability issues.

The stage of cooling influences considerably the structure of solder joints and thereby the quality and reliability of joints. A cooling too rapid can cause the cracking of components besides. In the case of high silver-content (>2.8 wt.%) solder alloys, a cooling rate too slow can contribute to the formation of shrinkage defect (Section 1.5.2).

The linear-type reflow profile has a similar shape to the soak-type profile; the difference is that the phase of soak is omitted. This shorter profile can increase the throughput of the manufacturing line. The disadvantage of linear-type profiles is the possibly higher ΔT in the peak temperature. So, this profile is recommended for not too complex assemblies.

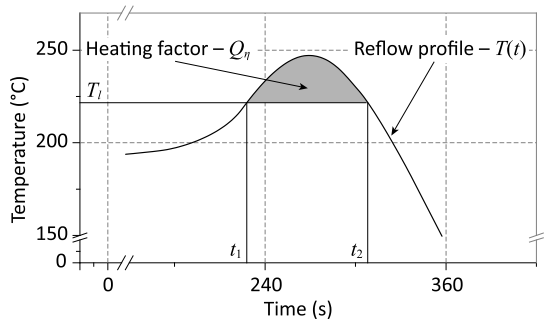

FIGURE 1.38 Representation of the heating factor.

$$Q_\eta = \int_{t_1}^{t_2} (T(t) - T_l)\mathrm{d}t \tag{1.36}$$

During soldering, two phenomena occur mainly. On the one hand, the solder wets the component metallization by the energy of surface tension. On the other hand, an IML will form at the solder–pad interface because of diffusion. Both phenomena and the respective parameters (surface tension and diffusion) depend strongly on the temperature and on the duration of the reflow phase. For addressing these phenomena, a new measure, the "heating factor" has been introduced recently to characterize this part of the reflow profile more precisely than that by the peak temperature and TAL. The heating factor is the area under the curve of the temperature profile in the phase of reflow (Fig. 1.38), and it is defined by (1.36) [40].where Q_η is the heating factor (K s), $T(t)$ is the measured temperature, t_1 is the onset of solder alloy melting, $(t_2 - t_1)$ is the TAL, and T_l is the melting point of the alloy.

1.5.2 Intermetallic layer formation

IMCs inherently form during soldering because of diffusion. Usually, the compounds precipitate in the solder bulk, and at the solder–pad interface are differentiated. IMCs precipitating at the solder–pad interface grow the IML. The properties of this layer essentially affect the quality and reliability of solder joints. The thickness of the IML depends mainly on the reflow profile (Q_η factor), on the solder alloy, and on the pad- and component metallization. If the surface finish on the PWB presents in the form of a thin layer (e.g., immersion tin, immersion silver, OSP), then the main compound of the IML is Cu_6Sn_5 (Fig. 1.39) [41].

Appropriate thickness, in this case, is ~ 2 and $\sim 4\,\mu m$ for lead-bearing and for lead-free solder alloys. The IML is thicker for lead-free alloys

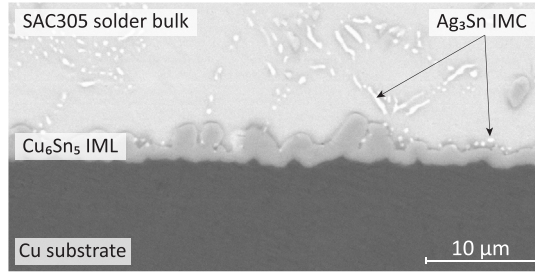

FIGURE 1.39 Intermetallic compound formation during soldering. *Reproduced with permission from O. Krammer, T. Garami, B. Horváth, T. Hurtony, B. Medgyes, L. Jakab, Investigating the thermomechanical properties and intermetallic layer formation of Bi micro-alloyed low-Ag content solders, J. Alloy. Compd. 634 (2015) 156–162.*

because of the high tin content and of the high value of the Cu-Sn interdiffusion coefficient. If the surface finish of the PWB is the so-called ENIG (electroless nickel and immersion gold), the main composition of the IML will be Ni_3Sn_4, and the thickness of the IML will be lower, 1–2 μm due to the lower value of Ni-Sn interdiffusion coefficient. The thickness of the IML should lie between these values. When the layer thickness is smaller than a critical value, fractures can occur inside the solder joint easily. The strength of solder joints increases with increasing reflow time, because Cu_6Sn_5 IMCs also precipitate in the solder bulk, strengthening the joint structure. If the thickness of the IML increases beyond a critical value, there is an onset of a brittle fracture in the IMC layer, resulting in decreased strength with reflow time.

A simple, diffusion limited model for estimating the average of IML thickness (or the rate of growth during soldering) includes the root of time (duration for intermetallic formation), and the temperature dependency by Arrhenius's law (1.37).

$$x\,(\text{mm}) = x_0 + t^n \cdot k_0 e^{(-E_a/RT)} \tag{1.37}$$

where x_0 is the initial layer thickness, which is practically zero by the process of soldering, but has a specific value if the layer growth is examined when carrying out aging tests, like high-temperature storage life (HTSL) tests. In (1.37), t is the time, and n is an exponent with a value lower than 1. The typical values for n are 0.3 and 0.5 for liquid–solid diffusion (e.g., soldering) and for solid–solid diffusion (e.g., HTSL test), respectively. Similarly, parabolic growth kinetics ($n = 0.5$) applies, when the layer growth is controlled by the volumetric diffusion; and subparabolic growth kinetics ($n = 0.3$) applies, when the layer growth is controlled by grain boundary diffusion [42]. E_a is the activation energy (J/mol), R is the universal gas constant, T is the absolute temperature, and k_0 is a preexponential factor. It is common in electronics that the activation energy is expressed in electron-

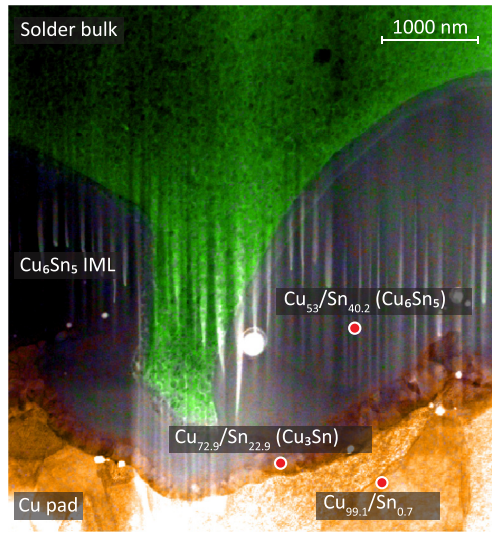

FIGURE 1.40 The intermetallic layer formed during soldering. *Reproduced with permission from O. Krammer, T. Garami, B. Horváth, T. Hurtony, B. Medgyes, L. Jakab, Investigating the thermomechanical properties and intermetallic layer formation of Bi micro-alloyed low-Ag content solders, J. Alloy. Compd. 634 (2015) 156–162.*

volt (eV). In this case, the Boltzmann constant (k_B) should be used instead of R, with the value (and with the unit) of 8.617×10^{-5} (eV/K). During the soldering, the growth rate of Cu_6Sn_5 (η phase) is more pronounced than that of the Cu_3Sn (ε phase). Oppositely, the growth rate of the ε phase is usually larger during life-time tests. Nevertheless, for example, Krammer et al. showed that the ε phase readily grows during soldering, but its thickness reaches only approximately 200 nm [41]. As an example, the element map of an IML over a TEM (transmission electron microscope) dark-field image is presented in Fig. 1.40.

It can be observed in Figs. 1.39 and 1.40 that the shape, the microstructure of the IML is usually not simply layer-type, but scallop-type. For describing the IML growth, more specific models than the simple one in (1.37) exist also.

According to the review of Tu and Zeng, the growing mechanism of the Cu_6Sn_5 IML can be described by two mass fluxes [43]. One of them is the diffusion of Cu atoms through the valley between every two scallops. The other flux is the so-called ripening reaction among the scallops. The growth equation was given as (1.38) [43]:

$$r^3 = \int \left(\frac{\gamma \Omega^2 D C_0}{3 N_A L R T} + \frac{\rho A \Omega v(t)}{4 \pi m N_p(t)} \right) dt \tag{1.38}$$

where r is the radius of an average size scallop, γ is the surface energy of the scallop, Ω is the average atomic volume, D is the atomic diffusivity in the molten solder, C_0 is the solubility of Cu in the molten solder, N_A is the Avogadro's number, L is the numerical relating the mean separation between scallops and the mean scallop radius, R is the Boltzmann coefficient, T is the absolute temperature, ρ is the density of Cu, A is the total area of the solder/Cu interface, v is the consumption rate of Cu in the reaction, m is the atomic mass of Cu, N_p is total number of scallops at the interface. In the equation, the first term is the interfacial reaction term, while the second term is the ripening term.

According to the findings of Krammer et al., the IML structure depends on the silver content of the solder alloy [41]. High Ag-content alloys form a more layer-type IML, whereas it is more scallop-type in low Ag-content alloys after the soldering. In their experiment, at high silver-content solder alloys, the ratio between the reaction term and the ripening term was shifted toward the reaction term due to the higher number of scallops (higher N_p). Contrary, in the case of low Ag-content solders, the ratio between the reaction term and the ripening term shifted toward the ripening term because of the lower number of scallops.

The rate of IML growth during soldering and life-time tests is also affected significantly by the silver content in the solder alloy. Silver forms the Ag_3Sn IMC with tin during soldering, and this IMC precipitates around the primary β-Sn dendrites. The Ag_3Sn IMCs can adsorb on the surface of the Cu_6Sn_5 IML, and they can obstruct the growing of that layer [44]. If the silver content in the solder is higher—especially in the case of alloys with hypereutectic silver compositions (>2.7 wt.%)—more Ag_3Sn IMC can adsorb, and thus lower IML can form. The different rate of IML thickness growth during Thermal Shock tests between low- and high silver-content alloys can be explained by the different extent of grain-boundary diffusion [45]. Krammer et al. showed that the number of grain boundaries along a unit of length correlates with the rate of IML growth, and a higher number of grain boundaries were found at high silver-content alloys than at low silver-content ones [41] (Fig. 1.41).

Finally, the silver content in the alloy affects both the quality and reliability of solder joints by the differing development of Ag_3Sn IMCs as the function of the cooling rate during soldering. Generally, three types of Ag_3Sn compounds morphology can be found: particle-like, needle-like, and also plate-like. The sequential evolution or modification of Ag_3Sn compounds during a decreasing cooling rate is usually particle-like → needle-like → plate-like [46]. These plate-like Ag_3Sn IMCs are very brittle, and during the cool-down phase of the reflow, they can initiate cracks in the solder joints and can result in the so-called shrinkage defect [47]. Additionally, they can promote crack propagation along their boundary during the lifetime of electronic circuits, thus reducing their reliability [48].

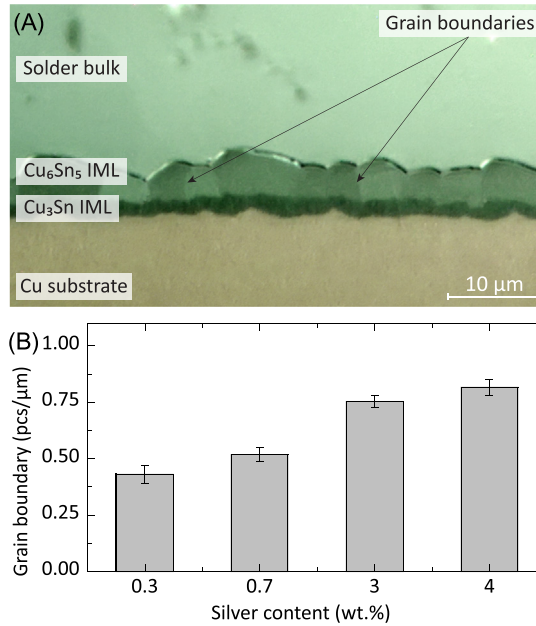

FIGURE 1.41 Grain boundaries in the solder joint: (A) polarized optical image of a low silver-content joint cross-section; (B) the specific amount of grain boundaries over silver content. *Reproduced with permission from O. Krammer, T. Garami, B. Horváth, T. Hurtony, B. Medgyes, L. Jakab, Investigating the thermomechanical properties and intermetallic layer formation of Bi micro-alloyed low-Ag content solders, J. Alloy. Compd. 634 (2015) 156–162.*

If the silver content in the solder is low, there will be less Ag_3Sn IMC inside; the large Ag_3Sn plates may effectively be minimized by using SnAgCu alloys with hypoeutectic silver compositions of approximately 2.7 wt.% or below [49]. The difference can be observed by comparing Fig. 1.39 and Fig. 1.42. Therefore besides the cost reduction, the decrease of silver content can have a positive effect on the quality of solder joints as well. However, the application of such reduced silver solder compositions in SnAgCu alloys will require careful evaluation with respect to their thermo-mechanical fatigue properties [50].

1.5.3 Component movements during reflow soldering

During soldering, forces acting on electronic components include the surface tension and the hydrostatic force exerted by molten solder. In the case of large-scale components (e.g., DPAK packages), inhomogeneity in temperature may results in inhomogeneity in the surface tension force, causing component skewing and/or open joint formation. A similar problem (the so-called "tombstone" effect) can arise if there is a difference in the onset of

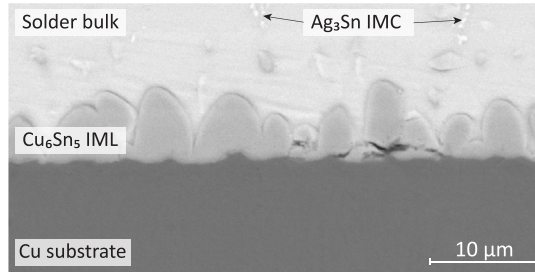

FIGURE 1.42 Structure of a low silver-content (~0.3 wt.%) solder joint. *Reproduced with permission from O. Krammer, T. Garami, B. Horváth, T. Hurtony, B. Medgyes, L. Jakab, Investigating the thermomechanical properties and intermetallic layer formation of Bi micro-alloyed low-Ag content solders, J. Alloy. Compd. 634 (2015) 156–162.*

solder melting between the opposite sides of two-terminal components. In this case, one end of the component is lifted by the torque arising at the opposite side, where the solder is already in the molten state. This phenomenon can cause the formation of open joints. Contrary, the forces arising during soldering can also aid in eliminating soldering failures. If a surface-mounted resistor or a capacitor is misplaced by the component placement machine, the surface tension force can restore the component to its central position; this phenomenon is called component self-alignment.

The first force models, which investigated the component movements during reflow soldering, were two-dimensional and mainly focused on the tombstone effect [51]. The model of Wassink and Verguld [51] assumed that there was no solder on the opposite face of the component, and it considered the solder fillet as a straight line instead of a curve. In addition, the model, due to its simple manner, did not take the hydrostatic pressure of the liquid solder into consideration. A more complex model has been described by Ellis and Masada [52], which took the hydrostatic and capillary pressure of the molten solder into account and considered the solder fillet as a curve. However, it was also a two-dimensional model like the Wassink–Verguld model. The model comprised further simplifications; it assumed that the component is brick-shaped (i.e., rectangle in 2D), and its mass center was in the geometrical center of the body. Also, the model presumed that the corner of the component was always in contact with the soldering surface (pad), and it rotated around that point. Though, the model included many specific details—the meniscus of the solder was not considered to be a straight line, the force due to hydrostatic pressure was taken into consideration, and the chip component was allowed to be displaced along its pad length to illustrate the effect of component misplacements.

Next, Krammer presented a three-dimensional force model for addressing the component movements during reflow soldering [53]. Based on that model, mainly five forces are acting on the chip components during reflow

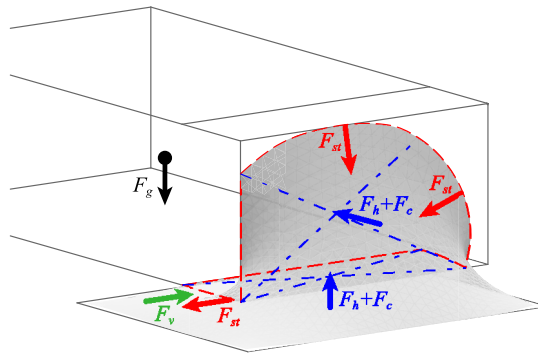

FIGURE 1.43 Forces acting during solder on a component misplaced parallel to its shorter side. *Reproduced with permission from O. Krammer, Modelling the self-alignment of passive chip components during reflow soldering, Microelectron. Reliab. 54(2) (2014) 457–463.*

soldering (Fig. 1.43). The force originating from surface tension ($\vec{F_{st}}$) is acting on the boundary contact line of the three phases, which are the solder, gas, and component metallization. The forces originating from hydrostatic ($\vec{F_h}$) and from capillary ($\vec{F_c}$) pressure are acting on the area of the component metallization, while the force originating from dynamic friction ($\vec{F_v}$) depends on the mass of the liquid solder, which should be actuated. The fifth force is due to the gravitational acceleration ($\vec{F_g}$) if there is no solder, for example, at the opposite side and dynamic friction between component and pad metallization should be calculated.

In the case of component misplacements (which are due to the placement machine inaccuracy), the main force promoting the self-alignment is originating from the surface tension of the liquid solder. The surface tension force acts on the appointment place of the three phases. In general case, the appointment place of a three-phase system is a space curve, which is called the contact line in soldering technologies. Therefore the net force originating from the surface tension can be obtained by integrating the term of surface tension (γ_{LG}) along the contact line (1.39) [53]:

$$\vec{F_{st}} = \int_v \gamma_{LG} \mathrm{d}\,\vec{l} \tag{1.39}$$

The forces, originating from hydrostatic- and capillary pressures of the molten solder, push the component out from the solder. These forces are acting on the vertical face- and bottom side metallization of the component, as illustrated in Fig. 1.43 ($F_h + F_c$). The capillary pressure is the pressure difference between the two sides of a curved liquid surface, and that pressure drop across the fillet (ΔP) can be determined by the Laplace's equation. Therefore the force originating from hydrostatic- and capillary pressures (F_p) can be determined by integrating the pressure along the surface of the

component metallization (1.40) [53]. However, this is a generalized expression, and in reality, the force due to capillary pressure does not act on the component but balances the change in hydrostatic pressure over the curved liquid surface based on the theorem of pressure continuity.

$$\vec{F_p} = \int_{A_{cs}} \left(\rho_s g \cdot h(\vec{r})\right) \mathrm{d}\,\vec{S} + \int_{A_{cs}} \left(\gamma_{LG}\left(\frac{1}{r_1(b(r\rightarrow))} + \frac{1}{r_2(b(r\rightarrow))}\right)\right) \mathrm{d}\,\vec{S} \tag{1.40}$$

where A_{cs} is the surface of component metallization, ρ_s is the density of molten solder, $r\rightarrow$ is the spatial vector, $h(r\rightarrow)$ is the height of liquid column, which is infinitesimally close to the point designated by the vector $r\rightarrow$ on the surface A_{cs}, $b(r\rightarrow)$ is the point on top of the liquid column, where the capillary pressure can be calculated.

The dynamic friction between liquid and solid phases slows the movement of components. The force originating from the dynamic friction between a solid and a liquid phase can be described by the Newton Viscous Force equation [54]. The liquid (molten solder) can be considered as a series of horizontal layers. The top layer in the molten solder is infinitesimally close to the bottom side metallization of component, and its velocity is equal to the speed of the component movement. The velocity of the bottom layer is 0, equivalent to the speed of the pad. Thus the decelerating force due to dynamic friction is (1.41) [53]:

$$\vec{F_v} = \int_{A_{cs}} \frac{\eta_s \cdot (v\rightarrow - \vec{v_0})}{d(r\rightarrow)} \mathrm{d}S \tag{1.41}$$

where η_s is the viscosity of the molten solder, $v\rightarrow$ is the speed vector of component movement, $\vec{v_0}$ is the velocity of a point at d distance from the A_{cs} surface, which is zero if it is on the pad, and not zero if the point is located on the surface of the molten solder, $d(r\rightarrow)$ is the distance between the pad or the surface of the solder and the location under investigation, which is designated by vector $\vec{r}$ on surface A_{cs}.

For determining forces by the hydrostatic pressure and surface tension, the solder profile should be known, it should be calculated. Two main methods are available for determining the solder profile; one is based on the principle of pressure continuity, while the other one is based on minimizing the energy originating from the surface tension and the potential energy due to gravity.

The principle of pressure continuity claims that in a static liquid, no pressure gradients exist horizontally, and the pressure in the vertical direction changes proportionally to the distance from the liquid surface (i.e., proportionally to the height of liquid column) [52]. Consequently, since the fillet profile decreases in height as a function of the distance from the chip component, a continuously changing pressure difference must exist along the curve of profile. Generally,

Laplace's equation is used to relate the pressure drop (ΔP) and the fillet surface geometry. In its most general form, the equation is (1.42):

$$\Delta P = \gamma \cdot \left(\frac{1}{r_1} + \frac{1}{r_2} \right) \tag{1.42}$$

where r_1 and r_2 are the radii of curvature of the fillet measured normal to the surface of the component face metallization. For two-dimensional models, the solution is (1.43) [52]:

$$\frac{\mathrm{d}^2 y}{\mathrm{d}x^2} = \frac{1}{\gamma}(\rho g y - \Delta P_0) \cdot \left[1 + \left(\frac{\mathrm{d}y}{\mathrm{d}x} \right)^2 \right]^{3/2} \tag{1.43}$$

where γ is the surface tension coefficient, while ΔP_0 is $P_{solder} - P_{atmosphere}$.

Eq. (1.43) is a second-order nonlinear differential equation, which solution defines the fillet profile. Once the correct profile is known, the points at which the surface tension forces and pressure forces act can be computed. In this approach, two boundary conditions are needed (i.e., the solder wets until the end of the pad, and the height of the solder fillet is equal to the height of the component), and ΔP_0 is an unknown. The problem that for a three-dimensional force model, this principle cannot be used because the equation system would be too complex.

Calculating the solder profile by minimizing the energy rests on that the equilibrium shape of a liquid meniscus at a liquid−gas phase boundary of a system—in which solid, liquid, and gaseous phases coexist—is given by the balance of forces acting on the system. In the case of reflow soldering, the liquid phase is the molten solder, the solid phases are the soldering surfaces (component metallization and pad), while the gaseous phase is the atmosphere of the reflow oven altered by the evaporation of flux. When the boundary condition is that the solder wets until the end of the metallization (the contact angle depends on the volume of the solder), the energy of the system which should be minimized is given by Eq. (1.44) [55]:

$$E = E_S + E_G \tag{1.44}$$

where E_S is the energy originating from the surface tension (1.45) [56]:

$$E_S = \int_A \gamma \mathrm{d}S \tag{1.45}$$

and E_G is the potential energy due to gravity (1.46) [57]:

$$E_G = \iiint_{x\ y\ z} \rho \cdot g \cdot z \cdot \mathrm{d}x\mathrm{d}y\mathrm{d}z \tag{1.46}$$

where γ is the surface tension coefficient, ρ is the solder density, g is the gravitational acceleration, and A is the surface of solder fillet.

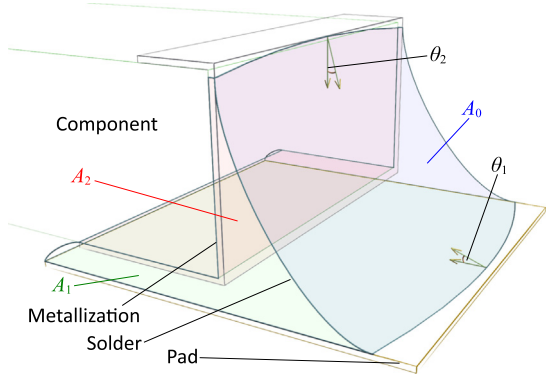

FIGURE 1.44 Boundary condition that the solder does not reach the end of the metallization. *Reproduced with permission from O. Krammer, Modelling the self-alignment of passive chip components during reflow soldering, Microelectron. Reliab. 54(2) (2014) 457–463.*

When the boundary condition is set in a way that the end of the pad is not reached by the solder (which is very common for lead-free solders), then the contact angle is equal to the wetting angle. In this case, the energy term due to the surface tension can be determined by the following. At first, divide the surface of the solder into three parts; A_0, A_1, and A_2 for indicating the surface on the liquid–gas boundary and the surface of the liquid–solid boundaries, respectively (Fig. 1.44).

Then, the energy originating from the surface tension forms as (1.47):

$$E_S = \int_{A_0} \gamma_{LG} \mathrm{d}S + \int_{A_1} \gamma_{LS_1} \mathrm{d}S + \int_{A_2} \gamma_{LS_2} \mathrm{d}S \tag{1.47}$$

where γ_{LG} is the surface tension coefficient between the liquid–gas boundary and γ_{LSi} is the surface tension coefficient between the liquid–solid boundary.

Besides, the Young equation claims that in a static liquid, the balance between the surface tensions is the following (1.48):

$$\gamma_{LS} = \gamma_{SG} - \gamma_{LG} \cdot \cos\theta \tag{1.48}$$

By substituting (1.48) into (1.47) and by omitting the zero value terms, the following equation can be obtained (1.49) [58]:

$$E_S = \int_{A_0} \gamma_{LG} \mathrm{d}S + \int_{A_1} -\gamma_{LG} \cdot \cos\theta_1 \mathrm{d}S + \int_{A_2} -\gamma_{LG} \cdot \cos\theta_2 \mathrm{d}S \tag{1.49}$$

where A_0 is the boundary area of the solder and the gas, A_1 is the boundary area of the solder and the pad, A_2 is the boundary area of the solder and the component metallization, θ_1 is the wetting angle on the contact line of solder and pad, and θ_2 is the wetting angle on the contact line of solder and component

metallization. Minimizing the energy term (1.44) can be performed by various methods and software tools, for example, by numerical modeling and by gradient descent method applied in the so-called tool Surface Evolver [59].

1.6 Pin-in-paste technology

Through-hole components cannot be substituted entirely by surface-mounted ones, and they are used even today, mainly on two application areas. On the one hand, the mechanical strength of through-hole joints can be larger than that of surface-mounted joints by even one order of magnitude. Therefore connectors in high-reliability devices are still used in the through-hole form. On the other hand, the continuous decrease in the size of surface-mounted components leads to the problem that heat dissipation became constrained to a smaller area, thereby reducing the power capacity of small factor surface-mounted components. This implies that through-hole components are used still in power electronics, and for high current applications.

The traditional mass soldering method for through-hole components is the so-called wave soldering. This technology needs 200−300 kg of solder to be heated up to 280°C−300°C, thus requiring a large amount of energy. Omitting this technology and using reflow soldering technology for both the surface-mounted and through-hole components would, therefore be beneficial from the energy consumption and environmental implication points of view. That is why the reflow soldering of through-hole components (PIP technology) started spreading in the early 2000s. This raised two requirements against the through-hole components: they should withstand the peak temperature of reflow soldering (up to 250°C) and should be packed in a form that component placement machine can handle them.

1.6.1 Steps of pin-in-paste technology

The steps of PIP technology are quite similar to the steps of reflow soldering technology. The only difference is the apertures that are opened (formed) also for through-hole components in the stencil (Fig. 1.45).

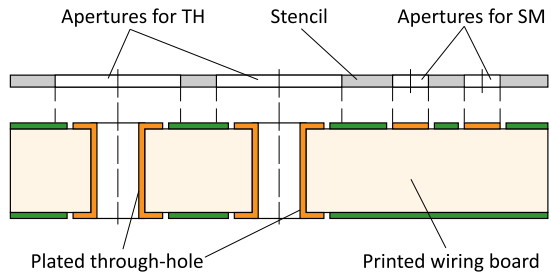

FIGURE 1.45 Stencil for pin-in-paste technology.

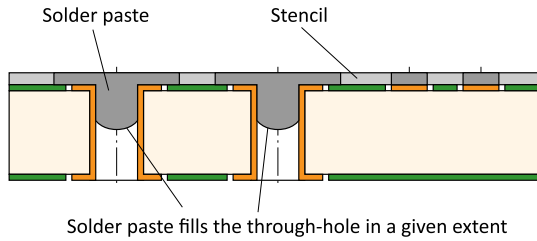

FIGURE 1.46 Pin-in-paste technology—stencil printing.

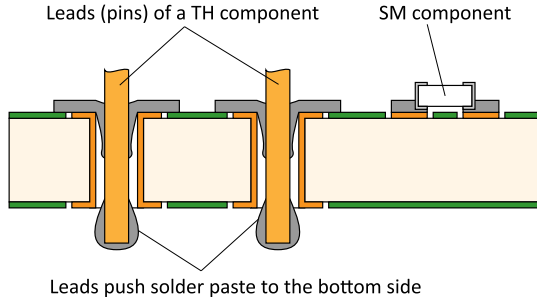

FIGURE 1.47 Pin-in-paste technology—component placement.

During stencil printing, the solder paste fills the through-holes in a given extent depending on the printing speed, on the squeegee attack angle, and on the through-hole diameter (Fig. 1.46). The through-hole filling of solder paste affects significantly the quality and reliability of the finally formed solder joints. Thus its value is carefully designed (Section 1.6.2) and controlled in this technology.

As a next step, the components are placed with automatic placement machines. Special placement heads (like dual inline package insertion heads) are used for the through-hole components occasionally, but in many cases, the same kind of nozzles can be used for both TH and SM components. The leads of the through-hole components tear the solder paste in the plated hole and push a part of the paste to the bottom side (Fig. 1.47). Under optimal conditions, this part of the solder paste will form the bottom side meniscus and will wet back to the plated hole during reflow soldering.

Lastly, the solder joints are formed by the same process as in traditional reflow soldering; the assembly is heated up above the melting point of the solder alloy, the solder wets the components' metallization and forms the solder joints (Fig. 1.48).

Care should be taken that, on the one hand, a larger amount of solder paste is necessary for through-hole components than for surface-mounted ones. On the one hand, the hole-filling by the solder paste (Fig. 1.46) cannot

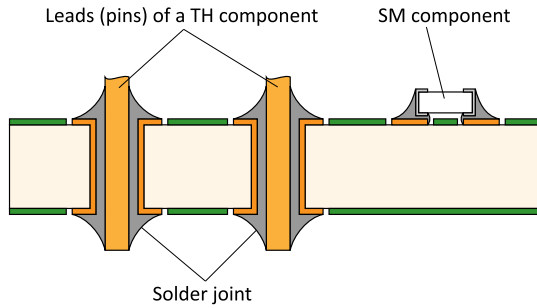

FIGURE 1.48 Pin-in-paste technology—soldering.

be inspected by SPIs (solder paste inspection machines). Thus PIP technology demands much tighter control of the process of stencil printing. Actually, the lack of possibility for inline, 100% inspection of hole-filling exhibits the biggest disadvantage of PIP technology. Only offline inspection is possible by utilizing X-ray machines with tilted detectors.

1.6.2 Calculating solder paste volume for pin-in-paste technology

Determining the optimal amount of solder paste for soldering through-hole components by PIP technology is the critical step from the electronic devices' quality and reliability point of view. Especially, because the 100% inspection of solder pastes deposited for the TH components is not feasible at the moment. Zarrow was the first who described the necessary solder paste volume for PIP technology. He took the volume of solder within the plated through-hole and the shrinkage factor of the solder paste into account (1.50) [60]:

$$P_{volume} = \frac{1}{S}\pi \cdot h\left({r_{hole}}^2 - {r_{lead}}^2\right) \tag{1.50}$$

where S is the shrinkage factor, h is the thickness of the Printed Circuit Board, r_{hole} is the radius of the plated-hole, and r_{lead} is the radius of the component lead. The shrinkage factor of the solder paste is regularly 0.5, since half of the volume is flux, and only half of the volume contributes to the solder joint formation. This expression underestimates the necessary volume, because the volume of solder fillet (defined by the solder meniscus) is neglected.

A more appropriate expression was given by Coleman, which also took the volume of the solder fillet into account (1.51) [61]:

$$P_{volume} = \frac{1}{S}\left[\pi \cdot h\left({r_{hole}}^2 - {r_{lead}}^2\right) + 2 \cdot 0.215 \cdot {r_{fillet}}^2 \cdot 2\pi\left(0.2234 \cdot r_{fillet} + r_{lead}\right)\right] \tag{1.51}$$

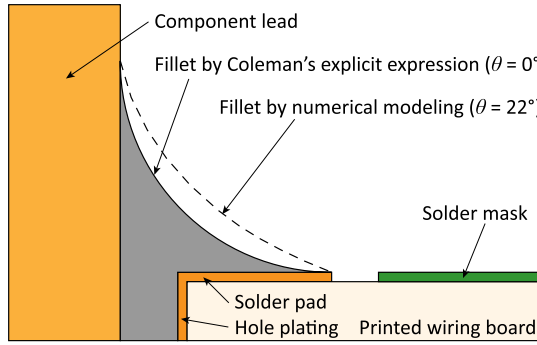

FIGURE 1.49 Solder profiles by Coleman's expression, and by numerical modeling (θ is the wetting angle).

This expression assumes that the solder wets the lead of the component exactly to the height, as the distance of the lead from the edge of the pad (r_{fillet}), as illustrated in Fig. 1.49. Furthermore, it assumes that the fillet is defined by a quarter arc of a circle, and the volume of the fillet is calculated by using Pappus's second centroid theorem [62]. This theorem claims that assuming that the rotating plane curve does not cross the axis, the solid's volume is equal to the length of the circle described by the plane curve's centroid multiplied by the area of the plane curve. Though (1.51) defines the necessary volume more precisely than (1.50), it is still a rough approximation. The fillet of a typical solder joint is more convex than a quarter arc of a circle (Fig. 1.49, dashed line), and the wetting angle is always higher than 0 degree, for example, 22 degrees for a $Sn_{96.5}Ag_3Cu_{0.5}$ alloy. Consequently, (1.51) underestimates the volume of the fillet and thereby also the volume of the solder paste necessary for TH components in PIP technology.

For obtaining the precise volume of solder joint for through-hole components, profile calculations can be performed by numerical modeling, which was mentioned in Section 1.5.3, and correction factors might be determined for Coleman's expression. The appropriate solder paste volume for through-hole components can be determined then by multiplying Coleman's expression with these factors. As an example, Krammer et al. determined correction factors considering both circular and square cross-section leads and various fillet radiuses [63]. Based on their calculations, the correction factor is (1.52) [63]:

$$\begin{aligned} C_{circle} &= 1.523 - 0.125 \cdot r_{fillet} + 0.1335 \cdot r_{lead} \\ C_{square} &= 1.243 + 0.1241 \cdot r_{fillet} - 0.006 \cdot edge\_length_{lead} \end{aligned} \tag{1.52}$$

The amount of solder paste, which should be pushed into the plated holes, is determined then, by subtracting the volume of stencil aperture from the necessary volume. Regularly, the hole-filling of the solder paste should be around 50%.

1.6.3 Controlling the solder paste deposition for pin-in-paste technology

The quality and reliability of PIP technology are greatly affected by the hole-filling of the solder paste. Both too low and too large amounts of solder paste can result in the formation of voids within the solder joints or in an insufficient wetted area by the solder on pads (solder rings). The hole-filling by the solder paste can be influenced by the stencil design and by the process parameters of stencil printing. If the diameter of a plated hole is too large (e.g., twice the diameter than the thickness of PWB), the hole-filling by solder paste can usually be also greater than the predefined value. In this case, the solder paste at the bottom side (pushed through by the component lead) might not wet back to the plated hole and can fall down from the lead or can remain at the end of the lead. The condition of solder wet-back can be described by the balance of two forces (1.53), the force due to surface tension, and by the gravity force.

$$F_{grav} = \rho V g \ll F_{surf.tens.} = 2\pi r \cdot \gamma_{LG} \cdot \cos\theta \tag{1.53}$$

where ρ is the density of solder ($\sim$7300 kg/m^3 for lead-free solders), V is the volume of solder pushed to the bottom side by the lead of through-hole component (note that the volume of solder is the half of the volume of paste because of shrinkage), g is the gravitational acceleration, r is the radius of component lead, γ_{LG} is the surface tension of solder ($\sim$550 mN/m for lead-free alloys), and θ is the wetting angle.

For appropriate solder wet-back, the force due to surface tension should be much larger. For this purpose, volume V should be reduced, which can be achieved by stencil webbing, that is, by designing crosses into the apertures (Fig. 1.50). With this design, the hole-filling by solder paste can effectively be reduced.

If the diameter of a plated hole is too small (e.g., half the diameter than the thickness of the PWB), the hole-filling by solder can be insufficient. In

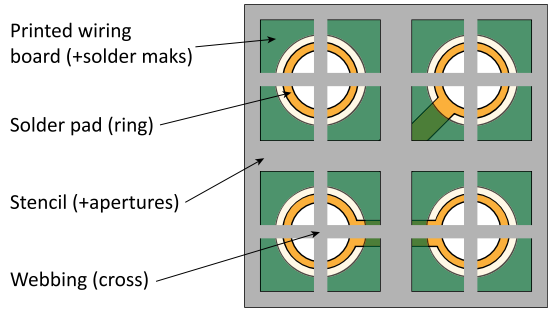

FIGURE 1.50 Stencil webbing (designing crosses into apertures) for reducing the hole-filling by solder paste in pin-in-paste technology.

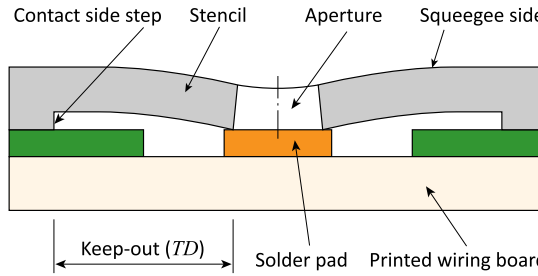

FIGURE 1.51 Keep-out distance (*TD*) necessary for achieving complete stencil contact with the solder pad.

this case, preform solders (preshaped, fluxless solders) or step stencils can be used. Step stencils exhibit selective increment in thickness ($\sim 25-75$ μm) at specific areas either on the top (squeegee) or the bottom (contact) side of stencil-foil. The thicker areas are located typically at the apertures for through-hole components or similarly at the apertures for ceramic BGA packages. The design rules for step stencils are overviewed in the standard of IPC-7525 [64]. It suggests a minimum distance (keep-out rule $K_1 = 36 \times step\_thickness$), which should be kept between a stencil aperture and the stencil-step so that the difference in the stencil levels does not result in printing failures. The standard defines that the same design rules apply for both types of step stencils; either the step is formed on the squeegee side or on the contact side. However, keep-out rule K_1 is only a rough estimation for stencils with steps on their bottom side because neither the thickness nor the material of stencil foil is taken into consideration. These parameters affect the deformation of stencil loaded by the squeegee during printing, and determine whether or not a stencil can bend down completely to a solder pad, which is located nearby to the edge of a stencil step (Fig. 1.51).

Krammer et al. investigated the stencil deformation during stencil printing for determining keep-out rules for stencils with steps on the contact side [36]. FEM simulations were carried out in their work by varying differences in stencil levels (step heights: $0-90$ μm) and stencil foil thicknesses ($75-150$ μm). Based on their results (Fig. 1.52), the necessary keep-out distance is much larger than that recommended by the standard of IPC7525. They also found that in the range of difference of $0-60$ μm, the specified keep-out distance is nearly linearly proportional to the step height and to the foil thickness (1.54) [36]. Note that the results of this investigation are valid for the generally used specific printing force of 0.3 N/mm.

$$TD = C \cdot h \cdot d \tag{1.54}$$

where *TD* is the necessary keep-out distance (mm), *C* is a coefficient of 1.6 (μm^{-1}), *h* is the stencil step height (μm), and *d* is the stencil foil thickness (μm).

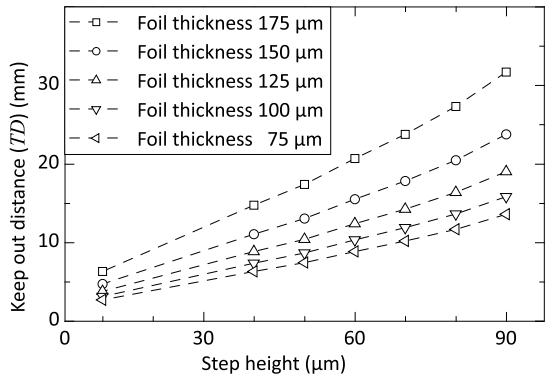

FIGURE 1.52 Keep-out distances (*TD*) as a function of step height and stencil foil thickness. *Reproduced with permission from O. Krammer, L.M. Molnár, L. Jakab, A. Szabó, Modelling the effect of uneven PWB surface on stencil bending during stencil printing process, Microelectron. Reliab. 52 (1) (2012) 235–240.*

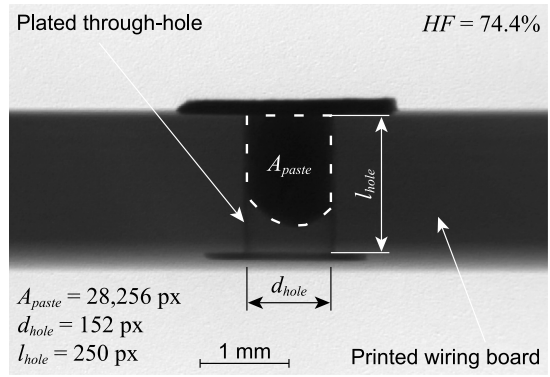

FIGURE 1.53 Calculating the hole-filling in X-ray images (image resolution: 6.2 µm/px; through-hole diameter: 942 µm). *Reproduced with permission from P. Martinek, O. Krammer, Analysing machine learning techniques for predicting the hole-filling in pin-in-paste technology, Comput. Ind. Eng. 136 (2019) 187–194.*

Process parameters of stencil printing also affect the hole-filling of solder paste in PIP technology. The optimization of the respective parameters, for example, printing speed can be performed by numerical modeling, or recently even by utilizing machine learning techniques. Martinek and Krammer analyzed various machine learning-based methods for predicting hole-filling in PIP technology [65]. The analyzed methods included the following: artificial neural networks (ANN) trained by Bayesian Regularization or by Levenberg–Marquardt method; adaptive neuro-fuzzy inference systems (AFNIS) with Gaussian and Triangular input membership functions; gradient boosted decision trees. They validated the prediction methods by

measuring the hole-filling of solder paste at different printing speeds (20−70 mm/s) and at different hole diameters (0.8, 1.0, 1.1, and 1.4 mm). The measurements were carried out by utilizing side-view X-ray images about the hole-filling of solder pastes (Fig. 1.53).

They analyzed then the prediction capability of investigated methods both for complete dataset and for incomplete datasets [65]. The latter means that given measured input parameter values were completely excluded from the training data, and the corresponding predicted values of hole-filling were compared to the measured values. The excluded values in four different test scenarios were the following: excluding all data with a hole diameter of 1.0 mm; excluding all data with a hole diameter of 1.1 mm; excluding all data with a printing speed of 40 mm/s; and excluding all data with a printing speed of 60 mm/s. This approach investigated the situation in manufacturing in a possible example, where the assembly of a new product was initiated, which product contained completely different hole-diameters than the products have been assembled before. In the case of complete datasets, the error of the predicted hole-filling values compared to the measured ones, by calculating the mean of absolute percentage error (MAPE). They found that the machine learning techniques exhibited quite low values of error in the prediction; the average MAPE values were below 1.5%−1.7% for all cases (Fig. 1.54).

In the case of incomplete datasets, the MAPE values increased significantly, meaning that machine learning-based methods are sensitive for the prediction of values completely missing from the training dataset. However, the performance was still acceptable in most cases (Fig. 1.55).

After analyzing and optimizing all of the evaluated methods for their experiment, the ANN trained with BR (Bayesian Regularization) method provided the best results. This method was recommended by Martinek and

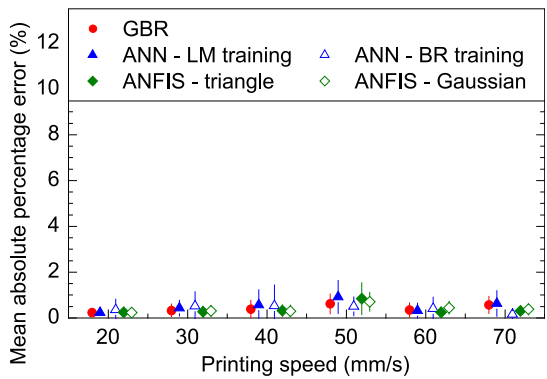

FIGURE 1.54 Prediction errors for hole-diameter of 1.0 mm over the printing speed—trained by the full dataset. *Reproduced with permission from P. Martinek, O. Krammer, Analysing machine learning techniques for predicting the hole-filling in pin-in-paste technology, Comput. Ind. Eng. 136 (2019) 187−194.*

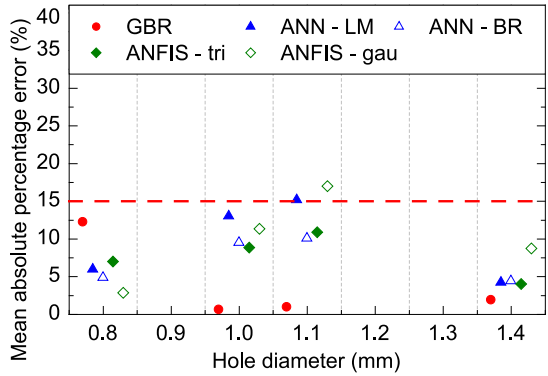

FIGURE 1.55 Prediction errors for incomplete dataset over the hole-diameter—printing speed of 40 mm/s was excluded from the training. *Reproduced with permission from P. Martinek, O. Krammer, Analysing machine learning techniques for predicting the hole-filling in pin-in-paste technology, Comput. Ind. Eng. 136 (2019) 187–194.*

Krammer for predicting the hole-filling in PIP technology [65]. In practice, the process parameters of PIP technology could be collected during the assembly even for all manufacturing lines in the concept of Industry 4.0, and the data can be fed-back to the design phase. By this, the design phase could be enhanced, engineering tasks for fine-tuning the process could be reduced or even eliminated, and the set-up time of manufacturing lines for new products could be shortened significantly.

References

[1] N.-C. Lee, Reflow Soldering Processes and Troubleshooting: SMT, BGA, CSP and Flip Chip Technologies, Newnes, 2002.

[2] G. Harsányi, Elektronikai Technológia és Anyagismeret, University Lecture Notes, BME-ETT, 2019, ISBN: 978-963-421-791-6.

[3] C.S. Lau, M.Z. Abdullah, F.C. Ani, Effect of solder joint arrangements on BGA lead-free reliability during cooling stage of reflow soldering process, IEEE Trans. Compon. Packag. Manuf. Technol. 2 (12) (2012) 2098–2107.

[4] T. Plookphol, S. Wisutmethangoon, S. Gonsrang, Influence of process parameters on SAC305 lead-free solder powder produced by centrifugal atomization, Powder Technol. 214 (2011) 506–512.

[5] W.Y.W. Yusoff, N. Ismail, N.S. Safee, A. Ismail, A. Jalar, M.A. Bakar, Correlation of microstructural evolution and hardness properties of 99.0Sn-0.3Ag-0.7Cu (SAC0307) lead-free solder under blast wave condition, Solder. Surf. Mt. Technol. 31 (2) (2019) 102–108.

[6] O. Krammer, K. Dušek, Numerical investigation on the effect of the printing force and squeegee geometry on stencil printing, J. Manuf. Process. 45 (2019) 188–193.

[7] M. Hirman, F. Steiner, Optimization of solder paste quantity considering the properties of solder joints, Solder. Surf. Mt. Technol. 29 (1) (2017) 15–22.

[8] T.N. Tsai, Modeling and optimization of stencil printing operations: a comparison study, Comput. Ind. Eng. 54 (3) (2008) 374–389.

[9] IPC J-STD-005, Requirements for Soldering Pastes, Solder Paste Task Group (5-22b) of IPC, Bannockburn, Illinois, 1995.
[10] J. Ferguson, Z. Kemblowski, Applied Fluid Rheology, Springer Netherlands, 1991, ISBN: 978-1-85166-588-4, .
[11] O. Krammer, B. Gyarmati, A. Szilágyi, B. Illés, D. Bušek, K. Dušek, The effect of solder paste particle size on the thixotropic behaviour during stencil printing, J. Mater. Process. Technol. 262 (2018) 571–576.
[12] N.N. Ekere, D. He, L. Cai, The influence of wall slip in the measurement of solder paste viscosity, IEEE Trans. Compon. Packag. Manuf. Technol. 24 (3) (2001) 468–473.
[13] H.A. Barnes, Measuring the viscosity of large-particle (and flocculated) suspensions—a note on the necessary gap size of rotational viscometers, J. Non-Newtonian Fluid Mech. 94 (2000) 213–217.
[14] A. Pietriková, M. Kravčík, Boundary value of rheological properties of solder paste, in: Proceedings of the 2011 34th International Spring Seminar on Electronics Technology (ISSE 2011), Tatranska Lomnica, Slovakia, 2011, pp. 94–97.
[15] T.A. Nguty, N.N. Ekere, The rheological properties of solder and solar pastes and the effect on stencil printing, Rheol. Acta 39 (6) (2000) 607–612.
[16] R. Durairaj, S. Mallik, N.N. Ekere, Solder paste characterisation: towards the development of quality control (QC) tool, Solder. Surf. Mt. Technol. 20 (3) (2008) 34–40.
[17] G.P. Glinski, C. Bailey, K.A. Pericleous, A non-Newtonian computational fluid dynamics study of the stencil printing process, Proc. Inst. Mech. Eng. C: J. Mech. Eng. Sci. 215 (4) (2001) 437–446.
[18] R. Durairaj, G.J. Jackson, N.N. Ekere, G. Glinski, C. Bailey, Correlation of solder paste rheology with computational simulations of the stencil printing process, Solder. Surf. Mt. Technol. 14 (1) (2002) 11–17.
[19] T.I. Al-Ma'aiteh, O. Krammer, Non-Newtonian numerical modelling of solder paste viscosity measurement, Solder. Surf. Mt. Technol. 31 (3) (2019) 176–180.
[20] J. Boyd, J.M. Buick, Analysis of the Casson and Carreau–Yasuda non-Newtonian blood models in steady and oscillatory flows using the lattice Boltzmann method, Phys. Fluids 19 (9) (2007) 093103.
[21] J.W. Goodwin, R.W. Hughes, Rheology for Chemists. An Introduction, second ed., RSC Publishing, Cambridge, 2008.
[22] S. Mallik, N.N. Ekere, A.E. Marks, A. Seman, R. Durairaj, Modelling of the time-dependent flow behaviour of lead-free solder pastes used for flip-chip assembly applications, in: 2nd Electronics System-Integration Technology Conference (ESTC-2008), Greenwich, UK, 2008, pp. 1219–1224.
[23] A. Pietriková, M. Kravcik, Investigation of rheology behavior of solder paste, in: 35th International Spring Seminar on Electronics Technology (ISSUE 2012), Bad Aussee, Austria, 2012, pp. 138–143.
[24] M. Holtzer, L. Nampo, Reducing print cycle time, SMT Mag. October (2015) 26–29.
[25] K.J. Vachaparambil, G. Mårtensson, L. Essén, Rheological characterization of non-Brownian suspensions based on structure kinetics, Solder. Surf. Mt. Technol. 30 (1) (2018) 57–64.
[26] W. Pabst, Fundamental considerations on suspension rheology, Ceramics – Silikáty 48 (1) (2004) 6–13.
[27] S.S. Zhang, Y.J. Zhang, H.W. Wang, Effect of particle size distributions on the rheology of Sn/Ag/Cu lead-free solder pastes, Mater. Des. 31 (2010) 594–598.

[28] X. Bao, N.C. Lee, R.B. Raj, K.P. Rangan, A. Maria, Engineering solder paste performance through controlled stress rheology analysis, Solder. Surf. Mt. Technol. 10 (2) (1998) 26–35.
[29] B. Illés, I. Bakó, Numerical study of the gas flow velocity space in convection reflow oven, Int. J. Heat Mass Transf. 70 (2014) 185–191.
[30] B. Illés, A. Géczy, A. Skwarek, D. Busek, Effects of substrate thermal properties on the heat transfer coefficient of vapour phase soldering, Int. J. Heat Mass Transf. 101 (2016) 69–75.
[31] V.N. Constantinscu, Laminar Viscous Flow, Springer-Verlag, New York, 1995, ISBN: 978-1-4612-8706-3, .
[32] S.H. Mannan, N.N. Ekere, I. Ismail, M.A. Currie, Flow processes in solder paste during stencil printing for SMT assembly, J. Mater. Sci. Mater. Electron. 6 (1) (1995) 34–42.
[33] D. Riemer, Analytical Engineering Model of the Screen Printing Process: Part I. Solid State Technology, August 1988, pp. 107–111.
[34] D. Riemer, Analytical Engineering Model of the Screen Printing Process: Part II. Solid State Technology, September 1988, pp. 85–90.
[35] W.S. Seo, J.B. Kim, Filling analyses of solder paste in the stencil printing process and its application to process design, Solder. Surf. Mt. Technol. 25 (3) (2013) 145–154.
[36] O. Krammer, L.M. Molnár, L. Jakab, A. Szabó, Modelling the effect of uneven PWB surface on stencil bending during stencil printing process, Microelectron. Reliab. 52 (1) (2012) 235–240.
[37] O. Krammer, L. Jakab, B. Illes, D. Bušek, I.B. Pelikánová, Investigating the attack angle of squeegees with different geometries, Solder. Surf. Mt. Technol. 30 (2) (2018) 112–117.
[38] A.M. Joglekar, Statistical Methods for Six Sigma, John Wiley & Sons, 2003, ISBN: 0-471-20342-4, .
[39] IPC-9850, Surface Mount Placement Equipment Characterization, Developed by the SMT Component Placement Equipment Subcommittee (5-41) of the Assembly Equipment Committee (5-40) of IPC, July 2002.
[40] P.L. Tu, Y.C. Chan, K.C. Hung, J.K.L. Lai, Study of micro-BGA solder joint reliability, Microelectron. Reliab. 41 (2001) 287–293.
[41] O. Krammer, T. Garami, B. Horváth, T. Hurtony, B. Medgyes, L. Jakab, Investigating the thermomechanical properties and intermetallic layer formation of Bi micro-alloyed low-Ag content solders, J. Alloy. Compd. 634 (2015) 156–162.
[42] D. Shangguan, Lead-Free Solder Interconnect Reliability, ASM International, Materials Park, OH, 2005, ISBN: 978-0-87170-816-8, .
[43] K.N. Tu, K. Zeng, Tin-lead (SnPb) solder reaction in flip chip technology, Mater. Sci. Eng. 34 (2001) 1–58.
[44] L.C. Tsao, Evolution of nano-Ag_3Sn particle formation on Cu–Sn intermetallic compounds of $Sn_{3.5}Ag_{0.5}Cu$ composite solder/Cu during soldering, J. Alloy. Compd. 509 (2011) 2326–2333.
[45] M. Yang, M. Li, C. Wang, Interfacial reactions of eutectic $Sn_{3.5}Ag$ and pure tin solders with Cu substrates during liquid-state soldering, Intermetallics 25 (2012) 86–94.
[46] H.T. Lee, Y.F. Chen, T.F. Hong, K.T. Shih, Effect of cooling rate on Ag_3Sn formation in Sn-Ag based lead-free solder, in: 11th Electronics Packaging Technology Conference (EPTC 2009), Singapore, 2009, pp. 875–878.
[47] E.F. Monlevade, W. Peng, Failure mechanisms and crack propagation paths in thermally aged Pb-free solder interconnects, J. Electron. Mater. 36 (7) (2007) 783–797.

[48] D.W. Henderson, T. Gosselin, A. Sarkhel, Ag_3Sn plate formation in the solidification of near ternary eutectic Sn−Ag−Cu alloys, J. Mater. Res. 17 (11) (2002) 2775−2778.
[49] S.K. Kang, D.Y. Shih, D. Leonard, D.W. Henderson, T. Gosselin, S. Cho, et al., Controlling Ag_3Sn plate formation in near-ternary-eutectic Sn-Ag-Cu solder by minor Zn alloying, JOM 56 (2004) 34−38.
[50] S.K. Kang, P. Lauro, D.Y. Shih, D.W. Henderson, J. Bartelo, T. Gosselin, et al., The microstructure, thermal fatigue, and failure analysis of near-ternary eutectic Sn-Ag-Cu solder joints, Mater. Trans. 45 (3) (2004) 695−702.
[51] R. Wassink, M. Verguld, Drawbridging of leadless components, Hybrid Circuits 9 (1986) 18−24.
[52] J.R. Ellis, G.Y. Masada, Dynamic behavior of SMT chip capacitors during solder reflow, IEEE Trans. Compon. Hybrids Manuf. Technol. 13 (3) (1990) 545−552.
[53] O. Krammer, Modelling the self-alignment of passive chip components during reflow soldering, Microelectron. Reliab. 54 (2) (2014) 457−463.
[54] M.B. Abot, D.R. Basco, Computational Fluid Dynamics: An Introduction for Engineers, Longman Scientific & Technical, Harlow, 1989.
[55] L.M. Racz, J. Szekely, Determination of equilibrium shapes and optimal volume of solder droplets in the assembly of surface mounted integrated circuits, ISIJ Int. 33 (2) (1993) 336−342.
[56] N.J. Nigro, S.M. Heinrich, A.F. Elkouh, X. Zou, R. Fournelle, P.S. Lee, Finite element method for predicting equilibrium shapes of solder joints, Trans. ASME J. Electron. Packag. 115 (1993) 141−146.
[57] N.J. Nigro, F.J. Zhou, S.M. Heinrich, A.F. Elkouh, R.A. Fournelle, P.S. Lee, Parametric finite element method for predicting shapes of three-dimensional solder joints, Trans. ASME J. Electron. Packag. 118 (1996) 142−147.
[58] X. Zhao, C. Wang, G. Wang, G. Zheng, S. Yang, An integrated system for prediction and analysis of solder interconnection shapes, IEEE Trans. Electron. Packag. Manuf. 23 (2) (2000) 87−92.
[59] K. Brakke, Surface Evolver. Available from: <www.susqu.edu/brakke/evolver/evolver.html> (accessed 19.09.19).
[60] P. Zarrow, Reflow soldering of through-hole components, J. Surf. Mt. Technol. 12 (4) (1999). Available at: <www.smta.org/knowledge/journal_detail.cfm?ARTICLE_ID = 19>.
[61] W.E. Coleman, D. Jean, J.R. Bradbury-Bennett, Stencil design for mixed technology through-hole/SMT placement and reflow, Solder. Surf. Mt. Technol. 12 (3) (2000) 8−12.
[62] J.W. Harris, H. Stocker, Solids of rotation, Handbook of Mathematics and Computational Science, Springer-Verlag, New York, 1998, pp. 111−113.
[63] O. Krammer, B. Varga, K. Dušek, New method for determining correction factors for pin-in-paste solder volumes, Solder. Surf. Mt. Technol. 29 (1) (2017) 2−9.
[64] IPC-7525, Stencil Design Guidelines, Developed by the Stencil Design Task Group (5-21e) of the Assembly and Joining Process Committee of IPC, May 2000.
[65] P. Martinek, O. Krammer, Analysing machine learning techniques for predicting the hole-filling in pin-in-paste technology, Comput. Ind. Eng. 136 (2019) 187−194.

Chapter 2

Infrared reflow soldering

2.1 Introduction

While reflow soldering in mass production shifted mainly to the forced convection-based solutions, and nonconventional assemblies are manufactured with vapor phase soldering (VPS), infrared (IR) reflow soldering is still a possible alternative used in the field. The attention on infrared soldering mostly shifted to the laboratories and the workshops of small and medium-sized enterprises (SMEs), it is still relevant to investigate the basics of infrared-radiation heat transfer and the application of IR heating in different reflow ovens.

IR ovens are based on applying infrared emitters, and the simplicity of this approach makes the technology straightforward and easy to use. To discuss the basic physics, the setup and geometry of the oven and the material setup of the printed circuit board (PCB) assembly need a thorough description. It is also important to note that during IR reflow, the connection of the heat source and heated sample (PCB) represents a nonequilibrium process, while the heat source is significantly hotter than the board. On the other hand, the heat source is based on the effect of radiation, and the medium inside the work zone of the ovens usually does not have definite temperatures. Depending on the heaters, the medium itself (practically air or N_2 gas) can absorb a significant part of the radiation, which means that the temperature of the heated sample will be depending on the distance of the heated surfaces the radiator units and the surrounding medium as well. This can be controlled further with forced convection of air, or air circulation inside the work zone.

The emitter control is straightforward, considering the microcomputers found in the IR ovens—however, to obtain the desired soldering profile, it is important to control the process parameters noting the construction aspects and (if available) feedback signals of the oven. It must be noted at this point, that the setup can be either batch-based, front-loading (or in other words: drawer loading) oven type, or in-line, conveyor belt based. The first type enables efficient laboratory work and small scale production; the second enables mass production, with a conveyor line. Both types can use different emitter-air circulation configurations. The discussed points above will be detailed in the next section.

Reflow Soldering. DOI: https://doi.org/10.1016/B978-0-12-818505-6.00002-9

2.2 Basics of IR heat transfer

2.2.1 Physical background

Radiation-based heating is a process, where the energy is transferred via the form of electromagnetic waves. For such heating processes, a defined medium is not necessary (radiation heating is present in space as well), but in case of the presence of, for example, air, the medium might be nonnegligible, from the aspect of the model establishment.

For the description of radiation, the starting point is the Stefan–Boltzmann law. The Stefan–Boltzmann law can be written in its simplest form with (2.1):

$$\frac{P}{A} = \sigma \cdot T^4 \tag{2.1}$$

for hot objects, radiating energy to the cooler surroundings is done according to (2.2):

$$\frac{\mathrm{d}Q}{\mathrm{d}t} = \varepsilon \cdot \sigma_0 \cdot A \cdot \left(T_b{}^4 - T_a{}^4\right) \tag{2.2}$$

where ε is the emissivity of the given body (1 for ideal radiators, and $0 < \varepsilon < 1$ for gray bodies depending on the material and the surface temperature), σ_0 is the Stefan–Boltzmann constant, T_b is the temperature of the body (°C), and T_a is the temperature of the ambient (cooler) (°C). The law states that the emitted energy by radiation is proportional to the fourth power of the temperature of the radiating surface (of a black body). In other words, the law describes power radiated from a black body in terms of the temperature. The Stefan–Boltzmann constant can be described with (2.3) in SI units:

$$\sigma_0 = 5.670373 \times 10^{-8} \ \left(\mathrm{W/m^2\ K^4}\right) \tag{2.3}$$

The constant is derived from the Boltzmann and Planck constants and the speed of light in vacuum. In imperial units, the constant can be written as 1.714×10^{-9} [Btu/(h ft^2 °R^4)] or 1.19×10^{-11} [Btu/(h in^2 °R^4)]. The given radiation for the applied temperature ranges is considered to be in the infrared region of the electromagnetic spectrum. If the discussed body is a good emitter, usually it can be considered as a good absorber as well. With black bodies, the level of radiation emitted or absorbed depends on the temperature, and it is independent of wavelength. In black bodies, emittance and absorptance are equal to unity. Electronic engineering materials are not exhibiting black body characteristics. Thus a so-called gray body emits and absorbs energy, which is independent of wavelength. Also, the emittance and absorptance values are less than unity. Consequently, the gray bodies do not absorb all energies [1]. The incident radiation of a gray body is presented in Fig. 2.1, where parts of the radiation can be reflected, absorbed, or in given cases, transmitted.

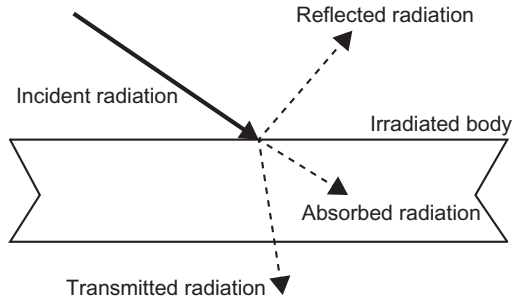

FIGURE 2.1 Irradiated gray body.

The absorptance, the reflectance, and the transmittance describe the behavior of the gray body [1], and can be written according to (2.4):

$$\alpha + \rho + \tau = 1 \tag{2.4}$$

where α is the absorptance (the ratio of absorbed energies), ρ is the reflectance (ratio of reflected energies), and τ is the transmittance (ratio of transmitted energies). While many materials can be considered to be opaque with zero transmittance (most solids), in this case, $\alpha + \rho = 1$ or $\varepsilon + \rho = 1$. This means that with lower reflectivity for a gray body, the higher its absorptance and emissivity will become.

During radiation, the radiated heat might be originated from a surface, which is viewed from an angle, like the case presented in Fig. 2.1. The cosine law of Lambert (2.5) describes this case:

$$\frac{\mathrm{d}Q_\beta}{\mathrm{d}t} = \frac{\mathrm{d}Q}{\mathrm{d}t} \cdot (\cos\beta) \tag{2.5}$$

where the term on the left represents the radiated heat in the given β angle. The radiative heat transfer between the surfaces of discussed bodies can be calculated as rates of energy transfer, between the surface of body 1 and the surface of body 2. In such cases, the radiative heat exchange equation can be written as (2.6):

$$\frac{\mathrm{d}Q_{1-2}}{\mathrm{d}t} = \sigma \cdot \left(\varepsilon_1 \cdot A_1 \cdot F_{1-2} \cdot {T_1}^4 - \varepsilon_2 \cdot A_2 \cdot F_{2-1} \cdot {T_2}^4\right) \tag{2.6}$$

where most of the parameters are known, the 1−2 numbers are representing the two bodies, and F_{1-2} is representing the view factor. The view factor can be considered as a proportional value of the radiation leaving the surface of body 1 and facing (arriving to) the surface of body 2. The view factor can be described [1] according to (2.7):

$$F_{1-2} = \frac{1}{A_1} \int_{A_1} \int_{A_2} \frac{\cos\beta_1 \cos\beta_2 \cdot \mathrm{d}A_1 \, \mathrm{d}A_2}{\pi r^2} \tag{2.7}$$

where A_1 and A_2 are the surfaces 1−2, β_1 and β_2 are angles between the normal vectors to the given surfaces, and r is the line of length connecting the points on the surfaces.

The wavelength of the radiation is also important from the aspect of oven construction and working principles. The wavelength can be written from Wien's displacement law (2.8):

$$W_{peak} = \frac{K_w}{T_e} \tag{2.8}$$

where W_{peak} is the peak emission wavelength (μm), K_w is Wien's constant (5215.6 μm °C), and T_e is the temperature of the body with the emission (°C). It is important to note that for shorter wavelengths, higher temperature emitters are needed. Also, it is important to note that below 500°C, the precise location of energy maximums has only reduced practical significance, while the maximums get progressively flatter with lower emitter temperatures [2].

2.2.2 Equilibrium−nonequilibrium reflow cases

To investigate the applied heat into a printed circuit board, the temperature of the emitters, the wavelength distribution, the reflectivity, and absorption parameters of the assembly (board, components, solder paste) must be taken into account. As noted before, infrared soldering can represent a nonequilibrium case when the temperature of the heat source is considerably higher as the intended reflow temperatures of the assembly.

During *nonequilibrium* cases, the following points must be taken into consideration [2]. The temperature of the heat source must be higher than the maximum reflow temperatures. In this case, the rate of temperature increase in the assembly depends on the temperature difference between the heat source and the assembly, the distance between the two elements, the heat capacity of the assembly, and the power of the source. During process control in nonequilibrium cases, the temperature/power of the heat source, the distance/exposure time can be controlled, according to the type of the oven. This will be discussed later in the chapter for the case of basic IR soldering.

In *equilibrium cases*, the temperature of the heat source is identical to the proposed reflow temperature on the assembly. Also, the rate of heating depends on the thermal coupling with the heat source in such cases. During the process control in equilibrium cases, the process control mainly aims for the regulation of exposure time of the assembly to the heat source. Wave soldering, VPS, or convection soldering can be considered as equilibrium case reflow.

2.3 Basic configurations of IR ovens

According to Prasad, infrared reflow soldering ovens can be categorized into two main groups [3]. The near-IR-soldering processes are characterized by IR radiation in the short wavelength range. In this case, radiation is the main source of energy transfer, the convection is only considered to take part in less than 5% of the heating. In this case, the wavelength range is in the 1−5 μm range. The 0.75−1.5 (or 2.5 μm) range is also called near or short-wave infrared radiation; the 2.5−5 μm range is considered to be the medium wave infrared radiation [3]. Other classifications also exist. According to the International Commission on Illumination (CIE) and the relevant DIN norm [4], the infrared radiation can be divided into IR-A (0.7−1.4 μm), IR-B (1.4−3 μm), and IR-C (3−1000 μm) ranges. The ISO 20474 standard [5] defines the near-infrared (NIR) range in 0.78−3 μm, the middle-infrared (MIR) range in 3−50 μm, and the far-infrared (FIR) range in 50−1000 μm. The divisions, however, can vary depending on the literature source and the application field (e.g., electronics, astronomy). It is usually said that with a shorter wavelength, the smaller components and boards will suffer from overheating; however, more uniform heating of the paste itself is achieved with such wavelengths. Longer wavelengths usually heat the air surrounding the emitters, and then this effect can be combined with convection for a more evenly heating [6].

2.3.1 Near-IR systems

In near-IR systems with quartz tungsten lamps, most of the energy is transmitted in the region of 2−3 μm. At this range of the bandwidth, conduction and convection also help the process of heat transfer on the level of the board; however, convection takes a minor role. Usually, lamp-based ovens are divided into different preheat zones, and in the zones with the higher heating power, the heat transfer is mainly originated from radiation. Near-IR penetrates the substrate, the solder paste, and the package; this enables heating from within the body.

It can be usually stated that near-IR systems have fast response times, due to the fact, that convection takes a smaller role in the process. Unfortunately, such ovens are very selective for different heating rates in different parts with different heat capacity. Even the PCB substrate takes part in the uneven heating, where epoxy warpage and discoloration can occur along the surface. In near-IR, the selectivity effect of color and of thermal mass is increased. NIR ovens are more difficult to profile as well, due to a selectivity effect of the thermocouple fixing methods [7].

2.3.2 Medium to far-IR systems

In the wider medium to far-IR range (usually the case of area-type emitters), the radiation bandwidth should be adjusted to the absorption capability of PCBs and usual assembly parts and components. In the PCBs, the effect of conduction can help heating the pad and the solder paste similarly as in the case of near-IR systems. The radiation bandwidth should also be optimized so that the absorption of the energy would be nonsensitive to the color of the different assembly parts. For double-sided assemblies, the reflow profiles must be carefully optimized according to the IR area-type emitters positioned in the oven ovens [7].

The absorption spectra are very similar for many materials in the medium and infrared range. Metal oxides and minerals absorb well from 3 μm consistently, while plastics on the contrary have characteristic absorption bands in this range. While water has a relatively wide spectrum in the medium-long range, mid- and far-IR heating becomes important for drying processes as well [8].

2.3.3 Medium-IR systems mixed with convection

Due to the possibility of medium heating inside the work zone, mixed convection and infrared (C/I)-based apparatuses emerged, where the wavelength region is usually considered to be in the 2.5−5 μm medium wave range. In this case, the IR radiation is considered to take part in only 40% of the heat transfer, while the remaining 60% is considered to be coming from the convective part of the process. This is in total contrast with the near-IR-based ovens. C/I ovens are usually mounted with internal fans, which circulate hot air or injected inert gas in the work zones of the ovens. The inert gas is usually nitrogen in C/I ovens. The circulation is not only important due to the ratio of convective heat transfer during the process, but the uniformity of the temperature distribution inside the work zone.

According to Pecht [9], the mixed C/I heaters are listed in the following manner. The so-called panel-convection IR systems are using mid-IR to generate heat energy. A heated panel is used to provide secondary emission, which provides additional heat to the components by convection from the air in the given work zone. The so-called forced convection IR systems are similar to the panel-convection method, but in such cases, the air is circulated in the work zone. Circulation is used to equalize the heat transfer on assemblies with various thermal masses, as discussed above.

2.3.4 Pros and cons

While the near-IR and mixed C/I ovens are nowadays becoming more and more obsolete technologies, the two methods were evaluated in the past

taking into account the pros and cons of the technology [3]. The near-IR was considered to be efficient, while it allows faster heating and complete reflow, due to the short-wave penetration into the board and the components. Also, the use of near-IR was favored in the past, due to the reduced solder balling. On the other hand, near-IR ovens were considered to be problematic from the aspects of shadowing and color sensitivity. In the case of near-IR ovens, shadowing is an increased problem compared to other reflow methods. While the convective aspect of the heat transfer is limited in such cases, the assembly parts, which are covered from irradiation due to geometry aspects, are remaining colder, than the directly irradiated surfaces and parts. This causes nonuniformity in the heating. Also, different parts with different colors absorb the radiation differently, which also causes nonuniform heating. The mass, geometry, and reflectivity also take part in escalating the problems of nonuniform heating.

In the ovens, which use mid-IR and C/I fan-based convection, these problems could be reduced—the constantly redistributed medium in the work zone offers equalization in terms of heat transfer along the surfaces of the assembly. In addition, the medium wavelength could be considered uniform across the spectrum of the colors used in the usual PCB assemblies. It must be noted that with the increased thermal requirements of the lead-free soldering principles, the packages need to withstand higher temperatures too. This further increases the problems, regarding nonuniformity in heating, also raising alarming questions regarding heat-sensitive component packages and connectors. According to today's market share, the forced circulation of the oven atmosphere is an essential feature for most of the IR ovens. According to Section 2.2, the modern IR ovens using fan-based circulation are no longer providing pure nonequilibrium processes [2].

2.3.5 Improving quality with inert gas

While lead-free reflow is usually performed nowadays in air/N_2 or N_2 mixtures (while N_2 may help to improve wetting and avoid oxidation) [10], common IR ovens work with air atmosphere. To provide an inert environment, N_2 gas can be introduced to the work zones of the ovens in various ways. During IR reflow, increased N_2 purity level in the oven might help to reduce board discoloration (10,000 ppm O_2), increase the ease of cleaning any residues originated from fluxes (500 ppm O_2), help to reduce solder balling (200 ppm O_2), and to solder with low residue solder pastes (below 100 ppm O_2). N_2 atmosphere also helps to minimize oxidation of lead-free solders. On the other side, the introduction of N_2 atmosphere in an oven might increase the design and fabrication cost of the oven, eventually increasing the commercial price, operating complexity, and service requirements. For IR ovens, it is practically easy to maintain the high level of nitrogen purity inside the oven and to minimize nitrogen consumption, compared to the convection-

heavy ovens. In ovens, where IR is the dominant form of heat transfer, there is no turbulent- and high-velocity flow, or flow-related resulting leakage of the inert gas. In addition (in the case of C/I type ovens), in order to save costs, recirculation of N_2 gas and ensuring a closed system is a must, when applying nitrogen to the work zone [3]. During the history of the technology, the usual nitrogen consumption rates of reflow ovens in mass production were lowered to a range of 20−30 N m^3/h from the higher 40−60 N m^3/h range [11].

2.4 IR emitters

Emitters used in electronics can be categorized from the aspect of low- and high-temperature applications [2]. For IR reflow, low-, medium- and high-temperature emitters are both used. Their structure can be either based on tubes, heated metal panels, or ceramic bodies.

Low- and medium-temperature emitters are usually structured in a panel format. The metal panels have the usual range of 250°C/480°F to 400°C/750°F, while the ceramic panels have a usual range of 300°C/570°F to 500°C/950°F. Usually, the total panel structure is heated in such configurations that the thermal mass of the heating elements adds to the response characteristics of the whole system. Timely transients are nonnegligible in such cases.

For high temperatures, quartz tubes (practically transparent from the aspect of IR waves) with an alloy heater coil (such as tungsten) are used. The temperature range of such emitters can be considered to be between 700°C/1290°F and 850°C/1560°F. They are dimmable and switchable, so the control of such heaters may enable considerably faster system response, compared to the lower temperature emitters.

During the years of IR-soldering machine developments, the emitter technology was in rapid development. Unfocused IR lamps were used in early concepts, which were producing a wide range of photonic radiation spectrum, weighed to the IR end. During the time, these lamps were reconstructed for a more focused radiation range [12]. According to Judd and Brindley [6], the more effective development started with the introduction of focused lamps in the NIR regime. Then diffuse lamps followed, as these components could be applied as a secondary reflector/emitter component as well. Later, far-IR diffuse vitreous flat panels were applied, which were improved with metal faces, suited for the natural and interstage recirculated convention. The metal panels could be then improved with additional holes and segregated zones for both uniform and zoned forced convection improvements. Later, the evolution brought the metal panels into improving the zone count, and such panels were also prepared for N_2 gas application. For IR reflow, the heaters usually (but not necessarily) have built-in thermocouples for improved temperature control on the heater modules themselves.

It is apparent from the list that the technology eventually improved from the pure IR heating to the more sophisticated C/I methodologies.

Emitters are usually located both above and under the position, where the PCB assemblies are handled, and they should be at least as wide, as the sample holder or the conveyor, in order to ensure a maximal surface for heating. The uniformity of heating around the emitters is depending on the heater construction, the feedback-loop coming from the thermocouple inside the heaters, the tunnel/work zone insulation, and in C/I cases, the mixing of convective heat transfer with radiation.

During direct heating, the radiation immediately reaches the surfaces of the assembly. In the case of indirect heaters, the assembly is shielded from direct near-IR radiation by panels—radiation takes place with a longer wavelength emitted by the shielding (or shutter) panels. This brings slower heating rates, and in the same time more evenly heating [12] (Fig. 2.2).

For the heaters, different coatings can be used to improve reflection, such as glass or aluminum. The gold coating is considered to be an effective reflector. On the other hand, a highly polished aluminum coat can be also used as a reflective surface, but the material loses its reflectivity due to the increasing oxide buildup on the surface of the coating. Quartz glasses can also be improved with additives to improve reflection and process parameter stability [13].

2.4.1 Tube emitters

Fig. 2.3 presents a typical construction of a tube-lamp IR emitter, with a heated filament, a quartz glass tube, and ceramic caps with termination on the end. The caps require carefully design geometry, to ensure thermal stability at the ends of the construction, and avoid any mechanical failure due to thermal expansion and the gradient inside the elements due to the cold−hot

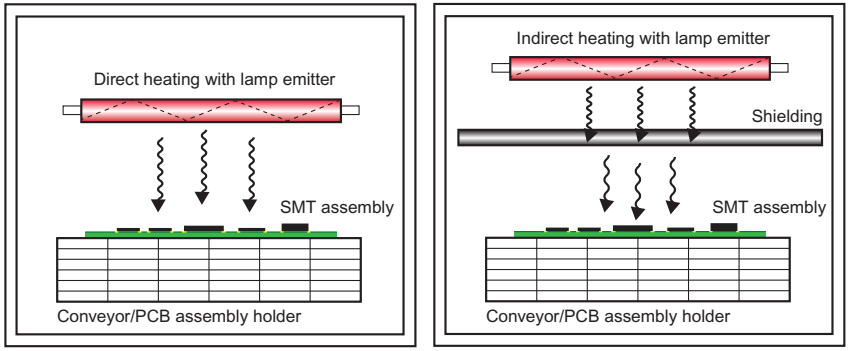

FIGURE 2.2 Direct (left) and indirect (right) heating with lamp IR emitter. Note the change of wavelength in the case of transmitted radiation.

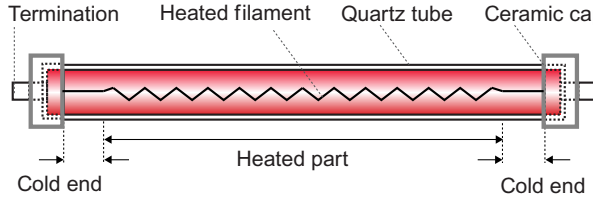

FIGURE 2.3 Typical construction of an IR tube.

transition. The termination and the ceramic cap can be varied according to different standardized sockets. (A typical lamp in IR application has R7S cap type connection with two ceramic one-pin terminals.) Note that in the tube itself there is a heated part, and at the perimeter, there are cold ends as well, according to the coil construction of the filament.

The quartz tubes are built around an internal tungsten coil. The tungsten coil radiates in the wavelength 0.3−2.5 μm range with peak radiation at 1 μm [13]. Usually, such coils have a fast response for a change in heating, and their temperature can extend even above 700°C [2].

It is important to note that most industrial emitters have an efficiency of 90%−95% [1]. A sorting of IR emitters can be found in Ref. [14]. For the near-IR, two different emitter types are mentioned: focused and a diffuse array of tungsten tube filament lamps. While the focused version can achieve 300 W/cm, the diffuse lamp moderates this value to 50−100 W/cm^2. While the focused lamp has improved power, the shadowing, thermal degradation, and board defects (warping, charring) can be significant during soldering. Diffuse array "nichrome" tube filament lamp setups are located near the middle IR range, reducing the wattage to 10−50 W/cm. This solution decreases the color selectivity and shadowing issues, and so at the same time, it improves the component density possibilities. On the contrary, panel-based secondary emitters work in the middle-to-far-IR regime, and provide a 1−4 W/cm^2 power. These emitters can be applied next to tubes, in order to improve shadowing and color sensitivity problems.

The tungsten filament-based quartz tubes are considered to be reliable and stable in the reflow temperature ranges [15]. However, such emitters tend to be prone to aging effects, which can be a problem from the point of operation and service requirements. The soldering profiles and the control would need constant recalibration when the lamps begin to age [7]. The aging problem can be avoided with the careful operation and proper maintenance. The modern bulbs usually share the positive aspects of optimized stability in wavelength; they have a working lifetime in the range of several hundred hours to a few thousand hours. Usually, they are dimmable, but rapid cycles can result in shortened lamp times. In order to understand geometry and lifetime concerns, the tube itself needs further discussion. With tungsten filament setup, the coil is usually enclosed in a quartz bulb with a

controlled amount of halogen gas. When the coil reaches the operating temperature, the tungsten material vaporizes partially, and in the colder volume of the bulb, the tungsten forms halides with the halogen. At the coil, the halide dissociates and the tungsten might deposit again on the filament. With stronger materials, smaller bulbs can be constructed, where higher pressures, similar gas density, and better mechanical stability can be achieved. The evaporation cycle can be reduced with smaller size, so longer life or increased performance can be achieved.

2.4.2 Panel or plate emitters

For mid- and far-IR range heating, mostly panel elements are used. The emitters can be used with different power ratings, ranging from $\sim 50-1500$ W in area oriented or focused manner, according to the given required applications in reflow soldering [15]. Such panel heaters (used as mostly secondary heaters, containing a primary source, in reflow ovens) are constructed from metal or ceramic plate structures. They are heated conductively with a resistance heater filament or by IR irradiation of one side [12]. The internally heated metal panels operate within a temperature range between 250°C and 350°C. Their response is slow, usually exceeding a minute range to respond to the change to the current, which is heating the resistance filament. The ceramic panels operating temperature can extend to 500°C−600°C, their response is considerably faster than the response of the metal heaters. However, there is still a non-negligible amount of transient effect, which might result still in a minute range response, in contrast with the sub-second short range bursts of quartz tubes, as reported in Ref. [2].

The emitted power depends on heater construction, its surface, and the temperature. A black ceramic panel might be more efficient heater on larger temperatures than the same construction with white ceramic. It is important to note that this effect is only observable at relatively higher temperatures, as it was also noted in (2.8). Fig. 2.4 describes [8] absorption of various materials.

The figure shows that aluminum absorbs only 15% of the iridescent radiation on the used temperatures of panel heaters, while white ceramic materials absorb about 90% of the same, black ceramic improves the absorption further in the 0°C−1000°C range [8]. The panel-type heaters usually emit on a broader bandwidth. Fig. 2.5 presents a typical construction of a panel heater with a thermocouple for temperature measurement and feedback for the control of the oven.

2.4.3 Thermal inertia

In IR ovens, thermal inertia can be a nonnegligible effect. The thermal inertia can be originated from the IR emitters as mentioned above, or from the

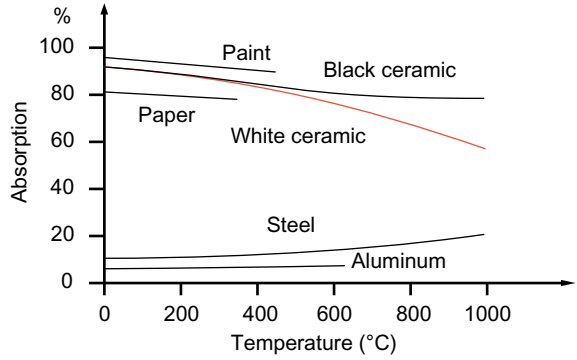

FIGURE 2.4 Absorption of different materials in 0°C−1000°C temperature range. *From Elstein, Ceramic Infrared Emitters, Elstein-Werk M. Steinmetz GmbH & Co. KG, White paper, 2016.*

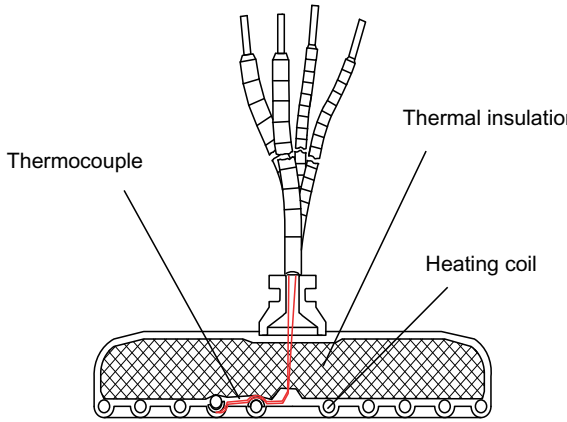

FIGURE 2.5 Typical construction of a ceramic IR panel with thermal insulation and an integrated thermocouple for temperature feedback. *From Elstein, Ceramic Infrared Emitters, Elstein-Werk M. Steinmetz GmbH & Co. KG, White paper, 2016.*

heating of the PCBs. In order to heat the emitters, the ovens provide considerably large electric currents (in the order of 10 A) for the heating. The heating of the wires may take tens of seconds to enable a response in the desired temperatures, after the program of the oven activates the heating. Due to this effect, it is important to calculate with such transients in the soldering profile as well and set the hold times of the programmed plots accordingly. It must be noted too that the assemblies can also have considerable thermal mass, which results in further problems in reaching the desired temperatures. Copper layers, thermal reliefs, large components, and the color of the components/solder mask may also affect the heating.

2.5 Batch-type IR oven examples

In this chapter, three different batch-type ovens are discussed, highlighting possible differences in oven design.

2.5.1 Batch-type oven with drawer design

The work zone of a typical batch-type oven is presented in Fig. 2.6. The oven is constructed with IR emitters on the top and bottom sides of the oven's work zone. The presented oven has a drawer design, with a front-loading setup. It is visible that the primary heater tubes have different winding inside along their length. It is also apparent that the tubes are heated separately. The secondary heaters can be seen under the grille. The work zone thermocouple extends over the printed circuit board assembly.

Physically, the oven has quartz-based IR lamps for both preheating and for reflowing peak temperatures. The maximum assembly size accepted by the oven is 350×250 mm. The machine can use ducted forced hot air, to further improve heat transfer with C/I possibilities. Different versions of the oven can accept or incorporate a hood and an extraction outlet, for fume extractions, with a coupling to the rear side of the oven.

The oven can accept an additional K-type thermocouple (so-called external sensor) into a socket on the sample holder drawer, which can be used as direct feedback from the surface temperature of the given assembly. The casing is insulated and the drawer is handled automatically. The drawer is held by a spring and a magnetic lock, which smoothly operates the drawer.

The oven works with internal control software, and it can also be connected to a PC for more efficient work. USB connection with easy-to-use software is not uncommon nowadays—this design approach began to appear in the last decade in such bench-top ovens, and improved the

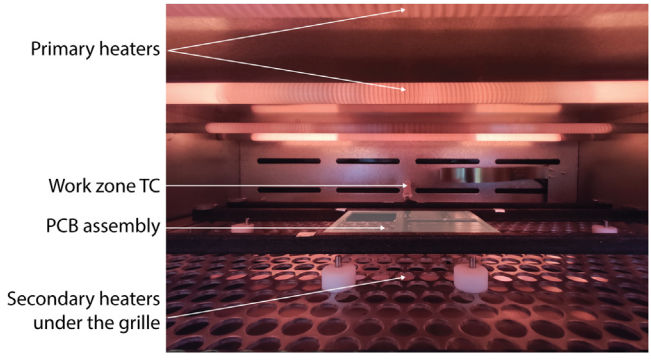

FIGURE 2.6 Work zone of a batch-type IR oven.

human–machine interface (HMI), resulting in shorter time to set up a machine. With appropriate continuously improving software, the ease of operation was radically improved during the years. The machine houses a 32-bit ARM processor with proprietary software. The storage enables five preprogrammed profiles without turning on the computer. According to the latest versions, the machine comes with either an older button-configurable HMI or an LCD touch screen, to ease the operation without the connection to a PC.

When connected to a computer, the provided software enables detailed control of the oven, with six profile sections for programming. The user may program the oven with the help of a graphical interface, where the breakpoints of a typical soldering profile might be modified in time and in temperature graphically. The user can also program the oven according to a table, which has six defined time–temperature points. Also, a preset temperature can be set with a possibility to define the reflow hold time.

It must be noted that the previously discussed thermal inertia and transient effects may be significant in the presented oven construction. As it was discussed in the previous chapter, and as the manufacturer highlights, the emitters have a well measurable delay in heating, also the structure of the assembly can slow the processes down. In the given oven, the sum of the thermal inertia may result in a considerable lag between the program and the reading of the external sensor attached to the assembly. During heating, the assembly practically will have a lower temperature, compared to the work zone of the oven. This difference can be in the range of 10°C according to practice. The desired difference between the programmed temperature and the actual reading can be set via software. Smaller differences may result in faster response, with increased overshoots; larger allowed differences may result in smoother corners in the profile, with longer thermal responses, and lower, sometimes not satisfactory peaks. When the emitters are regulated down (e.g., during the cooling phase of the profile), the assembly might continue to absorb heat from the heated air in the work zone, meaning that the actual soldering profile will be longer than expected. These effects must be calculated into the programming. Faster temperature increase can be achieved with spacers used in the work zone of the oven. If the assembly is elevated from the grille of the sample holder, the heating will be faster, while the grille itself will not reflect or absorb heat energy from the assembly. Summing up, empirical information is necessary to correctly set up a soldering profile for the required joint quality or paste manufacturer recommendation.

To further avoid thermal inertia effects, the external sensor is suggested to be positioned in a keep-out zone of copper planes of the assembly. (In other words, a bare region of the PCB, where there is no copper underneath the solder mask.) For the external thermocouple, either SMD adhesive, polyimide tape fixing, or alu-tape fixing is recommended due to good thermal

conductivity [16]; however, alu-tape fixing might result in false readings, while part of the radiation is reflected back from the shiny surfaces. In such cases, it is recommended to fix the thermocouple to the backside of the assembly, where lower radiation intensity (secondary heating) takes place. It is also important to note that the external thermocouple readings are performed by the processing unit inside the oven. The reading of the thermocouple might have an offset compared to the data of a calibrated profiler, while the internal data acquisition (DAQ) of the system (practically the cold side of the thermocouples) is not adequately separated (from thermal aspects) from the rest of the oven, resulting in slight drifts in the recordings. So, it is not recommended to skip the use of a separately calibrated profiler in favor of the additional K-type thermocouple in the oven. The noted imprecision is not critical, however, from the aspect of the temperature control, while the effects originated from the thermal inertia inside the work zone may be much more significant.

2.5.2 Batch-type oven with C/I heat transfer setup

Lau et al. [17] and Najib et al. [18] present a classical, cost-effective setup of C/I IR oven in their consecutive works. The oven is based on a drawer setup, constructed with circulating fans in the back, enabling C/I working methodology. "The investigated reflow oven contains a single temperature zone with multiple temperature segment control (infrared heaters). Based on the oven design there is a maximum of sixteen temperature control segments that can be set and stored accordingly. The main parts of the oven consist of six cylindrical-shaped infrared tubes, which heat the air and give off radiation. Two circulating fans are used to distribute the hot air inside the oven chamber, and the outlet holes are to release the air out of the oven. The temperature profile is automatically controlled using a microcomputer according to the set temperature. Infrared heat emitted from the tube is varied according to the set profile. For the cooling purpose, the infrared heater power is reduced, and the speed of the fan is increased to force the hot air out of the oven chamber. Fig. 2.7 shows the model of the oven and the actual view of the circulating fan. The fans are made of stainless steel plates with a thickness of 1.5 mm and a total diameter of 115 mm. The fans consist of 10 blades. Each blade has a shape of 90-degree angles with one side facing to the front of the oven, and the other side is considered to be perpendicular to it. The workbench area is 350×250 mm according to the manufacturer. During the reflow soldering process, the PCB is static on the plane at a height of 46 mm. The distance between the center of the IR tube and the bottom of the PCB is 116 mm. The temperature distribution due to convection and radiation is considered during the experiments and the simulations."

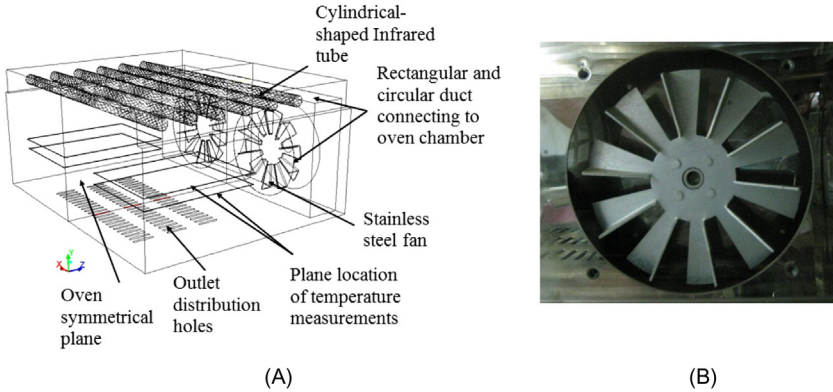

FIGURE 2.7 Setup of a typical batch-type convection/IR oven; A - components; B - circulating fan. *From A.M. Najib, M.Z. Abdullah, C.Y. Khor, A.A. Saad, Experimental and numerical investigation of 3D gas flow temperature field in infrared heating reflow oven with circulating fan, Int. J. Heat Mass Transf. 87 (2015) 49–58.*

2.5.3 Batch-type oven with advanced C/I heat transfer setup

The next oven is interesting from the advanced aspect of mixed C/I working principles, where convection itself has a more significant part in heating. The basic setup of the oven can be found in Fig. 2.8.

The oven has one heating and one cooling zone—this can be understood by observing the drawer-based design in Fig. 2.7. The sample holder (or board drawer), out of the ambient laboratory air, serves as both a loading bay and, at the end of the profile, a cooler zone. The loading bay of the holder is prepared with fans located on the sides, enabling increased precision in cooling. The heating zone has a relatively high work zone volume, for circulating air, and enabling vertical laminar airflow. The flow enables controlled heat transfer. The recirculation fans and the heater rods are situated under the work zone chamber. The heater rods heat up the air around them, the fans blow the heated air to the upward volume of the work zone. Four secondary quartz emitters are positioned at the top of the work zone, enabling precise IR control over the temperature profile. The oven is able to be heated up to 300°C temperature. The work zone has inner thermocouples in order to monitor the temperature of the work zone air medium. The oven enables increased precision, with the possibility to connect two additional thermocouples. The thermocouples then can be fixed to the boards, and the surface temperature measurement can be used to improve heat transfer control, with optional PC-based software.

It is important to investigate the technical data of the product [20]. The oven can receive a 400×300 mm PCB size with an overall height of 30 mm. The height is limited due to the setup of the quartz heaters and the

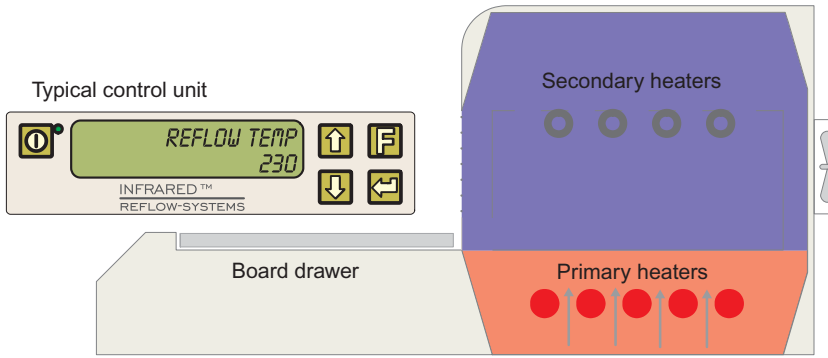

FIGURE 2.8 Advanced C/I oven. *From BME ETT, Virtual Laboratory, 2000–2018. http://www.ett.bme.hu/vlab/, 2019 (accessed 21.11.19)[19].*

thermocouple monitoring of the work zone of the oven. The drawer size is 440 × 350 mm, with the 30 mm entrance size—which limits the height of the entering assembly. The exhaust connection (to drive out the flux outgassing) is located on the backside. The producer of the ovens recommends 2000 W quartz emitters for the oven.

The programming of the oven is based on timely steps and related temperature values. The software contains the temperature values for each heating period, and the time period, for which the programmed temperature value is held. Usually, such ovens can store multiple programs as predefined/freely defined programs for different products and different reflow or curing applications. For each product, the program should be experimentally set for the optimal output. The main parameters for a program are the following:

- Base temperature (°C)
- Preheat/soak temperature (°C)
- Preheat/soak time (s)
- Reflow temperature (°C)
- Reflow time (s)
- Cooling temperature (°C)

It must be noted that the base temperature must be elevated from ambient temperatures up to 120°C in order to ensure repeatability, and avoid long thermal transients in the cooler parts of the profile.

The basic rules of soldering profile composition apply in C/I ovens as well:

- the liquidus point of the solder alloy must be reached and exceeded reliably;
- the impact of thermal inertia (e.g., due to the assembly) must be kept low.

2.5.4 Cheap bench-top IR solutions for hobbyists

According to the active communities around the web, inexpensive batch-type IR ovens might be an interesting source of applicable solutions. Custom modifications and firmware development [21] can be found for some of the commercially available ovens [22], where the existing controller hardware is improved with a new software solution. Also, the construction can be improved with home-made modifications, like replacing masking tapes, or custom pulse width modulation (PWM) based system fan control.

2.6 Example of conveyor-based in-line IR ovens

The conveyor-based in-line IR reflow ovens are nowadays considered as a secondary technology, while in conveyor-based production lines, convection ovens become the industry standard. However, at small workshops and laboratories, in-line IR ovens are still in operation. A typical in-line oven structure can be found in Fig. 2.9. The figure presents the conveyor, where the PCB assembly is traveling along heaters prepared for preheating. Then at the end of the tunnel, reflow takes place, so zones with more intense heating are set. The heating depends on the control (power) of the heaters and the speed of the conveyor line—alternatively, the addition of air venting. The heaters used in such ovens are usually panel heater modules. Before leaving the oven, the PCB assemblies can be cooled down in separate cooling zones, with forced convection of colder medium (e.g., air). In conveyor-based in-line ovens, it might be difficult to radiate areas with intentionally intensified or weakened power in a separated manner [8]. In such cases, metallic, shiny

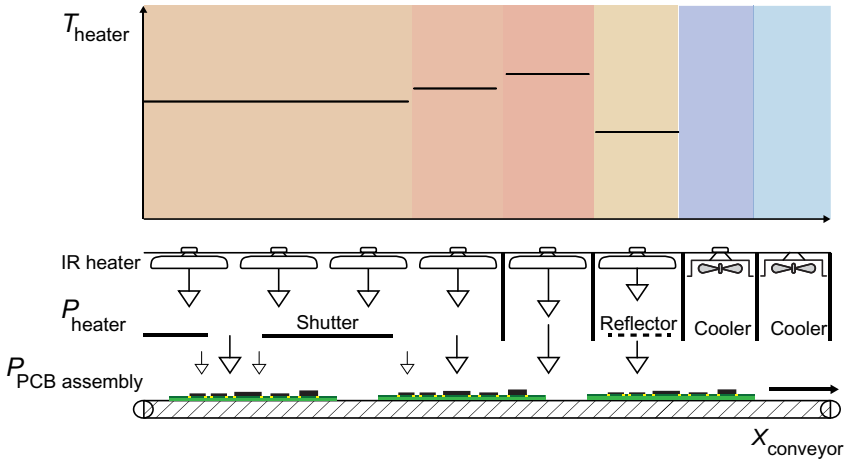

FIGURE 2.9 In-line IR oven. *Based on Elstein, Ceramic Infrared Emitters, Elstein-Werk M. Steinmetz GmbH & Co. KG, White paper, 2016.*

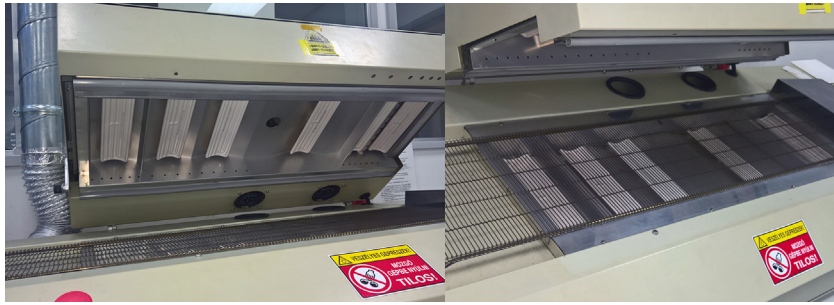

FIGURE 2.10 Work zone of an in-line oven; left—upper hood with different zones with plate heaters and air circulation; right—secondary heaters at the bottom side of the work zone.

reflector plates or absorber shutters are applied to control heat transfer in a delicate manner.

Fig. 2.10 presents a photo of the work zone of a conveyor-based in-line IR oven, where the panel heaters are positioned at the top and at the bottom of the construction, enabling secondary heating from the bottom. It is important to note that active air circulation is applied in the oven, presenting an example of a C/I technique applied in an in-line oven construction. It is visible on the upper hood that the last zone (with the conveyor direction moving from left to right) has two closer panel heaters for improved heating around reflow temperatures at the end of the line. The panels have internal thermocouples for temperature feedback at each zone.

2.7 Rework and other special applications with IR

In manual and automated rework of unsuccessfully soldered assemblies, IR heating remains an excellent solution, even for delicate, fine-pitch components, such as ball grid arrays (BGAs).

The rework stations can be differentiated according to their construction and heat transfer methodologies. One specific method used IR heat transfer combined with convective/hot air methodology. The bottom side (practically the sample holder table) of a rework station can work with 1000−1500 W IR preheating in the mid-IR bandwidth. This is combined with a hot gas nozzle and head for precision heating at the selected components. The IR preheating helps faster solder reflow for desoldering, and enables more homogeneous temperatures, thus reducing the warping and increasing the planarity of the reworked assembly. Such rework systems can also have front and back heating zones with a separate control.

The other group of IR-based rework stations uses unfocused, and iris-focused IR heating for local desoldering of components. Both types can be used in automated rework or desoldering purposes. The iris-focused IR rework method works with interchangeable lenses, and an x-y positioning

table moves the printed circuit board assembly under the IR source with the lens. The iris-focused IR heat source is located in a lamp housing, the near-IR bandwidth is used in approximately 1−1.2 μm range, depending on the power. The source connects to an upper lens, an iris (which is located between an attachment and the upper lens), a lens attachment, and the computer used to control the process. The iris can be used to control the spot size of the beam. The focused and unfocused IR rework stations are considered to be fast. The focused IR can be used to rework PLCCs, QFPs, LCCCs; the unfocused IR is able to perform adjacent component reflow and is suitable to rework chip size SMDs, transistors, diodes, and small-outline integrated circuits along with the previously mentioned packages. Compared to the hot gas method, IR rework does not blow small components away and avoids buildup of static electricity, while there is no gas flow. Also, the IR method may allow closed-loop control of component temperatures, shortening empiric studies of heating on different assemblies. For through-hole component rework, upper and bottom IR heaters can be used. IR reflow ovens are usually not suitable for desoldering and rework [23,24].

Recycling of electronics is becoming more and more important with the increasing amount of e-waste. For recycling printed circuit boards with SMDs, Yokoyama et al. [24] used a piece of equipment with IR heating, where the part removal processes are started with IR-based desoldering. In their process steps, the IR-heating was organized as a two-step methodology to ensure the desoldering of every remaining part [24].

A wave soldering equipment is used by Marconi et al. [25] for the desoldering of components on a disassembly cell. The preheater uses 5000 W infrared lamps in 4.5 μm wavelength, with adjustable power and adjustable temperatures.

Soldering of 3D MID devices (three-dimensional molded interconnect devices) need careful attention. “In Infrared furnaces the product clearance is limited and varies between 20 and 50 mm. So the height of the molded parts has to be lower than the fixed distance between IR emitter and transport system. To enlarge the geometric possibilities of Infrared furnaces a special soldering system was constructed, where the IR emitters are fixed on numeric controlled axes. By changing the distance between the molded parts and the emitters, the temperature on the board can be influenced and thereby the system allows a good adaptation on the geometric form of molded parts.” [26]

It is important to note that the infrared soldering is used for preheating in other soldering methods as well, such as wave soldering [27]. Both short-wave and long-wave preheaters can be used to equalize the temperature. In wave soldering, the different absorption characteristics of the given components and the board can cause mismatches in thermal expansion, so the use of an IR preheater can be advantageous. Also, the final zones of convection ovens can be improved with quartz tube heaters. Further examples will be presented in the chapter describing the VPS.

2.8 Latest improvements, optimizations, and findings

The chapter presents results from the last decades of literature regarding IR-based lead-free reflow soldering in an advancing timeline.

From an interesting reversed aspect, Svasta et al. [28] investigated the emissivity of surface-mounted devices on a heated plate with an IR-based thermo-camera, in order to improve soldering quality later in IR-based ovens. Their conclusions focused on the large variation of package emissivity, also confirming that the heat absorption on a high-density SMT assembly will not be uniform. They concluded that direct relation between smooth surface, color, and component emissivity is difficult to establish. They conclude their work with a recommendation to component manufacturers, to exactly specify the emissivity of their package surfaces and to enable improved quality control in IR reflow soldering. IR camera was also used by Mashkov et al. [29], for optimizing reflow processes.

The performance of VPS and IR was compared for a special PCB type; Plotog et al. [30] investigated soldering on Glass Circuit Boards (GCBs), and they found that C/I method resulted in poor results compared to VPS. It was found that for substrates, where heat is accumulated in a significant matter, the profile is hard to control, even with the advanced C/I methodology. Longer profiles are needed for heating, but this aspect conflicts with the recommendations of the solder paste manufacturers. Also, the longer exposure to heat in C/I oven resulted in "blisters" and delaminations on the GCB.

Mashkov et al. [31,32] developed a proprietary operational control for reflow soldering processes, with a developed IR oven. They applied the classical C/I solution with mid-IR heaters and gas flow circulation. They used heaters, which made of thin stainless steel sheets, with a thickness of 1.5 mm. They used coatings to improve the efficiency of emitters, where at the mid-IR range, they were able to obtain 0.9 value for optimized emissivity. Their heaters had lateral, sheet-shaped construction. Each heater had four flat heating elements with 9 mm distances. Their experimental soldering oven was built without a conveyor belt, and with one central fan to circulate the air from top to the bottom of the work zone. They concluded that their oven construction was able to perform reflow soldering with low thermal inertia. Their optimizing work aimed to improve soldering powerful LED devices on metal substrates with large thermal mass. Above the assembly prepared for reflow, they positioned an aluminum sheet, in order to homogenize heat transfer and solder delicate SMD components properly. Finally, they documented that their oven was able to solder BGAs and components/substrates with large thermal masses in an efficient manner.

Dušek and Váňa [33] investigated the influence of different component surfaces and their effect on the resulting temperature profile. They used an experimental memory module, where the surface-mounted chips were covered with a silver layer, in other case with an aluminum foil, or the chip was

left with the original surface of the packaging material. It was found that the intensity of the heating gradient and the peak temperature was decreasing according to the surface treatment in the following order: Original package > silver layer > aluminum foil. Their experiment reconfirmed the usually cited difficulties with IR, considering the reflective nature of different component surfaces.

Jánó and Fodor [34] optimized through-hole and surface-mounted assembly for ceramic capacitors. In their experimental setup, they compared convection-enhanced IR soldering with VPS. They focused their tests on the relative capacitance change and the equivalent series resistance. They found that regardless of the heat transfer method, quality and reliability of the soldered capacitors mainly depend on the fast cooling and slower exposure to high temperatures.

Krammer also investigated [35,36] the differences between IR and VPS. He found with aging tests and mean time between failure (MTBF) calculations that solder joints formed with VPS resulted in a better expected lifetime. Krammer further evaluated 0603 surface-mounted components and their resulting joints in IR and vapor phase. He developed an image processing algorithm to measure the thickness of resulting intermetallic layers. It was found that after aging, the intermetallic layer growth was more intense in IR than in VPS ovens. This work further presented the improved applicability of VPS ovens over IR. The technology of VPS is later discussed in Chapter 4, Vapor Phase Reflow Soldering Ovens.

Skácel et al. [37] designed infrared heaters with homogeneous energy transfer. Their heat emitter was evaluated in a FEM software from the aspect of optimized, evenly heated transfer. They tested different wire arrangements inside the heater panels. Eventually, they came across an optimized solution, which offered a 10°C−13.5°C temperature difference at the surface of the heater.

Wang et al. [38] used IR soldering as a novel approach for melting and joining nanowires. They used pure tin solder for the given process (Sn-based single or multisegment nanowires). The suspension of ethanol and tin-based nanowires was dripped on a piece of Si wafer, dried on air, and heated by IR. They used a polydimethylsiloxane (PDMS) cover to form a closed system. The total heating time was clocked in approximately 1 minute. They concluded their work with the statement that IR soldering can be used as a novel approach to solder nanowire systems. The work is important to connect IR-based soldering techniques with the scale of nanotechnology.

Ivanova et al. [39] developed an infrared soldering station to assemble LED devices. According to their conclusions, their control of the IR emitter-based reflow temperatures enables assembling without thermal damage on the board and the components.

IR soldering was applied very recently in the field of photovoltaics. De Rose et al. used IR soldering to prepare the interconnection of silicon

heterojunction solar cells with low temperature lead-free and leaded (PbSn) solder alloys. They achieved acceptable joints at 240°C for a very short time at 240°C, which was achieved with fast, pulsed IR soldering. The preheating was performed with heated plates, and then the fast peak was achieved with 1.35-second IR pulses at approximate temperatures at 200°C and 240°C [40]. Geipel et al. continued the common research with 2.2-second cycles. They found that with their approach, noneutectic Sn-Bi solder alloy without Ag compound is recommended for temperature-sensitive solar cells [41].

IR soldering can result in specific failures, which were discussed previously in Chapter 1, Introduction to Surface-Mount Technology. In a short summary, we must note that the most interesting failures in recent literature are presented here. McCluskey et al. [42] investigated PBGA popcorning in perimeter and full matrix array components. They found that with lower IR temperature ramps, the popcorn cracking can be inhibited and the extent of inner delamination can be reduced. Otáhal et al. [43] also investigated BGA components. They researched the quality of BGA joints according to the heating direction with IR heaters (top, bottom, mixed). They found that regardless of the heating direction, the destructive testing of solder balls resulted in ductile fracture. From the bottom heating, the Sn grains showed a single grain structure, contrary to the top/mixed heating. Bottom heated samples also showed the smallest roughness and grain size in the case of intermetallic layer roughness inspection.

It was reported that the fast rise times of near-IR can cause solder balls and flux spattering. Solder wicking can also occur in mid-IR ovens [7].

2.9 Temperature measurements inside IR and other reflow ovens

Appropriate soldering quality requires appropriate process control. In reflow technologies, it is important to record the temperature of the PCB and selected parts of the assembly. In general, for reflow technologies, thermometry is used to characterize the process, and for the purpose, thermocouples (TCs) are applied. TCs can be attached on the board, inside vias, on the components, on leads, or inside solder joints. In order to enable reproducible measurements, the thermocouples, and their construction (e.g., the "hot spot" beads) should be identical [12].

"The determination of the thermal profile and the settings for the IR radiation/forced convection reflow process are made by an 'expert' (usually a process engineer) on the shop floor. This method is based on experience and rules-of-thumb. A few boards are 'profiled' before an acceptable thermal profile and IR radiation/forced convection oven settings are determined. The absence of the expert, the use of trial and error, the use of suboptimal parameters, and the loss of time in arriving at acceptable results detract from facility productivity and product quality." [44]

The chapter presents the basics of how to obtain the "time−temperature graph which is used to properly control the thermal mass and heat distribution to form robust solder joints between the PCB and electronics components during reflow soldering" [45]. The methodology is presented in this chapter, also highlighting, that the basics stay mainly the same for the rest of the presented methods in future chapters.

2.9.1 Basics of thermocouples

Thermocouples are based on the Seebeck effect. If two different metal wires (pure metal or alloy) are connected on a common point, and this point is heated (hence the name: "hot spot"), potential difference (voltage) is measurable on the cold ends of the wires. This effect is due to the rearrangement of the electrons along the wires due to the temperature change. The charge transfer is originated from the conservation of momentum of electrons in the metal lattice, across the volume of the wire [46]. In the case of K-type thermocouples, the electrons can move about four times more easily in the NiAl wire, than in Ni-Cr. At the cold ends, the wires are overcharged with electrons; differently in the two wires. The measured potential difference is proportional with the temperature difference along the hot and cold ends of the wires. The voltage is heavily dependent on the materials and the temperature. The voltage is not dependent on the temperature gradient along the wires. The temperature can be calculated according to (2.9):

$$\Delta U = S \cdot \Delta T \tag{2.9}$$

where ΔU is the change of the potential (μV), ΔT is the change of the temperature (°C), and S is the Seebeck coefficient (μV/°C). If two different materials are used, then the voltage can be calculated as (2.10):

$$U = \int_{T_1}^{T_2} S_A(T) - S_B(T) \ \mathrm{d}T \tag{2.10}$$

where A and B denote the two different metal materials and T_1 and T_2 denote the temperature at the two different ends. The hot end of the thermocouple wires can be formed with different approaches [12]. The first and easiest method is to twist the wires together. This results in measurement problems due to problems in stable contacting. The other method is welding the two wires to form a hot spot. It is important to note that the nude, uninsulated ends of the cables might form an unintended contact after the hot spot joining, if the wires are not handled properly. This results in false readings, while the thermocouple will supply the data according to the closest contact point of the two wires to the cold end of the structure. The welded wire pair also helps to avoid noise-induced measuring error from the wire pair contact [12]. Nowadays, diameter of the welded hot spots can be reduced to 150%

of the original wire diameter. It is also important to keep the welded spot small, in order to avoid thermal inertia of the sensor itself. Welded hot spots are usually nonsensitive to smaller vibration, but inappropriate handling and manipulation might result in a broken hot spot at the welded end. In reflow profiling, usually exposed thermocouple ends are used, but there are grounded and insulated thermocouples available. (The latter can be used in the work zone of the ovens as well.)

It is important to note that signal conditioning in the μV range is not straightforward. There is a need of a precise cold point temperature measurement for reference, and the small voltage range can be distorted by EM effects. With shielded or twisted wire pairs, the problem can be mostly neutralized. Corrosion might also alter the precision of the utilized thermocouples.

According to the intended form of application, the thermocouples can be manufactured with different wire- and hot-spot diameter, and different insulation material and thickness. Usual insulation materials are PTFE (polytetrafluoroethylene), PFA (perfluoroalkoxy), and fiberglass clad coating. The different wire constructions may lead to flexibility issues, which can affect efficient positioning in reflow ovens [47,48]. It is recommended to use the finer, flexible TCs, noting that ultra-thin wire construction may result in fracture at the hot spot. Thick ceramic insulated thermocouples are considered to be too stiff for the delicate SMD populated PCBs, also transferring mechanical force to the fixture—this can cause further practical problems during reflow profiling [48]. Shorter thermocouple wiring may also result in better stability, while they are less prone to damage and detachment. To maximize stability, it is recommended to use mechanical supports, such as mounting holes to tie the wires, to add tape on the wires at other points of the PCB (if possible) or fix the wires on the PCB holder grille.

2.9.2 Thermocouple types

For soldering applications, usually, K-type thermocouples are used, which have chromel−alumel (Ni-Cr/Ni-Al) pairing of thermocouple wires. K-type thermocouples are cheap and precise on the temperature range of reflow soldering, and also their nonlinearity can be easily handled. There are other thermocouples, which can be used like T (copper/constantan—which have a faster response than K and have better wetting properties with usual lead-free solders [48]) or J (iron/constantan). Over 300 materials can be combined with the aim of thermocouple combinations [46]. Fig. 2.11 shows an assortment of different thermocouples with the same construction (0.2 mm wire thickness, PFA insulation). The different TC types have different color coding. The presented colors are according to the IEC 60 584-3 international standard, but in other countries, distinctive codes could be used (like US ANSI MC96.1, and DIN 13711).

FIGURE 2.11 Thermocouple assortment (K, N, J, T types).

2.9.3 Thermocouple attachment

The attachment of thermocouples is a crucial part of the profiling. In order to achieve proper attachment, polyimide tape, SMD or thermally enhanced epoxy adhesives, aluminum adhesive tape (alu-tape), or solder with higher melting temperature (e.g., Sn10Pb90, 302°C melting point) can be applied. The tapes are considered to be cost-effective solutions, and also, their use is easy and straightforward. Sinohui found that high temperature solder attachment results in the most precise and repeatable profiling results. On the contrary, the method is the most expensive solution, including the time and relative complexity of the preparation. Also, solder attachment can only be performed onto metallic surfaces. He also found that SMD adhesives have inconsistent thermal conductivity problems. During attachment, the hot end of the thermocouples should be in contact with the measured surface, and the glue can easily form a layer between the surface and the welded hot spot. The method is mostly recommended for single measurement runs [49]. Adhesives with thermal enhancement may be as reliable and repeatable as high temperature solders [48]. During preparation of adhesive attachment bonds, the curing time (up to a few minutes) must be also taken into account. The beads formed by the adhesive or the high temperature solder should be at the size of ~ 4 mm. While 2 mm can be problematic from the aspect of stability, larger beads may add [48] additional thermal inertia. According to Wickham and Hunt [48], it is more practical to lead the attached thermocouples in the level of the PCB along the surface and along the sample holder, routing it directly away from the fixing point. Angled, vertical, and horizontal parallel attachment may involve additional heat conduction to the hot spot, altering the intended results.

Thermocouple fixing positions may also alter the intended results [48]. If the component has a large thermal mass, the transient effects must be taken into consideration. If the measured component is in the proximity of large components with high thermal mass, the recorded maximums of the temperature can be suppressed. If the recorded temperatures are logged on a solder joint near the edge of the PCB, it will reach higher maximum temperatures, and the time above liquidus value will be considerably larger.

In practical applications, the thermocouple positions should be chosen according to the identified coldest and hottest parts of the PCB, in order to ensure that most extremes are within the recommended limit of the process.

In IR reflow ovens, the reflectivity might also affect the recorded temperatures, so in the case of tape-based fixing methods, it can be advantageous to fix the thermocouples on the side of the secondary heating.

2.9.4 Data logging

Temperature logging is usually performed with specific DAQ systems, where the two ports of the channels are prepared according to the + / − wires of the K-type thermocouples. Such systems are able to measure and convert the voltage drop at the end of the TC cables. They usually have built-in cold junction compensation.

The profiles and the attaching methods themselves can be evaluated from different aspects. The recorded temperature logs can be compared according to the following methods [47−49]:

- maximum temperature (°C),
- time spent on peak temperature (s),
- time above liquidus (of the solder alloy used in the evaluated processes) (s),
- slope (°C/s), and
- heating factor (s °C).

Tsai describes profile investigations with a comparative study [45]; he highlights the following critical points for evaluating a measured profile. This is shown in Fig. 2.12.

Further indications on how to properly assess a soldering profile are presented in Chapter 1, Introduction to Surface-Mount Technology.

The DAQ system can be either a hand-held device, a PC- or network-connected robust field logger, or a traveling logger for conveyor-based in-line ovens. The block diagram of a typical DAQ system can be found in Fig. 2.13.

Fig. 2.11 presents the signal chain after the thermocouple is connected to the DAQ. The + / − signal needs conditioning after the connection of the TC. The signal conditioning involves electrostatic discharge and overvoltage protection (ESD + OVP) and further possible filtering methods. After signal conditioning, amplification takes place with cold junction compensation. Usually, this process is handled by a dedicated integrated circuit (IC) or a channel of a dedicated IC. Then the signal is processed by an Analog-to-Digital (AD) converter (like a Σ-Δ type ADC), where the data are analyzed by a logic circuit. The processed data can be saved to internal memory, or in case of other DAQ systems, the data are transmitted via a bus or a port to a

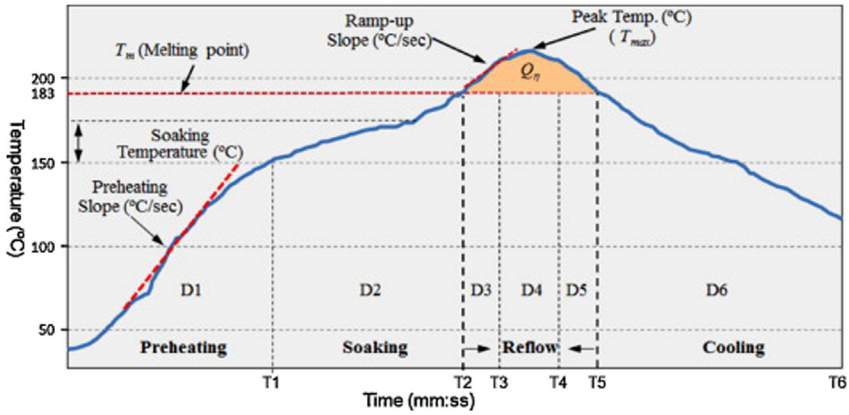

FIGURE 2.12 Typical reflow profile, with different aspects of evaluation: preheating slope, soaking temperature, melting point, ramp-up slope, and peak temperatures. With comparative study, the quality of temperature measurement can also be evaluated by analyzing the recorded profiles. *From T.-N. Tsai, Thermal parameters optimization of a reflow soldering profile in printed circuit board assembly: a comparative study, Appl. Soft Comput. 12(8) (2012) 2601–2613.*

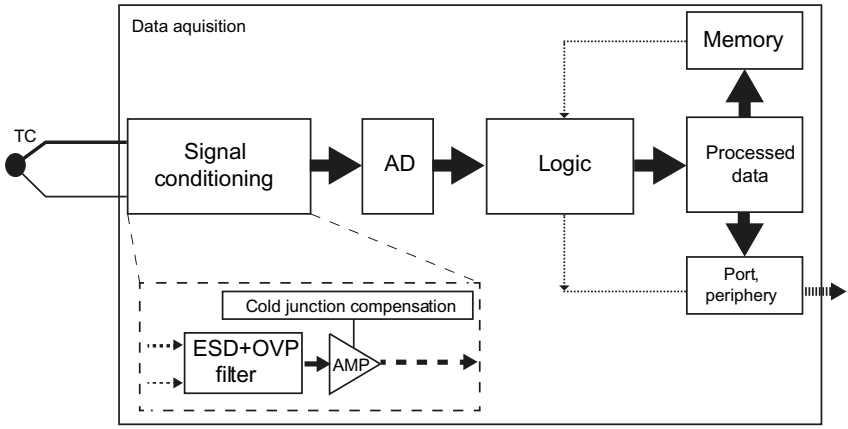

FIGURE 2.13 Typical block diagram of a data acquisition system for thermocouples.

periphery or a computer, on-the-fly, wired, or wireless in the wake of Industry 4.0 directives.

2.9.5 Voltage-to-temperature conversion

Voltage-to-temperature conversion is not straightforward [50], while the thermocouples are considered to be nonlinear devices. The simplest way to overcome this problem is to use a one-constant scale factor, or in other words, a

linearization on the given temperature range; however, this approach limits the precision of the system.

The next step in improving upon the precision is to implement a look-up table, where each thermocouple voltage sets are matching a given temperature value. Then linear interpolation can be used between the two in order to receive intermediate temperature values [51].

A more sophisticated and precise method involves polynomial calculations and the tables of the National Institute of Standards and Technology (NIST) [52,53], which enable direct conversion of the voltage/temperature scales. While there is a voltage difference between the reference, cold point junction, and the junction of the thermocouple, basic compensation is needed according to (2.11):

$$\Delta V = V_{J1} - V_{J2} \tag{2.11}$$

where ΔV is the output voltage of the thermocouple, V_{J1} is the voltage generated at the thermocouple junction, and V_{J2} is the voltage generated at the reference. In this case, the reference terminals should be kept on the same temperature (e.g., with an isothermal block). For thermoelectric voltage calculation [53] from a known temperature, direct polynomials are used (2.12):

$$E = a_0 + a_1 T + a_2 T^2 + a_3 T^3 + \cdots + a_n T^n \tag{2.12}$$

for temperature calculation, an inverse polynomial approach is used to describe the temperature. For this purpose, the equation can be defined as (2.13):

$$T = a_0 + a_1 E + a_2 E^2 + a_3 E^3 + \cdots + a_n E^n \tag{2.13}$$

In both definitions, T is the temperature, E is the electromotive force (EMF)-induced thermoelectric voltage of the TC (V), and a is the polynomial coefficient unique to each thermocouple. The n index denotes the constant as the maximum order of the polynomial description. It is easy to see that with the increase of the n value, the precision is increased. For example, when $n = 9$, the precision is $\pm 1°C$ [52]. To enable effective calculation, the nested polynomial form of (2.14) is used, where our example is presenting a fifth-order description:

$$T = a_0 + E(a_1 + E(a_2 + E(a_3 + E(a_4 \cdots + a_5 x)))) \tag{2.14}$$

It must be noted that for K-type thermocouples, the calculation of (2.12) can be performed by considering a so-called magnetic ordering effect:

$$E = \sum_{i=0}^{n} a_i (T)^i + a_0 e^{a_1 (T - a_2)^2} \tag{2.15}$$

where e is the natural logarithm constant, and the constants are the following: $a_0 = 0.118597600000 \times 10^0$, $a_1 = -0.118343200000 \times 10^{-3}$, and

$a_2 = 0.126968600000 \times 10^3$ [52,53]. T could be denoted more precisely with ITS-90 designated T_{90} of t_{90} which refers to International Kelvin Temperatures (T_{90}), or to International Celsius Temperatures (t_{90}). The NIST tables based calculation methodologies refer to these temperatures. If the reference temperature is different from 0°C, then reference compensation must be performed. The internal temperature measurement devices of an IR oven must take into account its temperatures at the reference junction as well, in order to perform precise measurements.

As an example, the ITS-90 table for K-type thermocouple has three main sections. The first part defines the thermoelectric voltage of the specific thermocouple in mV for the given temperatures. For K-type thermocouples, three subranges are defined for this table: −270°C to 0°C; 0°C−500°C; and 0°C−1372°C. The second section contains the given coefficients of (2.15) for a specific thermocouple for two subranges −270°C to 0°C and 0°C−1372°C. The third section contains the coefficient for the approximate inverse function (2.14). The subranges are similar to the first section of the K-type thermocouple ITS-90 table. The complete list of tables can be found at the official NIST ITS-90 Thermocouple Database [52,53].

While solving polynomial functions can be a demanding task for cheaper ICs, to increase the effectivity of calculation, the recorded voltage/temperature data can be divided into smaller sections, where lower order polynomial (e.g., third order) can be used for faster calculation. While thermocouple output can result in small voltages in the μV range (e.g., it results in 4 μV change if the temperature is increased with 0.1°C), applying noise rejection methodologies (filtering, guarding, integrating, and tree-based switching) is recommended [50]. The detailed description of such methods goes beyond the scope of the given chapter and the book.

2.9.6 Typical devices for reflow temperature logging

The simplest DAQ device suited for reflow capabilities usually has two or more channels for logging. While the devices are easy to control by operators at the manufacturing lines, the analysis of the recorded data requires the experience of an engineer.

A traveling logger is basically a hand-held device combined with a so-called jacket, which is comprised of a metallic shell with a thick insulator layer inside, and an outer insulator shell. The insulated shell closes on the data logger, where the thin TC wires are lead out on the side of the shell. Then the outer insulator is suited onto the outside of the metallic shell. The traveling logger is recommended to be kept at least one zone away from the assembly on the conveyor line, in order to avoid cross effects of the additional thermal mass. Also, the recording function of the logger (if it does not have built-in wireless communication) should be either initialized before closing the casing, or a trigger temperature should be set, where the logger

FIGURE 2.14 Traveling solder profile logger with double insulation.

starts recording automatically. The traveling logger must keep up with its inner temperature rise at the cold junction compensation. It must be noted that if the logger does not have outer insulation, the proximity of the oven or direct contact with the hot oven casing can alter the recorded temperatures, while the heated device might not be able to follow the cold side compensation performed by the internal temperature measurement device (e.g., a thermistor) and the connected logic unit. Modern loggers (reflow profilers) are mostly prepared for K-type thermocouple readings, with dedicated integrated circuit for amplifying and compensating,

Fig. 2.14 presents a traveling logger with the insulation metal casing and the outer jacket for additional thermal insulation.

2.9.7 Temperature logging of IR ovens in the literature

While the popularity and use of IR ovens saw a decline in the last decades, a few papers still mention the use of IR-based heat transfer and the importance of temperature measurement in them.

Pecht and Govind used an experimental setup in an IR oven, where they combined temperature measurements for control, X-ray equipment, and a strain gage bridge network for analyzing package deformation during IR reflow. The reflow subsystem was working with tungsten filament-based lamp IR heaters, and a thermocouple was fixed on the package body to provide feedback to the temperature controller, in order to replicate any given reflow profile [54].

Su et al. developed a special reflow profile identification system [44]. "The architecture of such a system is similar to that of a typical expert system. The designing of an expert system requires an intricate development and implementation process. The system developed in the research considered IR reflow soldering profile identification, adhesive cure identification,

contour profile identification, an update mechanism, explanation facility, and the knowledge base." They evaluated their system with a solid set of inputs and outputs. "Inputs required by the solder paste reflow profile identification system include the initial substrate temperature, the process length (or length of the reflow oven), the board length, the input rate of the process, the distance between the boards, and the thermal constraints of the solder paste, the components and the substrate. The outputs of the solder paste reflow profile identification systems include a graphical display of the optimal IR radiation/forced convection reflow temperature profile, the range between where IR radiation/forced convection reflow profile is still acceptable." In their system "associated information is presented in a textual form. This information includes the conveyor speed, process time, and output rate regarding maximum, optimum, and minimum thermal profiles." Nowadays, modern profile analyzer software work in a similar manner.

Whalley calculated heat transfer coefficient values from temperature measurement data [55]. Najib et al. also used a thermocouple for feedback, in order to control the C/I reflow [18]. They went further, however, by analyzing the uniformity of the work zone. "The uniformity of oven chamber temperature was determined from the recorded temperatures, and it was calculated as the temperature difference between the setting temperatures. The experiment was designed because no literature reported on the experimental thermal investigation of the desktop reflow soldering process. The initial temperature inside the chamber was controlled and determined to be in a range of 25°C−27°C. Experiments were carried out for the validation of the numerical model." They also used a large amount of thermocouples, which is rare in such measuring situations, due to the limitations of DAQ channels. "To record the temperature distribution of the oven chamber, a total of 60 thermocouple location was measured at selected plane. The thermocouples were placed at two different heights within the oven chamber. These thermocouples were positioned on a plane 61 (lower layer or oven rack) and 76 mm (upper layer, 15 mm above oven rack) from the bottom wall of the chamber. The thermocouple array for each plane was divided into three columns. During the experiments, 12 thermocouples, which located in each column measured the temperature of each running. The experiment was repeated, and the average values were computed for each plane. At certain positions, overlapping thermocouples were used to calculate the average values and the experiments were repeated to determine the repeatability of reflow setting. The thermocouple arrays were attached to the stainless steel frames and hold in finite position using Kapton tape. Experimental uncertainty analysis was conducted to estimate the percentage error of measurement. Measurements were repeated using one thermocouple at the selected position. The measurement at the position is selected as a reference value. The procedure is repeated with the increasing number of thermocouples surrounded the reference position until a total number of thermocouples have been reached.

Finally, the temperature measurements of the reference position are compared, and maximum temperature deviation is less than 1%. Moreover, the smaller size of thermocouple was used for the comparison and the difference

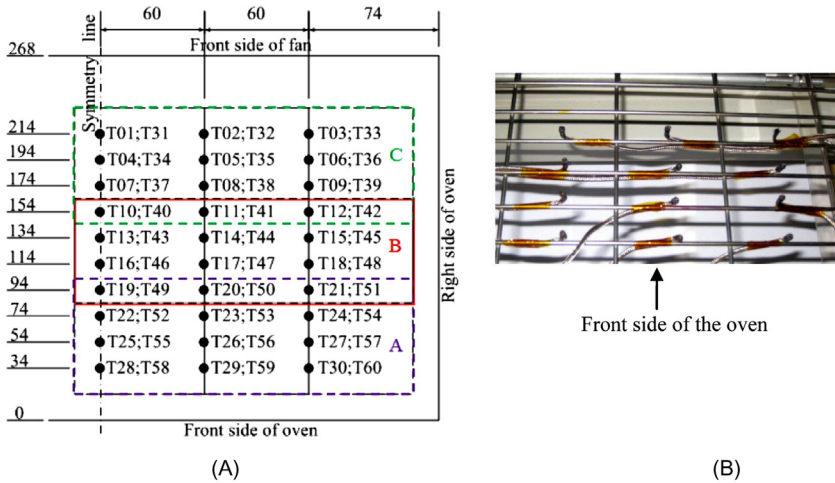

FIGURE 2.15 Thermocouple distribution on PCB assembly holder grille for investigating the temperature of a C/I reflow oven. A - thermocouple matrix; B - photo of positioned sensors. *From A.M. Najib, M.Z. Abdullah, C.Y. Khor, A.A. Saad, Experimental and numerical investigation of 3D gas flow temperature field in infrared heating reflow oven with circulating fan, Int. J. Heat Mass Transf. 87 (2015) 49–58.*

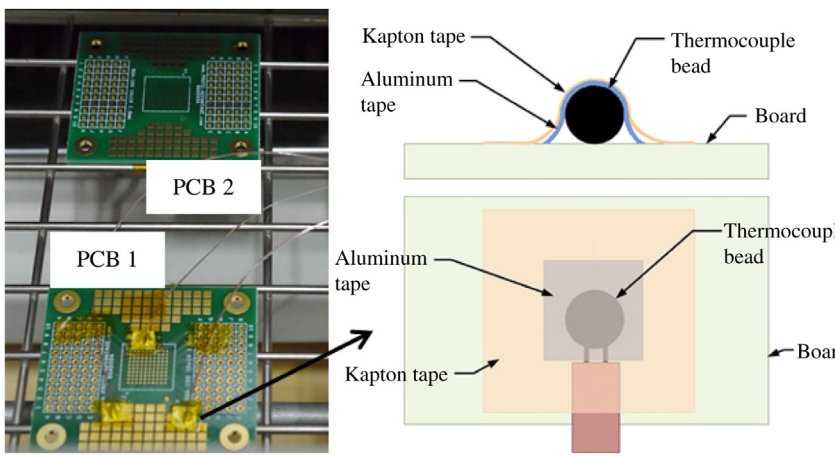

FIGURE 2.16 Thermocouple fixing on measurement boards. *From A.M. Najib, M.Z. Abdullah, C.Y. Khor, A.A. Saad, Experimental and numerical investigation of 3D gas flow temperature field in infrared heating reflow oven with circulating fan, Int. J. Heat Mass Transf. 87 (2015) 49–58.*

in measurement is less than 3%. Finally the thermocouple diameter size of 0.5 mm was selected for measurement of bulk air temperature from the oven to stabilize unwanted fluctuations from the smaller size of thermocouple." The distribution of thermocouples can be seen in Fig. 2.15.

Their test boards were used to measure temperature along the sample PCBs. "Each test board was instrumented with three type-K thermocouples, which were attached using aluminum tape in combination with Kapton tape to provide a secure connection with good thermal conductivity between board and thermocouple bead. Aluminum tape was cut to the size of approximately 5×5 mm and was used to secure the thermocouple to the PCB. The aluminum tape was then overlaid with 8×8 mm of Kapton tape to prevent lifting. The thermocouples measure the temperature of PCB surface. For each PCB position, average values were computed, and the peak temperature data of PCB during reflow were extracted. The temperature assessment of the measurement was used to validate the numerical model." Fig. 2.16 presents their attachment methods on the measurement PCB surfaces.

References

[1] A. Jamnia, Practical Guide to the Packaging of Electronics: Thermal and Mechanical Design and Analysis, Marcel Dekker, New York, US, 2003.

[2] R. Strauss, SMT Soldering Handbook, BH Newnes, Oxford, UK, 1998.

[3] R.P. Prasad, Surface Mount Technology, Principles and Practice, Springer Science, New York, US, 1997.

[4] DIN 5031-7 Standard, Optical radiation physics and illumination engineering; terms for wavebands standard by Deutsches Institut Fur Normung E.V. (German National Standard), 01/01/1984.

[5] ISO 20473:2007, Optics and photonics—Spectral bands (reviewed in 2015).

[6] M. Judd, K. Brindley, Soldering in Electronics Assembly, BH Newnes, Oxford, UK, 1999.

[7] J. Bergenthal, Reflow Soldering Process Considerations for Surface Mount Application, Kemet, 1995.

[8] Elstein, Ceramic Infrared Emitters, Elstein-Werk M. Steinmetz GmbH & Co. KG, White paper, 2016.

[9] M.G. Pecht, Soldering Processes and Equipment, John Wiley & Sons, New York, US, 1993.

[10] D. Shangguan, Lead-Free Solder Interconnect Reliability, ASM International, Ohio, US, 2005.

[11] M. Theriault, J. Uner, A. Rahn, Use of inert atmospheres in lead-free soldering, in: K.J. Puttlitz, K.A. Stalter (Eds.), Handbook of Lead-Free Solder Technology for Microelectronic Assemblies, Marcel-Dekker, New York, US, 2004.

[12] G.M. Freedman, Soldering techniques, in: C.F. Coombs Jr. (Ed.), Printed Circuits Handbook, sixth ed., McGraw & Hill, New York, US, 2008.

[13] B.E. Yoldas, T. O'Keefe, Deposition of optically transparent IR reflective coatings on glass, Appl. Opt. 23 (20) (1984) 3638.

[14] N.-C. Lee, Reflow Soldering Processes and Troubleshooting, BH Newnes, Boston, US, 2001.
[15] M. Schwartz, Soldering, Understanding the Basics, ASM International, Ohio, US, 2014.
[16] A. Géczy, B. Kvanduk, B. Illés, G. Harsányi, Comparative study on proper thermocouple attachment for vapour phase soldering profiling, Solder. Surf. Mt. Technol. 28 (1) (2016) 7–12.
[17] C. Lau, M. Abdullah, C. Khor, Optimization of the reflow soldering process with multiple quality characteristics in ball grid array packaging by using the grey-based Taguchi method, Microelectron. Int. 30 (3) (2013) 151–168.
[18] A.M. Najib, M.Z. Abdullah, C.Y. Khor, A.A. Saad, Experimental and numerical investigation of 3D gas flow temperature field in infrared heating reflow oven with circulating fan, Int. J. Heat Mass Transf. 87 (2015) 49–58.
[19] BME ETT, Virtual Laboratory, 2000–2018. http://www.ett.bme.hu/vlab/, 2019 (accessed 21.11.19).
[20] RO-06 Plus, Convection Reflow Oven Installation/Operating/Maintenance Manual, 4000013/01, 2014.
[21] B. Benchoff, Improving the T-962 Reflow Oven, Hackaday.com, https://hackaday.com/2014/11/27/improving-the-t-962-reflow-oven/, 2014 (accessed at 21.11.19).
[22] Improvements made to the cheap T-962 reflow oven utilizing the existing controller HW, www.github.com, 2019 (accessed 12.11.19).
[23] S. Yokoyama, M. Iji, Recycling of printed wiring boards with mounted electronic parts, in: Proceedings of the 1997 IEEE International Symposium on Electronics and the Environment, San Francisco, CA, 1997.
[24] S. Yokoyama, Y. Ikuta, M. Iji, Recycling system for printed wiring boards with mounted parts, in: Proceedings of First International Symposium on Environmentally Conscious Design and Inverse Manufacturing, Tokyo, Japan, 1999.
[25] M. Marconi, G. Palmieri, M. Callegari, M. Germani, Feasibility study and design of an automatic system for electronic components disassembly, J. Manuf. Sci. Eng. 141 (2) (2019). 02101-1-8.
[26] K. Feldmann, M. Gerhard, Direct soldering of electronic components on molded devices, CIRP Ann. 44 (1) (1995) 19–22.
[27] T. Nishimura, Wave soldering, in: K. Suganuma (Ed.), Lead-Free Soldering in Electronics, Science, Technology and Environmental Impact, Marcel Dekker, New York, US, 2004.
[28] P. Svasta, D. Simion-Zanescu, R. Ionescu, Components' emissivity in reflow soldering process, in: Proceedings of 54th Electronic Components and Technology Conference, Las Vegas, NV, 2004.
[29] P. Mashkov, T. Pencheva, B.S. Gyoch, Reflow soldering processes development using infrared thermography, in: Proceedings of 32nd IEEE International Spring Seminar on Electronics Technology, Brno, Czech Republic, 2009.
[30] I. Plotog, N. Codreanu, P. Svasta, T. Cucu, C. Turcu, G. Vărzaru, et al., Investigations on assembling of electronic packages onto glass substrates using lead-free technology, in: Proceedings of 31st IEEE International Spring Seminar on Electronics Technology, Budapest, Hungary, 2008.
[31] P. Mashkov, T. Pencheva, D. Popov, Application of low inert infrared heaters for soldering processes, in: Proceedings of 27th IEEE International Spring Seminar on Electronics Technology, Bankya, Bulgaria, 2004.

[32] P. Mashkov, T. Pencheva, B.S. Gyoch, Development of reflow soldering processes using heaters' operation control, in: Proceedings of 32nd IEEE International Spring Seminar on Electronics Technology, Brno, Czech Republic, 2009.

[33] K. Dušek, T. Váňa, Study of temperature profiles of the infrared continuous furnace, in: Proceedings of 34th IEEE International Spring Seminar on Electronics Technology, Tatranska Lomnica, Slovakia, 2011.

[34] R. Jánó, A. Fodor, Soldering profile optimization for through−hole and surface mounted ceramic capacitors, in: Proceedings of 37th IEEE International Spring Seminar on Electronics Technology, Drezden, Germany, 2014.

[35] O. Krammer, M. Nagy, Reliability comparison of infrared and vapour phase soldering, in: Proceedings of 18th IEEE International Symposium for Design and Technology in Electronic Packaging, Alba Iulia, Romania, 2012.

[36] O. Krammer, Comparing the reliability and intermetallic layer of solder joints prepared with infrared and vapour phase soldering, Solder. Surf. Mt. Technol. 26 (4) (2014) 214−222.

[37] J. Skácel, A. Otáhal, I. Szendiuch, Designing of infrared heater with homogenous heat transfer, in: Proceedings of 39th IEEE International Spring Seminar on Electronics Technology, Pilsen, Czech Republic, 2016.

[38] J. Wang, F. Gao, Z. Gu, Infrared (IR) soldering of metallic nanowires, in: Proceedings of IEEE 67th Electronic Components and Technology Conference, Florida, 2017.

[39] V.R. Ivanova, A.S. Ivanov, L.V. Fetisov, The development of an automated station for group soldering of the led lines, in: Proceedings of XIV International Scientific-Technical Conference on Actual Problems of Electronics Instrument Engineering (APEIE), Novosibirsk, Russia, 2018.

[40] A. De Rose, T. Geipel, D. Eberlein, A. Kraft, M. Nowottnick, Interconnection of silicon heterojunction solar cells by infrared soldering—solder joint analysis and temperature study, in: Proceedings of 36th European PV Solar Energy Conference and Exhibition, Marseille, France, 2019.

[41] T. Geipel, D. Eberlein, A. Kraft, Lead-free solders for ribbon interconnection of crystalline silicon PERC solar cells with infrared soldering, AIP Conf. Proc. 2156 (2019) 020015.

[42] P. McCluskey, R. Munamarty, M. Pecht, Popcorning in PBGA packages during IR reflow soldering, Microelectron. Int. 14 (1) (1997) 20−23.

[43] A. Otáhal, J. Somer, I. Szendiuch, Influence of heating direction on BGA solder balls structure, in: Proceedings of European Microelectronics Packaging Conference, Warsaw, Poland, 2017.

[44] Y.Y. Su, K. Srihari, C.R. Emerson, A profile identification system for surface mount printed circuit board assembly, Comput. Ind. Eng. 33 (1-2) (1997) 377−380.

[45] T.-N. Tsai, Thermal parameters optimization of a reflow soldering profile in printed circuit board assembly: a comparative study, Appl. Soft Comput. 12 (8) (2012) 2601−2613.

[46] C. Reebals, WIKA Handbook, Pressure & Temperature Measurement, U.S. Edition, 2008, HB001-1000 8/08.

[47] M.A. Alaya, V. Megyeri, D. Busek, G. Harsányi, A. Géczy, Effect of different thermocouple constructions on heat-level vapour phase soldering profiles, Solder. Surf. Mt. Technol. (2020). in press. https://doi.org/10.1108/SSMT-10-2019-003410..

[48] M.J. Wickham, C.P. Hunt, Thermal Profiling of Electronic Assemblies, National Physical Laboratory Report, MATC(A)50, 2001.

[49] C. Sinohui, A comparison of methods for attaching thermocouples to printed circuit boards for thermal profiling, in Proceedings of Nepcon West, Anaheim, CA, No. TS-19, 1999.
[50] Practical Temperature Measurements, Omega, Agilent Technologies, 2000.
[51] M. Duff, J. Towey, Two ways to measure temperature using thermocouples feature simplicity, accuracy, and flexibility, Analog Dialogue 44 (10) (2010).
[52] Temperature-Electromotive Force Reference Functions and Tables for the Letter-Designated Thermocouple Types Based on the ITS-90, National Institute of Standards and Technology Monograph 175, 1993.
[53] NIST ITS-90 Thermocouple Database, NIST Standard Reference Database 60, Version 2.0 (Web Version), Last Update to Data Content, 1993.
[54] M.G. Pecht, A. Govind, In-situ measurements of surface mount IC package deformations during reflow soldering, IEEE Trans. Compon. Packag. Manuf. Technol. C 20 (3) (1997) 207–212.
[55] D.C. Whalley, A simplified reflow soldering process model, J. Mater. Process. Technol. 150 (1-2) (2004) 134–144.

Chapter 3

Convection reflow ovens

Nowadays, convection heating and cooling are often used by a lot of industrial processes as well as in our everyday life. Some industrial examples are convection soldering, convection annealing, and drying systems. Some applications from our household include air-conditioning systems, convection ovens, and hairdryers. The popularity of the convection type thermal management is due to efficient heat transfer and well controllability (compared to the IR heating, see in Chapter 2, Infrared Reflow Soldering).

The conveyor-type convection reflow ovens are still the most frequently used soldering devices by electronics manufactures. Their main advantages are precise thermal management and high productivity. However, from the other side, their flexibility is lower, and their operation cost is higher compared to the other heating technologies. The physical background of convection heating is crucial for understanding the function of main parts in these ovens, which are heating, gas circulation, and distribution systems. The most critical aspect of each soldering technology is thermal management. Therefore, characterization and measurement techniques mostly determine the temperature and the heat transfer coefficient (*HTC*) in the working zones. Due to the half-closed structure and the harsh environment in the working zones, the appropriate settings of these measurement methods are crucial for achieving relevant and accurate information about the current status of one's oven. Although convection reflow ovens are robust systems, inappropriate settings and maintenance can result in soldering failures.

3.1 Basics of convection heating

If we would like to investigate and describe the operation of convection reflow ovens, first we need to be aware of the related physical parameters of the forced convection heating. These are the flow velocity, the pressure, and the density of the flowing gas, together with the temperature distribution and the *HTC*s. Therefore, this chapter starts with the presentation of the basic gas flow models, the theory of free-streams, the vertical−radial transformation of gas flows, and the radial gas flow layer formation on a board. The presented examples illustrate how the velocity, the pressure, and the density of fluid flow can be investigated and how these parameters affect the *HTC*.

Reflow Soldering. DOI: https://doi.org/10.1016/B978-0-12-818505-6.00003-0

The convection heat transfer is realized by the movement of particles/molecules within a fluid (which can be liquid, gas, and rheid), so it is a combination of heat and mass transfer. The convective heat and mass transfer take place by diffusion—random Brownian movement of particles in a fluid—and by advection, which means that the heat is transported by the larger scale motion of the particles in a fluid [1]. There are two main types of convection. During "*natural convection*" (or free convection), the heat flow itself results in the motion of the fluid (due to thermal expansion and buoyancy force). At the same time, heat is also transported by bulk motion of the fluid. During "*forced convection*" (or heat advection), the heat is transported by the movement of fluid, which is independent of the heat transfer. The fluid is forced to move by external forces, like ventilation or pumping (if forced convection and natural convection occur together, it is called mixed convection).

3.1.1 Basics of steady-state fluid dynamics

In convection reflow ovens, it is usually enough to study fluid dynamics in steady state since the transient formation of flow space is not relevant from the aspect of the general operation of the oven. For the description of a fluid movement, Newton's second axiom must be used, which makes a relationship between changes of the momentums and the acting forces on the fluid particles. The net force can be originated from forces acting on the mass of the fluid particles (e.g., gravity force) and from forces acting on the surface of the fluid particles (e.g., pressure force). If the friction is neglected (in the case of gases, it is a common approach) and the flow is steady state (Fig. 3.1A), the most common momentum equation is the Euler equation [2]:

$$\overline{v}\frac{\mathrm{d}\overline{v}}{\mathrm{d}\overline{r}} = \overline{g} - \frac{1}{\rho}\operatorname{grad} p \tag{3.1}$$

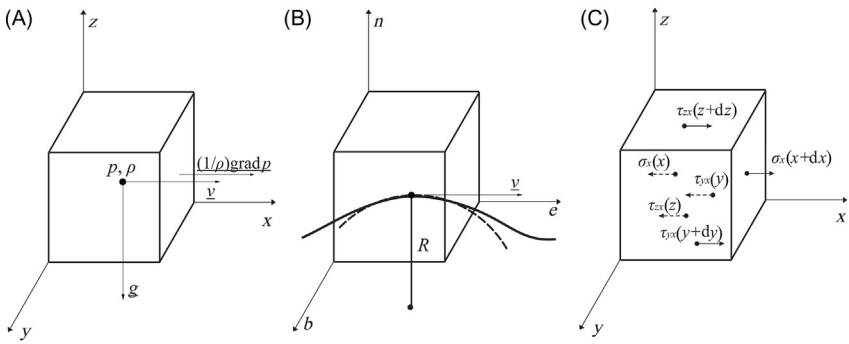

FIGURE 3.1 Description of and elementary fluid particle: (A) acting forces on an elementary fluid particle; (B) elementary fluid particle in a natural coordinate system; (C) acting stresses on the elementary fluid particle toward the *x*-direction.

where v is the velocity (m/s), ρ is the density (kg/m^3), p is the pressure (Pa), g is the gravitational acceleration, t is the time (s), and r is the spatial vector.

Eq. (3.1) is often used in the natural coordinate system (Fig. 3.1B), mainly in the case of the vertical−radial transformation of fluid flows (see in Section 3.22). The natural coordinate system is always connected to the investigated streamline. Normal (n) and basic (b) coordinate axes are perpendicular to the velocity vector (v) while tangential (e) axes is parallel. In the infinitesimal ambient of the connection point, the streamline can be supplemented with an arc that has a radius R. In this case, the Euler equation can be formulated in the following way (vectorial format):

$$\overline{v}\frac{\partial \overline{v}}{\partial e} = g_e - \frac{1}{\rho}\frac{\partial p}{\partial e}; \quad -\frac{v^2}{R} = g_n - \frac{1}{\rho}\frac{\partial p}{\partial n}; \quad 0 = g_b - \frac{1}{\rho}\frac{\partial p}{\partial b} \tag{3.2}$$

Until this point, the friction between the fluid particles was neglected. However, in numerous applications, when the flow velocity or the density of the moving fluid is high, this is a nonaccurate approach. The friction in the moving fluid can be expressed as a force that acts on the surfaces of the moving fluid particle similarly to pressure. Fig. 3.1C shows an interpretation of this expression toward the x direction. To integrate the friction into the Euler equation, one shall introduce the stress tensor, which contains the shear stresses (τ) (Pa) and the tensile stresses (σ) (Pa):

$$\underline{\underline{\Phi}} = \begin{bmatrix} \sigma_x & \tau_{yx} & \tau_{zx} \\ \tau_{xy} & \sigma_y & \tau_{zy} \\ \tau_{xz} & \tau_{yz} & \sigma_z \end{bmatrix} \tag{3.3}$$

If the fluid is incompressible, then the tensile stresses are equal with the pressure, and the shear stresses can be expressed with Newton's law of viscosity:

$$\sigma = -p; \quad \tau_{yx} = \mu\left(\frac{\partial v_y}{\partial x} + \frac{\partial v_x}{\partial y}\right) \tag{3.4}$$

where μ is the dynamic viscosity [kg/(m s)], τ_{yx} expresses the tensile stress toward the x-direction on the plane with y normal, and so on. The steady-state momentum equation supplemented with the stress tensor has the following form:

$$\overline{v}\frac{\mathrm{d}\overline{v}}{\mathrm{d}\overline{r}} = \overline{g} + \frac{1}{\rho}\underline{\underline{\Phi}}\,\underline{\nabla} \tag{3.5}$$

where $\underline{\nabla}$ is the Nabla vector. The mostly used vector format of the momentum equation toward the x-direction is the following:

$$v_x\frac{\partial v_x}{\partial x} + v_y\frac{\partial v_x}{\partial y} + v_z\frac{\partial v_x}{\partial z} = g_x + \frac{1}{\rho}\left(-\frac{\partial p}{\partial x} + \mu\left(\frac{\partial^2 v_x}{\partial x^2} + \frac{\partial^2 v_x}{\partial y^2} + \frac{\partial^2 v_x}{\partial z^2}\right)\right) \tag{3.6}$$

In the case of compressible gases (or extreme high velocities), the tensile stresses must be substituted in the following way:

$$\sigma_x = -p + 2\mu \frac{\partial v_x}{\partial x} - \frac{2}{3}\mu \operatorname{div} v \tag{3.7}$$

Eq. (3.7) results in changes in Eq. (3.6), the mixed second-order derivatives appear in the momentum equation.

3.1.2 Convective heat transfer

During the convection heating or cooling, the most interesting part is the heat transfer process between the heated or cooled solid structure and the heating or cooler fluid. The efficiency of the convection heating depends on the *HTC*, and it can be calculated with the convection heat, which flows from the heating fluid to the heated solid structure (so-called Newton's law) [3,4]:

$$\frac{\mathrm{d}Q_c}{\mathrm{d}t} = HTC \cdot A \cdot (T_f(t) - T_s(t)) \tag{3.8}$$

where $T_f(t)$ is the temperature of the fluid (K), $T_s(t)$ is the temperature of the solid material (K), A is the heated area (m^2), and *HTC* is the heat transfer coefficient [W/(m^2 K)]. The energy of the convection heating can be calculated by the integration of Eq. (3.8) over the time of heating. The *HTC* parameter is not a "material property" like the thermal diffusivity; it can be described as a "concentrated parameter" of the convection heat transfer. It depends on the velocity and type of the flow (laminar or turbulent), the density and temperature of the heating fluid, the incidence angle between the solid structure and the heating fluid, and the roughness of the heated surface [5]. The value of the *HTC* parameter can vary between 5 and 500 W/(m^2 K) in the case of gases. In most applications, the density of the heating fluid and the roughness of the heated surface do not change during the heating process. Therefore, mainly the parameters related to the flow (velocity, type, and incidence angle) determine the *HTC*.

Eq. (3.8) is straightforward, so the calculation of convective heat transfer is also straightforward if we know the exact value of the *HTC*. The problem is that in most cases, this value is unknown or only approximately known. Although the parameters (like flow velocity or fluid density) affecting the *HTC* are usually measureable or calculable, the extent of dependence can change in every application. Explicit formulas to calculate the *HTC* parameter exist only for some simple cases, and they are based on some "similarity laws" and negligence. The simplest way to approximate the value of *HTC* is based on the linear combination of the velocity and some constants [6], but it provides useful information only for big geometrical dimensions, like buildings. Other methods approximate the *HTC* values according to the

average mass flow [7–9]. But the exact determination of the mass flow (by numerical simulations or measurements) can be complicated in such a harsh environment as in convection reflow ovens.

During the convection reflow soldering, Inoue approximated the *HTC* parameter with the following expression [10]:

$$HTC = \frac{\lambda}{d}\frac{\sqrt{(\pi/4)(D/l)^2}\left(1 - 2.2\sqrt{(\pi/4)(D/l)^2}\right)}{1 + 0.2(H/D - 6)\sqrt{(\pi/4)(D/l)^2}} \times \mathrm{Re}^{0.66}\mathrm{Pr}^{0.42}\left[1 + \left(\frac{H/d}{0.6/\sqrt{(\pi/4)(D/l)^2}}\right)^6\right]^{-0.05} \tag{3.9}$$

where λ is thermal conductivity of the heating gas [W/(m K)], H is the height of the heating zone (m), d is the diameter of the gas intakes, r is the distance between the gas intakes (m), Re and Pr are the Reynolds and Prandtl numbers, respectively. Eq. (3.9) is derived from a systematic series of experiments, but this equation provides only an average *HTC* value. Most of the thermal models of reflow soldering process [10,11] use still only an average (or some averages) value of the *HTC* for the whole oven, but this is not a correct approach. The *HTC* value can highly vary according to the location in each heating zones. This effect is caused by the changes in the gas flow parameters, the possible inhomogeneities in the gas circulation system, and the different contamination levels of the gas distribution system.

Furthermore, without numerical simulations or sophisticated measurements, it is difficult to determine the exact value of the flow parameters, which are necessary to calculate the Re and Pr numbers. Other researchers like Dittus–Boelter, Croft–Tebby, and Soyars faced similar problems (a survey of these methods can be read in Ref. [12]). Consequently, in the case of convection reflow ovens, there are two ways to determine the exact *HTC* values. One is direct measurement (see in Section 3.3). The other is the numerical calculation of the flow parameters (see in Section 6.2) and inclusion of these data in calculation of the *HTC* values with the previously presented methods.

3.2 Structure and operating principle of convection reflow ovens

In this section, the typical build-up of a modern convection reflow ovens, the function of the main parts, and some analysis of the working principle are presented. This section aims to make familiar the readers with the principal and critical elements of this widely used technology.

3.2.1 Typical structure of convection reflow ovens

Since the most used convection reflow oven is the conveyor type, this chapter focuses only on this type. The batch type ovens are briefly presented in Chapter 1, Introduction to Surface-Mount Technology. The conveyor-type convection reflow ovens are built up from zones. Preheating, peak, and cooling zones are distinguished according to the function of the given zone. The typical number of the zones can vary between 8 and 16 depending on the accuracy and throughput demands of the user. The block diagram of a conventional 12-zone oven can be seen in Fig. 3.2. The ovens use double heating and cooling panels, over and below of the soldered assembly.

To ensure the heat flow stability of the system and to minimize the heat radiation outward, the convective reflow ovens have optimum insulation between the process chamber and the exterior wall. It is usually built up from a stainless steel sheet (to block the heat radiation and ensure the mechanical construction of the oven), which is covered with good heat insulator material (like glass wool). However, the zones are not hermetically separated from each other, except in the case if peak zones use a vacuum option (see later).

The oven manufacturers usually apply the same pitch size of the zones, which allow them to use a modular design during the oven construction easily. The structures of the heating and the cooling zones are similar; the only considerable difference is that the cooling zone does not contain heating elements [13]. During the reflow soldering process, the assembly is dragged by a conveyor (transport line) through the zones. The set temperatures of the zones and the velocity of transport determine the thermal profile of the soldering (see in detail in Chapter 1, Introduction to Surface-Mount Technology). In the case of convection reflow soldering, the thermal profile usually does not reach the set temperatures of the zones [14].

One of the most critical parameters is the rate of throughput, which determines the optimum process zone length. If frequent product changes and multishift operations are necessary, then additional options will be required to be considered. The oven manufacturers try to serve the differing and frequent production demands of the users; therefore, they offer flexible conveyor options. Usually, the following conveyor settings are available in modern ovens (Fig. 3.3): single-lane transport, means only one adjustable chain; dual-lane

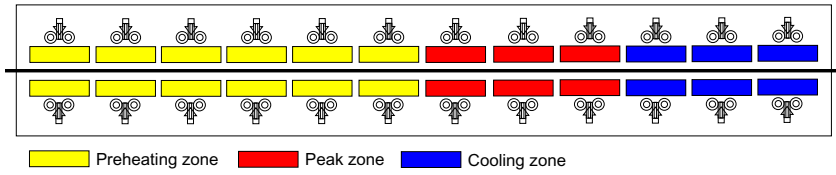

FIGURE 3.2 Construction of a 12-zone convection reflow oven.

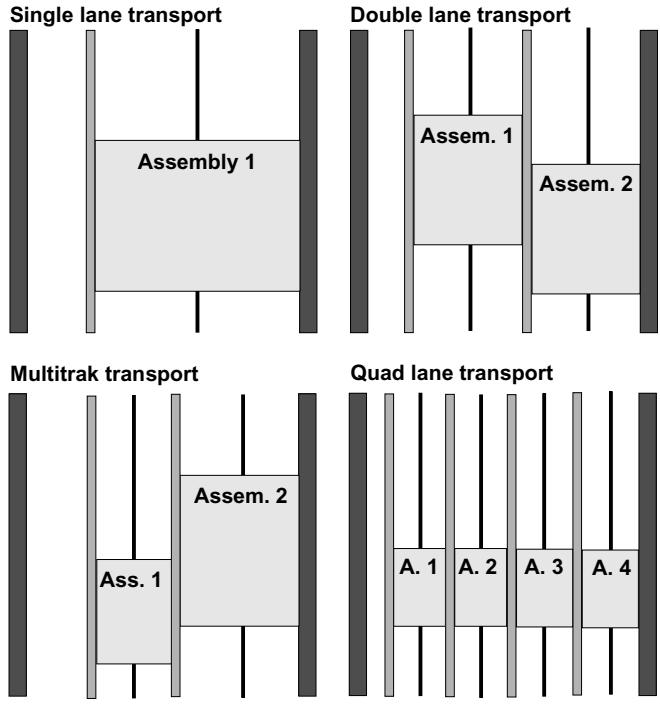

FIGURE 3.3 Different conveyor settings of a convection reflow oven.

transport, means two adjustable chains with synchronous/asynchronous transport speed; multitrack transport, means three adjustable chains with synchronous/asynchronous transport speed; quad lane transport, means four adjustable chains with synchronous transport speed and width adjustment. The different options result in that conveyor paths are located in an asymmetric position in the oven.

The main parts of the heating zones are as follows: an electrical heater, which heats the applied heating gas (N_2 or air); a fan, which makes the heating gas to move; and a gas distribution system, which forms heating gas streams on the surface of the assembly. As an inert gas, nitrogen is the ideal heat transfer medium that prevents the oxidation of the solder joints during the liquid state of the solder alloy. A block diagram of peak and cooling zones can be seen in Fig. 3.4. The ovens usually have flexible and independently controllable zones within fan frequency (effects on the flow velocity), and temperature can be controlled separately from each other, which assures the best possible thermal profiles. The system provides operation data, such as speeds, motor temperatures, and electric power characteristic values, to be used in the concept of an Industry 4.0 system. Novel convection reflow ovens use efficient EC (Electronically Commutated) fans. The benefits of

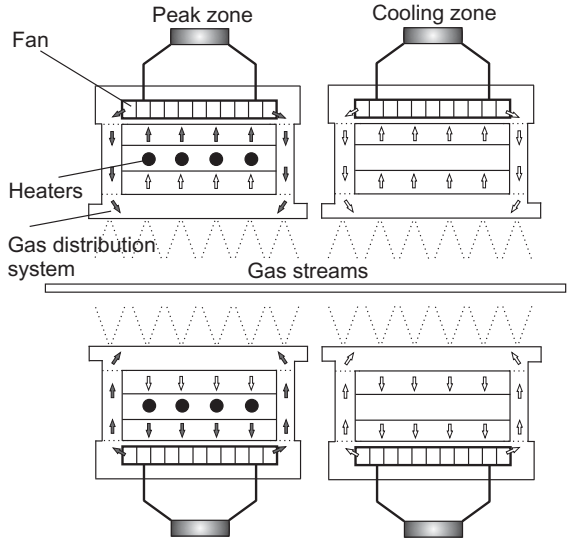

FIGURE 3.4 Block diagram of a peak and of a cooling zone. *Reproduced with permission from B. Illés, G. Harsányi, Investigating direction characteristics of the heat transfer coefficient in forced convection reflow oven, Exp. Therm. Fluid Sci. 33 (2009) 642–650.*

EC motors compared to AC (Alternating Current) technology are the lower noise level and minimal energy consumption. (There is no need for frequency converters).

Furthermore, flow velocities and heating temperatures of the upper and lower heating zones can separately be controlled, assuring that the assembly is heated up entirely and uniformly. It prevents the stressing of the printed circuit boards, which could disturb the soldering process. Usually, bottom heaters are set to lower temperatures, and the fans have lower rotation frequencies to prevent the reflow of the already formed solder joints on the bottom side of the assembly. Besides, this system can ensure that smaller components will not be overheated, and bigger ones will be heated up enough.

The latest reflow ovens use the nozzle-matrix gas distribution system, which has two main types the "nozzle-sheet" and the "multijet" method (Fig. 3.5). It is common in both that the nozzle matrix contains parallel nozzle lines, which generate numerous vertical gas streams.

The hole nozzle geometry of the nozzle-sheet system, which is usually equipped with monitored, adjustable overpressure in the heating module, guarantee homogeneous and gapless heat transfer to the assembly. However, the energy and gas consumption of this nozzle system is usually higher than that of a multijet system. The multijet systems ensure excellent process stability even when the oven is running on maximum capacity. Furthermore,

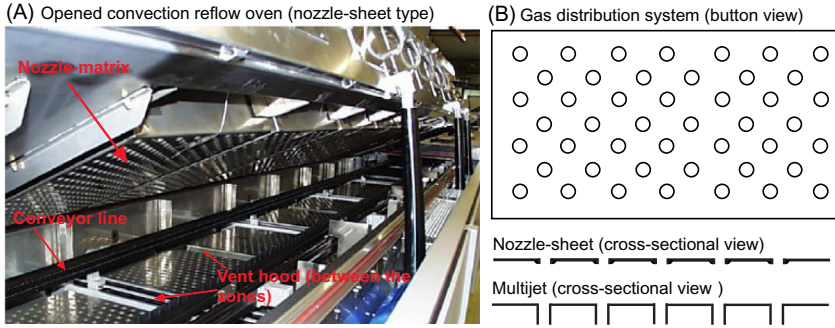

FIGURE 3.5 Gas distribution systems: (A) opened convection reflow oven (nozzle-sheet type); (B) structure of the gas distribution systems. *Reproduced with permission from B. Illés, I. Bakó, Numerical study of the gas flow velocity space in convection reflow oven, Int. J. Heat Mass Transf. 70 (2014) 185–191 [15].*

cyclic and continual loading does not affect the long-term process stability of the machine. Usually, multijet nozzle system provides very low energy and gas consumption.

In the process zones, the inert process atmosphere is assured throughout the entire soldering process by the closed system, which ensures that no external air gets into the oven. Furthermore, insulation materials keep the heat energy in the oven and avoid heat radiation into the environment. The heat flow within the system is carried out by circulation of the process gas, which means that the gas is extracted, cleaned, and reinserted into the process at the sides.

The demands about the cooling system in convection reflow ovens are continuously growing since the cooling gradient plays an essential role in the formation of solder joints. For lead-free solder alloys, JEDEC recommends a cooling gradient between 2°C/s and 6°C/s to achieve an optimal solder joint microstructure and prevents component damages, like different crackings. Furthermore, the exit temperature of the assembly is also essential due to the further handlings, like post reflow automatic optical inspection (AOI), which requires assembly temperature to be at near room temperature. Usually, cooling systems use the standard water-cooled solution with heat exchanger and adjustable ventilation. It provides the possibility to control the temperature of the cooling medium, thereby achieving a desired cooling gradient in the profile.

Innovative cooling systems use coolant-water-free method with liquid nitrogen cooling. The liquid nitrogen, at −196°C, cools down the inside of the cooling tract, evaporates, and is used for inertization while in a gaseous state. During inerting, the present oxygen is displaced by a nonreactive gas until a nonignitable mixture is present. It provides the cooling system with the necessary coldness and with the inert environment. As an important

consequence, the coolant water (which consumes a high amount of energy during the recooling process), as well as the cooling unit and refrigerant are no longer required in the oven. This novel method could save around 30 kWh energy per system, per year without the emission of a dozen tons of carbon dioxide.

The cleaning of the applied heating gas from the flux residues is an essential aspect of the convection reflow ovens since they contaminate the system (mainly the nozzles). In simple ovens, the heating gas is extracted from the process zone between the last peak and the first cooling zone. Subsequently, it is cooled down, cleaned, and led back to the system in the cooling zone. The flux residues are condensed and collected in condensate traps, which must be cleaned at regular intervals.

New convection reflow ovens are equipped with further cleaning stages in the heating zones as well. The cleaning is carried out in a two-step filtering system. The first step is pyrolysis, which is performed in a cartridge filled with fine-grained granulate cleaning material. When the heating gas is passing through the granulate material, long molecular chains are broken down (cracked) into smaller ones using thermal fission at the temperature of about 500°C. Afterward, the smaller molecules are taken up by the granulate. In the second step, the heating gas is routed through a heat exchanger (the simple condensation trap) where the remaining liquid residues are condensed. Depending on the size of the oven, it is equipped with 2, 3, or 4 condensation traps and even with double pyrolysis. The heating gas is removed through a conduit, at the end of the last preheating zone and from the last peak zone. After cleaning, it is leaded back into the oven at the beginning of the first preheating zone. With two-steps filtering, any liquid and crystalline residues can effectively be removed.

The latest convection reflow ovens can be equipped with a vacuum option, which removes voids and outgassing from the solder joints, when the solder alloy is in the liquid phase. Void rates can be reduced under 2% with a vacuum between 10 and 100 mbar (which is measured in the process chamber and not at the vacuum pump). The vacuum chamber is installed as an enhancement of the last peak zone. The system usually contains an integrated pyrolysis unit, in order the filter the extracted gas from the vacuum chamber. To be able to control the time of vacuum treatment (and the cooling time), these ovens have separately controllable conveyor parts for the heating zones, vacuum zone, and cooling zones.

3.2.2 Analysis of the operating principle of a convection reflow oven

In this section, the most critical aspects of the convection reflow soldering are studied, which are the formation of gas streams from the nozzles and the establishment of the flow field in the process zones. To understand the

operating principle of convection reflow ovens, a simple gas flow model is presented illustrating the effect of changes in the flow parameters on the *HTC*.

In the following case study, let us consider the application of a nozzle-sheet system. The nozzles create so-called free-streams that enter a free space (the process zone) (Fig. 3.6).

No blocking objects face the stream in its closest ambient. The free-streams can be characterized by the following properties: the initial velocity of the flow is v_0, and the flow is laminar. The free-stream contacts with the standing gas in the process zone and start to make it move. It results in that the radius of the area, where the stream velocity is still v_0, narrows due to the inertia of the standing gas.

The decrease in velocity is proportional to the distance from the nozzle. At the distance of $z = 5d_0$, the velocity of the free-stream is equal with v_0 only at the axis of the nozzle (Fig. 3.6). Below this distance, there is the so-called initial area of the free-stream. Over the distance $z > 5d_0$, there is a "slowing area" of the free-stream. The *HTC* can be considered to be constant under the nozzle in the initial area of the free-stream (h_0) since the mass flow rate is near constant. At the sides of the free-stream, the *HTC* is at least one order of magnitude smaller than h_0. In the slowing area of the free-stream, both the mass flow rate and the *HTC* decrease exponentially.

In convection reflow ovens, the assembly is usually closer to the nozzles than the interface of the initial area. Dimensions of the nozzle matrix are larger than dimensions of the assembly; consequently, a free space is supposed to be around the heated assembly. The nozzle matrix generates numerous vertical gas streams that are considered to be laminar. Since the diameter of the nozzles is much smaller than the horizontal dimensions of assembly, it

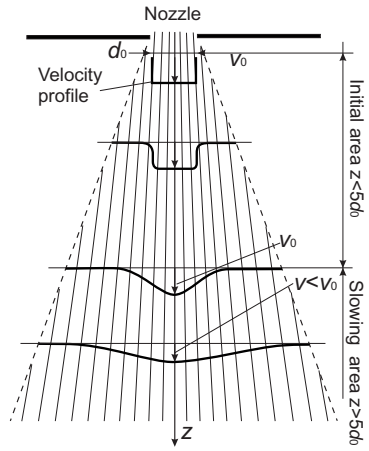

FIGURE 3.6 Cylindrical free-stream.

acts as an obstacle for the gas streams. The vertical gas streams from the nozzle matrix join into a continuous radial flow layer above the board [14]. At a given point on the assembly, the flow direction of the radial layer is determined by a so-called balance line. The balance line marks that location in the given zone where the main flow direction changes.

A schematic view of the gas flow field can be seen in the moving direction (x-axis) in Fig. 3.7A and perpendicular to it (y-axis) in Fig. 3.7B. The origin of the coordinate system is set to the geometrical center of the boars. The direction of a gas stream from a given nozzle depends on the position of the board in the oven. Along the length of the zone (x-axis, Fig. 3.7A), the balance line oscillates around the center of the assembly caused by the movement of the assembly in the zone. However, the system is symmetrical along the moving direction (x-axis), and it enables assuming that the transported mass and energy are nearly equal toward $-x$ and $+x$ directions during the reflow soldering process [14].

As it was presented in Section 3.2.1, the conveyor line can have an asymmetric position in the oven ($Y1 \neq Y2$). Since the assembly does not move along the width of the oven (y-axis), the balance line of the y-axis is fixed, but it can have an asymmetric position. It is always closer to the oven wall next to the specific conveyor (Fig. 3.7B). The asymmetric position of the

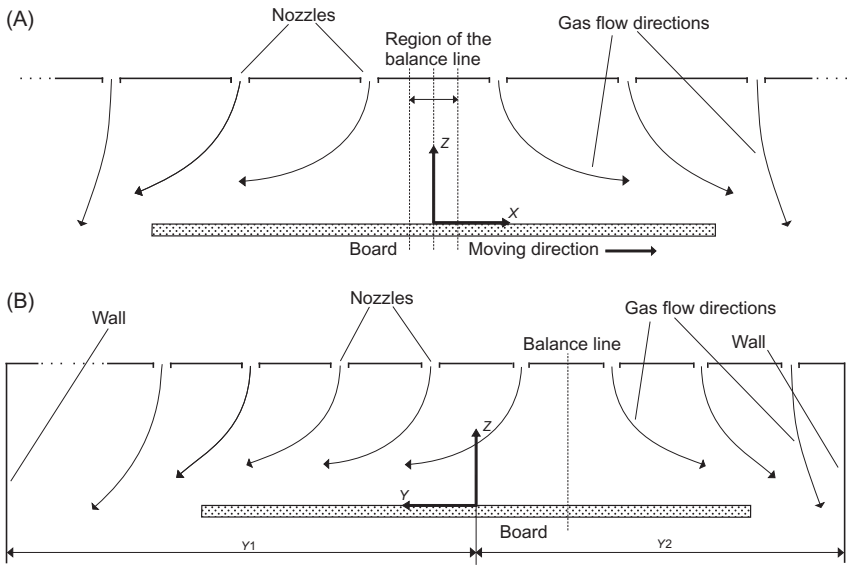

FIGURE 3.7 Gas flow field above the assembly board: (A) cross-sectional view, x-axis; (B) cross-sectional view, y-axis. *Reproduced with permission from B. Illés, G. Harsányi, Investigating direction characteristics of the heat transfer coefficient in forced convection reflow oven, Exp. Therm. Fluid Sci. 33 (2009) 642–650.*

conveyor can cause differences in the transported mass and energy toward the $-y$ and $+y$ directions [14].

The model of the radial layer formation in a steady-state condition can be seen in Fig. 3.8. The changes in flow parameters are much faster than the changes in gas temperature or the velocity of the conveyor. Therefore, the model of the radial layer formation can be considered to be isothermal and stationary. The radial flow layer can be separated into further layers from $L(1)$ to $L(m)$. In a layer, the velocity of the gas flow, the pressure, and the density of the gas are considered to be constant. (In Fig. 3.8, the dashed lines represent the borders of flow layers L and not streamlines.)

The radial layer formation can be described with the analyze of the movement of an elemental amount of gas in a constant V volume. The m (kg) mass in the V volume (m^3) passes to the radial layer along an arc. During this, an F_{CP} centripetal force (N) and an $F_{p(n)}$ force (N) from the pressure change (normal to the movement orbit) act on the elemental amount of gas. The force of the pressure change is defined by the simplified Euler equation (3.1) in a normal coordinate system [13]:

$$\underline{F}_{p(n)} = m_g \cdot \frac{|\underline{v}|^2}{R_a} = m_g \cdot \frac{1}{\rho} \cdot \frac{\mathrm{d}p}{\mathrm{d}n} \tag{3.10}$$

The layer scaling effect of entrance gas streams starts in the direction of the radial flow layer. Radii of the arcs decrease from $L(1)$ to $L(m)$. Density of the gas also grows toward the surface of the assembly: $\mathrm{d}p_n(1) < \mathrm{d}p_n(2) < \cdots < \mathrm{d}p_n(m)$ due to the isothermal condition [13].

The momentum equation in the stationary model can be described by Eq. (3.5). In the case of gas flows, the gravitational acceleration can be neglected. As it was discussed in Section 3.1, $\underline{\underline{\Phi}}$ contains tensile σ (Pa) and shear τ (Pa) stresses. In the radial flow layer model, tensile stresses are

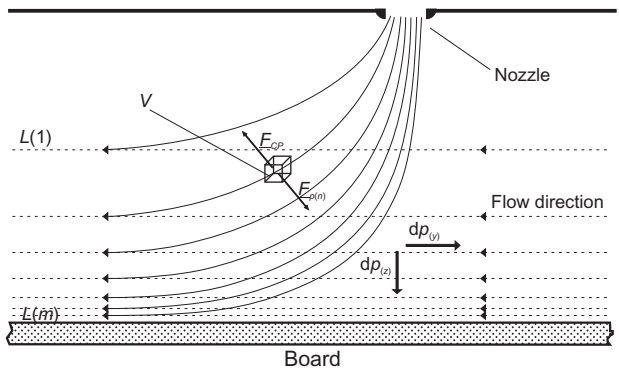

FIGURE 3.8 Radial layer formation (cross-section, y-axis). *Reproduced with permission from B. Illés, G. Harsányi, Investigating direction characteristics of the heat transfer coefficient in forced convection reflow oven, Exp. Therm. Fluid Sci. 33 (2009) 642–650.*

$\sigma_{xx} = \sigma_{yy} = \sigma_{zz} = -p$ and shear stresses are caused by friction. Considerable friction occurs only between flow layers, so the variation in v_z components along the x- and y-axes can be neglected. Therefore, the stress tensor can be reduced, and it contains only the following elements [13]:

$$\underline{\underline{\Phi}} = \begin{bmatrix} -p & 0 & \mu \cdot (\partial v_x / \partial z) \\ 0 & -p & \mu \cdot (\partial v_y / \partial z) \\ 0 & 0 & -p \end{bmatrix} \tag{3.11}$$

According to the reduced stress tensor, some terms in the left side of the momentum equations (3.5) are reduced as well [13]:

$$v_x \cdot \frac{\partial v_x}{\partial x} + v_z \cdot \frac{\partial v_x}{\partial z} = \frac{1}{\rho} \cdot \left(-\frac{\partial p}{\partial x} + \mu \cdot \frac{\partial^2 v_x}{\partial z^2} \right) \tag{3.12}$$

$$v_y \cdot \frac{\partial v_y}{\partial y} + v_z \cdot \frac{\partial v_y}{\partial z} = \frac{1}{\rho} \cdot \left(-\frac{\partial p}{\partial y} + \mu \cdot \frac{\partial^2 v_y}{\partial z^2} \right) \tag{3.13}$$

$$v_z \cdot \frac{\partial v_z}{\partial z} = \frac{1}{\rho} \cdot \left(-\frac{\partial p}{\partial z} \right) \tag{3.14}$$

The reduced momentum equations (Eqs. 3.12−3.14) show that mainly the pressure change affects the velocity. As it was discussed, the pressures of the flow layers increase toward the assembly (Fig. 3.8). It results in that v_z decreases along the z-direction toward the assembly, as well as the *HTC* of the inlet gas streams. Besides, the v_x and v_y velocity components and the density of the gas increase toward the assembly. The larger density and velocity yield larger mass flow and a larger *HTC* in the lower radial flow layers. Consequently, the radial layer formation has the following effect on the *HTCs*: the *HTC* of the inlet gas streams decreases toward the heated assembly along the z-direction, but oppositely the *HTC* of the radial flow layer increases toward the assembly along the x and y directions.

3.3 Characterization of the convection reflow ovens

According to Newton's law (Eq. 3.8), the convection reflow soldering process can be characterized by the temperature of the heated assembly and the *HTC* parameter of the gas flow. The temperature of the heating gas is supposed to be known and to be constant. The temperature of the assembly is usually measured with thermocouples. They are fixed at different locations on the surface of the assembly or inside the assembly body to get a complete view about temperature distribution during the soldering process. Usually, K-type thermocouples are used, and the measurement is carried out at least 4−8 places. The thermocouples can be fixed with heat-resistant polyimide tape, aluminum tape, hard (high temperature) soldering, or with simple SMD adhesive. In the case of long conveyor-type reflow ovens, a data logger needs to

be traveling inside the oven, usually behind 50–70 cm of the assembly. The data logger is always placed into a temperature protecting box (Fig. 3.9).

After the measurements, thermal profiles are downloaded from the data logger into a specific evaluation software. In this software, essential profile parameters (minimum and maximum temperatures, dwell time, heating and cooling gradients, time above liquidus) can be investigated. More details about thermal profiles can be seen in Chapter 1, Introduction to Surface-Mount Technology, and more information about the execution of thermal profiling can be seen in Chapter 2, Infrared Reflow Soldering, and Chapter 4, Vapor Phase Reflow Soldering Ovens.

In the following, the HTC in convection reflow ovens is investigated. As it was presented in Section 3.1.2, many gas flow parameters (pressure, density, velocity, etc.) should be determined to be able to calculate the *HTC* parameter. The exact measurement of gas flow parameters is usually complicated and lingering due to the extreme conditions in the convection reflow oven (like small space and high temperature). Besides, to calculate a fine distribution of the *HTC* parameter, the initial parameters must also be determined in a fine resolution. An alternative solution is to examine the heating capability of gas flow.

Measurement instrumentations and calculation methods are presented to characterize the *HTC*, which based on the study of the temperature distribution changes during the reflow soldering process. In the first step, the *HTC* distribution under the nozzles is determined when the soldered assembly travels under the nozzle matrix. The obtained results provide crucial information about the homogeneity of the heating and the possible contamination of the nozzle matrix. In the second step, the direction characteristics of the *HTC* of the radial flow layers on the soldered assembly are investigated. The obtained results provide crucial information about the optimal position of the conveyor belt in the oven and about height limitations of the soldered components.

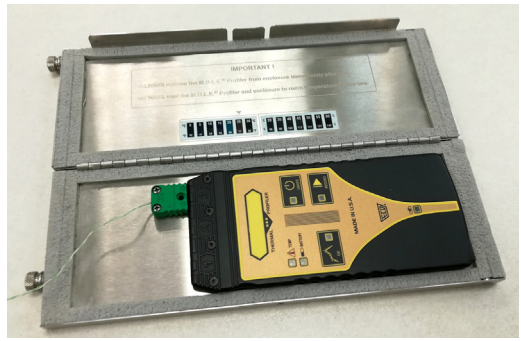

FIGURE 3.9 Data logger in the temperature protection box.

3.3.1 Distribution of the *HTC* parameter under the nozzle matrix

To be able to determine the *HTC* parameter of the heating gas steams, the temperature changes are measured at different locations in the heating gas streams. The temperature changes must be measured with the minimum of disturbance to the gas streams. For this purpose, "point probes" can be used, like the K-Type rigid (steel coat) thermocouples with a maximum diameter of 1 mm. (The typical diameter of the nozzle is 4−6 mm.) The rigid coating ensures that the thermocouples are being kept in the appropriate position during the measurement process. The thermocouples are pinned through holes on a prepared FR4 test board (Fig. 3.10). The role of the test board is only to hold the probes in proper position during the measurement, so it should not contain any metal wiring, which could disturb the measurements. The measurements are carried out below the nozzles facing toward the heating gas streams [16,17].

The nozzle matrix is constructed from parallel nozzle lines. The nozzle lines are also parallel with the moving direction of the assembly during the soldering process. During the soldering process, the assembly is drifted under the nozzle lines. Hence, practically the *HTC* parameter of a whole nozzle line can be determined. The distance between the nozzle matrix and the soldered assembly is usually between 30 and 35 mm; however, the standard height of the applied SMD components is between 1 and 15 mm. Therefore, it is suggested to determine the distribution of the *HTC* parameter at more measurement heights from the assembly, like 1, 3, 6, 9, 12, and 15 mm. The investigated oven has 12 nozzle lines (NLs). Altogether, this would mean 72 individual measurement points (12 nozzle lines multiplied with 6

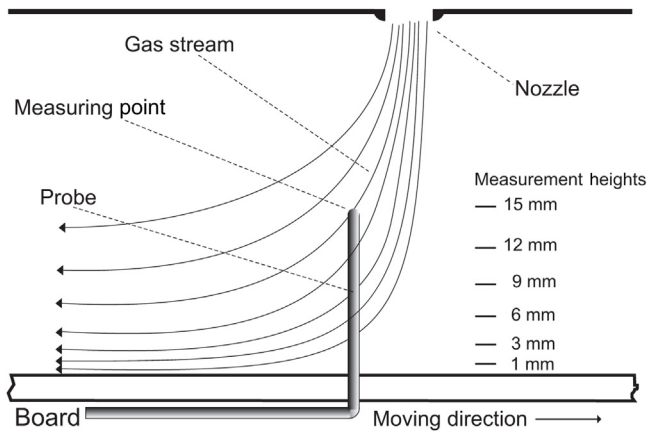

FIGURE 3.10 Measurement position of the *HTC* parameters of the heating gas streams (cross-section view). *Reproduced with permission from B. Illés, Distribution of the heat transfer coefficient in convection reflow oven, Appl. Therm. Eng. 30 (2010) 1523−1530.*

measurement heights), which is a high number form a mass-production aspect [16,17]. However, necessary measurement steps can be reduced by the following technique.

In the first step, the *HTC* parameter is measured under a reference nozzle line as a function of height. The chosen reference nozzle line was NL6 (Fig. 3.11). In the second step, the heating efficiency of the neighboring nozzle lines is compared with the reference at a constant height (suggested to use the closest measurement height to the nozzle matrix, 15 mm). The nozzle-line positions above the board and the layout of the measurement system can be seen in Fig. 3.12.

Finally, *HTC* parameters of all nozzle lines are calculated at all measurement heights from combined results of the first and second steps (details of this calculation are presented below). With the application of this method, the necessary measurement points can be reduced from 72 to 18.

For the calculation of the *HTC* parameter, a similar method can be applied [18,19].

First, analytical curves are fitted onto the measured temperature changes to calculate the heating temperature (T_h) and time coefficient of the heating

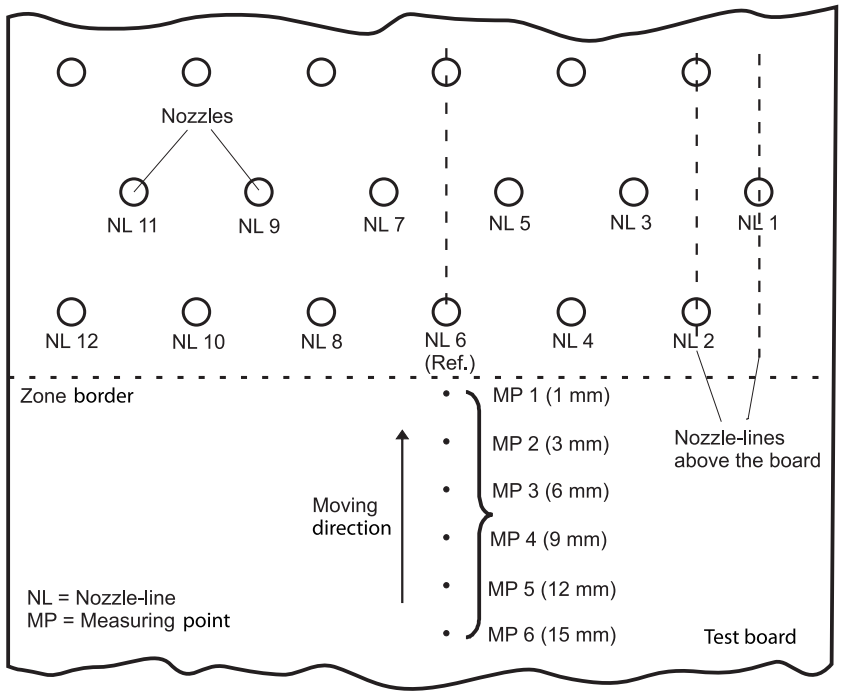

FIGURE 3.11 Measurement layout 1 (step 1, top view). *Reproduced with permission from B. Illés, Distribution of the heat transfer coefficient in convection reflow oven, Appl. Therm. Eng. 30 (2010) 1523–1530.*

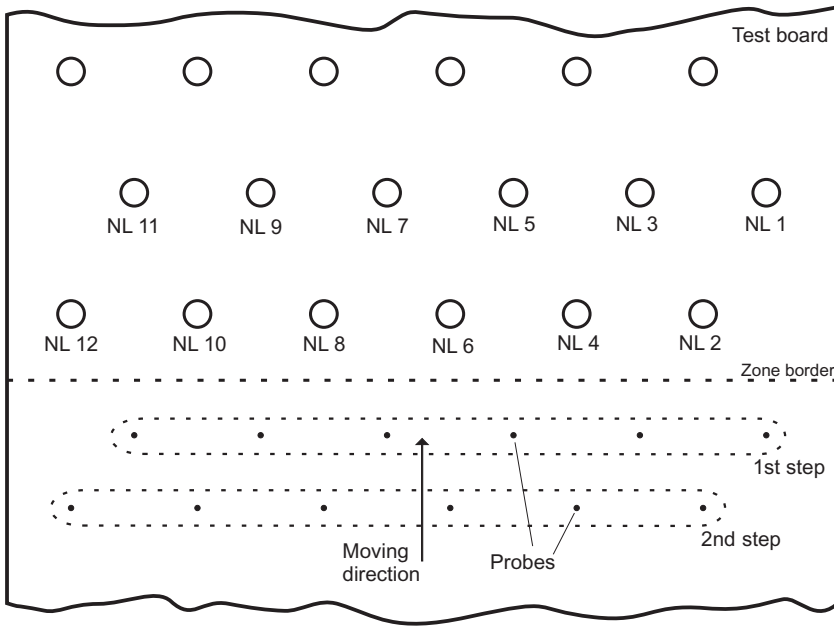

FIGURE 3.12 Measurement layout 2 (step 2, top view). *Reproduced with permission from B. Illés, Distribution of the heat transfer coefficient in convection reflow oven, Appl. Therm. Eng. 30 (2010) 1523–1530.*

(τ). Since the temperature change is parabolic saturation type, the following model curve is applied:

$$T(t) = (T_h - T(t_0)) \cdot (1 - e^{-t/\tau}) \tag{3.15}$$

where the time coefficient of the heating is [16,17]:

$$\tau = \frac{t_r}{\ln\left(1 - (T(t_r) - T(t_0))/(T_h - T(t_0))\right)} \tag{3.16}$$

Although the set temperatures of the heating zones are known, these are not equal to T_h since the measurement system (just like the soldered assembly) has a cooling effect on the heating zones unfortunately. This effect highly depends on the location of the measurement system in the oven because the oven tries to maintain a set temperature in the heating zones. Therefore, the exact values of T_h have to be calculated by using an iterative curve fitting method. The T_h is iterated from the last measured temperature [$T(t_r)$] with 0.01°C increments. The iteration stops when the fitting failure has reached the minimal value (it can vary in each given case).

Since the oven tries to maintain the set temperature, the application of a single T_h value for a whole heating zone does not provide enough accurate

fitting. In Fig. 3.13, the dashed curve is calculated with only one T_h value for the entire curve, while the continuous line is calculated with two T_h values, one for the first part $[t_0, t_1]$ and one for the second part $[t_1, t_r]$ of the curve. Of course, it will result in two time coefficients as well. As it is clearly visible, the error of fit is much lower in the case of two T_h values. The most significant changes in T_h ($12°C - 19°C$) were observed in those heating zones where the gradient of the heating was also high (zones 1, 5, and 6). In all heating zones, more significant changes of T_h were located on lower measurement heights ($1 - 5$ mm), the changes in T_h are smaller at higher positions (over 5 mm, it is only $2°C - 5°C$) [17]. If the values of T_h and τ are known, then the convection heat can be calculated by the integration of Newton's law (Eq. 3.5) over the duration of heating $[t_0, t_r]$:

$$\begin{aligned} Q_c &= \int_{t_0}^{t_r} HTC \cdot A \cdot (T_h(t) - T(t)) \\ &= HTC \cdot A \cdot \left[(T_{h1} - T(t_0)) \cdot \tau_1 \cdot \left(1 - e^{-t_1/\tau_1}\right) + (T_{h2} - T(t_1)) \cdot \tau_2 \cdot \left(1 - e^{-tr/\tau_2}\right) \right] \end{aligned} \tag{3.17}$$

The thermocouples (except the measurement point) are insulated from the steel coating with a glass wool layer, which has a very low thermal conductivity [< 0.5 W/(m K)] to decrease the impact on the environment. However, a parasite conduction resistance (R_k) must be considered between the data logger (DL) and the measurement points (MPs). The initial measurement proved that this parasite conduction effect must be considered in the case of thermocouple measurements.

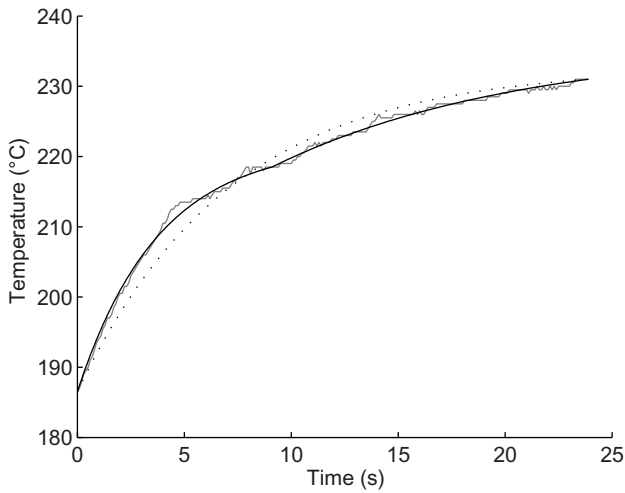

FIGURE 3.13 Analytical curve fitting. *Reproduced with permission from B. Illés, Distribution of the heat transfer coefficient in convection reflow oven, Appl. Therm. Eng. 30 (2010) 1523–1530.*

The MP is modeled as a sphere, as it is shown in Fig. 3.14 [17]. The thermal potential difference between the DL and MP generates the parasite conduction heat flow F_k on R_{NiCr} and R_{NiAl}:

$$F_k = \frac{T_{MP} - T_{DL}}{R_{NiCr}} + \frac{T_{MP} - T_{DL}}{R_{NiAl}} \tag{3.18}$$

The physical properties of the thermocouples can be seen in Table 3.1.

The Q_k parasite conduction heat is calculated with the integration of Eq. (3.18) to the duration of heating $[t_0, t_r]$:

$$Q_k = \int_{t_0}^{t_r} F_k(t) = \int_{t_0}^{t_r} \frac{T(t) - T_{DL}(t)}{R_{NiCr}} + \frac{T(t) - T_{DL}(t)}{R_{NiAl}} \tag{3.19}$$

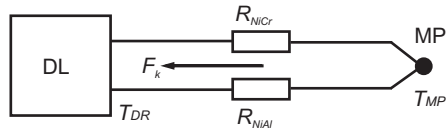

FIGURE 3.14 Thermal model of the measurement system. *Reproduced with permission from B. Illés, Measuring heat transfer coefficient in convection reflow ovens, Measurement 43 (2010) 1134–1141.*

TABLE 3.1 The physical properties of thermocouples [17].

Properties of the MP	**Value**
Equivalent density, ρ (kg/m^3)	8.21×10^3
Equivalent thermal capacity, C [J/(kg K)]	4.74×10^2
Radius, r_{MP} (m)	0.40×10^{-3}
Effective surface, $A = 4/3 \cdot \pi \cdot r_{MP}^2$ (m^2)	1.04×10^{-6}
Volume, $V = 4/6 \cdot \pi \cdot r_{MP}^3$ (m^3)	1.31×10^{-10}
Mass, $m = \rho \cdot V$ (kg)	1.07×10^{-6}
Properties of the wires	**Value**
Length, l (m)	0.70
The radius of the wires, r_w (m)	0.40×10^{-3}
Cross-sectional area of the wires, A_w (m^2)	5×10^{-7}
Specific thermal conductivity NiCr(90:10), λ_{NiCr} [W/(m K)]	13
Specific thermal conductivity NiAl(95:5), λ_{NiAl} [W/(m K)]	25
Thermal resistance NiCr(90:10), $R_{NiCr} = l/(\lambda_{NiCr} \cdot A_w)$ (W/K)	1.08×10^5
Thermal resistance NiAl(95:5), $R_{NiAl} = l/(\lambda_{NiAl} \cdot A_w)$ (W/K)	5.6×10^4

The absolute inaccuracy of thermocouples is usually $\pm 0.5°C$. But it does not cause considerable measurement error since it is eliminated from the results by the integration of temperature in Eq. (3.19). During the measurements, the data logger is placed into a refractory box (see in Fig. 3.9) to avoid the heat shock of the system. Therefore, its temperature changes only between 25°C and 60°C and $T_{DL}(t)$ can be modeled with the linear part of an exponential saturation in the temperature change:

$$T_{DL}(t) = 25 + 35 \cdot \frac{t}{t_{end}} \tag{3.20}$$

where t_{end} is the duration of the heating. It is supposed that the thermal capacity of the data logger is infinite compared to the thermal capacity of the MP; hence, the $T_{DL}(t)$ does not change due to F_k.

As it was discussed in Section 3.2.2, convection reflow ovens do not contain infra-radiation tubes, and inside wall of these ovens is made of polished stainless steel. It means that their emissivity is very low (~ 0.1). Therefore, radiation heat [20,21] can be neglected during the calculations. Accordingly, the applied heat equation of the measurement system is:

$$Q_a = Q_c - Q_k \tag{3.21}$$

The amount of absorbed thermal energy is calculated [22]:

$$Q_a = C_{MP} \cdot m_{MP} \cdot (T(t_r) - T(t_0)) \tag{3.22}$$

where C is the thermal capacity and m is the mass of the measurement point. Finally, the HTC values can be calculated by applying Eqs. (3.17)–(3.19):

$$HTC = \frac{C_{MP} \cdot m_{MP} \cdot (T(t_r) - T(t_0))}{A \cdot \left[(T_{h1} - T(t_0)) \cdot \tau_1 \cdot \left(1 - e^{-t_1/\tau_1}\right) + (T_{h2} - T(t_1)) \cdot \tau_2 \cdot \left(1 - e^{-tr/\tau_2}\right) \right]} \tag{3.23}$$

From the results of the first measurement layout (Fig. 3.11), HTC parameters of the reference nozzle-line $HTC^{ref}(MH, HZ)$ can be determined with Eq. (3.20) as a function of measurement heights (MH) and heating zones (HZ). From the results of the second measurement layout (Fig. 3.12), heating efficiency of the nozzle lines (NLs) is compared to that of the reference nozzle line at 15 mm height over the heating zone (HZ) [16,17]:

$$\eta(NL, HZ) = \frac{HTC^{n}(15\ \text{mm})}{HTC^{ref}(15\ \text{mm})} \tag{3.24}$$

With the multiplication of HTC parameters of the reference nozzle-line $HTC^{ref}(MH, HZ)$ and heating efficiency ratios $\eta(NL, HZ)$, $HTCs$ can be calculated for the whole oven as a function of nozzle lines, heating zones, and measurement heights [16,17]:

$$HTC(NL, HZ, MH) = \eta(NL, HZ) \cdot HTC^{ref}(MH, HZ) \tag{3.25}$$

The investigated convection reflow oven had seven heating zones (the first five were preheating zones followed by two peak zones) and one cooling zone. A simple soak thermal profile was used during the soldering process. The $HTC^{ref}(MH, HZ)$ results under the reference nozzle line can be seen in Fig. 3.15, separately for each heating zone and measurement height. The changes of HTC^{ref} values followed a similar shape in each heating zone. They were nearly constant from the height level of the nozzles down to the level of 12 mm above the board. From 12 to 3 mm, they had a linear decrease of 2.9−3.9 [W/(m^2 K)]/mm, and below 3 mm, the decrease was even more pronounced. The results of the seventh heating zone (second peak zone) could not be processed because the temperature changes in this zone were too small, only 1°C − 2°C.

As it was expected, the *HTC* highly depends on the measurement height. *HTC* was nearly constant until a height level where the gas flow direction begins to change and the radial flow layers start forming (Fig. 3.8). In the investigated oven, it was around 12 mm above the assembly, while the initial area of the gas streams (Fig. 3.6) forms approximately till 25−30 mm below the nozzles. Since the distance between the nozzle matrix and the assembly is usually 30−35 mm, it can be concluded that the mentioned interfaces are matching. The differences in heating efficiency between the zones were 15% − 25%, which can be caused by the different contaminations of the nozzles or the not optimal state of the gas circulation system.

The *HTC*(*NL*, *HZ*, *MH*) values at a given measurement height can be presented as a surface that represents the distribution of *HTC* parameters of

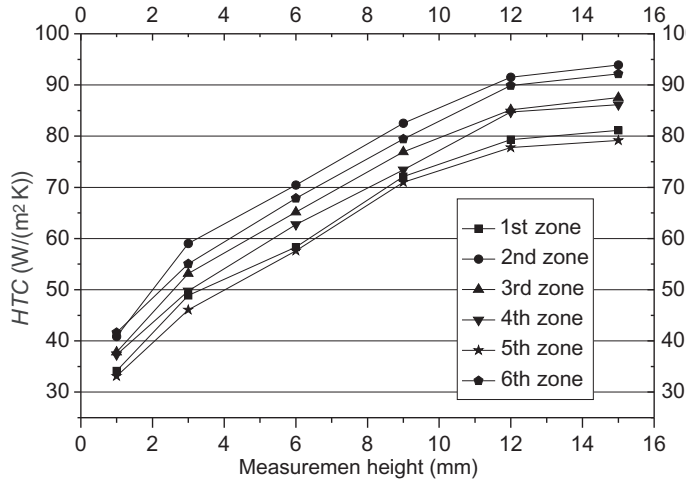

FIGURE 3.15 $HTC^{ref}(MH, HZ)$ values of the reference nozzle line in function of measurement height. *Reproduced with permission from B. Illés, Distribution of the heat transfer coefficient in convection reflow oven, Appl. Therm. Eng. 30 (2010) 1523−1530.*

heating gas streams in the oven. Between the measured values, linear interpolation was used to calculate the whole surface. This visualization method ensures a sufficient view of changes in *HTC* values in the entire oven. An example can be seen in Fig. 3.16 at measurement height of 12 mm, right after cleaning the oven [16,17].

Differences between 15% and 20% were observed in the *HTC* parameters of the nozzle lines. The examined oven was six years old. Therefore, the differences were probably caused by the inhomogeneity in the gas circulation system (the different attrition of the fans). The increase of the gas stream velocity might homogenize the gas distribution as well as the *HTC* values. However, this might have some risk since the increase in mass flow could yield the displacement of components prior to the melting of the solder alloy.

As it was discussed in Section 3.2.1, during convection reflow soldering, flux residues can deposit into the nozzles, which can partially seal the nozzles and can block the gas flow. This effect can result in further inhomogeneities in heating efficiency. To illustrate this negative effect, the measurements were repeated after three months of oven operation without cleaning. The results can be seen in Fig. 3.17. In this case, the maximum differences between the *HTCs* almost reached 85%. The most significant *HTC* drop was observed in zones 4 and 5 where the flux was being activated, and the evaporation rate was the highest.

Differences in heating efficiency result in inhomogeneous temperature distributions in the oven, which can lead to soldering failures. *HTC* differences mostly cause component skewing and displacement type failures, mainly at the large-size components. Heating differences at the opposite sides of two-terminal components result in difference in the onset of solder

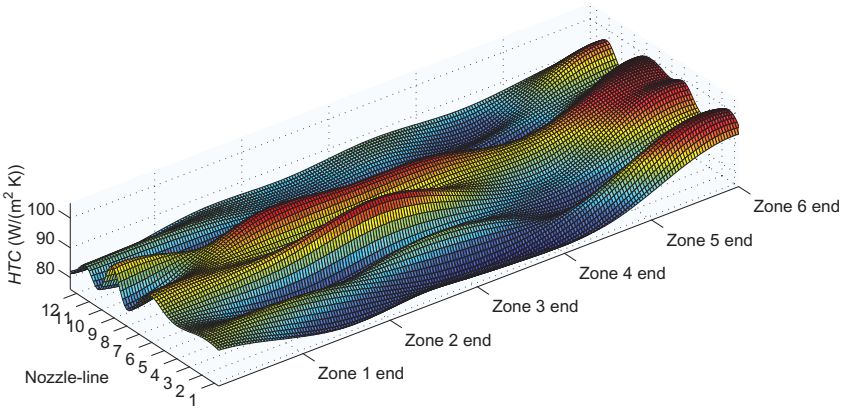

FIGURE 3.16 Distribution of the *HTC* parameter at measurement height of $h = 12$ mm, directly after cleaning the oven. *Reproduced with permission from B. Illés, Distribution of the heat transfer coefficient in convection reflow oven, Appl. Therm. Eng. 30 (2010) 1523–1530.*

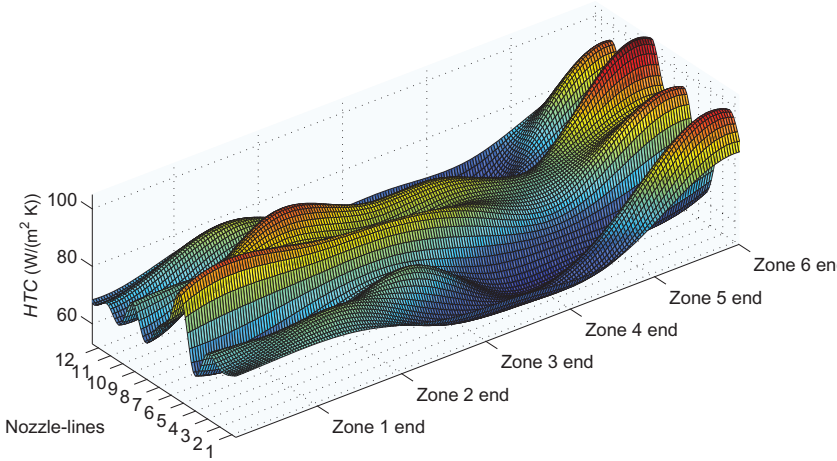

FIGURE 3.17 Distribution of the *HTC* parameter at $h = 12$ mm measurement height, after three months of oven operation without cleaning. *Reproduced with permission from B. Illés, Distribution of the heat transfer coefficient in convection reflow oven, Appl. Therm. Eng. 30 (2010) 1523–1530.*

melting. This effect breaks the balance of the wetting forces and increases the possibility of component movement or of the so-called tombstone effect.

3.3.2 Direction characteristics of the heat transfer coefficient in radial flow layers

According to the conclusions of the gas flow model presented in Section 3.2.2, the transported energy by the radial flow layers is considerable. It highly depends on the location in and on the construction of the reflow oven. Therefore, a measurement system was designed to investigate the *HTC* parameter in radial flow layers. The basic idea and the calculations of the *HTC* parameter from measured temperature changes were the same as it was presented in Section 3.2.1, so only the physical build-up of the system is shown here.

The same convection reflow oven as in Section 3.3.1 was used for the tests with a single conveyor line located in an asymmetric position in the oven (Fig. 3.7B). The aim was to illustrate the effect of asymmetrical conveyor position on the *HTC* values of the radial flow layers. Twelve measurement locations (MLs) were chosen on the surface of a test board, each located equally around a circle aligned to the center of the test board. The ring had a radius of 30 mm (Fig. 3.18). During the calibration of the measurements, it was observed that the radial layer was stable from 10 mm from the center till the edge of the board. In the given case, the edge of the test board was 70 mm from the center. It means that the measurement distance

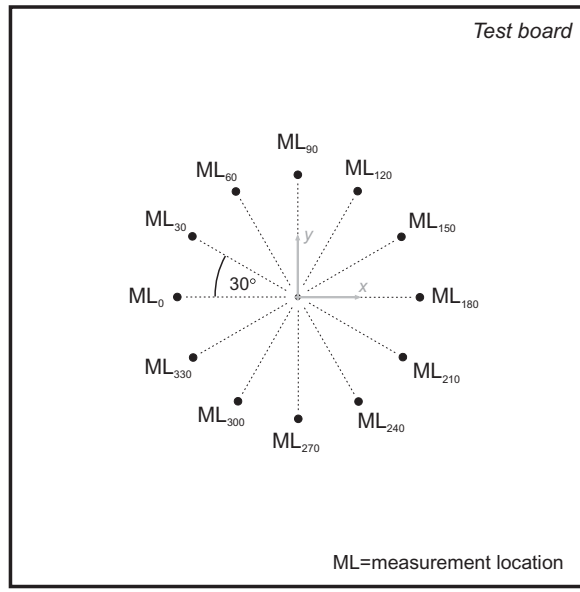

FIGURE 3.18 Measurement locations (MLs) on the test board (top view). *Reproduced with permission from B. Illés, G. Harsányi, Investigating direction characteristics of the heat transfer coefficient in forced convection reflow oven, Exp. Therm. Fluid Sci. 33 (2009) 642–650.*

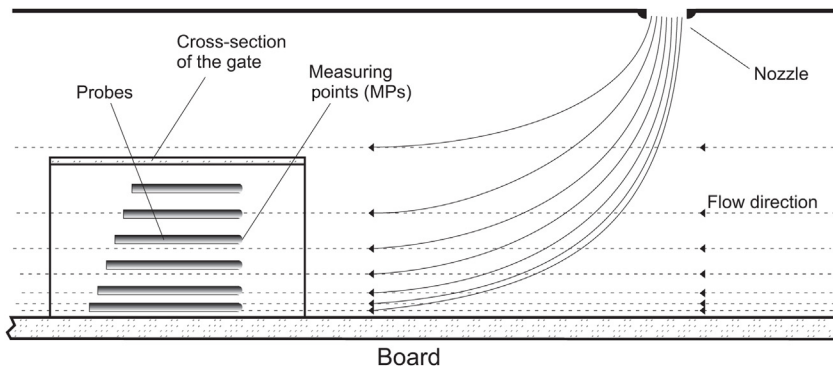

FIGURE 3.19 The measurement system for the radial flow layers. *Reproduced with permission from B. Illés, G. Harsányi, Investigating direction characteristics of the heat transfer coefficient in forced convection reflow oven, Exp. Therm. Fluid Sci. 33 (2009) 642–650.*

from the center of the test board was relevant between 10 and 70 mm; the distance of 30 mm was chosen [13].

The same K-type rigid (steel coat) thermocouples with a diameter of 1 mm were applied. The probes were fixed in a measurement gate (measurement box), which held them in position (Fig. 3.19). The front and the rear

end of the gate were opened so that the radial flow could pass through it, but the roof of the gate protected the probes from the disturbing effect of entering gas streams. The gate was made from FR4 ($d = 0.8$ mm), with a width and length of 30 mm and a height of 20 mm. The probes were driven into the gate through small holes on the left lateral side. The measurement gate was positioned to all MLs (defined in Fig. 3.19) facing toward the center of the test board [13]. An advantage of this arrangement was that the probes obstruct the gas flow field only at the measurement points since they were parallel to the radial flow layers. The obstruction and measurement point overlapped and the disturbance of the radial layers was minimal. The same measurement heights were applied as in Section 3.3.1, namely 1, 3, 6, 9, 12, and 15 mm.

HTC parameters of the measurement location ML_{270} can be seen in Fig. 3.20. Like in the case of the *HTC* distribution measurements in Section 3.3.1, the results of the seventh zone (peak 2) could not be processed due to the moderate temperature change in this zone (only 1°C − 2°C). As we expected, according to the results of the gas flow model (Section 3.2.2), *HTC* values of the radial flow layers increased when getting closer to the assembly until a specific height above the board. The peak value was near to 3−4 mm above the assembly. It was caused by the growth of density and velocity in the radial flow layers toward the assembly. However, the friction became significant nearby to the board (0−2 mm), and it slowed down the velocity in larger extent than the density grew, thus decreased the values of *HTC*. Usually, *HTC* values were similar at the measurement heights of both 1 and 15 mm [13].

Some differences in efficiency (15%−20%) were also observed between the heating zones, which were 15%−20%. This effect was probably caused

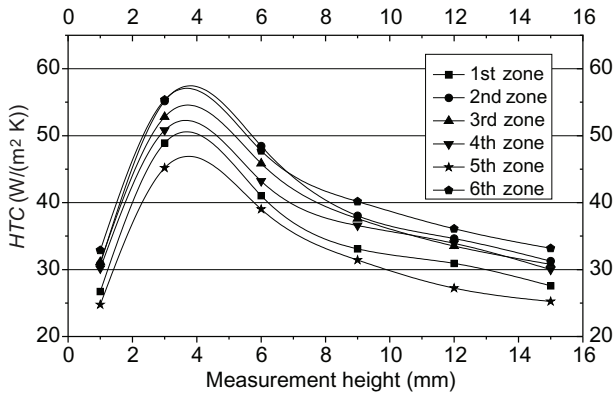

FIGURE 3.20 Results of ML270 from first to sixth heating zones. *Reproduced with permission from B. Illés, G. Harsányi, Investigating direction characteristics of the heat transfer coefficient in forced convection reflow oven, Exp. Therm. Fluid Sci. 33 (2009) 642−650.*

by the inhomogeneity in the gas circulation system and the different contamination levels of the nozzle matrices.

The measurement location had a considerable effect on the *HTC* values due to the construction of the reflow oven. Fig. 3.21 shows *HTC* values at ML_0, ML_{90}, ML_{180}, and ML_{270}. *HTC* values were much larger (80% − 120%) at MLs where the measurement gate positioned parallel or near parallel to the walls of the oven than at those MLs where it was perpendicular or near perpendicular to the walls.

In addition, considerable differences (30% − 40%) were between the opposite walls (when the measurement gate faced the opposite walls, ML_{90}, and ML_{270}). It was caused by the asymmetrical position of the conveyor line in the oven (Fig. 3.7B). Only minor deviations (1% − 5%) were found between the MLs where the measurement gate faced toward the zone entrance and exit (ML_0 and ML_{180}).

From the measurement results, direction characteristics of *HTC* values can be composed separately in each heating zone. It means that *HTC* values were illustrated above the $x-y$ plane according to the MLs and the measurement height around the center of the board. Appropriate values were attached with wrapping curves due to better visualization. Values of a given measurement height were attached with a horizontal curve, and values of a given ML were attached with a vertical curve. In this form, illustration of the results is more expressive because the heating capability of the reflow oven can be analyzed in each direction. Fig. 3.22 shows direction characteristics of *HTC* values in the sixth heating zone. In the main axes (x and y), the minimum and maximum *HTC* values are marked.

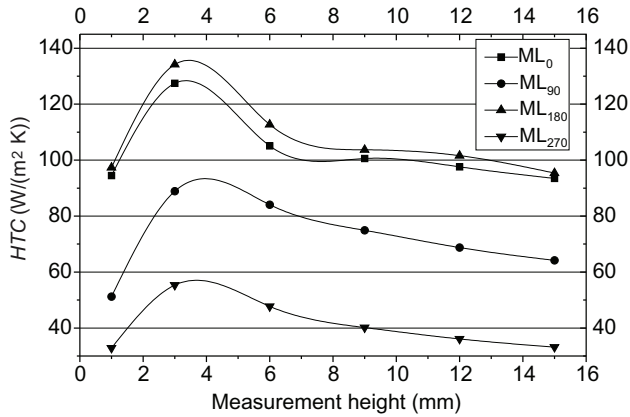

FIGURE 3.21 *HTC* values at ML_0, ML_{90}, ML_{180}, and ML_{270} in the sixth heating zone. *Reproduced with permission from B. Illés, G. Harsányi, Investigating direction characteristics of the heat transfer coefficient in forced convection reflow oven, Exp. Therm. Fluid Sci. 33 (2009) 642–650.*

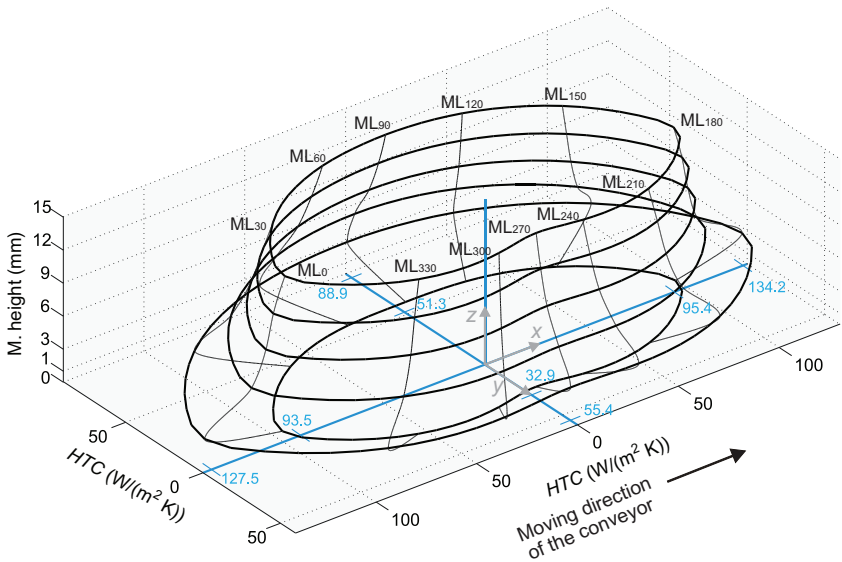

FIGURE 3.22 Direction characteristics of *HTC* values in the sixth heating zone. *Reproduced with permission from B. Illés, G. Harsányi, Investigating direction characteristics of the heat transfer coefficient in forced convection reflow oven, Exp. Therm. Fluid Sci. 33 (2009) 642–650.*

3.3.3 General *HTC* values in convection reflow oven

Finally, the general characteristics of *HTC* values regarding the gas streams and the radial flow layers were determined over the distance between the nozzle matrix and the assembly. For this purpose, measurement results from four similar convection reflow ovens were compared. All observed ovens used a nozzle-matrix system and had the same construction, only the dimensions (max. ~5%–10%), and the number of heating zones was different. Due to the minor dimensional differences, the measurement heights were defined on a relative scale: *H*/2, *H*/2.5, *H*/3.5, *H*/5.5, *H*/12, and *H*/60, where *H* was the distance between the nozzle matrix and the assembly. *HTC* values were also presented on a relative scale.

HTC characteristics of the heating gas streams can be seen in Fig. 3.23. *HTC* values were constant from the entrance of the gas streams down to the height *H*/2.5. From *H*/2.5 to *H*/12, *HTC* values decreased linearly by 2.9–3.9 [W/(m^2 K)/]mm gradient. At *H*/12, there was a cut-off point, and the slope of the decrease grew [17]. Characteristics of the radial flow layer show that *HTC* values at *H*/60 and *H*/2 measurement heights were the same (Fig. 3.24). From *H*/2 to *H*/12, the rate of growth increased, and at *H*/12, the *HTC* value reached 160% of the initial value (HTC_0). From *H*/12 to *H*/60, the *HTC* value decreased back to the HTC_0 value.

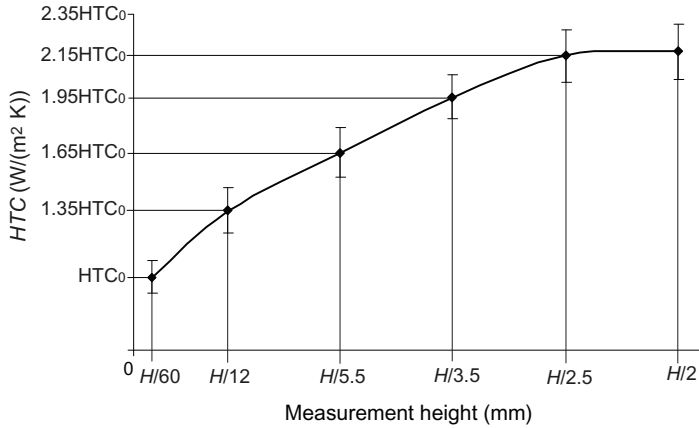

FIGURE 3.23 *HTC* values of the heating gas stream over the distance between the nozzle matrix and the assembly. *Reproduced with permission from B. Illés, Measuring heat transfer coefficient in convection reflow ovens, Measurement 43 (2010) 1134–1141.*

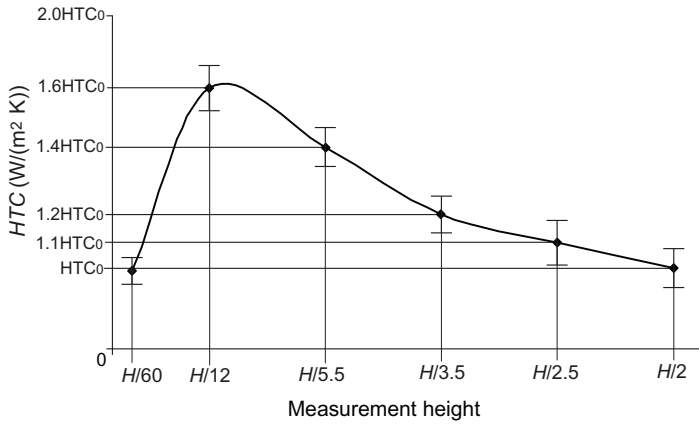

FIGURE 3.24 *HTC* values of the radial flow layer as a function of the distance between the nozzle matrix and the assembly. *Reproduced with permission from B. Illés, G. Harsányi, Investigating direction characteristics of the heat transfer coefficient in forced convection reflow oven, Exp. Therm. Fluid Sci. 33 (2009) 642–650.*

These results also proved our assumptions according to the gas flow model (see in Section 3.2.2). The *HTC* parameter was nearly constant (inflowing phase) until a height above the assembly where the radial flow layer started forming. This height was generally located about at height *H*/2.5. With the application of the general *HTC* characteristics (Figs. 3.23 and 3.24), it is enough to measure an initial HTC_0 value at a given measurement location, and characteristics of the *HTC* parameter can be calculated.

The previously presented measurement methods can be useful for monitoring the operation of convection reflow ovens, in order to predict soldering failures and to generate input parameters for numerical modeling. It was showed that the *HTC* values could change considerably in the heating zones. Therefore, the application of average *HTC* values is not appropriate. The importance of proper oven maintenance was also highlighted with a comparison of results concerning clean and contaminated oven operating for three months. The contamination of the flux residues can cause considerable differences in heating efficiency in the oven, which results in inhomogeneous temperature distribution and can lead to soldering failures.

References

[1] F.P. Incropera, D.P. De Witt, Fundamentals of Heat and Mass Transfer, 3rd ed., John Wiley & Sons, Hoboken, NJ, USA, 1990.

[2] B. Illés, G. Harsányi, Thermal characterization of solid structures during forced convection heating, in: A. Belmiloudi (Ed.), Heat Transfer—Mathematical Modelling, Numerical Methods and Information Technology, chapter 21, Intech, Rijeka, Croatia, 2011, pp. 529–552.

[3] A. Castell, C. Solé, M. Medrano, J. Roca, L.F. Cabeza, D. García, Natural convection heat transfer coefficients in phase change material (PCM) modules with external vertical fins, Appl. Therm. Eng. 28 (2008) 1676–1686.

[4] Y. Gao, S. Tse, H. Mak, An active coolant cooling system for applications in surface grinding, Appl. Therm. Eng. 23 (2003) 523–537.

[5] W. Kays, M. Crawford, B. Weigand, Convective Heat and Mass Transfer, 4th ed, McGraw-Hill Professional, New York, USA, 2004.

[6] B. Blocken, T. Defraeye, D. Derome, J. Carmeliet, High-resolution CFD simulations for forced convective heat transfer coefficients at the facade of a low-rise building, Build. Environ. 44 (2009) 2396–2412.

[7] K. Bilen, M. Cetin, H. Gul, T. Balta, The investigation of groove geometry effect on heat transfer for internally grooved tubes, Appl. Therm. Eng. 29 (2009) 753–761.

[8] A.S. Dalkilic, S. Yildiz, S. Wongwises, Experimental investigation of convective heat transfer coefficient during downward laminar flow condensation of R134a in a vertical smooth tube, Int. J. Heat Mass Transf. 52 (2009) 142–150.

[9] Y. Yin, X. Zhang, A new method for determining coupled heat and mass transfer coefficients between air and liquid desiccant, Int. J. Heat Mass Transf. 51 (2008) 3287–3297.

[10] M. Inoue, T. Koyanagawa, Thermal simulation for predicting substrate temperature during reflow soldering process, in: IEEE Proceedings of 55th Electronic Components and Technology Conference, Lake Buena Vista, FL, 2005, pp. 1021–1026.

[11] N.V. Steenberge, P. Limaye, G. Willems, B. Vandevelde, I. Schildermans, Analytical and finite element models of the thermal behavior for lead-free soldering processes in electronic assembly, Microelectron. Reliab. 47 (2007) 215–222.

[12] P.K. Gupta, P.K. Kush, A. Tiwari, Experimental research on heat transfer coefficients for cryogenic cross-counter-flow coiled finned-tube heat exchangers, Int. J. Refrig. 32 (2009) 960–972.

[13] B. Illés, G. Harsányi, Investigating direction characteristics of the heat transfer coefficient in forced convection reflow oven, Exp. Therm. Fluid Sci. 33 (2009) 642–650.

[14] B. Illés, G. Harsányi, Heating characteristics of convection reflow ovens, Appl. Therm. Eng. 29 (2009) 2166–2171.
[15] B. Illés, I. Bakó, Numerical study of the gas flow velocity space in convection reflow oven, Int. J. Heat Mass Transf. 70 (2014) 185–191.
[16] B. Illés, Distribution of the heat transfer coefficient in convection reflow oven, Appl. Therm. Eng. 30 (2010) 1523–1530.
[17] B. Illés, Measuring heat transfer coefficient in convection reflow ovens, Measurement 43 (2010) 1134–1141.
[18] D.F. Barbin, L.C. Neves Filho, V. Silveira Jr., Convective heat transfer coefficients evaluation for a portable forced air tunnel, Appl. Therm. Eng. 30 (2010) 229–233.
[19] M. Sakin, F. Kaymak-Ertekin, C. Ilicali, Convection and radiation combined surface heat transfer coefficient in baking ovens, J. Food Eng. 94 (2009) 344–349.
[20] V. Eveloy, P. Rodgers, M.S.J. Hashmic, Application of numerical analysis to the optimization of electronic component reliability screening and assembly processes, J. Mater. Process. Technol. 155–156 (2004) 1788–1796.
[21] V. Eveloy, P. Rodgers, Prediction of electronic component-board transient conjugate heat transfer, IEEE Trans. Compon. Packag. Technol. 28 (2005) 817–829.
[22] B. Sahin, Y. Ust, I. Teke, H.H. Erdem, Performance analysis and optimization of heat exchangers: a new thermoeconomic approach, Appl. Therm. Eng. 30 (2010) 104–109.

Chapter 4

Vapor-phase reflow soldering ovens

4.1 Introduction

Vapor-phase soldering (VPS), or in other words, condensation soldering, is a developing alternative of reflow soldering, which is fundamentally different from the other methods, due to its nonconventional filmwise condensation-based heat transfer processes.

The phenomenon of condensation is applied in various heat transfer methodologies, while the heat transfer during filmwise condensation is considered to be even and intensive. This particular heat transfer method can be found in nuclear power technologies, in consumer- or industrial-refrigerating and heating, heat pumps, different heat exchanger structures, semiconductor technology, etc.

The structure of a basic VPS oven can be seen in Fig. 4.1 based on the early works of Pfahl and Ammann [1]. The simplest ovens available today on the market are very similar to this original design. The oven consists of a tank, where the work zone is located—this part of the oven is filled with the boiling vapor of the heat transfer medium fluid. The fluid is in direct contact with a heater module, which can be a plate-shaped contact/immersion heater,

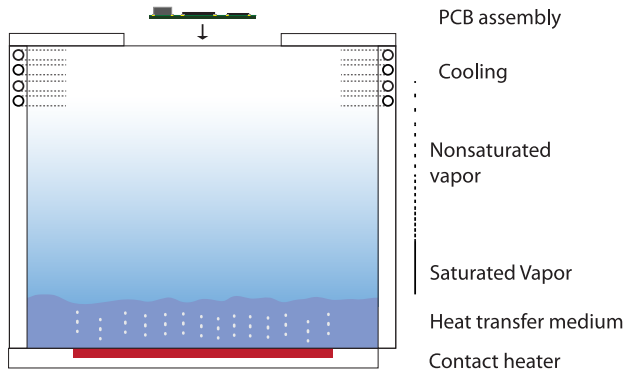

FIGURE 4.1 Basic structure of a vapor-phase soldering oven.

Reflow Soldering. DOI: https://doi.org/10.1016/B978-0-12-818505-6.00004-2

or a set of tube-shaped heater rods, with full contact around the surfaces with the fluid. Due to the heating, the fluid eventually reaches the temperature of boiling, where the intense evaporation starts. The generated blanket of vapor starts to fill the reservoir above the surface of the fluid, and the height of the blanket starts to increase. This increase stops at the upper side of the work zone, where a cooling system (usually working with water) condenses the excess vapor and forms an upper zone of the tank, which has a gradient in the vapor concentration. Such ovens are usually equipped with an opening on the top, where the PCB assembly is inserted into the work zone. Due to the condensation around the opening and the cooling, the colder condensed fluid flows back to the bottom of the work zone, into the reservoir. The cooling can be set in one fixed height of the tank, or in two-three heights, with primary, secondary, and tertiary cooling coils for enabling different vapor concentration (and fluid/vapor mixtures) along with the height of the oven [2]. When the PCB assembly is entering the vapor, the condensing fluid immediately covers the surface of the board, the components, and the solder joints as well. It is important to note that the condensed fluid flows in and around any openings and gaps on the PCB assembly, totally covering the surfaces. The filmwise condensation is the basis of the evenly heating, which is one of the main benefits of the method. It is important to note that the film layer keeps out the oxygen from the surfaces (most importantly, from the surface of the solder alloy). Even some of the earliest VPS works report that the evenly heating and the resulting solder joint quality is basically independent of product geometry [3]. This effect was also noted by Wood [4], mentioning that all items on the PCB assembly are heated evenly, regardless of shape and form.

The filmwise condensation phenomenon is considered to be relatively complex in its nature (in comparison with the other reflow heat transfer methods), that is why it is rare to find comprehensive descriptions of the process in deep detail. Modern VPS methodologies emerged from the basics are described above. They are utilizing the gradient in the concentration, the possible construction variations of the work zone, and sensor feedback for sample holder movement, or power regulating in order to control the ramps during the soldering. The in-line operation of a VPS oven further complicates the machinery required to apply the technology efficiently in the mass manufacturing of electronic assemblies.

A practical presentation of differences in soldering methodologies is shown in Fig. 4.2 based on Ref. [5]. The minimum and maximum values for the peak temperature and the duration of confrontation between the substrate and the solder are presented in the figure, where the differences between IR, convection, laser, and VPS are easy to differentiate. A PCB assembly in a VPS oven has a very narrow temperature range during actual reflow of the alloy, which—in comparison with IR or convection methods—can be a huge advantage over other mass- or selective-soldering methods. The classical

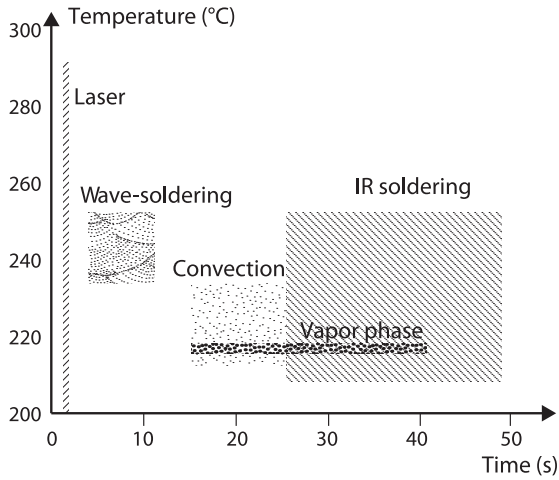

FIGURE 4.2 Thermal characteristics of different soldering technologies. *Based on K. Feldmann, M. Gerhard, Direct soldering of electronic components on molded devices, CIRP Ann. 44(1) (1995) 19–22.*

VPS dwell time is shorter than usual time above liquidus values: soldering with saturated vapor requires 40–60 seconds dwell of the printed circuit board assembly inside the VPS ovens [2].

Anjard [2] noted that VPS enables soldering of dual-sided components, chip carrier soldering, early double-triple-multiple stacks of PCBs at the same time. Solder paste and preforms are both applicable during the process for joining [5]. Leaded and lead-free alloys ranging from low [6,7] to high reflow temperatures are all suitable for VPS. The method can be applied to traditional through-hole technology mounting, surface mounting, and mixed methods, like pin-in-paste (PIP) [8].

While the basics were covered in this short introduction, the following sections aim to elaborate on the fundamental aspects, from the history, physical background, oven constructions, and the latest concerns and results from the global literature.

4.2 History of vapor-phase soldering

The invention and the basic idea of VPS came from Pfahl and Ammann. The invention was aimed to effectively perform soldering, fusing, and brazing, with the main focus on soldering [1]. While the methodology of condensation was novel at the time, there have been several attempts to improve soldering processes, like in Wittmann's work, where peanut oil was used as a heat transfer medium [9]. As an all-around solution, Pfahl and Ammann provided three ideas in their groundbreaking work to apply the condensation

heating. The main design involved a single chamber work zone, where the assembly is lowered into the vapor. The second design involved an additional conveyor line so that the machine can be adopted into in-line manufacturing. The third design adapted a wave-soldering module with a solder wave-fountain so that the vapor around the fountain could preheat the assembly before actual contact with the solder wave.

Their invention listed almost all aspects, which are important nowadays for a VPS construction. The medium (heat transfer fluid) should have at least equal to, or even higher, boiling temperature, as the melting temperature of the solder alloy, which is a basic requirement for the process. They defined the fluorocarbons as the basic heat transfer medium, highlighting the inert and chemically stable, nonconducting, nonoxidizing nature of such fluids. The sharp boiling point was noted as an important attribute, to enable precise soldering temperatures. They also highlighted that the condensate flow might also flush away contaminations from the prepared assemblies. At that time, they suggested FREON E4 or E5 type fluids for soldering, which were considered to have an optimal boiling point of 193.8°C and 224.2°C, respectively.

Wenger and Mahajan investigated the methods of early soldering capabilities [10]. Wenger compared the different fluids used in the process of heat transfer [11]. The environmental impact and the harmful composition were found to be critical with chlorofluorocarbon (CFC) products [12], which raised alarms during this time. Alternative perfluorocarbon (PFC) liquids used for heat transfer have been produced since the 1950s. The basic PFC heat transfer process was originally developed during World War II as part of the Manhattan Project. The large range of perfluorocarbons is mostly formed by dense, colorless, odorless fluids. They have great thermal and chemical stability and are essentially nontoxic. They also have electrical insulating and heat transfer properties and are good solvents for gases. Early VPS ovens applied PFCs as well, like perfluoro-perhydro phenanthrene; with the boiling point of 215°C. “Other electronic uses of PFCs included various testing procedures and cooling which involve direct immersion of an electrical device in a perfluorocarbon liquid” [13]. Later two different fluids remained as a possible choice for heat transfer medium: Fluorinert, which was a product of 3M, and Galden, which was a product of Solvay. The former material is considered as a part of the perfluorocarbon (PFC) fluid family; on the contrary, Galden is a perfluoropolyether (PFPE) type fluid—which will be later discussed in this chapter in technical details and in contrast with the other popular heat transfer media. PFCs (such as Fluorinert FC-70) were widely used in the 1980s, as Caswell reported [2]. The material was even mixed with Freon-TF, which had lower density and boiling temperature—enabling the second layer of vapor above the FC-70. Later the PFCs were considered to have a significant global warming potential (GWP). In order to keep the emissions low, the material also fell out of favor, making

way to the Galden, which is now the de facto standard heat transfer fluid in the market.

Vapor-phase reflow was originally proposed for mostly prototyping jobs and small runs of highly critical and complex PCB assemblies. During the years, VPS was involved in production for industrial, aerospace (interplanetary), and military applications [14]. Caswell [2] noted the high reliability of SMD in aerospace applications (GPS). Lal et al. [15] also emphasized the application of VPS in space technology. They both noted that the versatility, repeatability, production speed, economy, and adaptability of the VPS method were exceptional for the space-product assemblies. Military application of the technology was reported early in the same decade. The wide aspect of utilization from military to commercial was also highlighted by Anjard [3]. Rubin reported in the 1980s [16] that with the increase of SMD components in hybrid technology, VPS was gaining more importance. Spigarelli [17] noted that in hybrid technology, the use of basic VPS methodology started as early as in the 1970s and was led into the 1980s. As he mentioned, "Solder reflow times from 20 seconds down to as low as 4 seconds are feasible with extremely good uniformity. Precise temperature controls are not required." VPS was used in thin-film hybrid circuit fabrication as well, where the spin-coated photoresist layer was used as sufficient mechanical protection and a suitable solder stop for VPS [18]. Hagge [19] discussed the cost-effective processing and reliable performance of VPS in hybrid technologies, with leadless components. By the end of the 1980s [20], the technology was used from the United States to Europe and the Far East in many different oven constructions developed by local laboratories.

At the beginning of the 1990s, the technology started to fall back with the ban of CFCs [21], remaining only to cover markets with niche products. Another factor, which lowered the popularity of the method, was a number of design faults in the in-line equipment. The design choices resulted in excessive loss of the heat transfer medium [6]. The second generation started after the early years of the 1990s, then the sales of the VPS reflow ovens began to turn around 1998 [14]. In the next years, the market realigned itself to lead-free products; this is the point when the comeback of the VPS was documented. Now with the increased use in power electronics, the quality and energy-saving aspects and the market of VPS technology are still expanding [21].

4.3 Basics of boiling and heating

This chapter aims to describe the basics of boiling, which is essential for the main heat transfer medium: the vapor itself.

To generate the heat for soldering, electrical energy is converted into heat at the contact or immersion heaters located at the bottom of the tank, where the heat transfer fluid is located. This presents a classic case of so-

called pool boiling. With proper contact of the heating elements at the bottom of the reservoir, with good insulation to the "outside," and direct contact with the fluid, the energy input to the boiling can be considered virtually lossless. The power consumption of the heating elements is thus approximately equal to the heat output of the heaters.

To understand the vapor generation caused by the immersed heaters, it is important to summarize the process of boiling inside the VPS ovens. VPS ovens operate in a mode of boiling, which is called the "nucleate boiling regime."

Fig. 4.3 presents the classical case of a boiling curve, where the different regimes of boiling are highlighted. If the temperature of the surface of the immersed heater is below or slightly exceeding the boiling point temperatures, then the heat transfer between the heater and the fluid is caused by free convection. Convection results inflow around the heater, causing currents in the fluid, which circulate the heat transfer medium, eventually causing the superheated liquid to be evaporated at the free surface. If the heating power is increased, vapor nuclei form eventually, later growing into bubbles. This part of the boiling curve is called nucleate boiling. If the heating power is further increased, then the bubbles grow and rise to the free surface of the fluid pool. The most important point from the aspect of VPS is (A) point in the figure. This is the point of power limitation, or in other words, the point of typical temperature excess of heater surface (compared to the boiling point), from where the nucleate boiling regime goes into a transition and eventually arrives to the film boiling regime. During this transition, the

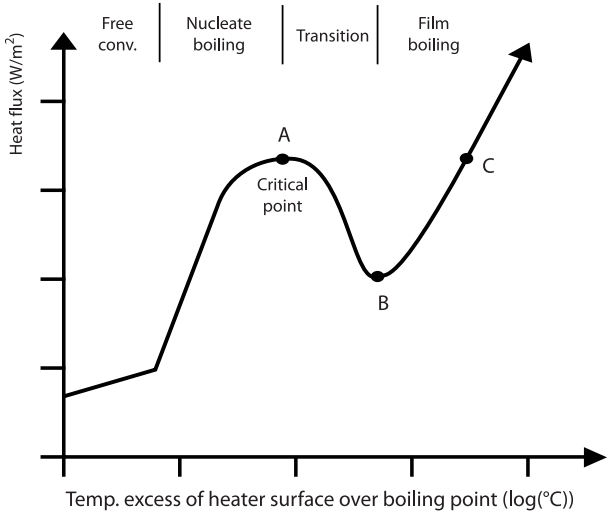

FIGURE 4.3 Boiling curve for nondecomposing liquids.

bubbles collide and merge to continuous columns along the heater surface at different sites. At point (B) the columns grow to a nonnegligible size when local fluid streams are closed out of the surface of the heater—any additional fluid replacing the evaporated volume will not reach the heater surface. This results in a vapor film blanket, which covers the heater surface, so the state of film boiling is reached.

With proper heating control, it is safe to utilize the VPS oven in the region of nucleate boiling. From this aspect there is a critical heat flux $(Q/A)_{crit}$ at point (A), where the system starts to develop the continuous vapor film, resulting in a critical temperature increase at the heater surface, and an abrupt jump from point (A) to (C). To sum up, the control of VPS ovens must tend to be kept below the critical $(Q/A)_{crit}$ value, while also managing the slope before the critical point. The sudden increase of the heater surface results in degradation of the fluid, which situation can be further complicated by any flux residues left in the tank, or at the heater surface [22]. Floating contaminants usually does not affect the process [6]. It must be noted that the boiling curve of VPS heat transfer fluids might slightly alter in characteristics from the presented one in Fig. 4.3.

It can be stated that the energy consumption of a VPS oven is considered to be 1/5 times of a conventional reflow oven. It is usually listed during the discussion of VPS energy requirements that cutting nitrogen costs, the omission of compressed air systems, and fast setups reduce the overall cost of the VPS ovens. The reduced heating power reduces the air conditioning costs of a manufacturing plant as well [21]. It was found that while the energy requirements of VPS is not comparable with the low values found at laser soldering [23], VPS ovens are still more energy-saving devices than similar scale-forced convection ovens. It was also found in practical use that the initial heating up phases after powering the machine and the medium boiling point recognition phases of the ovens often need optimization to further reduce idle times and thus energy waste of the ovens.

4.4 The heat transfer medium

While Section 4.2 discusses a few of the chlorofluorocarbons used in obsolete machines, the current chapter presents the most widespread medium used in the industry, which is called Galden. A commercially available bottle of Galden LS230 is presented in Fig. 4.4.

As it was noted before, the key to the reemergence of VPS was the application of the perfluoropolyether (PFPE) heat transfer fluids. These fluids are based on ether chains, which are closed with carbon−fluorine bonds. Setting the length of the ether chain serves as a basis of PFPE production, resulting in different boiling point temperatures. PFPEs do not contain chlorine—in contrast with the obsolete heat transfer fluids—and therefore do not contribute to chlorine-based catalytic destruction of stratospheric ozone [24].

FIGURE 4.4 Galden LS230 in a commercial pack.

According to Matsuda et al. [25], “the fluorous solvents with high boiling points can be used as a recyclable alternative to organic reaction solvents.” The formula of PFPEs can be described with (4.1):

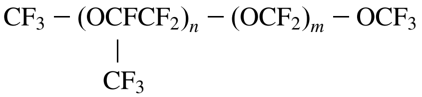

$$CF_3-(\underset{\displaystyle CF_3}{\underset{|}{OCFCF_2}})_n-(OCF_2)_m-OCF_3 \tag{4.1}$$

The molecular weights are typically in the range of 10^3-10^4, and the m/n ratio is in the range of 20–40 [22]. PFPE fluids can be produced between 150°C and 260°C; the most important product (Galden) is also available in a wide range of boiling temperatures. The different types of Galden are isolated by fractional distillation. The 260°C boiling temperatures enable soldering of 95Sn5Ag (221°C–245°C melting range) and 95Sn5Sb (232°C–240°C) soldering [22]. To enable precise soldering in VPS, it is a must to define precise boiling point temperatures—this is achieved via the narrow molecular weight distribution, the flexible ether link, and the strong carbon–fluorine bond.

From the aspect of environmental issues, Galden is considered to be inert, noncorrosive, nontoxic, nonflammable [14,26]. It was reported that Galden has zero ozone depletion potential (Zero ODP). The particular PFPE fluid has different types for industrial use; the title HT denotes the use for general heat transfer processes [27], SV is used in the semiconductor industry, while testing of hermetic sealing is performed with D02 type. PFPEs are also used in nano- and microtechnology, while can be applied as lubricants in microelectromechanical systems (MEMS) or the advanced nanoelectromechanical systems (NEMS) in interface nanotribology processes [28].

TABLE 4.1 Physical parameters of different Galden fluids.

	Density (kg/m^3)	Specific heat capacity (J/(kg K))	Specific thermal cond. (W/(m K))	Latent heat (fluid−vapor) (J/kg)	Avg. molecular weight (amu)	Thermal exp. coeff. ($cm^3/(cm^3\,^\circ C)$)
LS215	1800	973	0.07	63,000	950	0.0011
LS230	1820	973	0.07	63,000	1020	0.0011
HS240	1820	973	0.07	63,000	1085	0.0011

The carbon–fluorine bonds in Galden allow high stability, which is required due to the continuous thermal stress on the fluid [29].

Table 4.1 presents the most important material parameters of selected Galden types used in soldering applications [30].

The most important heat transfer fluids were compared by Lea [22]. Table 4.2 summarizes the properties of the materials, highlighting FC-70 (Fluid A), Fluorinert FC-5311 (Fluid B), and Galden LS230 (Fluid C).

Lea [22] found that with an immersion of a 2 mm thick Cu calorimeter plate, the results of heat transfer coefficient at 200°C (around melting point of Pb-based alloys) resulted $\sim$250–400 W/m^2 K values, also noting that the horizontal/vertical alignment resulted in significant differences. The alignment change led to a more significant change in the heat transfer coefficient than the change of the fluids. The critical heat flux (point A, described in Fig. 4.3) was found to be the smallest for the Galden LS230. It was found that the solubility of solid rosin flux in the boiling fluid is the smallest in Galden. After 50% of the fluid that has boiled away, the vapor temperature rise was 4.4°C for Galden. This is considered to be a moderately significant instability of the fluid, and this is often described in later literature as well with the documented boiling point drifts. While the phenomenon does not cause critical failures in lead-free reflow temperatures, the drift can be non-negligible in precise profile controls and soldering on sensitive substrate materials. According to the toxic material release tests during thermal degradation, the perfluoro-isobutylene (PFIB) release of the fluids was insignificant for B and C (Galden) and was significant for Fluid A in the case of

TABLE 4.2 Physical parameters of different Galden fluids.

Measured parameters	Fluid A	Fluid B	Fluid C	Unit
h during immersion for horizontal surface at 200°C	300	250	280	W/m^2 K
h during immersion for vertical surface at 200°C	400	360	380	W/m^2 K
Critical heat flux	15.5	15.7	13.9	W/cm^2
Rosin flux solubility	0.10	0.20	0.06	wt.%
Boiling point drift after 50% volume loss	2.1	0.3	4.4	°C
Thermal degradation, PFIB release in vapor, 15°C heater excess	Trace	NA	NA	
Thermal degradation, PFIB release in vapor, 50°C heater excess	2–5	Below 0.001	0.003	ppm/h
Aerosol droplet diameter at early stages	9–12	8–9	10–14	μm

50°C heater temperature excess. Degraded Fluids B and C (including Galden) also posed fewer problems in corrosivity issues compared to Fluid A. The evaporative loss in ambient room temperatures with and without airflow across the surface of the liquid also resulted in the practical optimum of the PFPE (Fluid C). Actual loss rates are varying from one oven to the other, so Lea did not draw further conclusions from these tests. The loss is identified by diffusion (molecular evaporation), aerosol effect, ventilation, drag-out, and filtration system issues, characteristic to each oven. Aerosol droplet diameters at the early stages of aerosol formulation resulted in an average of 10 μm overall for all fluids. Lea also noted that droplets with diameters as small as 0.01−500 μm can be recorded.

4.5 Physical background

To describe the physical background of the VPS, one has to start from Newton's law of cooling to investigate the special case of filmwise condensation on the horizontal boards and the components.

4.5.1 Basics of condensation heating

If a colder body (PCB assembly) is immersed into the hot vapor (which was generated from, e.g., heat transfer fluid), condensation occurs on the surface. This condensation results in a wet surface, and in the case of VPS, the surface is covered with a thin fluid film layer of PFPE fluid. This is called filmwise condensation. During condensation, the released latent heat is immediately transported into the cold body (the PCB and the components). With this step, the board is heated, and the system tries to achieve the energetically favorable state of equilibrium. Assuming horizontal position of the board, any excessive condensate fluid flows and finally drips down at the edges of the PCB assembly. On the bottom surface of the body, wavy filmwise condensate is formed; the excess drips down at the bottom surface of the body. The released latent heat can be calculated with (4.2):

$$Q = m \cdot h_{lv} \tag{4.2}$$

where Q is the energy released during condensation (J), m is the mass of the condensing material (kg), and h_{lv} is the specific latent heat (J/kg). If we assume that the heating is uniform, the dynamic behavior of the PCB assembly can be described (4.3) as a classical first-order (lumped model) system [31]:

$$c \cdot m \cdot \frac{\mathrm{d}T}{\mathrm{d}t} = h \cdot A \cdot (T_v - T_b) \tag{4.3}$$

where m (kg) denotes mass of the heated body, c (J/kg °C) denotes specific heat capacity, t (seconds) is the time in which the heating takes place, A (m^2) is the surface where the heating and condensation takes place, h (W/

(m^2 °C)) is the heat transfer coefficient of the filmwise condensation, T_b is the body temperature, and T_v (°C) is the temperature of the saturated vapor.

It is assumed that the laminar flow of the condensate results in homogeneous heating along with the total surface of the PCB assembly. However, it must be noted that local inhomogeneity or thermal inertia effects can be recorded in smaller-scale investigations at different parts on the surface of the PCB during ramps in the profile.

It is assumed that for the continuous heating, permanent vapor source and (given the basic vapor-phase methodology) permanently saturated vapor is needed. Condensation draws and condenses away fractions of the vapor from around the cooling, the walls, and the PCB assembly. Eventually, this brings a need for continuous vapor supply from the surface of the boiling fluid. During the process, the film layer cools down, while heat is transferred to the PCB assembly. On the colder condensate, continuous condensation follows, and the process continues, until the maximum temperature, the boiling point of the fluid is reached. At this point, the steady-state of the PCB assembly is reached, the heating is practically finished. Based on the Newton law of cooling [26], the following form can be written (4.4):

$$\ln\left(\frac{T_v - T_b(t)}{T_v - T_b(0)}\right) = -\frac{h \cdot A}{m_b \cdot C_b} \cdot t \tag{4.4}$$

where $T_b(0)$ is the initial temperature of the body (K). In this case, the temperature of the body over time $T_b(t)$ is written according to (4.5), where the equation gives an exponential plot for the temperatures (Fig. 4.5):

$$T_b(t) = (T_v - T_b(0)) \cdot \left(\frac{T_v}{(T_v - T_b(0))} - e^{-\left(\frac{h \cdot A}{m_b \cdot C_b}\right)}\right) \tag{4.5}$$

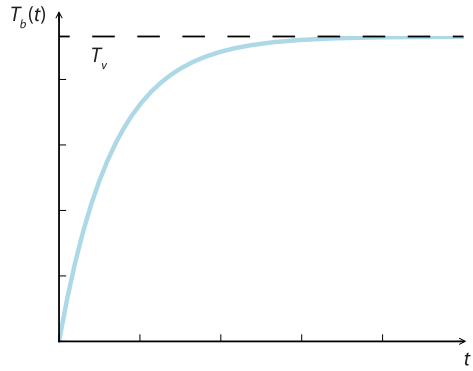

FIGURE 4.5 Exponential heating in saturated vapor.

4.5.2 Analytical solutions for heating PCBs in saturated vapor

The heat transfer coefficient can be obtained numerically from measured data, with the time-stepping finite difference method. In this case, a numerical based time-stepping formula for the calculation can be described with (4.6):

$$h_i = \frac{T_{i+1} - T_i}{\Delta t} \cdot \frac{c \cdot m}{A \cdot (Tsat - T_i)} \tag{4.6}$$

where i is an index for the steps.

Calculating the heat transfer coefficient can also be performed with different analytical approaches. One is to investigate filmwise condensation on the top and at the bottom surfaces and to find the proper explicit formula for the given case [32]. "During the VPS process, the PCB is immersed into the vapor in a horizontal orientation. The top side of the PCB can be considered as an upward-facing plate, with free edges, so the condensed liquid is able to spill down at the edges, back to the reservoir at the bottom of the tank. The steady-state thickness of the film is settled with the balance of the condensation rate on the surface and the downward flow rate along the edges. The condensate forms a wavy surface of the fluid film, according to the Rayleigh–Taylor instability. The generated condensate drips down intermittently from the wavy film."

The geometry in Fig. 4.6 shows the PCB from the side. Note that this approach omits the components on the top. The PCB has an edge with L dimension and a plate height of H ($L \gg H$). We assume that the flow on the top is laminar among length L, and the condensate thickness is the largest at the center of the PCB. We also need to assume the following conditions [32,33]:

- there is conductive heat transfer between the solid body and the film,
- there is a no-slip condition at the solid–liquid boundary,
- there is uniform solid body temperature,

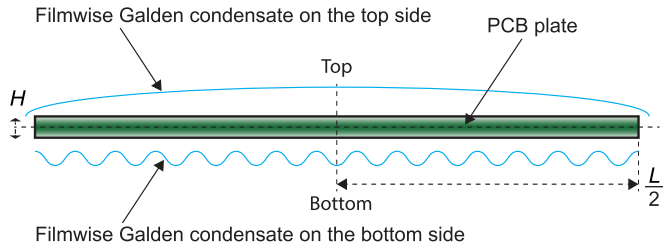

FIGURE 4.6 Condensation of Galden on the PCB. *From A. Géczy, B. Illés, Zs. Illyefalvi-Vitéz, Modeling method of heat transfer during vapour phase soldering based on filmwise condensation theory, Int. J. Heat Mass Transf. 67 (2013) 1145–1150.*

- there is saturated unperturbed-quiescent vapor (which is already set to a steady-state of saturation),
- there is a lack of interfacial resistance to heat transfer at the liquid−vapor interface,
- there is a lack of momentum effect in the condensate (no downward drag caused by the vapor),
- the consumed vapor is always regenerated by the boiling Galden in the vapor space,
- the dynamic material properties are controlled in function of temperature.

Nusselt was the first to describe the heat transfer during filmwise condensation on walls. His model was based on the starting object of a vertical wall, which is not suitable for discussing the VPS on PCBs. "During the years the Nusselt model had been refined for horizontal cases according to experimental-analytical data. After years of investigations with different horizontal plates [32], Bejan added the condition of zero film thickness at the top edge of the plate, where the flow rate reaches its highest finite value [33]. Rohsenow [34] showed that the latent heat of vaporization should be refined if the temperature of the filmwise condensate is allowed to have a nonlinear distribution within the film itself," according to (4.7):

$$h'_{lv} = h_{lv} + 0.68 \cdot C \cdot (T_v - T_b) \tag{4.7}$$

where h'_{lv} (kJ/kg) is the corrected form of the latent heat and C (J/kg K) is the specific heat of the condensate (the Galden itself). According to Drew, an additional empirical correction should be applied [35]. He highlights that the physical properties and dynamic material parameters should be evaluated at a reference temperature presented by (4.8):

$$T_{REF} = T_{SAT} - K \cdot (T_{SAT} - T_b) \tag{4.8}$$

where K is a constant, which was defined to be 0.75. Drew suggested his correction for the cases where $1/\mu_l$ can be considered linear. In the case of Galden and VPS processes the relevant temperature range the nonlinearity is approximated with a linear solution. According to the calculated formula of Bejan, the heat transfer coefficient h_{L_BE} for the top side of the plate is (4.9):

$$\overline{h_{L\_BE}} = 1.079 \cdot \frac{k_l}{L} \cdot \left(\frac{h'_{lv} \cdot \rho_l \cdot (\rho_l - \rho_v) \cdot g \cdot L^3}{(T_{sat} - T_b) \cdot \mu_l \cdot k_l} \right)^{1/5} \tag{4.9}$$

where L is the z dimensional length of the film condensed on a vertical wall (m), h_L is the L-averaged heat transfer coefficient (W/m^2 K), Nu is the L-averaged Nusselt number, k_l is the thermal conductivity (W/m K), h_{lv} is the latent heat of vaporization (kJ/kg), ρ_l is the density of the liquid (kg/m^3), ρ_v is the density of the vapor (kg/m^3), g is the gravitational constant (m/s^2), T_{SAT} is the temperature of the vapor (K), T_b is the temperature of the body (K), and μ_l is the dynamic viscosity (kg/m s). The effect of condensation

was investigated by Gerstmann and Griffith on the bottom side of horizontal plates [36]. Their analytical approach can be used as a complementary solution—in addition to the calculations on the top side [37]. According to their work, the Nusselt number (Nu_{GG}) is shown in (4.10):

$$\overline{Nu_{GG}} = 0.69 \cdot Ra_{GG}^{1/5} \tag{4.10}$$

where Ra is the Rayleigh number, $_{GG}$ index refers to the original authors' names. The coefficient is calculated with (4.11),

$$Ra_{GG}{}' = \frac{g \cdot \rho_l' \cdot (\rho_l' - \rho_v) \cdot h_{lv}'}{\mu_l' \cdot (T_{sat} - T_b) \cdot k_l} \cdot \left(\frac{\gamma}{g \cdot (\rho_l' - \rho_v)} \right)^{3/2} \tag{4.11}$$

where γ is the interfacial tension (N/m) and $'$ denotes corrections according to Drew and Rohsenow. Finally, the heat transfer coefficient for the bottom side can be calculated with (4.12):

$$\overline{h_{L\_GG}}' = \overline{Nu_{GG}}' \cdot \frac{k_l}{D} \tag{4.12}$$

The analytical solution gives a fast and efficient approximation of the heating during the simple VPS process in saturated vapors. The measurement of a PCB, the analytic calculation, and multiphysics modeling of the same setup are presented in Fig. 4.7 [32] for low-temperature Galden used in soldering with low melting point pastes.

The results show that the multiphysics calculations (later described in Chapter 6, Numerical Simulation of Reflow Ovens) offer similar results, but are more close to actual measurements. The precision of the multiphysics approach is finer, because it handles how the vapor is consumed around the board, and this results in a breakpoint in the measured data too. The deviance from the classical analytic model suggests that despite a properly prepared saturated vapor volume (where the measurement was taking place), the actual heating slows down in a minor, but nonnegligible manner.

The method above can be extended to round PCBs as well. While in other reflow methods, the shape and corners of a PCB might not be significant from the aspect of process descriptions, on the other hand filmwise condensation requires.

Round-shaped PCBs ("disc-shaped plates" in heat and mass transfer terminology) and rounded corners are becoming more important from the aspect of miniaturization and design aspects, where the device casings (e.g., LED lamps) define the shape of the circular PCB carrier. Common PCB designer tools and PCB manufacturers are all prepared for round PCB outlines. [37] Filmwise condensation for upward-facing disc-shaped plates were investigated by Bejan [33] and later by Chiou and Chang [38]. Their works serve as a starting point for investigating the case of round-shaped PCBs. According to Bejan, the solution on the laminar condensate film on a circular

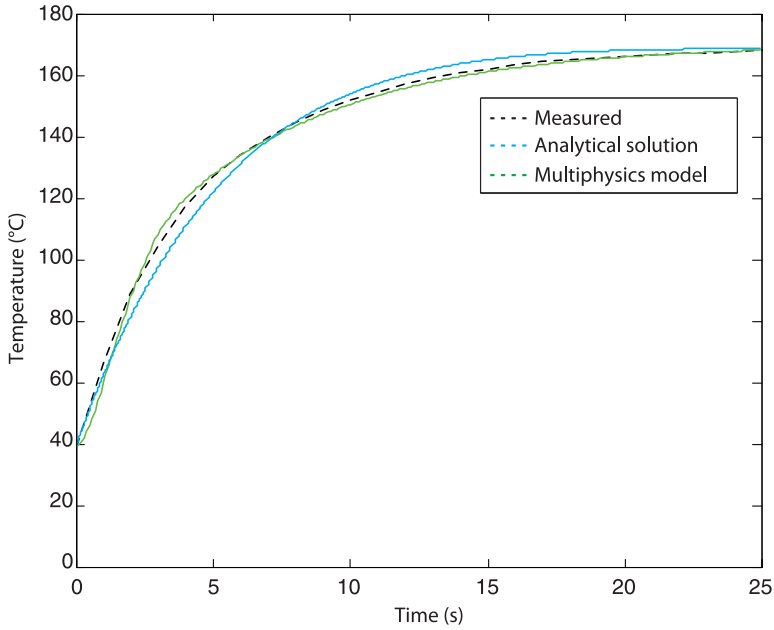

FIGURE 4.7 Comparison of measurement, analytical calculation of filmwise condensation, and multiphysics approach on VPS modeling. *From A. Géczy, B. Illés, Zs. Illyefalvi-Vitéz, Modeling method of heat transfer during vapour phase soldering based on filmwise condensation theory, Int. J. Heat Mass Transf. 67 (2013) 1145–1150.*

plate (with a diameter of D) is analogous with the rectangular case. He assumes that the film thickness is noticeably thinner on a disc, while the condensate can run in all directions away from the central region." This can be seen in Fig. 4.8, where the direction of the condensate flow is from the center to edges.

Bejan [33] presented a heat transfer coefficient along the diameter of a horizontal disc according to (4.13):

$$\overline{h_{D\_BE}} = 1.368 \cdot \frac{k_l}{D} \cdot \left(\frac{h'_{lv} \cdot \rho_l \cdot (\rho_l - \rho_v) \cdot g \cdot D^3}{(T_{sat} - T_b) \cdot \mu_l \cdot k_l} \right)^{1/5} \tag{4.13}$$

where D is the diameter of the disc (m). Chiou and Chang [38] also offered an explicit formula, starting from the function of Ra/Ja (Rayleigh number/Jakob number). According to their work, there is a critical minimum value of film thickness at the disc edge, and this value is not zero, like in the case of [33]. The heat transfer coefficient for a disc with an r radius (m) can be written as (4.14):

$$h_{r\_CC} = X \cdot \frac{r}{k_l} \cdot \left(\frac{Ra}{Ja} \right)^{1/5} \tag{4.14}$$

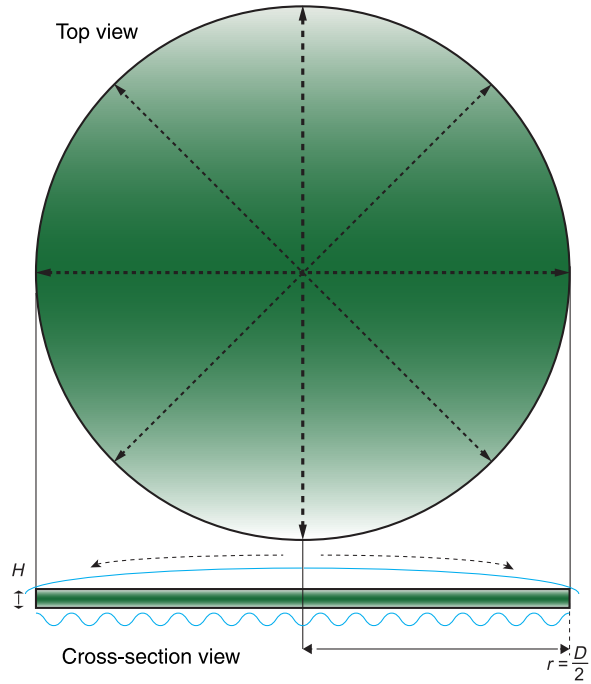

FIGURE 4.8 Condensation on disc-shaped PCB. *From A. Géczy, B. Illés, T. Darnai, Investigating condensation heat transfer during vapour phase soldering on round-shaped PCB plates, Int. J. Heat Mass Transf. 86 (2015) 639–647.*

where X is a numerical constant (dimensionless, described later), Ra and Ja are the dimensionless Rayleigh (4.15) and Jakob (4.17) numbers. The Rayleigh number can be written from the classical form:

$$Ra = \frac{g \cdot \beta \cdot (T_{SAT} - T_b) \cdot D^3}{\nu \cdot \kappa} \tag{4.15}$$

where β is the coefficient of expansion ($cm^3/cm^3\,^\circ C$), ν is the kinematic viscosity (m^2/s), and κ is the thermal diffusivity (m^2/s), D serves as the characteristic length (m). Thermal diffusivity can be obtained with the following formula:

$$\kappa = \frac{k_l}{\rho_l \cdot C} \tag{4.16}$$

For (4.14), the Jakob number can be written as:

$$Ja' = \frac{C \cdot (T_{sat} - T_b)}{h'_{lv}} \tag{4.17}$$

The X numerical constant shown in (4.14) is exactly 1.0295 in the works of Chiou and Chang which was defined for water steam from the formula shown in (4.18):

$$X = 1.03 - 0.188 \cdot \frac{Ja'}{Pr'} \tag{4.18}$$

The Pr is the dimensionless Prandtl number (4.19) formula for the disc:

$$Pr' = \frac{C_l \cdot \mu_l'}{k_l} \tag{4.19}$$

The equation of (4.14) is valid if,

$$\frac{Ja}{Pr} < 0.1 \tag{4.20}$$

In the presented case of Galden heat transfer fluid, the ratio is ~ 0.014 [37]. It was found [37] that both approaches for calculations can provide a proper result, however (4.13) yields a slightly better result from the aspect of modeling precision. It was also found that rectangular PCBs, with given rounded corners, "the 'disc effect' can be neglected during modeling by using rectangular approximations with an acceptable error margin if the proper thermal mass is taken into consideration" [37].

While explicit descriptions for heat transfer on vertical slab and vertical cylinder with horizontal surface are also available [33] (the vertical walls of the given structures are also taken into account), these methods are difficult to apply to the small scales of modern SMD components, and thus, to explicitly calculate heat transfer on the total surfaces and subsections of the PCB assembly. It is also important to note that with more sophisticated process control methods, involving nonsaturated vapor, the explicit descriptions may not be entirely valid or may need further corrections.

4.5.3 Heat transfer coefficients during vapor-phase soldering

The heat transfer coefficients can be calculated from measurements, albeit with limitations in the precision and the smoothness of the obtained results. The heat transfer coefficient (h) can be assumed to be a fixed value or to be dynamic. The first approach is simpler, however, it can be used only for saturated vapors with certain limitations in precision. Even in saturated vapor, slight dynamics can be observed in the initial collapsing of the vapor around the PCB assemblies. This renders the need for dynamics to be introduced in the discussion of the h value. For more sophisticated VPS methods, dynamic h values should be calculated. Such methods are not available yet in the literature.

While the certain parameter of the heat transfer coefficient can depend on the surface, the materials of the assembly, the horizontal, angled, vertical

positioning, and the state of the vapor, ususally not fixed values are presented, but ranges of h are presented in the literature.

It can be stated that usual heat transfer coefficients are around 100−400 W/m^2 K depending on the parameters discussed above [12,39]. This value is considerably smaller from the 40−150 W/m^2 K values discussed in convection soldering.

Measurements on test PCB boards revealed that the heat transfer coefficient values may considerably differ even on a simple rectangular board shape and surface during heating; a central zone and edges-corners of the rectangular board can be defined. The effect is more emphasized on boards with corners (as mentioned in Section 4.4.2), however edge effect is also observable on disc-shaped boards as well. The corner/edge effect is presented in Fig. 4.9, where heat transfer is increased with ∼20% around the corners, and with ∼10% on the edges compared to the center of the board. The nature of the filmwise condensation causes this observation, while the condensate flows down at the edges and at the corners, increasing flow rate,

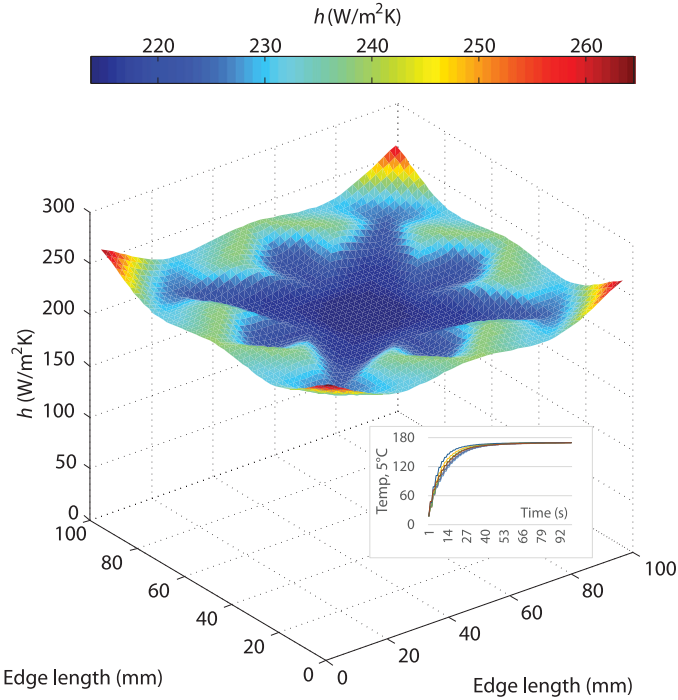

FIGURE 4.9 Overall distribution of (h) on a rectangular PCB at $t = 12$ seconds after immersion into saturated vapor and heating curves of measurement points. *From A. Géczy, Investigating heat transfer coefficient differences on printed circuit boards during vapour phase reflow soldering, Int. J. Heat Mass Transf. 109 (2017) 167−174.*

decreasing the thickness of condensate, thus increasing the heat transfer coefficient [39].

As for controlled inclination, certain investigations concluded [40] that even a small inclination (~1 degree) can affect the heat transfer and temperature distribution along the surface of a PCB assembly. Intended inclination can be used for faster, more effective heating, without changing the heat transfer medium or regulating the power unit of the heater. Controlled inclination can reduce the effect of heat transfer differences along the surface. While literature refers to experimenting with inclination, modern commercial ovens do not utilize the method yet [40].

4.6 Vapor-phase soldering ovens

4.6.1 Basic vapor-phase soldering ovens

According to Section 4.1, Fig. 4.10 shows an experimental laboratory setup with basic VPS in saturated vapor. Anjard reported in the early 1980s that many adopters of VPS technology used internally manufactured systems. This is due to the relatively simple design of the basic VPS methodology [3].

While the homogeneous vapor simplifies the description of the method and enables efficient heating of assemblies with large thermal mass, the lack of control results in very high gradients. Before leading to the omission of the method in mass manufacturing, fast heating of basic VPS processes was gaining praise in the 1980s, when the elevated heating rates were considered favorable due to the efficiency [4]. Heilmann [41] reported cautiously high heating rates: 16°C/s for SOT-89 packages and 10°C/s for PLCC packages. He noted that the cause of slower heating for large components is due to the different surface to mass ratio. Fig. 4.11 shows heating of a rectangular and disc-shaped PCB in saturated vapor, where both the initial gradients and the gradients around the melting point are considered to be steep. As an addition, the

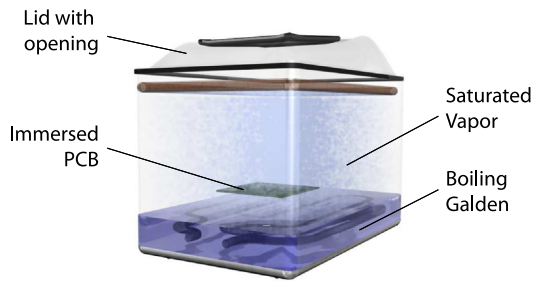

FIGURE 4.10 VPS oven with saturated vapor. *From A. Géczy, B. Illés, T. Darnai, Investigating condensation heat transfer during vapour phase soldering on round-shaped PCB plates, Int. J. Heat Mass Transf. 86 (2015) 639–647.*

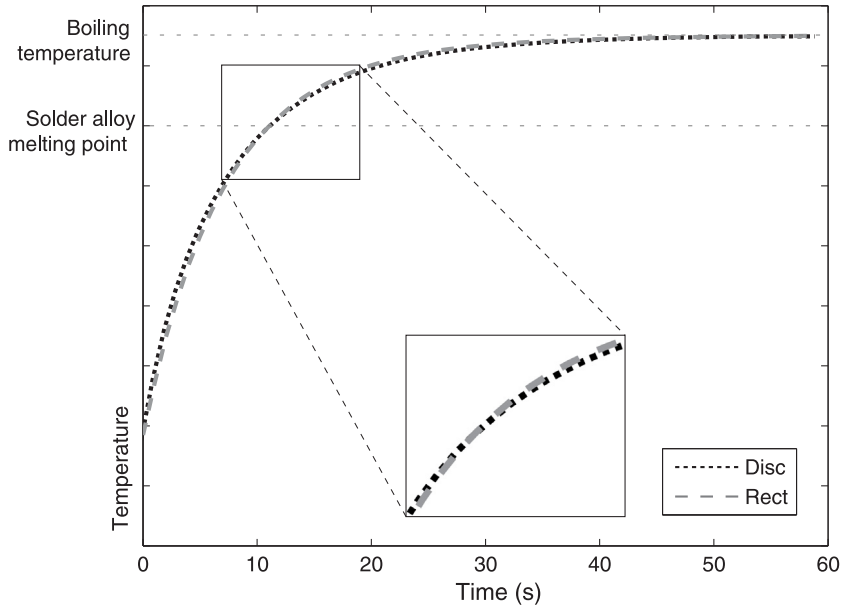

FIGURE 4.11 Fast exponential curves of heating in saturated vapor. *From A. Géczy, B. Illés, T. Darnai, Investigating condensation heat transfer during vapour phase soldering on round-shaped PCB plates, Int. J. Heat Mass Transf. 86 (2015) 639–647.*

highlighted part in the figure also shows that the different shape with the same thermal mass result in almost indistinguishable temperature curves [37].

With the increased component density and smaller component lead pitches, the rapid heating method can result in classic failures. Components with different thermal masses are heated with observable thermal inertia, and this effect can be more emphasized in the profiles with fast heating rates. In cases, when the differences are significant locally (such as the case of the thin component leads and the large component package bulk and the printed circuit board itself), solder wicking can occur. Solder always flows from lower to higher temperatures, due to the temperature dependence of surface tension. In such cases, the wicked up solder can cause dry joints, as noted by Wassink and van Gerven[42]. Also, the effect of component floating away from the intended position, and "drawbridging" or tombstoning was observable in early VPS soldering ovens [42]. These failures are discussed later in deeper detail.

Some oven producers applied IR heat preheating stages to their ovens, or other constructions applied to dip the board into upper unsaturated layers. The preheating concept was later further improved with abrupt vaporization of a controlled amount of heat transfer fluid with the help of a heating plate in a preheat zone of the oven [43]. With preheating, the problems of

spluttering paste, tombstoning, and damaged components can be avoided. On the other hand, the preheating processes might allow oxygen to reach the metallic surfaces resulting in possible oxidation [44].

Despite its drawbacks, VPS in the saturated vapor is still used in the industry in special cases. In recent reports [45], the application in space technology with leaded alloys was discussed. Tegehall and Dunn [45] also highlighted the importance of preheating at 65°C and then preheating at 185°C for 400 seconds. Then in the next step of the reported process, the assemblies are lowered into the saturated vapor for 25 seconds.

4.6.2 Heat-level vapor-phase soldering ovens

The working principle of a heat-level oven is based on a modified control over the basic VPS method discussed in Section 4.5.1. The PCB assembly is positioned on the PCB holder (workpiece carrier), which moves down the PCB into the soldering height. With the cover closed, the heater set to the desired power level, and a temperature limit set for stopping the process, the soldering cycle starts. The machine heats up, and the vapor is generated from the bottom, up to the PCB assembly. The significant amount of energy is transferred from the saturated vapor arriving at the PCB surfaces. When the PCB assembly reaches the boiling point temperature, the vapor is able to rise above the level of the assembly. If the vapor reaches a thermocouple detecting the rising level, the heating power is reduced to zero, and cooling starts, eventually collapsing the remaining vapor inside the work zone. The residual heat of the PCB assembly enables remaining condensate to evaporate from the surfaces and finally, the workpiece carrier rises up to the position of cooling. The machine provides a signal to show when the oven is finished with the process. Fig. 4.12 presents a typical oven setup, where the PCB is lowered to a set soldering level, and when resting in that position, the vapor is generated onto the surfaces from the bottom.

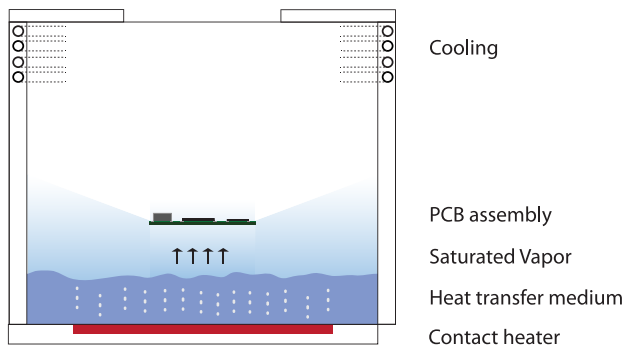

FIGURE 4.12 Heat-level vapor-phase soldering oven.

The heat-level method was gaining attention lately, because of the gradient control possibility. This can be achieved with the setting of heating power [43]. In order to emulate the profiles of convection systems with soaking plateaus, active vapor cooling can be applied, so in given oven constructions, cooling coils are positioned around the height of the board position in the work zone [46]. When the PCB assembly reaches a given temperature, active water circulation slows down the heating, and condenses a specific amount of vapor, resulting in soaking periods. In given oven constructions, additional cooling can be positioned in the reservoir of the heat transfer fluid, or underneath the tank [47]. It is important to note that some VPS ovens apply injection of vapor for more precise control, in contrary to direct boiling from the bottom of a reservoir.

4.6.3 Soft-vapor-phase soldering and plateau capable ovens

The soft-vapor-phase soldering (S-VPS) oven houses a vertical level-setting PCB assembly holder [12], where the board is moved into different levels of the vapor. In order to achieve height-based control, the vapor is set to have a concentration gradient along with its height. This vertical movement results in a process with custom profiles of plateaus, also reducing failures and improving overall quality. The process of S-VPS is as follows. The PCB assembly is immersed into the vapor, then when the soak temperature is reached, the board is moved up to the upper boundary of vapor. Then the PCB has moved again downward in selected levels. The oven control moves the board according to the programmed gradients and the time above liquidus period. Finally, the board is moved to a position in the oven where controlled cooling is applied to the assembly. With proper temperature sensor feedback, the cycles can be monitored and matched to a reference profile. This provides repeatability even for complex assemblies [48]. A typical setup of an S-VPS oven is presented in Fig. 4.13.

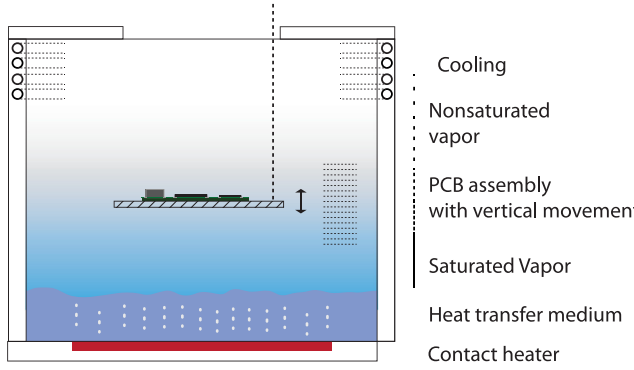

FIGURE 4.13 Soft-vapor-phase soldering oven.

It must be noted that some of the S-VPS ovens are the most advanced VPS ovens in the field, often incorporating IR preheaters, custom cooling system, Industry 4.0 preparedness, with automatic barcode/product management and network capabilities.

While the S-VPS title is a commercialized name of the height-based gradient control of a specific oven producer, similar control mechanisms with plateau capabilities can be found in the market. Heating power can be controlled with PWM (pulse width modulation), turning a switch between supply and load on and off. Having reached the operation temperature, the assembly remains in such a state for a given period of time. The workpiece carrier is moved into the cooling position afterward in two steps by a lifting unit. There is a short evaporation period of $\sim$10 seconds between the phases; after the elevator is moved into its initial position, there is a longer evaporation period that lasts for $\sim$50 seconds. The vapor reservoir closes at the bottom as the lift reaches its upper terminal position and the cooling fan is switched on. After the cooling time has expired, a signal indicates release for the removal of the workpiece. With the method, plateaus can be set on the profile, enabling improved mechanical strength of the joints and optimized intermetallic layer thicknesses above the contact pads [49].

At this point, it can be also noted that a blank soldering cycle or an initial heat up tempering run of ovens with more complex control is essential before profile recording or soldering. This is not a unique feature of the technology—the phenomenon had been also suggested with other types of reflow systems. At given construction and control, this process is performed automatically, but sometimes the operators must take note of the initial machine state. Fig. 4.14 presents a run of the PWM-controlled oven after cold startup, and after a few cycles of operation.

4.6.4 Vacuum vapor-phase soldering ovens

The basic idea of vacuum enhanced VPS comes from the need of reducing the void inside the reflowed solder joints. Fig. 4.15 presents a simplified look on a vacuum-VPS oven.

Until reaching the melting temperature of the solder paste, the vacuum VPS oven works like the basic one with a nonhermetic soldering chamber. First, the PCB assembly is loaded (Step 1 in Fig. 4.15) and conveyed into the vapor workspace [50]. After the melting of the solder alloy (Step 2), the assembly is conveyed up to the vacuum zone of the oven, then a cap closes the soldering chamber hermetically and forms a vacuum chamber (Step 3 in Fig. 4.15). The vacuum chamber described in Ref. [51] has $325 \times 325 \times 85$ mm dimensions. A suction pipe is located at the top center of the closing cap with 13 mm inner and 24 mm outer diameter made from silicone rubber. The vacuum pump of the oven works with the so-called volume separation method, meaning that the pump separates (draws out) the

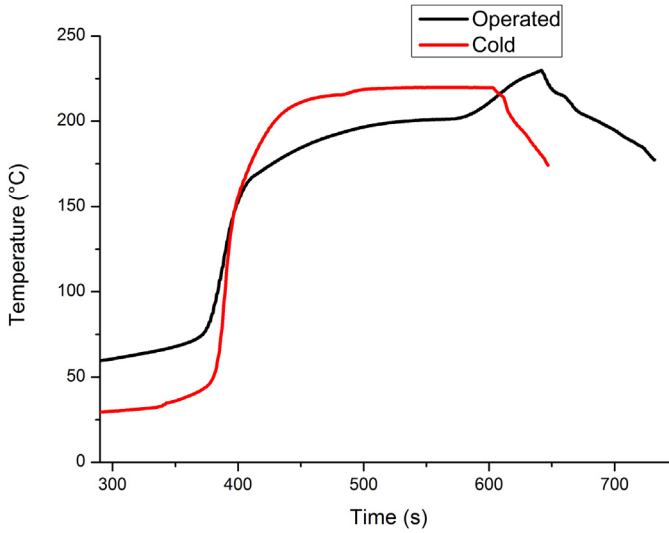

FIGURE 4.14 Obtained profiles with the same program but different oven state (cold/operated).

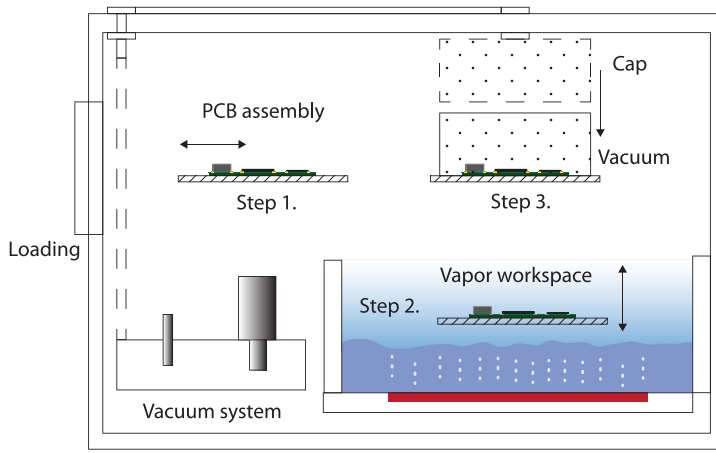

FIGURE 4.15 Vacuum VPS oven with loading (Step 1), reflow (Step 2), and vacuum treatment (Step 3).

given volume of vapor from the cap in a given time. This implies a constant decrease in the relative pressure between the suction pipe and the vacuum chamber. The vacuum pump decreases the pressure to 5 kPa in 7−15 seconds and the assembly spends further 5−10 seconds at this state to allow the voids to leave the solder joints. Then normal pressure is set in the vacuum chamber, then the PCB assembly is moved to cool, then it is led out in the

exiting and unloading bay [50]. The ultimate pressure in the vacuum chamber is usually ~40–50 mbar during the treatment part of the process [51]. In selected vacuum VPS ovens, the heat transfer medium can be injected into the vacuum. This can be combined with an additional prevacuum step, from the initialization of the soldering process at the pressure level of 100 mbar, to ensure a smoother transition into the liquidus phase of the used alloy [52]. The prevacuum can be also used to prevent oxidation to enable efficient drying, to preclean, and to improve the homogeneity of heat transfer medium distribution for 3D assemblies (described later). It is usually reported that vacuum generally improves void reduction, improves the filling of micro-vias and through-hole solder joints, and also improves the wetting of solder on contact surfaces.

The vacuum chamber positioning of a VPS oven depends on the manufacturer and the patented construction. The vacuum chamber can be at the same vertical level, as the soldering [53]. Investigations are continuous in the literature [54]; the quality and reliability concerns are discussed later in the chapter.

4.6.5 Custom vapor-phase soldering ovens

Special experimental ovens can be found in the literature, which is usually not applied in larger-scale production but are developed to validate proof of concept ideas and catalyze basic research of the technology. An experimental oven was presented in Ref. [55], which was used later in several works for investigating different sensor applications for VPS process monitoring. This aspect is discussed later in Section 4.8. Lam et al. presented an experimental oven [56], where the usual contact heating was exchanged to Peltier heaters. The assumption is that closed-loop control is difficult with classic constructions, due to the thermal capacities, and the resulting thermal transients of the system. Their construction incorporated five layers of Peltier elements, where the cold side of the bottom element is kept on the temperature of the environment. The current of each Peltier layer is increased from the bottom to the top. Peltier elements also allow fanless cooling with reversed control of elements.

Examples of VPS ovens constructed by hobbyists are also appearing in the last years. Such projects [57–59] are usually built with a small form factor to reduce Galden use, to reuse/recycle the medium, and to solder small hobby projects. Further DIY ovens start from simple constructions (like adding internal or external heaters to Pyrex glass beakers [58]) to the complexity where the oven is in line with commercially available constructions [59].

4.6.6 Batch and in-line ovens

While VPS is often portrayed as an oven technology with offline batch constructions, in-line machines are also available for industrial mass production.

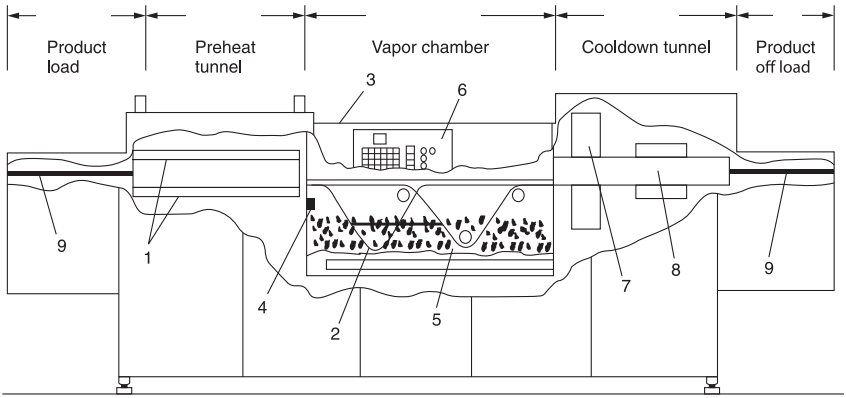

FIGURE 4.16 In-line vapor-phase oven with IR preheating. The oven includes ceramic IR preheaters (1), horizontal board movement (2), observation window (3), vapor tank (4) with saturated vapor (5), control system (6), cooldown and vapor reclaim apparatus (7), tunnel (8), and exit pallet zone (9). *From N.-C. Lee, Reflow Soldering Processes and Troubleshooting, BH Newnes, 2001.*

Such ovens are usually the most expensive ovens in the VPS lineups. They are usually prepared with SMEMA mechanical equipment interface [60] for the conveyor line application. A possible working procedure can be described with the following steps. The PCB assemblies arrive from the conveyor line to a loading bay. The loading bay prepares a collection of PCBs (e.g., six boards). The collected (buffered) batch of PCBs enter an IR/preheat zone and then move to the vapor-phase heating zone, which can have previously presented types of control or even the addition of vacuum. Finally, the batch of boards exit through a cooling area, and in the meanwhile, the collector prepares the next batch for preheating and soldering. One machine can have one or two parallel loading bays, all connected to the conveyor line via SMEMA in order to form a "multiline" system. A possible construction is presented in Fig. 4.16 [61].

The multiline carrier ovens can be interlinked to form a chain of machines in one line, increasing the throughput. Due to a design feature of conveyor management with SMEMA standards, PCB assemblies can bypass an oven while it is busy, to arrive at the second, idle oven. The shortest cycle time with multiline technology can be approximately 20 seconds/board. The disadvantage of the technology is the relatively high cost of the apparatus [53].

4.6.7 Medium extraction and filtration

Medium extraction, recirculation, and filtration is an important step of the process, while any loss of the relatively expensive heat transfer fluid raises the cost of production. Filtration is necessary as well, while small particles,

dust, and flux residues can contaminate the fluid. Smaller VPS ovens require manual drainage of the Galden and manual filtration (with, e.g., filter paper) must be applied on the fluid. More complex commercial ovens suited for mass production are equipped with excess vapor and fluid extraction systems, often suited with filter granule cleaning blocks. It is often communicated that modern machines can recover 99.9% of the fluid during soldering cycles. The process chambers are usually cleaned manually with solvents suited for flux residue removal.

4.7 Quality and reliability concerns in the lead-free era

Joint quality and reliability is an important aspect of every reflow process. Furthermore, the quality and reliability of the VPS soldered packages and the PCB assembly are also under continuous research. Tombstoning, voiding, wicking, and flux spattering were widely investigated in early reports of VPS research. Nowadays the more sophisticated control of machines enables avoiding such challenges; numerous examples can be found in the literature, where optimization is presented with the available toolset.

4.7.1 On the joints and alloys

While early VPS constructions were applied widely due to the unique capabilities of the system, the fast ramps and rapid heating was one of the key features, which ultimately limited the general use of this particular reflow method. With modern ovens and the era of lead-free soldering, quality and reliability of the joints are investigated extensively in the literature, highlighting key features of joints soldered with VPS in contrary to usual methods.

Munroe [62] showed that according to resistance change over time and shear force required to remove specific investigated components (SOIC16), the VPS created tin-lead and lead-free joints showed equivalent performance with the ones soldered in convection reflow. He concluded that VPS could be applied in RoHS compliant assembly processes.

Dumitru et al. [63] found that SAC305 gives overall better results than SN100C in VPS processes. Krammer [64] compared the reliability and the intermetallic layer of SAC305 joints reflowed with IR and heat-level VPS methods. He found that the thickness increment of Cu_6Sn_5 layer is higher for IR and lower for VP after HAST tests (105°C, 100RH%, +0.5 atm overpressure). His investigations concluded that the joints achieved with VPS showed improved shear strength [65] and overall reliability.

Pietriková et al. [66] investigated the nonlinearity of $C-V$ characteristics of different lead-free pastes soldered in VPS on different surface finishes with SAC (96.5Sn3Ag0.5Cu) and SABI (90Sn3.5Ag0.5Bi6In) pastes. They found that the ENIG surface finish was performing better, compared to

HASL, Sn, and Cu finishes. The difference between pastes was insignificant. The team also presented [67] a comparison between convection reflow and VPS with lead-free SAC305 paste, from the aspect of aging and Vickers hardness of joints after damp heat and thermal cycling tests. Ultimately VPS results were found to perform better, both from microstructure and hardness aspects.

Bunea et al. compared laser soldering of low-temperature SnBi pastes with VPS. He found that the control on laser soldering enables more uniform grain structure inside the joint and less voiding [23].

Hurtony et al. [68] investigated spatial microstructure in lead-free joints with SEM (scanning electron microscopy) and EDS (energy dispersive spectroscopy. The research compared the heat-level VPS process with selective laser soldering. They concluded three main points: (1) the existence of Cu_6Sn_5 tubes in conjunction with the thicker and scallop-type Cu_6Sn_5 intermetallic layer at the Cu−Sn interface in the case of VPS; (2) the Ag_3Sn net is finer and the average cell size is smaller as well in the case of selective laser soldering; and (3) the solder joint created with laser soldering contains voids at which the Ag_3Sn phase tends to precipitate. Fig. 4.17 presents SEM images of solder joints created with different techniques.

Krammer et al. [69] investigated the thermomechanical properties and intermetallic layer formation of Bi microalloyed low-Ag content solders formed in VPS, similarly to the work presented in Ref. [68]. They concluded the work with the following findings: "the microalloyed solders have the same or better thermomechanical properties compared to the traditional SAC alloys along with reduced occurrence of large, plate-like Ag_3Sn intermetallic compounds. Therefore, the most prevalent failure mechanism in today's high

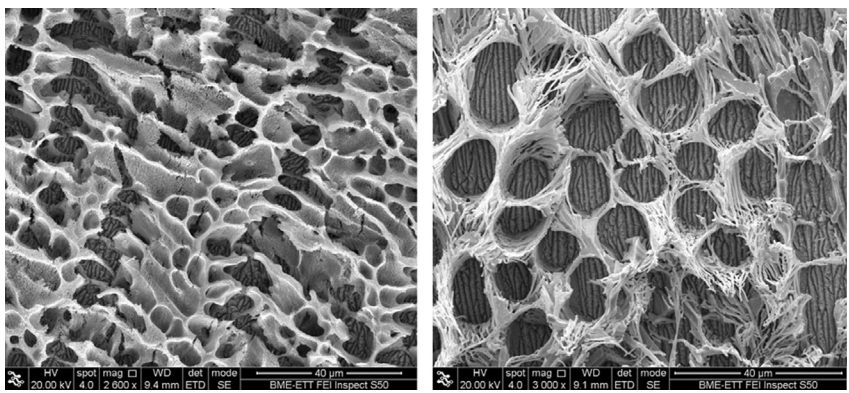

FIGURE 4.17 SEM images of solder joints created with different soldering techniques. Left: CO_2 laser soldering, right: VPS. *From T. Hurtony, A. Bonyár, P. Gordon, G. Harsányi, Investigation of intermetallic compounds (IMCs) in electrochemically stripped solder joints with SEM, Microelectron. Reliab. 52 (2012) 1138−1142.*

integrity packages (e.g., micro BGA—Ball Grid Array), the shrinkage defect can be eliminated."

4.7.2 Tombstones

Tombstones are usually avoided with reducing the slopes around the liquidus temperatures. Modern ovens are capable of presenting preprogrammed anti-tombstone measures around the melting point of the given alloys. Dušek recently investigated the effect of Galden on the mentioned failures, especially on tombstoning [70]. He found that "the use of soldering fluid Galden changes the surface tension equilibrium vectors of the molten solder. The presence of the fluid changed the wetting force of SnPb solder by up to 20%, the change for SAC alloy was up to 10%. This behavior was confirmed at different temperatures (235°C and 245°C) and for both tested soldering fluids Galden LS230 and Galden HS240. The presence of a soldering fluid during VPS is also a very important factor in terms of surface tension (wetting force) and associated issues (wetting properties, tombstoning, voids). The change in the surface tension equilibrium vectors affects the wetting force, which has a crucial impact on, for example, the tombstone effect. This may explain the more frequent incidence of tombstoning in VPS technology."

Plotog et al. [71] found that the axial dimension of the stencil printed paste deposit affects the process more than the axial dimension of a chip-size surface-mounted component, from the aspect of tombstones. His research team also highlighted that due to the intensive heating in VPS, small chip-size components with one pad connected to the larger copper plane, and the other connected to thin trances need attention from the aspect of tombstoning, while the temperature difference between the pads can lead to misalignment [72]. The team also investigated soldering of 0402 components in VPS in search of tombstones. They found that the spacing between the pads and paste type affects tombstoning in VPS significantly. The pad width, pad length, pad shape, home plate, inverted home plate, and standard rectangular stencil aperture design did not affect tombstoning significantly [73].

4.7.3 Voids and void separation in vacuum

Voids are usually kept to minimum levels with vacuum-VPS methodologies. Synkiewicz et al. [54,74] found that the vacuum decreases the number of voids in both lead-free SAC and Pb/Sn solders. She found a significant influence of the suction process on the quality regarding void formation. With the vacuum option, the number voids reduced significantly, however, the thickness of the solder layer and the distance of the SMD component affected the arrangement of voids on the investigated samples. Voiding in SAC decreases by almost four times and in Pb/Sn decreases by more than five times after

the vacuum application. In the case of the vacuum soldering option, larger voids (420 μm) were found in samples soldered with SAC. In Pb/Sn a total elimination of voids bigger than 20 μm was also observed. The use of the vacuum significantly reduced the diameter of voids identified in all solder joints, which is especially important during power electronics assembly. Fig. 4.18 presents the average quantity of solder voids in joints of a soldered thermoelectric generator.

Dziurdzia and Mikolajek [75] and Dziurdzia et al. [76] investigated the efficiency of void reduction with vacuum VPS during the soldering of LED modules and BGAs. Their statistical analysis revealed significant void number and diameter reduction compared to convection reflow.

The void separation efficiency was further investigated [77] with substrates such as FR4, $CaCu_3Ti_4O_{12}$ (CCTO), and ZnO technical ceramics. It was found that the averaged ratio of the void area was statistically decreased when the FR4 board was thicker than 1 mm. The CCTO substrates enabled almost void-free soldering. In the case of ZnO substrates, voiding was not avoided, however, the average void area is three to four times lower than with the cases of the conventional PCB substrates. The explanation is simple: the smaller heat capacity of the FR4 boards compared to ceramic substrates enabled faster cooling during vacuum VPS, thus trapping voids inside the structure of the joints. It must be noted at this point that the methodology of vacuum VPS is susceptible to unwanted energy losses, which might render the proposed soldering profiles unreliable under different thermal masses and different PCB substrates [77]. The achievable quality and reliability in vacuum VPS ovens are often investigated by other power electronics aspects [78]. Skwarek applied vacuum VPS for thermogenerators and power diodes on DBC substrates successfully [79,80]. The team used lead-free SAC305 solder alloy, with 95 kPa vacuum option. It was found that the shear strength

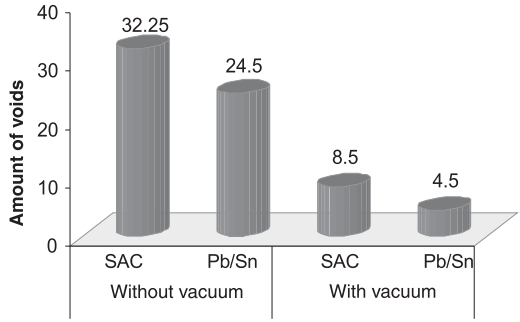

FIGURE 4.18 The average quantity of solder voids in solder joints (SAC and Pb/Sn) of the thermoelectric generator. *From B. Synkiewicz, A. Skwarek, K. Witek, Vapour phase soldering used for quality improvement of semiconductor thermogenerators (TEGs) assembly, Mater. Sci. Semicond. Process. 38 (2015) 346–351[74].*

of the obtained results yielded an overall improvement of 15% with vacuum upon conventional VPS and convection reflow ovens. They used computer tomography [80] and SEM analysis, which showed that the smallest size and amount of voids were found in joints soldered with vacuum VPS. The Au precipitations and intermetallics (Ag_3Sn) were also investigated. Thicker and more coherent IMCs were found with VPS, also more significant Au precipitations were found in the same joints, which results might weaken the mechanical stability of the joints.

Lüngen et al. [81] investigated different vacuum pressure profiles with different pad and aperture designs for SM components ranging from chip-size components to bare die IGBT modules. The application of the vacuum affected the wetting area, the void content, the solder beading, and the height differences of the given SM devices.

Diehm et al. searched for alternative methods to avoid vacuum step in VPS, and they found [82] that with optimized fluxes for optimized wetting of surfaces, the number of voids can be reduced effectively. The reduction can also be achieved with the variation of atmospheric pressure in convection ovens too. Wohlrabe showed that with a batch-based VPS oven the amounts of voids can be reduced compared to convection ovens with SAC305 lead-free pastes mixed with different fluxes [83].

To sum up the topic of voiding, it must be stated that some results from the literature can often be controversial, regarding void formation under different VPS methods; the usual assembly and process parameters (such as the alloy/paste type, thermal pads, aperture shapes on the stencil [84]) must be considered for specifying the voiding problem.

4.7.4 Electrochemical migration, contaminations, flux

Electrochemical migration (ECM) was investigated on boards soldered with VPS [85], where the method did not change the development time of the dendrites, also no significant reliability issue was concluded from the aspect of ECM on VPS soldered test boards.

Veselý et al. [86] suggested that flux spattering issues would be completely inhibited by using VPS, as the layer of inert heat-transfer fluid condensate on the PCB would protect the surface from contamination. It was noted [87,88] that VPS allows better wetting and fluxes with lower activation can be used in a wide range of conditions in vapor-phase ovens.

4.7.5 Popcorning and package stability

The effect of popcorning is a serious issue in reflow technologies. Lee and Earmme [89] noted that during VPS processes, the entire plastic packages of components are exposed to the high temperatures of the Galden vapor. The preabsorbed moisture at the defects in the interface of the leadframe and the

epoxy molding compound (EMC) is vaporized during VPS, and it acts as a pressure loading on the delaminated interface. The package is also subjected to the thermal loading due to the mismatch of the thermal expansion coefficient. Thus, the interface of leadframe and EMC is fully delaminated, and subsequently the delaminated interface (or interface crack) propagates into the inside of EMC, which is usually called the popcorn package crack. Lee analyzed the failure with modeling methods, in terms of the energy release rate, which increased as the resin thickness/leadframe size ratio decreases and the interfacial crack length/leadframe size ratio increases.

Rovensky et al. [90] investigated the stability of nontrimmed thick- and thin-film resistor packages soldered in VPS. They found that the particular heat transfer method has no significant influence on the relative resistance change of the thick- and the thin-film resistors and thus VPS mass reflow based production of electronic devices with embedded resistors should not increase the failure rate.

4.8 Special applications

4.8.1 3D-MID devices

Soldering of 3D-MID (three-dimensional molded interconnect devices) is considered to be an ideal and standard solution for many MID-geometries when uniformity of temperature is a requisite of the assembly process. In addition, reproducibility and simple profiling are important for the sophisticated MID substrates. However, the method itself is not straightforward from technical aspects. If a 3D substrate has borders around the solderable components, the produced condensate cannot flow off. The design should incorporate outlets or cavities for the condensate to flow off. Also, it is important to note that the 3D-MID modules must not be higher than the thickness of the vapor blanket. Also, the thermal mass of the workpiece carriers needs to be taken into account, while it can alter the intended soldering profile. Their shape should be skeletal, without pockets or cavities, so that no condensed medium is carried out of the oven. To sum up reflowing 3D-MID assemblies, the best reliability comes if the substrate is a high-temperature thermoplastic (e.g., LCP) with standard SAC305 solders. If more sensitive polyamides are applied, then 170°C−175°C process temperature is suggested with SnBi58 type pastes [91]. In the range of available PFPE fluids, such temperatures are available not only for general heat transfer processes but also for VPS applications too. Fig. 4.19 presents the usual assembly flow of the 3D-MID devices.

VPS was applied successfully for soldering surface-mounted devices (ASIC, Melf diode, SOT23 transistor, LED, resistance, capacitor) on Laser Direct Structured (LDS) MID devices, with SnAgCu solder. LDS substrates are based on dotted thermoplastics, on where the tracks are realized with

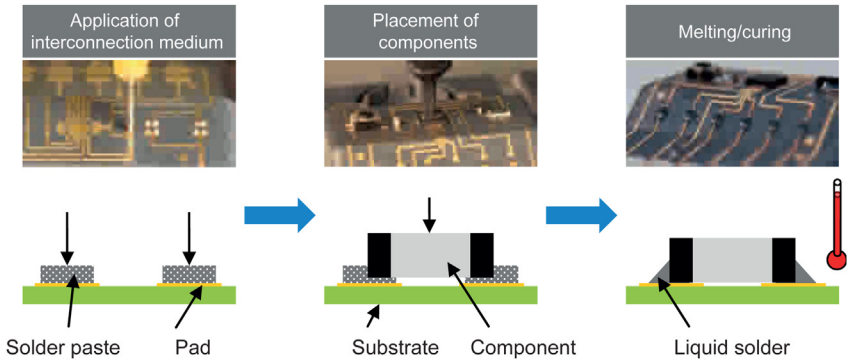

FIGURE 4.19 Process chain of reflow soldering or electrically conductive-adhesive gluing processes with application of the interconnection medium, placement of electronic components, and remelting of the solder or curing of the conductive adhesive, favorably with VPS technology. *From J. Franke, Three-Dimensional Molded Interconnect Devices (3D-MID): Materials, Manufacturing, Assembly and Applications for Injection Molded Circuit Carriers, Hanser Publishing, München, 2014.*

targeted laser activation, and then metalized in a chemical bath. The ultimate product was prepared for automotive application [92]. Later SVP [93] and vacuum VPS methodology was applied for similar LDS enabled 3D-MID constructions [52]. With the lowered pressure, void content and count were reduced, and with prevacuum, the heat gradients were also leveled out. It was found that the prevacuum helped the quicker and more uniform heating of components with large thermal masses. The vacuum also prevents drag-out of heat transfer media in the case of 3D substrates with the geometries enabling pool formation of the condensate.

4.8.2 Flexible circuits

Flexible circuits are widely used in modern electronics, due to their role in miniaturization and 3D-folding capabilities. Flexible circuits, support carriers (pallets) are used with significant modification or skeletal geometry. The retaining of the fluid must be avoided by positioning holes under the circuit, reducing the drag-out effect, similarly to 3D-MID devices [94]. According to the flow of the fluid during VPS, joints/components on flex boards can be susceptible to tombstoning and voiding, but with careful profiling and design, VPS lead-free reflow can be an economical and flexible process for flex circuits [94]. The flex circuits, however, need extra care from the aspect of profiling due to the significantly lower thermal mass or the additional thermal mass of the support. In a recent investigation [95], it was shown that with heat-level VPS soldering, the overall joint quality (from the aspect of shear strength, intermetallic thickness, wetting, and voiding, the latter

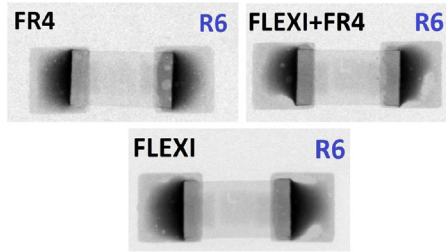

FIGURE 4.20 X-ray analysis of VPS soldered 0603 joints with minor differences in wetting, voiding and alignment on FR4, Flexible and Flexible PCBs supported with FR4 fixture.

presented in Fig. 4.20) on rigid and flex PCBs can be very similar. However, in cases, where no support is used, the same oven settings can lead to different FR4 and flex profiles. In the same work, it was suggested that the copper trace adhesion might suffer a quality loss on flex PCBs during VPS if there is no solder mask applied to the traces.

4.8.3 Biodegradables

It was found that the wide options of heat transfer fluids, and the advanced control methods of VPS, soldering on heat-sensitive biodegradables could be realized.

Bioplastics are either biodegradable or compostable but not biobased; biodegradable or compostable and biobased; nonbiodegradable but biobased. The end of the lifetime of PCB assemblies fabricated on biodegradables result in more eco-friendly waste; however, the technology is not widespread in the industry, mostly basic research is performed in the field [96,97]. The most important parameters of biodegradables from reflow aspect are the low melting point and glass transition temperatures.

It was reported recently that BiSn alloy (138°C melting point—NC-SMQ81; 58Bi/42Sn) is applicable with proper VPS heat control. The solder paste was deposited with manual dispensing, and then the components were mounted with a manual pick and place machine. Galden fluid of 170°C boiling point was applied for reflow. With a controllable sample holder in an experimental oven (applying a LabVIEW SW + HW setup), it was possible to find profiles for adequate heat transfer, joint quality without significant warpage of the boards [96].

Fig. 4.21 presents a biodegradable (cellulose-acetate) PCB assembly with SMD and components soldered in the aforementioned experimental VPS oven. The substrate was devoid of reinforcement fibers, so minor deformations are still observable after optimized VPS reflow. This did not affect the overall functionality of the working prototype circuit.

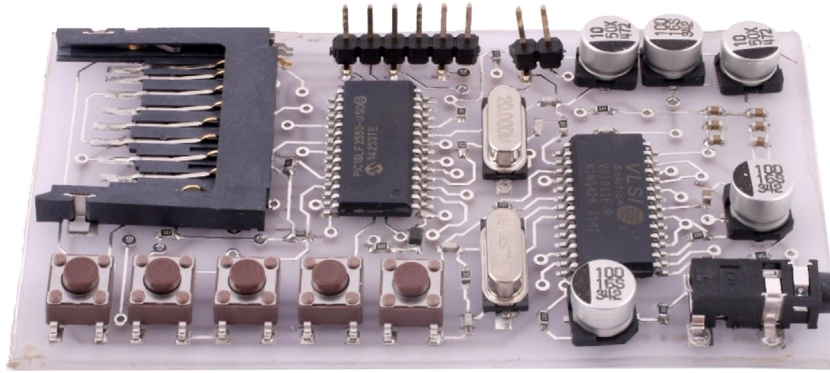

FIGURE 4.21 PCB assembly with SMD components on a biodegradable circuit, soldered with optimized VPS (170°C Galden with sample holder movement).

4.8.4 Curing

Wood [6] reported that with proper heat transfer fluid and VPS apparatus settings, several other technological processes can be, though sometimes, with obvious limitations. The curing of solvent-free solder-masks can be performed with fluids at a boiling point around 160°C in a short time. If the mask contains volatiles, then the evaporation must be calculated before condensation-heating–based curing. Paint curing can be used with low-temperature liquids (~100°C). Flexible PVC item curing is also possible—noting that the heat transfer fluid is chosen accurately to avoid overheating of the PVC compound. The stress relief of electroplated items or plastic laminates with proper boiling temperatures is also possible.

The heat-based curing of adhesives (e.g., adhesives used to fix SMD components to PCBs) can be also performed with condensation heating. Electrical encapsulants with heat requirement for curing can be joined with condensation heating. This is especially relevant in cases where the item and the encapsulant have high thermal mass. Thermally unreliable components and packages can be shocked thermally in condensation heating ovens. With a lower temperature medium, a mixed-joining methodology can also be elaborated; the already soldered SMD or THT components remain intact, and components with the special requirement of adhesive fixing can be joined to the PCB in vapor with lower temperature.

4.8.5 Special components, stacked systems, pin-in-paste

As it was reported by Huang et al. [98], VPS can be used efficiently to solder ceramic column grid array (CCGA) packaging structures, which are

applied in, for example, FPGA technology. With VPS, shadowing effects can be avoided in order to ensure coplanarity of joints in such packages. Vacuum-based VPS can also be applied to such components, enabling void-free soldering. For BGAs, the pumping rate of the vacuum oven needs further empirical information for optimization, while BGAs are reported [98] to suffer under voiding, even when soldered in VPS ovens with vacuum. Vacuum further accelerates IMC growth. Vacuum-enabled VPS was successfully adopted to special diffusion soldering of power electronic applications [99]. Górecki et al. [100] found that the reflow soldering method affects the efficiency of heat dissipation in soldered LED modules. The best properties of soldered LEDs were achieved with vapor-phase technology with the vacuum option.

It is documented that VPS can be optimized for BGA, LGA, CGA, Package on Package, Flip Chip soldering, heat sink, reel, ceramic, and metal-core joining [53]. The soldering of IGBTs, semiconductors, and power modules with baseplate of Direct Bond Copper packaging can be reflowed with VPS peaks of 235°C−240°C, without common CTE mismatch failures [53]. Miniature 3D stacks of PCBs for sensor applications can be efficiently joined with VPS [101]. Soldering of three-dimensional, multilayer PCB "power sandwiches" with components having double-sided surface mount terminations ("X-dim") can also be assembled with VPS. While convection and IR-based ovens cannot achieve reflowing of double-sided component joints, the stacked assemblies can be efficiently soldered with VPS [102].

VPS is an optimal choice for soldering LED modules, either with surface mounting or through-hole mounting with PIP technology [103]. Jánó investigated the PIP solderability of different capacitors in VPS. He [104] noted that aluminum electrolytic capacitors require slow slopes in order to avoid deformation of the casing. Ceramic capacitors require rapid cooling for less significant changes in the parameters during lifecycle. Plastic dielectric capacitors are prone to deformation and failure during PIP soldering, but polypropylene packages can be soldered in VPS with slow cooling rates.

4.8.6 Special substrates

Svasta et al. worked on optimizing reflow soldering on metal-backed PCBs, and glass circuit boards (GCBs). With the optimization of S-VPS profiles, they were able to perform appropriate reflow soldering without serious delamination and further quality issues [105]. Novel SiC (silicone-carbide−based) power modules for automotive applications were successfully soldered with VPS by An et al. [106] highlighted low void content of the resulting joints.

4.8.7 Space technologies

While the method was praised in the early stages of its application, modern VPS with lead-free had to be reconsidered for space technologies. The following points were developed as requirements by the ESA (European Space Agency) [107] for reflowing in a VPS oven:

- VPS ovens shall not transfer movement/vibration into the PCB assemblies, which can result in disturbed solder joints or misalignment.
- The apparatus should be capable to preheat the PCB assembly to a preheat temperature before reflow, recommended by the specific paste manufacturer.
- The reflow fluid should have 12°C excess boiling point temperature above the melting point of the alloy.
- The preselected temperature should be maintained within ±5°C in the reflow part of the soldering profile.
- The extraction system should conform to Facility Cleanliness ECSS-Q-70-08A, subclause 5.1 and Environmental Conditions ECSS-Q-70-08A, subclause 5.2.

4.8.8 Rework

For rework, similar methods are available in the market, from each producer. In VPS, any additional rework/desoldering tool must be added to the work zone of the ovens without perturbing the vapor and the process itself. So the positioning of the desoldering device needs to be performed before lowering the PCB assembly to the vapor. Usually, spring-based devices are used with rocker arms, which are connected to the critical package to be removed. The arm is usually fixed with a plastic pin, which deforms during heating, thus releasing the spring. Finally, the component is lifted from the PCB surface. In order to precisely activate the lifting process, the desoldering apparatus is positioned slightly above the assembly with few millimeter seconds. The delayed arrival of the vapor (in, e.g., heat-level processes) enables the avoiding of premature spring activation. A desoldering tool is presented in Fig. 4.22.

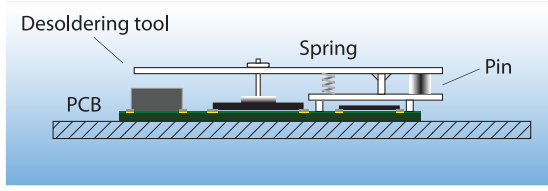

FIGURE 4.22 Rework/desoldering tool for VPS.

4.9 Measurements inside vapor-phase soldering ovens

In VPS ovens the measurement apparatus easily perturbs the heat transfer medium in its vapor form. This chapter presents the most important methods for revealing the state of vapor and the soldering workloads during VPS processes.

4.9.1 Thermocouples

As a basic approach, K-type thermocouples (TC) are used in VPS for profiling reflow temperatures (attached on PCB assemblies in different positions, representing the lowest to the highest thermal masses), or for providing feedback on the state of the oven. The basics are similar to the discussion found in Section 2.9. Liquid and vapor temperatures are usually measured in PFPE fluids and their vapors by K-type thermocouples, immersed either into the vapors or into the liquid at different depths [27]. It is important to note, however, that TC application in the vapor is not entirely straightforward.

The filmwise condensate covers the PCB assembly with a continuous film layer. The heat transfer fluids used in VPS usually bear excellent wetting characteristics on the surfaces of an assembly, resulting in a possible wetting up around the thermocouple wire. The section of the wire end after the welded spot of the thermocouple is covered with the filmwise condensate, which couples additional heat into the measurement spot. Ultimately this can affect the recorded data, misleading the profiling process. The wetting condensate on the TC wires is presented in Fig. 4.23.

The manufacturers [108] suggest that the thermocouples should have as long insulation on the wires as possible and that the bare ends should be covered with SMD adhesives or thermally insulating tape. Avoiding such problems can be further achieved with preparing via on the surfaces (PCB, component) and fixing the welded spot inside. It must be noted that unwanted shorts in bare wire ends might cause faulty readouts too. It was found that for VPS it is recommended to use high-temperature solder and alu-tape for fixing TC with proper repeatability [109]. It is also possible to use heat-resistant polyimide tape and SMD adhesives, but with reduced precision. It must be noted that tape-based fixing is susceptible to detachment due to the underflow effect of Galden. If channels and bubbles are left under

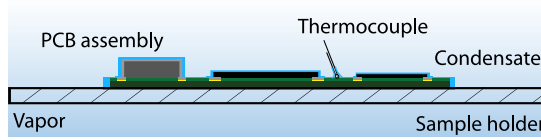

FIGURE 4.23 The filmwise condensate wets up the end of the thermocouple on the PCB assembly.

the tape, the heat transfer fluid can flow under the fixing, resulting in false readings and at times total detachment of the thermocouples.

The industry can use different thermocouple constructions for profiling. The range is wide from ultrathin wires (0.08 mm conductor, 0.2 mm overall) to thick PFA-insulated thermocouples suited to be used in wet and damp environments (□0.5 mm conductor, 1 mm overall). It must be noted that the different thickness can result in different unwanted alterations in the reflow profile. The differences in thickness mean different thermal masses, with two possible orders of difference in the energy to heat up, for example, 1 m wire inside the vapor zone. Thicker thermocouples with more robust insulation are less susceptible for heat coupling effect described above, due to their larger thermal mass and insulation properties. On the other hand, they are more difficult to handle and their thermal mass can alter the soldering profile inside the working zone of, for example, a heat-level VPS oven (due to vapor loss by additional condensation). Thinner thermocouples might be heated up faster than intended, but they are also handled easier, and at the same time their perturbing effect is insignificant on the vapor.

As the thermal mass of the wires alone can alter the process of temperature profiling and programming of the VPS oven, this effect must be taken into account during solder profile preparations. While manufacturers often suggest fixing with the wire lead-out vertically (Fig. 4.23) from the measurement point in an immediate manner (to avoid heat radiated from the components and PCB surface in the vicinity), this usually results in semicontrolled wire arrangement in the work zone. To reduce the perturbing of the vapor, the excess wire length must be arranged in a controlled manner around the level of the PCB holder (as seen in Fig. 4.24). These two effects must be in balance for the most precise profile settings.

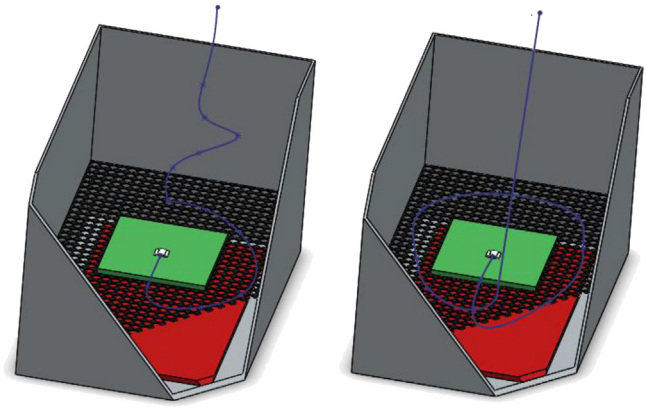

FIGURE 4.24 Partially organized (left) and organized (right) TC wires in the work zone of a VPS oven.

Thermal profiler devices are used for investigating process temperatures in VPS, similarly to other reflow methodologies. Radio-controlled dataloggers (with 2.4 GHz wireless communication) can be positioned in high-temperature seal with Teflon coating, where the cover is O-ring sealed to protect the device. Some of these devices are suited to be set to directly control the commercially available ovens and vacuum machines. Commercial solutions might include a specific workpiece carrier with sensor integration, antennas in the process and cooling zones, and connected antennas in both chambers. Further examples from the literature also provide a good understanding on the topic of sensor-based measurements.

Livovsky applied TC measurement for real-time feedback in their experimental VPS oven [110]. Their system incorporated a 19-bit AD converter for accepting K-, J-, N-, T-, E-, B-, R-, and S-type thermocouples. Their setup eventually used K-type TCs. This temperature value is then used in smart management of temperature inside the VPS chamber. The sensor feedback enables the setting of the height of samples, the speed of vertical movement, according to the sample size and the height level of the working fluid. For the control, PID control was implemented in a proprietary ARM processor-based system. Their temperature sensor-based feedback enables a precision with only $\pm 2°C$ deviation on the predetermined profile, even for special power electronic components and DBC substrates. The thermocouple system is shown in Fig. 4.25.

Platinum resistance thermometers can also be used to reveal changes in the vapor. A sensor ladder is presented in Ref. [55], which uses Pt500 sensors along with the height level of the vapor. The considerable thermal mass

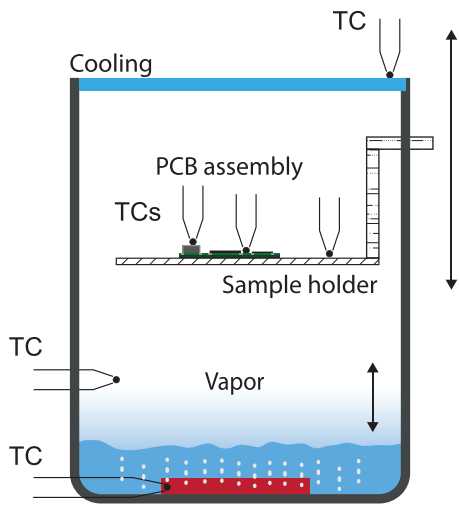

FIGURE 4.25 Thermocouple feedback on multiple points of the oven and the assembly.

of the sensor elements and the mechanical sensitivity of such components need attention during work zone profiling.

4.9.2 Height detection with special sensors

During the years, many sensor technologies become accessible and cheap, resulting in creative solutions to detect the height of the vapor. While temperature detection with thermocouples is a reliable and tested method in reflow soldering, the thermal mass of the sensor element, the resulting response times, and the fact that temperature is not necessarily in correlation with local vapor concentration can alter the intention of the operator or the process engineer. Therefore, it was necessary to improve the detection of the vapor blanket inside ovens. Fig. 4.26 presents novel ideas for vapor height detection in VPS ovens.

With dipping control, an optical probe can be applied to reveal the actual state (propagation) of vapor blanked during its development. The two confronting optical fibers serve as a probe. One end is connected to a LED, the other end is interfaced to a photodiode. The output then can be investigated with proper DAQ system. The thermal capacity of the probe is negligible, and despite condensation on the ends of the fibers, the probe is able to detect the state of saturated vapor, also verifying the top boundary of the vapor, in the same time verifying the effect of upper cooling inside the work zone [55].

The state of the vapor can be constantly monitored with pressure measurements. Cheap and sensitive pressure sensors (vapor sniffers) enabled the use of this monitoring technology in prototype ovens. The end of a heat-resistant probe tube is immersed to a fixed height above the boiling fluid.

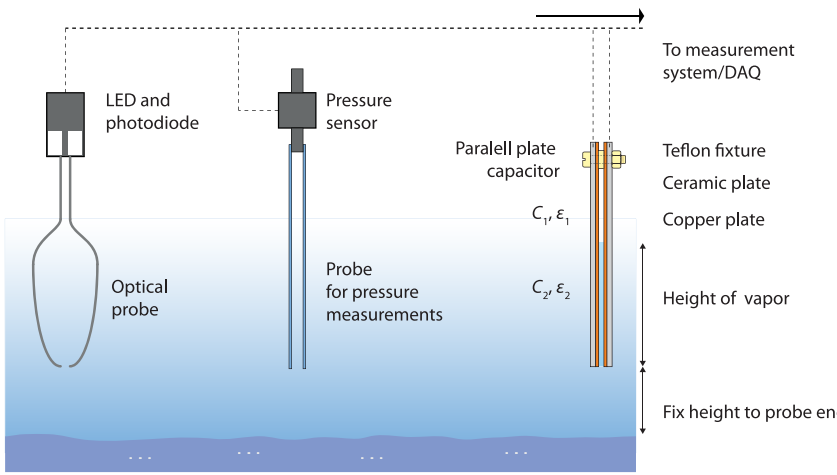

FIGURE 4.26 Detection of vapor height with optical probe (left), pressure sensor and probe (center), and parallel plate capacitor (right).

The measured hydrostatic pressure of the developed vapor changes with the vapor blanket height increase. This effect can be recorded with sensitive gage-type pressure sensors. As an addition, the dynamics of vapor development can be investigated with dynamic flow sensors. With sub-Pascal resolution, the pressure sensors are able to detect the height with subcentimeter precision, can be used to optimize heating power, and evaluate pressure drop (vapor collapse) when immersing PCB assemblies [111]. It was found that temperature measurements can be extended (fused) with pressure measurement to properly define the state of saturated vapor height inside the oven—temperature sensors can read very close values to boiling point temperatures, while the actual state of saturation is not fulfilled [111].

Livovsky presented a high-temperature plate capacitor for height monitoring [112]. The change of dielectric properties within the two plates of the capacitor change as the saturated vapor condenses between the plates. The change of capacity is characteristic in the given oven and can be measured for different widely used Galden types (e.g., LS200, LS230, HS260). The capacity change can be used to fine-tune the heater's control via a PID controller.

References

[1] R.C. Pfahl, H.H. Ammann, Method for Soldering, Fusing or Brazing, US Patent 3,866,307, February 18, 1975.

[2] G. Caswell, Vapour phase soldering of SMDs—reliability characteristics, Circuit World 11 (4) (1985) 17–27.

[3] R.P. Anjard, Solder pastes for microelectronics, Microelectron. J. 15 (2) (1984) 53–64.

[4] E.R. Wood, Soldering and fusing by condensation heat transfer, Circuit World 6 (3) (1980) 34–36.

[5] K. Feldmann, M. Gerhard, Direct soldering of electronic components on molded devices, CIRP Ann. 44 (1) (1995) 19–22.

[6] R. Wood, A new phase for vapour-phase—an overview of the current status of vapour phase technology for soldering and related applications, Circuit World 30 (3) (2004) 21–25.

[7] M. Branzei, M. Vladescu, I. Plotog, T. Cucu, Comparative shear tests of two low melting point solder pastes relating to their thermal diffusivity, in: IEEE 40th International Spring Seminar on Electronics Technology, 2017.

[8] I. Plotog, G. Varzaru, C. Turcu, T.C. Cucu, P. Svasta, N.D. Codreanu, VPS solution for lead-free soldering in EMS industries, in: IEEE 2nd Electronics System-Integration Technology Conference, 2008, pp. 121–124.

[9] A.E. Wittmann, Method of Coating Circuit Paths on Printed Circuit Boards with Solder, US Patent 3,359,132, 1967.

[10] G.M. Wenger, R.L. Mahajan, Die Technology des "Löten in der Dampfphase", Fluorinert - Nachrichten 3/1981, 1981.

[11] G.M. Wenger, Evaluation and characterisation of condensation soldering fluids without sophisticated analytical equipment, in: Proceedings of the Technical Program, NEPCON WEST '87, Anaheim, CA, 1987, pp. 135–150.

[12] H. Leicht, A. Thumm, Today's vapor phase soldering—an optimized reflow technology for lead-free soldering, in: SMTAI Conference Proceedings, August 17–21, 2008, Orlando, 2008.
[13] C.R. Sargent, Industrial scale production, properties and applications of perfluorocarbon liquids, J. Fluorine Chem. 35 (1) (1987) 201.
[14] J. Sprovieri, Getting the Vapors, Electronics Assembly, BNP Media, 2012.
[15] C. Lal, M.V. Shah, S.C. Bawa, Fabrication techniques for space electronics, IETE Tech. Rev. 10 (5) (1993) 489–493.
[16] W. Rubin, *Electron. Prod.* 13 (August 1983) Microelectron. Reliab. 24(3) 1984, p. 595.
[17] D.J. Spigarelli, Vapor phase solder reflow for hybrid circuit manufacturing, Solid State Technol. 50 (1976).
[18] H.J. Krokoszinski, H. Oetzmann, H. Gernoth, C. Schmidt, An inorganic-organic passivation double layer for thin-film circuits, Thin Solid Films 135 (1) (1986) 1–8.
[19] J.K. Hagge, Critical component requirements for vapor phase soldering leadless components on circuit board assemblies for military electronics, IEEE Trans. Compon. Hybrids Manuf. Technol. 6 (4) (1983) 443.
[20] J. Ruffing, Vapor phase soldering basics, Electron. Manuf. 34 (7) (1988) 20–21.
[21] J. Lipp, High-Quality Reflow Soldering With Vapor Phase, The New Approach of Vapor Phase Technology, Arizona Sonora SMTA Arizona Expo, 2012.
[22] C. Lea, Heat transfer fluids for vapour phase soldering—an appraisal, Solder. Surf. Mt. Technol. 1 (1989) 23–32.
[23] R. Bunea, P. Svasta, Zs. Illyefalvi-Vitéz, R. Bátorfi Réka, A. Géczy, Optimizing laser soldering of SMD components: from theory to practice, in: 17th International Symposium for Design and Technology of Electronics Packages, 2011, pp. 55–58.
[24] T.J. Wallington, M.D. Hurley, O.J. Nielsen, The radiative efficiency of $HCF_2OCF_2OCF_2CF_2OCF_2H$ (H-Galden 1040x), Atmos. Environ. 43 (27) (2009) 4247–4249.
[25] H. Matsuda, Y. Hirota, K. Kurihara, K. Tochigi, K. Ochi, Liquid–liquid equilibria containing fluorous solvents as environmentally benign solvent, Fluid Phase Equilib. 357 (2013) 71–75.
[26] W. Leider, Dampfphasenlöten – Grundlagen und praktische Anwendung, Eugen G. Leuze Verlag, Bad Saulgau, Germany, 2002.
[27] G. Guglielmini, M. Misale, C. Schenone, Experiments on pool boiling of a dielectric fluid on extended surfaces, Int. Commun. Heat Mass Transf. 23 (4) (1996) 451–462.
[28] L. Dai, N. Satyanarayana, S.K. Sinha, V.B.C. Tan, Analysis of PFPE lubricating film in NEMS application via molecular dynamics simulation, Tribol. Int. 60 (2013) 53–57.
[29] M. Avataneo, W. Navarrini, U. De Patto, G. Marchionni, Novel perfluoropolyethers containing 2,2,4-trifluoro-5-trifluoromethoxy-1,3-dioxole blocks: synthesis and characterization, J. Fluorine Chem. 130 (2009) 933–937.
[30] Solvay, Galden LS/HS, Vapor Phase Soldering Fluids, Specialty Polymers, Datasheet, 2015.
[31] Y.A. Çengel, A.J. Ghajar, Heat and Mass Transfer, fifth ed., McGraw-Hill, New York, 2015.
[32] A. Géczy, B. Illés, Zs Illyefalvi-Vitéz, Modeling method of heat transfer during vapour phase soldering based on filmwise condensation theory, Int. J. Heat Mass Transf. 67 (2013) 1145–1150.
[33] A. Bejan, Film condensation on an upward facing plate with free edges, Int. J. Heat Mass Transf. 34 (1991) 582–587.

[34] W.M. Rohsenow, Heat transfer and temperature distribution in laminar film condensation, Trans. ASME 78 (1956) 1645–1648.
[35] T.B. Drew, (personal communication), in: W.H. McAdams (Ed.), Heat Transmission, third ed., McGraw-Hill, New York, 1954, p. 330.
[36] J. Gerstmann, P. Griffith, Laminar film condensation on the underside of horizontal and inclined surfaces, Int. J. Heat Mass Transf. 10 (1967) 541–569.
[37] A. Géczy, B. Illés, T. Darnai, Investigating condensation heat transfer during vapour phase soldering on round-shaped PCB plates, Int. J. Heat Mass Transf. 86 (2015) 639–647.
[38] J.S. Chiou, T.B. Chang, Laminar film condensation on a horizontal disk, Heat Mass Transf. 29 (1994) 141–144.
[39] A. Géczy, Investigating heat transfer coefficient differences on printed circuit boards during vapour phase reflow soldering, Int. J. Heat Mass Transf. 109 (2017) 167–174.
[40] A. Geczy, D. Nagy, B. Illes, L. Fazekas, O. Krammer, D. Busek, Studying heat transfer on inclined printed circuit boards during vapour phase soldering, Solder. Surf. Mt. Technol. 29 (1) (2017) 34–41.
[41] N. Heilmann, A comparison of vapor phase, infrared and hot gas soldering, in: Fourth IEEE/CHMT European International Electronic Manufacturing Technology Symposium, 1988.
[42] R.J.K. Wassink, J.A.H. van Gerven, Displacement of components and solder during reflow soldering, Solder. Surf. Mt. Technol. 1 (1) (1989) 5–11.
[43] C. Zabel, M. Zöller, Vapor Phase Soldering Technology—Secure Lead-Free Processes, Asscon, VP2000-2-2/9, 2007.
[44] R. Strauss, SMT Soldering Handbook, second ed., BH Newnes, Oxford, UK, 1998.
[45] P.E. Tegehall, B.D. Dunn, Impact of Cracking Beneath Solder Pads in Printed Board Laminate on Reliability of Solder Joints to Ceramic Ball Grid Array Packages (ESA STM-267), 2003.
[46] A. Duck, C. Zabel, Vapour phase reflow—profiling for lead-free alloys, in: SMTA Proceedings of International Conference on Soldering and Reliability, Toronto, Ontario, 2010.
[47] Imdes Mini Condens-IT Profiler, Preliminary Owner's Manual, Version 2.0, 2019.
[48] R. Mora, Vapor phase making strong comeback, US-Tech.com, 2019 (accessed 13.12.2019).
[49] Zs Péter, A. Géczy, D. Rigler, M. Ruszinkó, Zs Illyefalvi-Vitéz, Evaluation of solder joints formed by different vapour phase soldering systems, Proceedings of the 36th International Spring Seminar on Electronics Technology (2013) 167–171.
[50] C. Zabel, J.B. Byers, Void-free soldering with a new vapor-phase with vacuum technology, in: Asscon/SMTA Proceedings, 2013.
[51] B. Illés, A. Skwarek, A. Géczy, O. Krammer, D. Bušek, Numerical modelling of the heat and mass transport processes in a vacuum vapour phase soldering system, Int. J. Heat Mass Transf. 114 (2017) 613–620.
[52] P. Wild, H. Oettl, Vacuum improves 3-D vapor-phase soldering process, EDN Network, 2015.
[53] IBL Löttechnik GmbH, The benefits of vapour phase reflow soldering, Company-, Process- and Product-Presentation, 2017.
[54] B.K. Synkiewicz, A. Skwarek, K. Witek, Voids investigation in solder joints performed with vapour phase soldering (VPS), Solder. Surf. Mt. Technol. 26 (1) (2014) 8–11.
[55] A. Géczy, Zs Illyefalvi-Vitéz, P. Szőke, Investigations on vapor phase soldering process in an experimental soldering station, Micro Nanosyst. 2 (2010) 170–177.

[56] D.M. Lam, M. Novak, I. Uhlir, Vapour soldering system with Peltier heater, in: IEEE Applied Electronics, IEEE, 2009.
[57] A. Lukats, Christian, "vapsy"—a tiny vapor phase reflow oven, hackaday.io, Project 7495, 2015.
[58] M. Szczys, Vapor Phase Reflow Soldering, Hackaday.com, 2010.
[59] R. Sulyok, Vapor Phase Soldering Machine (Handiwork), Youtube.com, 2016.
[60] SMEMA, Mechanical Equipment Interface Standard, 1.2, Surface Mount Equipment Manufacturers Association.
[61] N.-C. Lee, Reflow Soldering Processes and Troubleshooting, BH Newnes, Boston, US, 2001.
[62] C. Munroe, Vapor phase vs. convection reflow in RoHS compliant assembly, in: SMTA International Conference, Orlando, 2008.
[63] G.I. Dumitru, A. Tudor. G. Chisiu, I. Plotog, Mechanical characteristics of electronic printed circuit obtained by the vapour phase soldering process, Appl. Mech. Mater. 658 (2014) 71−76.
[64] O. Krammer, Comparing the reliability and intermetallic layer of solder joints prepared with infrared and vapour phase soldering, Solder. Surf. Mt. Technol. 26 (4) (2014) 214−222.
[65] T. Novak, F. Steiner, Influence of intermetallic compounds growth on properties of lead-free solder joints, IEEE 35th International Spring Seminar on Electronics Technology (2012) 213−217.
[66] A. Pietriková, J. Banksy, J. Durisin, Measurement of nonlinearity of lead-free vapour phase reflowed solder joints, Acta Electrotech. Inform. 3 (7) (2007) 1−4.
[67] A. Pietriková, J. Ďurišin, M. Bazu, V. Ilian, Influence of different methods of ageing on microstructure of solder joints, 37th International Spring Seminar on Electronics Technology (2014) 202−206.
[68] T. Hurtony, A. Bonyár, P. Gordon, G. Harsányi, Investigation of intermetallic compounds (IMCs) in electrochemically stripped solder joints with SEM, Microelectron. Reliab. 52 (2012) 1138−1142.
[69] O. Krammer, T. Garami, B. Horváth, T. Hurtony, B. Medgyes, L. Jakab, Investigating the thermomechanical properties and intermetallic layer formation of Bi micro-alloyed low-Ag content solders, J. Alloys Compd. 634 (2015) 156−162.
[70] K. Dušek, D. Bušek, M. Plaček, A. Géczy, O. Krammer, B. Illés, Influence of vapor phase soldering fluid Galden on wetting forces (tombstone effect), J. Mater. Process. Technol. 251 (2018) 20−25.
[71] I. Plotog, G. Varzaru, C. Turcu, T.C. Cucu, N.D. Codreanu. DFM Solutions for Tombstoning in Vapour Phase Soldering Technology, Research Project CEEX-X2C09, UCP AMTRANS, 2007.
[72] I. Plotog, G. Varzaru, R. Bunea, I. Busu, T. Cucu, P. Svasta, Investigation on the efficiency of thermal relief shapes on different printed circuit boards, IEEE 16th International Symposium for Design and Technology in Electronic Packaging (2010) 289−290.
[73] M. Pantazică, C. Marghescu, C. Tămaş, H. Wohlrabe, K.J. Wolter, P. Svasta, Evaluation of the effects of the layout design on the quality of surface mount boards, IEEE 36th International Spring Seminar on Electronics Technology (2013) 140−145.
[74] B. Synkiewicz, A. Skwarek, K. Witek, Vapour phase soldering used for quality improvement of semiconductor thermogenerators (TEGs) assembly, Mater. Sci. Semicond. Process. 38 (2015) 346−351.
[75] B. Dziurdzia, J. Mikolajek, X-ray inspection and Six-Sigma in analysis of LED thermal pad coverage, Solder. Surf. Mt. Technol. 29 (1) (2017) 28−33.

[76] B. Dziurdzia, M. Sobolewski, J. Mikolajek, Convection vs vapour phase reflow in LED and BGA assembly, Solder. Surf. Mt. Technol. 30 (2) (2018) 87–99.
[77] B. Illes, A. Skwarek, A. Geczy, D. Szwagierczak, K. Witek, Void separation efficiency of vacuum VPS technology on FR4 and LTCC substrates, in: 2017 IEEE 23rd International Symposium for Design and Technology in Electronic Packaging (SIITME), 2017, pp. 68–72.
[78] T. Stockmeier, Y. Manz, J. Steger, Novel high power semiconductor module for trench IGBTs, in: Proceedings of 2004 International Symposium on Power Semiconductor Devices & ICs, Kitakyushu, 2004, pp. 343–346.
[79] A. Skwarek, B. Synkiewicz, J. Kulawik, P. Guzdek, K. Witek, J. Tarasiuk, High-temperature thermogenerators made on DBC substrate using vapour phase soldering, Solder. Surf. Mt. Technol. 27 (3) (2015) 125–128.
[80] A. Skwarek, B. Illes, B. Synkiewicz, S. Wronksy, J. Tarasiuk, K. Witek, Characterization of solder joints made with VPS on DBC substrate, J. Mater. Sci.: Mater. Electron. 28 (2017) 1769–1776.
[81] S. Lüngen, A. Klemm, H. Wohlrabe, Evaluation of the quality of SMDs according to vacuum vapour phase soldering, IEEE 38th International Spring Seminar on Electronics Technology (2015) 218–222.
[82] R. Diehm, M. Nowottnick, U. Pape, Reduction of voids in solder joints an alternative to vacuum soldering, in: IPC APEX EXPO Proceedings, 2012.
[83] H. Wohlrabe, M. Pantazica, Correlations between process, material and quality characteristics and the reliability of solder joints, in: IEEE Electronics System Integration Conference, 2014.
[84] R. Batorfi, M. Ruszinko, Examination of voiding at the drain pad of high-power FETs, in: IEEE 20th International Symposium for Design and Technology in Electronic Packaging (SIITME), 2014, pp. 41–44.
[85] B. Illés, B. Medgyes, A. Horváth, Electrochemical migration behaviour of surface finishes after vapour phase reflow soldering, in: 2014 IEEE 20th International Symposium for Design and Technology in Electronic Packaging (SIITME), 2014, pp. 253–257.
[86] P. Veselý, D. Bušek, O. Krammer, K. Dušek, Analysis of no-clean flux spatter during the soldering process, J. Mater. Process. Technol. 275 (2020) 116289.
[87] E. Guené, A.-M. Laügt, C. Puechagut, A. Docoulombier, Vapor phase and convection reflow: comparison of solder paste residue chemical reliability, in: SMTA International Conference Proceedings, 2011.
[88] E. Guené, A. Docoulombier, Reliability study of no clean chemistries for lead-free solder paste in vapour phase reflow, in: 2016 IEEE 18th Electronics Packaging Technology Conference (EPTC), 2016, pp. 157–164.
[89] K.W. Lee, Y.Y. Earmme, Effect of geometric parameters on popcorn cracking in plastic packages during VPS process, Finite Elem. Anal. Des. 30 (1998) 81–96.
[90] T. Rovensky, A. Pietrikova, I. Vehec, L. Livovsky, Stability of miniaturized non-trimmed thick- and thin-film resistors, Microelectron. Reliab. 84 (2018) 88–94.
[91] J. Franke, Three-Dimensional Molded Interconnect Devices (3D-MID): Materials, Manufacturing, Assembly and Applications for Injection Molded Circuit Carriers, Hanser Publishing, München, 2014.
[92] N. Heininger, D. Ahrendt, W. Eberhardt, H. Kück, L. Blassmann, C. Hanisch, et al., Laser-based Production of Multifunction Packages taking Innovative Rotary Encoders for Automation and Automotive Technology as Examples, Project: IMDAKT, 2005.
[93] A. Brose, T. Leneke, S. Hirsch, B. Schmidt, Aerosol deposition of catalytic ink to fabricate fine pitch metallizations for moulded interconnect devices (MID), in: IEEE 3rd Electronics System Integration Technology Conference ESTC, 2010.

[94] J. Fjelstad, Flexible Circuit Technology, fourth ed., BR Publishing, Inc., Seaside, OR, 2011.
[95] A. Géczy, R. Bátorfi, G. Széles, Á. Luhály, M. Ruszinkó, R. Berényi, Vapour phase soldering on flexible printed circuit boards, in: 2014 IEEE 20th International Symposium for Design and Technology in Electronic Packaging (SIITME), 2014, pp. 1–6.
[96] B. Kovács, A. Géczy, G. Horváth, I. Hajdu, L. Gál, Advances in producing functional circuits on biodegradable PCBs, Period. Polytech. Electr. Eng. Comput. Sci. 60 (4) (2016) 223–231.
[97] C. Henning, A. Schmid, S. Hecht, K. Harre, R. Bauer, Applicability of different bio-based polymers for wiring boards, Period. Polytech. Electr. Eng. Comput. Sci. 63 (1) (2019) 1–8.
[98] L. Huang, Z. Zhu, H. Wu, X. Long, Board-level vapor phase soldering (VPS) with different temperature and vacuum conditions, Multidiscip. Model. Mater. Struct. 15(2) (2019) 353–364.
[99] J. Storgies, K. Wilke, Universal high-temperature suitable joint adapting diffusion soldering, in: IEEE Electronics System-Integration Conference, 2014.
[100] K. Górecki, B. Dziurdzia, P. Ptak, The influence of a soldering manner on thermal properties of LED modules, Solder. Surf. Mt. Technol. 30 (2) (2018) 81–86.
[101] K.D. Lang, V. Grosser, K.A. Jam, J. Wolf, P. Semionyk, S. Schmitz, et al., Industrially compatible PCB stacking technology for miniaturized sensor systems, in: IEEE Electronics Packaging Technology Conference, 2005, pp. 13–18.
[102] I. Josifović, J. Popović-Gerber, J.A. Ferreira, New power electronics components concept for automated manufacturing, in: IEEE 13th European Conference on Power Electronics and Applications, 2009.
[103] I. Plotog, G. Varzaru, C. Turcu, T.C. Cucu, P. Svasta, A. Vasile, Pin-in-paste DFM constraints in vapor phase soldering technology for optoelectronic components, in: Proceedings of SPIE—The International Society for Optical Engineering, 2009.
[104] R. Jánó, D. Pitică, P. Svasta, G. Văzaru, Effects of reflow soldering methods on the lifetime of capacitors, IEEE 35th International Spring Seminar on Electronics Technology (2013) 183–188.
[105] P.M. Svasta, I. Plotog, N.D. Codreanu, A. Vasile, G. Varzaru, A. Marin, Printed circuit boards with different material core assembling quality analysis based on 4 P soldering model, in: 2009 32nd International Spring Seminar on Electronics Technology, 2009.
[106] B.N. An, V. Wegelin, M. Bernd, B. Leyrer, M. Meisser, H. Demattio, et al., A highly integrated full SiC six-pack power module for automotive applications, in: PCIM Europe 2016, Germany, 2016, pp. 1979–1986.
[107] Space product assurance, High-reliability soldering for surface-mount and mixed technology, ECSS Secretariat, ESA-ESTEC, Requirements & Standards Division, Noordwijk, The Netherlands, ECSS-Q-70-38A, 2007.
[108] Asscon, Operation Instructions, Quicky 450-2 04.2009. 23–24.
[109] A. Géczy, B. Kvanduk, B. Illes, G. Harsányi, Comparative study on proper thermocouple attachment for vapour phase soldering profiling, Solder. Surf. Mt. Technol. 28 (1) (2016) 7–12.
[110] L. Livovsky, A. Pietrikova, Real-time profiling of reflow process in VPS chamber, Solder. Surf. Mt. Technol. 29 (1) (2017) 42–48.
[111] M.A. Alaya, A. Geczy, B. Illes, D. Busek, G. Harsanyi, Advances in pressure sensing for vapour phase soldering process monitoring, Solder. Surf. Mt. Technol. 31 (3) (2019) 169–175.
[112] L. Livovsky, A. Pietrikova, Measurement and regulation of saturated vapour height level in VPS chamber, Solder. Surf. Mt. Technol. 31 (3) (2019) 157–162.

Chapter 5

Special reflow techniques

5.1 Die-attach technologies

5.1.1 First-level interconnections

In the case of integrated circuit (e.g., BGA or QFP packages—see Section 1.1.2) packages, the first-level electrical interconnection (inside the package—between the semiconductor chip and the leadframe or interposer) can be formed traditionally by three techniques: wire-bonding, tape-automated bonding (TAB), and by flip-chip technique (Fig. 5.1) [1].

The mechanical and electrical connections between the semiconductor chip and the leadframe are separated from each other in wire-bonding and TAB technologies. This makes these technologies more reliable than flip-chip technologies where both the mechanical and electrical connections are established by small (solder) bumps. The mechanical connection (die-attach) in wire bonding and TAB is usually prepared by using adhesives or by special reflow technologies. The electrical connection is established then in wire bonding by ultrasonic or thermocompression bonding [2]. In TAB technologies, the electrical connection is formed by bonding copper ribbon wires utilizing thermocompression onto the gold bumps of the chip, after the leads are soldered to the pads on the substrate. In these technologies, the end product is usually a packaged chip in the form of a packed integrated circuit, for example, surface mount technology/reflow soldering (see Chapter 1, Introduction to Surface-Mount Technology).

In power electronics, an additional substrate technology appears, the so-called direct copper bonding (DCB). The semiconductor chips are attached by die-attach techniques onto these substrates also (Fig. 5.2). The DCB substrate is prepared by laminating Cu foil (thickness can range from 100 to 1000 μm) directly onto the surface of oxide ceramics, like alumina (Al_2O_3) or BeO, without a joint layer. In the DCB, the copper oxide forms eutectic melt with the ceramics material (e.g., copper-aluminate) at a given temperature and oxygen concentration, and this eutectic melt wets the surface of the ceramic, providing excellent adhesion between them.

The layout of the copper layer (traces and contact surfaces) can be formed in two ways. Former technologies utilized the layout formation separately by laser cutting; then the formed layer was laminated onto the ceramic

Reflow Soldering. DOI: https://doi.org/10.1016/B978-0-12-818505-6.00005-4

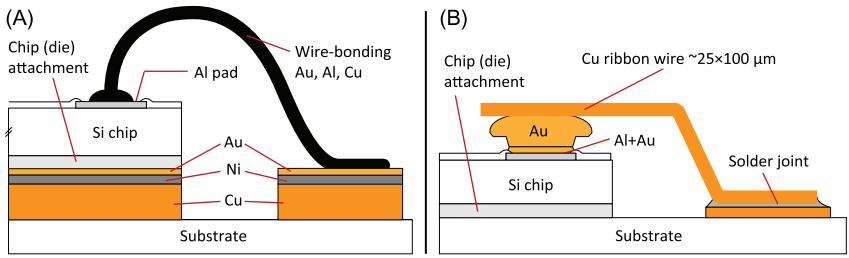

FIGURE 5.1 First-level interconnection technologies: (A) wire-bonding technology; (B) tape-automated technology. *Reproduced with permission from G. Harsányi, Elektronikai Technológia és Anyagismeret, University Lecture Notes, BME-ETT, 2019, ISBN: 978-963-421-791-6.*

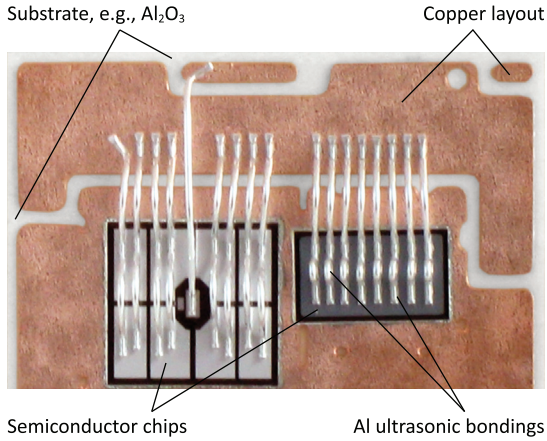

FIGURE 5.2 Direct copper bonding substrate.

substrate at 1065°C. Recently, the full layer of copper is laminated onto the ceramic substrate, and the layout is formed then by photolithography. The latter provides a better resolution and quality of layout formation. DCB substrates provide excellent thermal conductivity, along with low thermal expansion and decent wire bondability.

The semiconductor chips on DCB substrates are quite often diodes or, for example, insulated-gate bipolar transistor (IGBT) modules for inverters in electric vehicles. In a given inverter module, some separated DCB substrates (e.g., 4−8) are placed and soldered together onto a base plate (covered by Ni layer) for attaching them to a heat sink. Further application and installation examples are wind power generators, solar power generators, electric vehicle (EV), hybrid electric vehicle (HEV), railways, ships, power LED, and solid-state relay (SSR).

The primary difficulty in the assembly of DCB substrate is the ability of copper to oxidize heavily. For successful wire bonding to occur, oxidation of

the Cu bond pad surface must be carefully controlled. The adverse effects of surface contamination can be reduced by the use of a plasma clean step immediately prior to wire bonding. Two types of plasma cleaning exist: direct and indirect methods. Indirect plasma cleaning methods involve the use of an active plasma species such as O_2 to chemically combine and remove organic contamination present on bond pad surfaces. In no instance should an indirect O_2-plasma process be used for DCB substrates. Any contaminant present on the pad will not be removed, but heavily oxidized, which will further reduce bondability. The preferred method for plasma cleaning is direct plasma cleaning or sputtering at these substrates. This method uses a highly energetic plasma species such as Ar to physically bombard the metallic contaminants, which then causes them to dislodge from the bond pad surface. One drawback to this method is that the metallic contaminants have the potential to be redeposited if they are all not removed through the plasma system's exhaust. Therefore, to prevent excessive metallic removal and redeposition, care should be taken not to use too long of a cleaning time [2].

5.1.2 Die-attach techniques

For the die-attach, the adhesives can be insulating or conductive ones. The conductive adhesives can either be thermally conductive or electrically insulating or both thermally and electrically conductive ones. In both cases, the conductivity is achieved by including filler materials in the resin base of the adhesives. Thermally conductive adhesives usually contain AlN, Al_2O_3 (alumina), or boron-nitride fillers, whereas electrically conductive adhesives include Ag, Au, or Cu flakes. The electrically conductive adhesives can be isotropic (conducts in all directions) or anisotropic (conducts in a specified direction). Nevertheless, the disadvantages of adhesives are the lower mechanical strength of the die-attaches, lower temperature resistance, low thermal conductivity, and void formation due to the outgassing of compounds from the adhesives. To overcome these issues, solder materials are used for the die-attach, especially in high-power or high operating temperature applications.

The solder materials for die-attach are available mainly in three forms: solder paste, coating/surface finish (preplate), and preform foil. Preparing die-attach with solder pastes utilizes the really same steps as in traditional reflow technologies; printing the solder pastes onto the pads on the substrate (leadframe/interposer), placing the semiconductor chip into the solder paste, and establishing the die-attach by remelting and solidifying the solder alloy in the paste (see Sections 1.2−1.5). Preform foils are preshaped solder alloys with a thickness usually of 20−50 μm. These are placed between the chip and the pad, and the whole structure is fastened by a special clamp during the soldering process. In the third form, preplates are formed by depositing solder materials onto the chip and the pad typically utilizing the

electroplating process. In the case of using preform and preplate solders, there is no flux in the system. So, cleaning the surfaces to be attached and preventing their oxidation is achieved by using inert (N_2) or reducing atmosphere (e.g., H_2 or formic acid—HCOOH) during the soldering. This disadvantage of fluxless soldering technologies is balanced by the elimination of one of the most uncompromising qualities and reliability problem of die-attach processes, the void formation in the attachment due to the outgassing of flux. Void formation reduces the mechanical strength and the thermal conductivity of die-attaches significantly (see Sections 5.4 and 5.5). Recently, the sintering of silver nanoparticles is also investigated for die-attach purposes. Kisiel and Szczepański compared the use of adhesives, Au/Ge solders preforms, and Ag nanoparticles for die-attach of SiC power devices. They found that die-attaches with good initial mechanical strength were obtained by using the Ag nanoparticles. The stability of Ag nanoparticle sintering joints was investigated too by nondestructive tests during aging at 350°C in their work. Every 24 hours, after cooling to room temperature, the shear stress of 100 N/cm^2 was applied to the SiC die with dimensions of 5×5 mm. Till 72 hours of aging, the adhesion was appropriate, but after 96 hours of aging, the SiC die was sheared off by the stress level of 16 N/cm^2. The fracture surface showed the presence of Ag oxide almost on the whole surface, indicating that silver oxidation had caused joint failure [3].

5.2 Gold–silicon eutectic soldering

A die-attach technology, which is traditionally used in VLSI (very large scale integrated circuit) for silicon die bonding to the substrate, is the so-called gold–silicon eutectic soldering [4]. Here, an Au/Si hard solder preform is used in a eutectic composition ($Au_{96.8}/Si_{3.2}$ wt.%), taking advantage of that the silicon–gold binary system exposes a significant reduction in the liquidus point. The melting temperature is reduced from 1064°C at pure gold to 363°C in eutectic composition [5], as illustrated in Fig. 5.3.

During the process, the Au/Si eutectic preform solder is placed onto the leadframe with Au surface finish and heated up to a temperature ($\sim$395°C), which is only slightly higher than the eutectic temperature (363°C). The silicon chip is picked up with a heated vacuum nozzle and pushed to the preform solder (Fig. 5.4) [1].

Note that the Au/Si preform solder remains solid at the beginning of the process, because the leadframe temperature is only slightly above the melting temperature, and the thermal contact is not perfect between the preform solder and the substrate making the thermal resistance high in between. When the silicon chip is pushed to the preform solder by the vacuum nozzle, the thermal resistance will decrease between the leadframe and solder, and the solder preform will melt. During the soldering, the melted solder

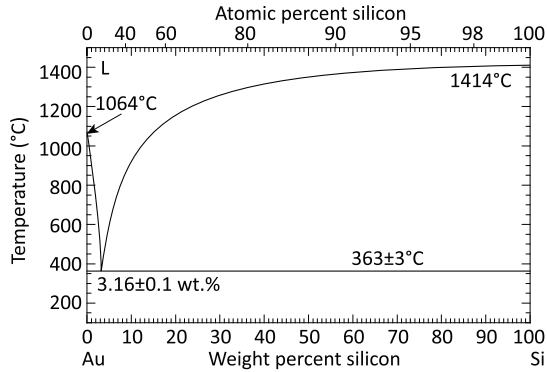

FIGURE 5.3 Au/Si phase diagram.

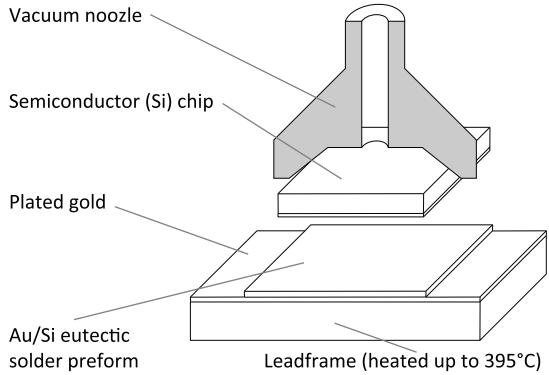

FIGURE 5.4 Process of gold–silicon eutectic soldering. *Reproduced with permission from G. Harsányi, Elektronikai Technológia és Anyagismeret, University Lecture Notes, BME-ETT, 2019, ISBN: 978-963-421-791-6.*

dissolves gold from the leadframe finish, and the composition shifts from the eutectic one.

Although this technique has typically been used in die-attach processes, it can, in principle, also be employed for silicon wafer-to-wafer bonding with Au/Si as an intermediate layer. Problems associated with gold eutectic bonding are the long-term drift in sealed-cavity devices and the possible trap formation halfway to the bandgap. Contamination of silicon with gold would result in a severe reduction of the minority carrier lifetime in integrated active devices. However, many micromachining processes are already designed in such a way that the actual micromachining steps are performed as low-temperature postprocessing steps outside the cleanroom. The intermediate eutectic gold bonding would be a natural extension of this approach. Under normal conditions, silicon dissolves in the liquid gold and not vice versa, so there is, in principle, no gold doping of the wafer [6].

5.3 Die-attach with soft solders

Besides the Au/Si eutectic solder alloy, further alloys are used, especially in the manufacturing of power electronics devices. These alloys include but not limited to Pb_{95}/Sn_5 (melting point 314°C), Au_{80}/Sn_{20} (280°C), Sn_{95}/Sb_5 (235°C−240°C), $Sn_{65}/Ag_{25}/Sb_{10}$ (233°C), and $Sn_{96.5}/Ag_3/Cu_{0.5}$ (219°C−221°C). The soldering can be performed in fluxless soldering ovens, for example, for silicon and SiC die-attach to metal substrates. For forming gas, a mixture of 10 vol.% H_2 and 90 vol.% N_2 can also be used in these processes, which is sometimes called a "dissociated ammonia atmosphere" due to the reaction which generates it (5.1). The dilute N_2 intakes are used to dilute the forming gas for decreasing the H_2 concentration at the entrance and the exit of the oven, thereby avoiding explosion hazard.

$$2NH_3 \rightarrow 3H_2 + N_2 \tag{5.1}$$

The process area of the oven is 8 m long, 0.24 m wide, and 0.08 m high. The main parts of the oven are the following (Fig. 5.5): 1—entrance trapdoor; 2—entrance vent hood; 3—entrance gas blocks; 4—entrance dilute N_2 intake; 5—heater zone; 6—forming gas intake; 7—cooling zone; 8—cooling N_2 intake; 9—exit dilute N_2 intake; 10—exit vent hood; 11—exit gas blocks; 12—exit trapdoor. The vent hoods contain funnels with a diameter of 80 mm and these are equipped with controllable throttle valves [7].

The heating area is a steel duct bushed with ceramic plates to increase its heat capacity. The steel duct is heated at four points with electrical heaters. The temperature of the heating area can be controlled by the power of the electrical heaters. The temperature of the cooling zone cannot be controlled. The cooling is facilitated by cold water pipes placed on the wall of the cooling zone and by the intake of cold N_2 gas.

During operation, most of the forming gas is flowing toward the entrance of the oven through the heating area. The cool N_2 gas is flowing toward the

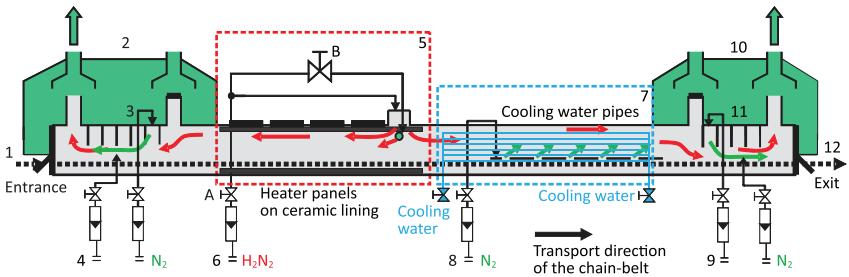

FIGURE 5.5 Block diagram of a high-temperature, fluxless soldering oven (not to scale). *Reproduced with permission from B. Illés, G. Kristóf, L. Jakab, Thermal and gas flow characterization of a fluxless Si solder bonding oven, Exp. Therm. Fluid Sci. 35(1) (2011) 29–36.*

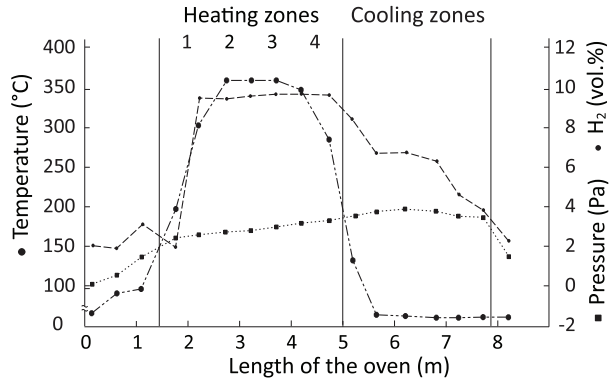

FIGURE 5.6 Process parameter conditions during fluxless soldering. *Reproduced with permission from B. Illés, G. Kristóf, L. Jakab, Thermal and gas flow characterization of a fluxless Si solder bonding oven, Exp. Therm. Fluid Sci. 35(1) (2011) 29–36.*

exit of the oven. Along the oven, only the gas blocking lamellas cause major cross-sectional narrowing at the entrance and at the exit of the oven. Besides, the area between the gas blocks is pressurized during soldering. This ensures that the gas flow can proceed through the gas blocks only toward the entrance and the exit of the oven, thus blocking the air out from the oven. The pressure balance can be controlled by the amount of gas at the intakes and by the vent hoods. The balance of gas flow is one of the most important points of this soldering technology. The efficiency of the pressurized block can easily decrease due to improper operation of the vent hoods or due to draught, formed in the production area where the oven is operated. In this case, the flowing direction of the forming gas may change and it flows into the cooling zone instead of the heater zones. This effect results in defective solder joints, with possible void formation. The typical process parameter conditions during this process are illustrated in Fig. 5.6 [7].

5.4 Thermal transient characteristics of die-attaches

The reliability of packaged electronics strongly depends on the die-attach quality because any void or a small delamination may cause an instant temperature increase in the die, leading sooner or later to failure in operation. Die-attach materials have a crucial role in the thermal management of high power packages by providing low thermal resistance between the heat-generating chips and the heat-dissipating heat spreader [8]. Thermal transient analysis is used to evaluate the thermal behavior of all of the packages for a long time [9]. This method is based on that the time dependence of temperature is characteristic of the geometrical and material structure of the surroundings of the chip, such as the heat flow path of the structure. Evaluation of this curve may lead to various models of this heat flow path. Die-attach quality can be checked then by analyzing its thermal

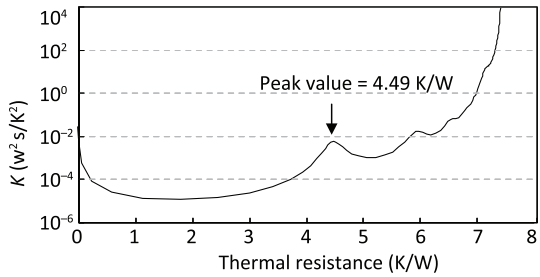

FIGURE 5.7 Differential structure function of a structure including a power semiconductor, die-attach, and the silicon substrate. *Reproduced with permission from H.H. Kim, S.H. Choi, S. H. Shin, Y.K. Lee, S.M. Choi, S. Yi, Thermal transient characteristics of die-attach in high power LED PKG, Microelectron. Reliab. 48 (2008) 445–454.*

transient characteristics [10,11]. Methods for checking die-attach quality have been developed based on the structure–function evaluation, which function is obtained from thermal transient characteristics measurements. The structure functions can be calculated by mathematical transformations from the measured or simulated thermal temporary response functions of a system [12]. Structure functions provide a map of the cumulative thermal capacitances of the heat flow path concerning the thermal resistances from the junction to the ambient. The local peaks and valleys indicate reaching new materials or changed surface areas in the heat flow path. More precisely, the peak point usually means the middle of any new region. This implies that the values of the structure functions and their slopes depend on parameters of die-attach materials (Fig. 5.7) [8].

It should be noted that the structure functions are valid for structures that one-dimensional heat flow path is assured by the applied thermal boundary conditions. All in all, by knowing the geometric and materials parameters, one can determine the thermal resistances of die-attach materials by evaluating structure functions from fast and straightforward thermal transient measurements.

Kim et al. compared three types of die-attach materials from the mechanical and thermal characteristics' points of view. The investigated materials were Ag paste, solder paste with SAC305 ($Sn_{96.5}/Ag_3/Cu_{0.5}$) alloy, and preformed Au_{80}/Sn_{20} eutectic alloy [8]. They used a structure, which included a high power LED PKG, die-attach material, and silicon heat slug. The size of the LED chip was 900×900 μm. They found by shear strength measurements, that among die-attach materials, the strength of solder paste with the average value of 42 N was higher than that of Au/Sn eutectic bonding and Ag paste with the average values of 25 and 15 N, respectively.

Fig. 5.8 shows measured differential structure functions of the high power LED packages with the three different die-attach materials. As shown in Fig. 5.7, peaks correspond to regions of high thermal conductivity, and valleys show regions of low thermal conductivity here also.

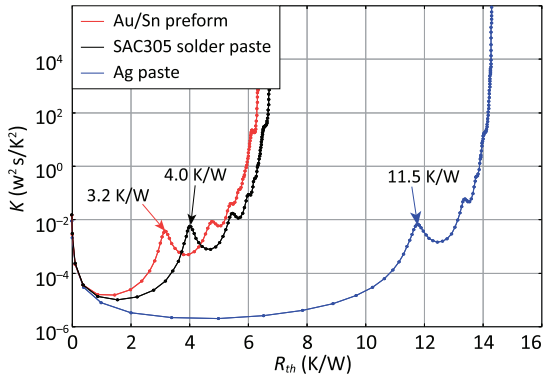

FIGURE 5.8 Differential structure function regarding the compared die-attach materials. *Reproduced with permission from H.H. Kim, S.H. Choi, S.H. Shin, Y.K. Lee, S.M. Choi, S. Yi, Thermal transient characteristics of die-attach in high power LED PKG, Microelectron. Reliab. 48 (2008) 445–454.*

The thermal resistances of die-attaches by Au/Sn eutectic bonding, solder paste, and Ag paste took the values of 3.2–3.6 K/W, 4.0–4.6 K/W, and 11.5–14.2 K/W, respectively. In the case of Au/Sn eutectic bonding and die-attach by solder paste, the values of the thermal resistance from the chip to the die-attach are uniformly distributed. But in the case of die-attach by Ag paste, the thermal resistance is more distributed because of the uncertainty in the curing process of Ag paste. In their fabricated high power LED packages, the quality of Au/Sn eutectic bonding was much better than that of the die-attaches by solder paste and Ag paste in terms of the total thermal resistance.

5.5 Effect of void formation on the properties of die-attaches

The presence of voids in the die-attaches is known to adversely affect the thermal resistance of the packaged device at chip level [13]. Unfortunately, such voids are easily formed in the solder layer during assembly and are found to nucleate, grow, and coalesce with thermal cycling [14] and thermal stressing [15]. Voids in the die bond material can be roughly categorized into two groups: small, randomly distributed voids; and large, contiguous voids [16]. Under normal packaging conditions, the type of void that forms cannot be precisely controlled; both types are commonly present in the same bond layer. The investigations into the effects of voids on the properties of die-attaches relies on the imaging and characterization of existing void patterns after bonding through utilizing ultrasonic microscopy scanning techniques [17], photothermal interface microscopy [18], and thermal transient measurements (Section 5.4). Katsis and van Wyk [15] used a scanning acoustic microscope to determine the percent of voiding in the die-attach layer after a certain number of thermal cycles. Their

data, while scattered, suggest a roughly linear relationship of thermal resistance and void area, which becomes stronger with an increasing number of thermal cycles. Strifas et al. [14] used scanning infrared microscopy and finite element analysis (FEA) methods to investigate the effect of die-attach voids on surface temperature. Voids that occurred directly below the power transistors were found to significantly increase thermal resistance, resulting in surface temperature increases of up to 10%. Chandran et al. [19] used a numerical technique to predict a 16% increase in chip surface temperature caused by a large contiguous void directly under the power source and covering 20% of the die-attach area. Ciampolini et al. [20] used infrared thermography to validate an FEA simulation of a complex hybrid circuit with large, contiguous die-attach voiding of varying size, location, and aspect ratio. The results show that the junction temperature is proportional to the void area only if a case-specific, package-dependent coefficient is used.

Although the relationship between package thermal resistance and voids has been examined extensively, little data exist concerning the precise effects of void size, configuration, and position. Fleischer et al. performed an investigation to overcome this shortcoming [21]. In their experiment, the voids were etched to a depth of 127 μm directly into the backside of a silicon chip, rather than being created in the die-attach layer itself. By using a carefully controlled bonding process, the only voids between the silicon chip and the die-attach layer are those precisely etched in the chip in a particular geometric pattern. The void geometry was varied in type (random or contiguous), in size, and in void percentage, $V\%$ (fraction of the interface that is occupied by voids). Contiguous voids took the form of one large, square, centrally located void and while "random" voids were modeled as a 5×5 matrix of evenly spaced square voids with the same total void area as the contiguous voids. A control chip was also fabricated with no voids. The thermal resistance of the investigated structure for each void pattern was determined for a fixed applied power of 7.5 W. Their results can be seen in Fig. 5.9.

They found that an increase in the void percentage causes the thermal resistance to increase. When the void percentage is below 20%, the increase in thermal resistance was small for both the random and contiguous void patterns. As $V\%$ increased, the thermal resistance increased and a distinct difference in thermal behavior was observed for the random and contiguous void patterns. The thermal resistance of the random void patterns increased almost linearly to a maximum increase of 30% with 73% voids and was well correlated by $\theta_{jc} = 0.007V\% + 1.499$. For the contiguous void pattern, the same void percentage led to a much higher increase in thermal resistance of 200% to a final value of 4.7°C/W. This was well correlated by an exponential fit: $\theta_{jc} = 1.43e^{0.154V\%}$. The difference in the thermal resistance behavior for random and contiguous void patterns was qualitatively explained through the effects of spreading resistance and the thermal conductivity of silicon on the overall thermal resistance [21].

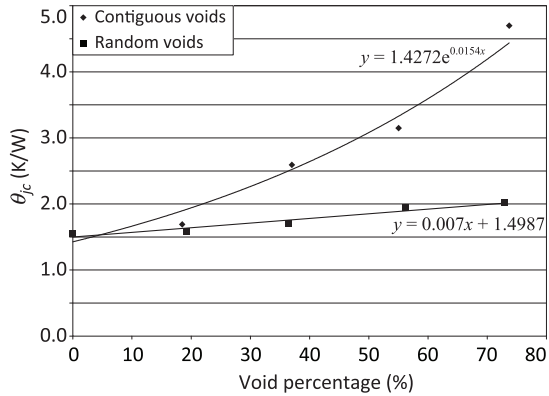

FIGURE 5.9 Differential structure function regarding the compared die-attach materials. *Reproduced with permission from A.S. Fleischer, L.H. Chang, B.C. Johnson, The effect of die-attach voiding on the thermal resistance of chip level packages, Microelectron. Reliab. 46 (2006) 794–804.*

Besides, a strong influence of void geometry on the resultant chip surface temperature was presented. One can quickly distinguish the underlying void pattern as it was qualitatively reproduced in the surface temperature contours. A large, contiguous void resulted in a temperature distribution across the chip face, which featured the hottest spot at the chip center and a cooling gradient toward the edges. A random void pattern resulted in a series of high-temperature points on the chip face corresponding to the center of each void. This temperature distribution was similar to that described as a "hot void" by Carlson et al. [22], in which the heat flow is restricted to the non-void areas, creating a hot spot above each void.

Similar hot spots can form in high power electronics on DCB substrates, especially due to a fjord-like crack in the solder joint between the DCB substrate and the heat spreading base plate (Fig. 5.10).

This failure can be originated back to the so-called shrinkage defect, which typically arises in solder alloys with hypoeutectic Ag composition (wt.% > 2.8%) [23], like the alloy of SAC305—$Sn_{96.5}/Ag_3/Cu_{0.5}$. In high Ag-content alloys, the main affecting factor concerning the thermo-mechanical properties is the morphology of the Ag_3Sn intermetallic compounds, which form during the soldering. They can cause not just shrinkage defects but can promote crack propagation along their grain boundary [24]. The morphology of the precipitating Ag_3Sn IMCs depends on the cooling rate of the soldering process. These intermetallic compounds can basically form in three types: plate-like, needle-like, and particle-like [25]. The higher cooling rates can generate a more spherical, finer Ag_3Sn particle distribution [26]. Contrary, lower cooling rates promote the formation of plate-like IMCs, which type has the largest area. It can reach 100–300 μm in length,

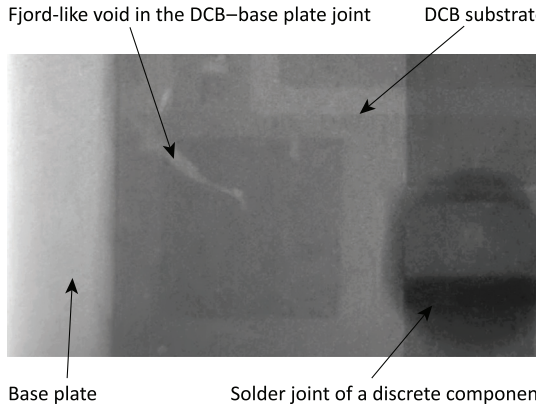

FIGURE 5.10 X-ray image of a fjord-like crack in a solder joint between DCB substrate and base plate.

and it occurs in high silver content solder joints more likely. As a consequence, rates of cooling higher than 1.5 K/s are recommended for preparing die-attaches with high silver-content solder alloys. Actually, elimination of this soldering failure is the main reason for the continuous development of third-generation solder alloys, namely low Ag-content alloys doped with minor tracing elements or nanoparticles.

Void formation in solder joints of passive components on DCB substrates was investigated by Skwarek et al. [27], where the solder material was deposited in paste form by stencil printing. They utilized vacuum vapor phase soldering (Chapter 4, Vapor Phase Reflow Soldering Ovens) with and without vacuum option for preparing the solder joints, and the void formation was inspected by CT (Computed Tomography) X-ray. They also characterized the mechanical strength of the prepared solder joints by shear strength measurements. They found that using vacuum (−95 kPa), during the vapor phase, soldering increased the shear strength of the prepared solder joints by approximately 25%. They confirmed this result both by visual observation voids on the fracture surfaces and by X-ray analyses.

Based on their results, samples prepared by vacuum vapor phase soldering were almost void-free. The minimum void area was 46 μm^2, whereas the maximal was 0.066 mm^2. The total area of voids relatively to the joint area reached only 7% in this case. During the shear strength test, the joints cracked in the intermetallic layer, which provides the highest mechanical strength of the solder joints. On the contrary, worse quality solder joints were observed in the case of using vapor phase soldering without vacuum. The solder joints contained large voids, mainly localized under the component. During shear strength tests, these joints cracked at the voids and not in the IMC layer [27].

5.6 Low temperature, fluxless soldering

The elimination of void formation in die-attaches induces the investigations in the field of fluxless soldering. Recently, selective localized heating of solder material for die-attach and applying new materials for joining the semiconductor chip to the substrate at low temperatures came into focus.

Localized heating can be produced by embedded microheaters instead of global heating furnaces to prevent thermal problems during the die-attach process [28]. These microheaters are constructed in a way that heating is restricted to a small region that is surrounded by insulation materials, such as silicon dioxide. Thus, the bonding process can be conducted locally while the whole wafer is maintained at low temperature. The use of resistive heating from microheaters can introduce complexity to the bonding design and in many cases, electrical wiring is not preferred [29]. Another novel wafer bonding method is localized induction heating solder bonding [30], where electroplated magnetic Ni/Co film was heated using induction heating to melt the solder and form the die-attach. However, this method is not suitable for attaching devices that are sensitive to a magnetic field.

Qiu and Wang described a bonding process of silicon wafers with reactive multilayer foils [31]. They used reactive multilayer Ni/Al foils as local heat sources to melt solder layers and thus attach silicon wafers. Reactive multilayer foils contain hundreds of nanoscale Ni and Al bilayers. With a small thermal pulse (e.g., by electrical spark), these foils can react exothermically and generate a self-propagating reaction. Self-propagating formation reactions in such foils are driven by a reduction in chemical bond energy. This local reduction of chemical bond energy produces a large quantity of heat that is conducted down the foil and facilitates more atomic mixing and compound formation [31]. In their work, Ni/Al reactive multilayer foils were fabricated by magnetron sputtering. The total thickness of the Ni/Al foils is 60 μm, the bilayer thickness is 40 nm (Fig. 5.11), and the heat of reaction was calculated to be −57.9 kJ/mol.

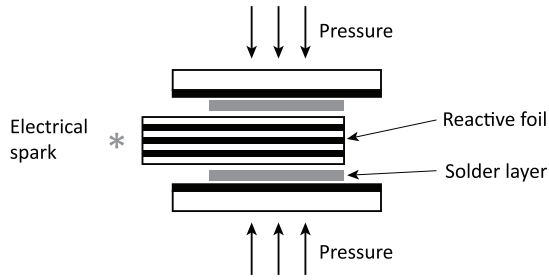

FIGURE 5.11 Schematic of a die-attach process using reactive foils. *Reproduced with permission from X. Qiu, J. Wang, Bonding silicon wafers with reactive multilayer foils, Sens. Actuators A 141 (2008) 476–481.*

New materials have intensively been investigated by Kim and Lee to be used in fluxless soldering. In one of their research works, eutectic Sn−Bi−Au alloy (in preplate form) was used for attaching a semiconductor chip to a silicon substrate [32]. The silicon chip had Cr/Bi/Sn/Au metallization and the silicon substrate had Cr/Au metallization, and the die-attach material is deposited by high vacuum thermal evaporator. They found that the phase formation during the plating process of the alloy included the following: The Sn_{57}/Bi_{43} binary system has a 139°C solidus line extending from a tin composition of 0.2−86.7 at.% [33]. There are one eutectic point and two terminal solid solutions, (β-Sn) and (Bi). There is no additional intermediate phase or intermetallic compound in this system. When the Bi and Sn layers are deposited, they form Bi−Sn alloy with typical eutectic lamellar structure due to the long deposition time and the heat inside the chamber. The lamellar structure consists of two distinct regions: one is the Bi-rich phase (Bi) and the other, Sn-rich phase (β-Sn). As the Au layer is deposited in the same vacuum cycle, Au atoms react with the (β-Sn) region to form Au−Sn intermetallic compounds, resulting in a capping layer. During deposition, the temperature is high and the (β-Sn) phase would contain a significant amount of Bi [33]. The Bi atoms in the (β-Sn) phase and in the (Bi) phase react with the Au−Sn compounds to form capping layer of Bi rich matrix with imbedded Au−Sn intermetallics. This capping layer covers the most outer surface of the samples and inhibits the formation of the oxide layer due to the minimizing exposure of (β-Sn) phase to the air. They also stated that the relatively small Au−Sn intermetallic crystallites were randomly distributed in the Bi matrix.

During the solder joint formation, the silicon chip, the substrate, and the solder preform in between were held together with a static pressure of 510 kPa using a specially designed fixture. To reduce oxidation during the bonding process, reduction in the ramp time is necessary. A high temperature, vertical box furnace was set to 1000°C. The sample was let into the oven till its temperature reached 250°C; then it is cooled down. The ramp time was about 15 seconds to reach the peak temperature of soldering, and the cooling time was less than 5 minutes till reaching 30°C. The process of soldering is illustrated in Fig. 5.12. Before the die-attach process, the silicon chip is placed on the silicon substrate, as shown in Fig. 5.12A. When the temperature exceeds the 139°C solidus temperature of the Sn−Bi alloy, the alloy will change into a molten eutectic phase mixed with either (Bi) or (β-Sn) grains. At even higher temperatures, that is, at the 250°C soldering temperature, the Sn−Bi alloy would convert almost entirely to a molten phase, as depicted in Fig. 5.12B. The molten phase dissolves the Bi matrix in the capping layer and breaks it up, resulting in a mixture of molten phase with small crystallites of $AuSn_2$ and $AuSn_4$, as exhibited in Fig. 5.12C. Since the melting temperatures of $AuSn_2$ and $AuSn_4$ are higher than 250°C, these compounds remain in the form of small solid crystallites during the

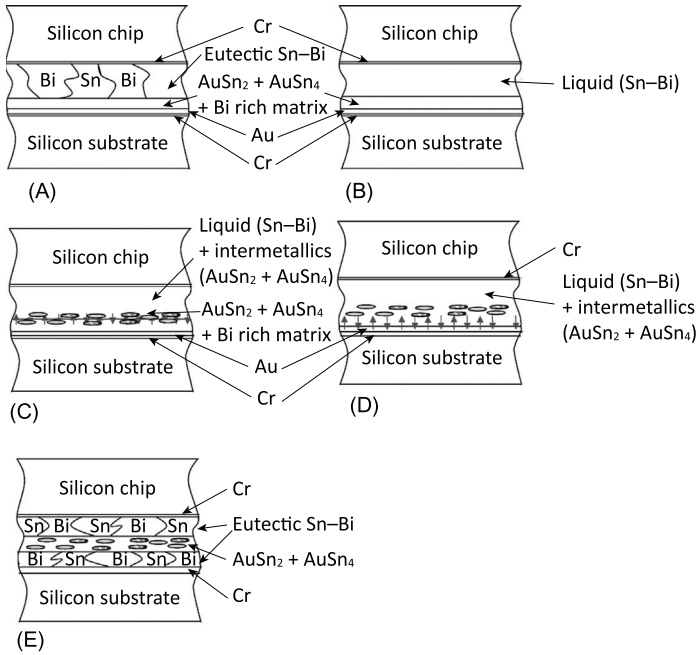

FIGURE 5.12 Schematic of soldering process using Sn/Au/Bi preplated solder. (A) As deposited; (B) 139°C–250°C; (C) bonding temperature; (D) joint formation; (E) joint solidification. *Reproduced with permission from D. Kim, C.C. Lee, Fluxless bonding process in air using Sn–Bi–Au design, Mater. Sci. Eng. A 372 (2004) 261–268.*

soldering. The molten phase now has chemical contact with the thin Au layer on the silicon substrate and reacts with the Au layer to produce more $AuSn_2$ and $AuSn_4$, as displayed in Fig. 5.12D. When this happens, a joint is essentially achieved. Upon cooling down to room temperature, the joint solidifies into Sn–Bi eutectic matrix with Au–Sn intermetallic grains, as shown in Fig. 5.12E [32].

They found by solder melting experiments that the melting temperature of Sn/Bi/Au deposited alloy is 225°C. SEM and EDX results revealed that the joint is composed of near eutectic Sn–Bi alloy with a ribbon-shaped Au–Sn intermetallic layer in the middle with shear strength higher than the military standard of 50 N for a die size of 4×4 mm.

Kim and Lee also investigated the possibility of attaching flip-chips to Cu-laminated polyimide films by fluxless soldering process [34]. The Au_{80}/Sn_{20} solder alloy is broadly used in optoelectronic industries due to its excellent fatigue resistance and creep resistance. But due to the high melting temperature (280°C) of this alloy, the authors looked into Au/Sn alloys with high tin composition to lower the melting temperature down to approximately 220°C. The solder bumps onto the flip-chip were fabricated by rotary

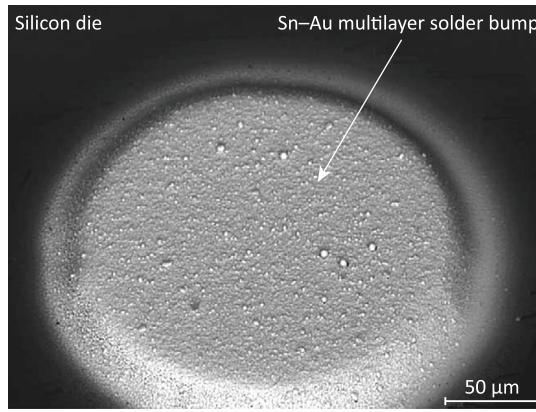

FIGURE 5.13 Flip-chip solder bump prepared from Sn−Au multilayer composite. *Reproduced with permission from D. Kim, C.C. Lee, Fluxless flip-chip Sn Au solder interconnect on thin Si wafers and Cu laminated polyimide films, Mater. Sci. Eng. A 416 (2006) 74−79.*

multicrucible vacuum thermal evaporator (0.00026 Pa), depositing Sn−Au multilayer composite with overall composition of 95 at.% Sn and 5 at.% Au (91.8 wt.% Sn and 8.2 wt.% Au). The solder bumps were prepared with a diameter and height of 200 and 20 μm, respectively (Fig. 5.13).

The surface of the bumps was bright gray after the sample is taken out of the vacuum chamber. This appearance clearly indicated that diffusion between tin and gold has already taken place during the deposition. It is well known that the rapid diffusion of gold atoms into a tin-rich matrix can occur even at room temperature via grain boundary mechanism.

The substrate was a 50 μm thick polyimide film laminated with a 17 μm thick copper layer. Prior to soldering, the surface contaminants and oxides were removed by sulfuric acid treatment. During the soldering, the $AuSn_4$ layer on the solder bumps acts as an oxidation barrier as well as a diffusion barrier. Since the solid solubility of Cu in Sn is negligibly small compared to liquid state, Cu−Sn intermetallic growth is retarded until the $AuSn_4$ layer actually is dissolved into the molten solder. As the temperature reaches 217°C−220°C, molten tin starts to dissolve Cu. After a short time, the Cu dissolved in the molten solder reaches local equilibrium solubility with Sn and Cu−Sn intermetallic. As a result, Cu_6Sn_5 starts to form on the interface. Since Cu_6Sn_5 is not an equilibrium phase with Cu, solid-state diffusion reaction between Cu_6Sn_5 and Cu will continue to develop stable Cu_3Sn intermetallic. After a joint is formed, Cu continues to diffuse through Cu_3Sn and Cu_6Sn_5 with a grain boundary mechanism. The Cu atoms arrive at Cu_3Sn−Cu_6Sn_5 and Cu_6Sn_5−Sn-rich Au−Sn solder interfaces and form IMC layers thicker

The joints were evaluated then by using scanning acoustic microscopy. Voids show up clearly in the acoustic image with very high contrast because of

mismatch in acoustic impedance between the void and the metallic joints. Nearly void-free joints could be achieved. Debonding tests were also performed on several samples. The noneutectic Au−Sn solder joints melted at about 220°C, which is close to the second eutectic temperature of the Au−Sn system.

The research works mentioned above proved that semiconductor dies can be attached to substrates even at low temperatures. This makes possible the die-attach process for temperature-sensitive application and also makes possible the applicability of flexible substrates for advanced packaging of, for example, MEMS devices and sensors.

References

[1] G. Harsányi, Elektronikai Technológia és Anyagismeret, University Lecture Notes, BME-ETT, 2019, ISBN: 978-963-421-791-6.

[2] G. Harman, Wire Bonding in Microelectronics, 3rd ed., McGraw-Hill, New York, NY, USA, 2010, ISBN: 978-0-07-147623-2.

[3] R. Kisiel, Z. Szczepański, Die-attachment solutions for SiC power devices, Microelectron. Reliab. 49 (2009) 627−629.

[4] R.K. Shukla, N.P. Mencinger, A critical review of VLSI die-attachment in high-reliability applications, Solid State Technol. July (1985) 67−74.

[5] H. Baker, ASM Handbook, Volume 3—Alloy Phase Diagrams, ASM International, Materials Park, OH, 1992, p. 114.

[6] R.F. Wolffenbuttel, K.D. Wise, Low-temperature silicon wafer-to-wafer bonding using gold at eutectic temperature, Sens. Actuators A 43 (1994) 223−229.

[7] B. Illés, G. Kristóf, L. Jakab, Thermal and gas flow characterization of a fluxless Si solder bonding oven, Exp. Therm. Fluid Sci. 35 (1) (2011) 29−36.

[8] H.H. Kim, S.H. Choi, S.H. Shin, Y.K. Lee, S.M. Choi, S. Yi, Thermal transient characteristics of die-attach in high power LED PKG, Microelectron. Reliab. 48 (2008) 445−454.

[9] B.S. Siegal, Measuring thermal resistance is the key to a cool semiconductor, Electronics 51 (1978) 121−126.

[10] M. Rencz, Thermal issues in stacked die packages, in: 21st IEEE SEMI-THERM Symposium '05, March 15−17, 2005, San Jose, CA, 2005.

[11] M. Rencz, V. Szekely, Die-attach quality control of 3D stacked dies, in: Proceeding of the IEMT Symposium of SEMICON West, July 12−16, 2004, San Jose, CA, 2004, pp. 78−84.

[12] M. Rencz, V. Szekely, Structure function evaluation of stacked dies, in: Proceedings of the IEEE SEMI-THERM Symposium, March 9−11, 2004, San Jose, CA, 2004, pp. 50−55.

[13] N.F. Khory, The impact of die bond voids in power semiconductor devices on thermal resistance and long term reliability (an analytical approach), in: Proceeding of the International Symposium on Microelectronics, 1986, 275-280.

[14] N. Strifas, P. Yalamanchili, A. Christou, Thermal analysis modeling and investigation of die-attach void on MMIC surface temperature, Am. Soc. Mech. Eng. EEP Appl. Exp. Mech. Electron. Packag. 13 (1995) 11−16.

[15] D.C. Katsis, J.D. van Wyk, Void induced thermal impedance in power semiconductor modules: some transient temperature effects, IEEE Trans. Ind. Appl. 39 (2003) 1239−1246.

[16] M. Mahalingam, M. Nagarkar, L. Lofgran, J. Andrews, D.R. Olsen, H.M. Berg, Thermal effect of die bond voids, Semicond. Int. 7 (1984) 71−79.

[17] S.K. Iliev, Thermal performance comparison of chip-onboard, flip chip-on-board and standard TQFP package, in: Proceedings of the IEEE 14th Annual Semiconductor Thermal Measurement and Management Symposium, 1998, pp. 161–168.
[18] K. Kurabayashi, K.E. Goodson, Precision measurement and mapping of die-attach thermal resistance, IEEE Trans. Compon. Packag. Manuf. Technol. A 21 (1998) 506–514.
[19] B. Chandran, M.H. Gordon, W.F. Schmidt, Comparison of CVD diamond to other substrate materials for thermal management, in: Proceedings of the 5th Intersociety Conference on Thermal Phenomena in Electronic Systems, 1996, pp. 226–232.
[20] L. Ciampolini, M. Ciappa, P. Malberti, P. Regli, W. Fichtner, Modeling thermal effects of large contiguous voids in solder joints, Microelectron. J. 30 (1999) 1115–1123.
[21] A.S. Fleischer, L.H. Chang, B.C. Johnson, The effect of die-attach voiding on the thermal resistance of chip level packages, Microelectron. Reliab. 46 (2006) 794–804.
[22] R.O. Carlson, A.J. Yerman, J.F. Burgess, C.A. Neugebauer, Voids, cracks and hot spots in die-attach, in: 21st Annual Proceedings of Reliability Physics, 1983, pp. 138–141.
[23] T. Garami, O. Krammer, Quantitative analyses of Ag_3Sn intermetallic compound formation in SnAgCu solder alloys, J. Mater. Sci.: Mater. Electron. 26 (2015) 8540–8547.
[24] K.S. Kim, S.H. Huh, K. Suganuma, Effects of cooling speed on microstructure and tensile properties of Sn–Ag–Cu alloys, Mater. Sci. Eng. A 333 (1-2) (2002) 106–114.
[25] H.T. Lee, Y.F. Chen, T.F. Hong, K.T. Shih, Effect of cooling rate on Ag_3Sn formation in Sn-Ag based lead-free solder, in: 11th Electronics Packaging Technology Conference (EPTC), 2009, pp. 875–878.
[26] M. Kerr, N. Chawla, Creep deformation behavior of a Sn-3.5Ag solder at small-length scale, JOM 56 (2004) 50–54.
[27] A. Skwarek, B. Illés, B. Synkiewicz, S. Wroński, J. Tarasiuk, K. Witek, Characterization of solder joints made with VPS on DBC substrate, J. Mater. Sci.: Mater. Electron. 28 (2017) 1769–1776.
[28] Y.T. Cheng, W.T. Hsu, K. Najafi, T.C. Nguyen, L. Lin, Vacuum packaging technology using localized aluminum/silicon-to-glass bonding, J. Microelectromech. Syst. 11 (2002) 556–565.
[29] C. Luo, L. Lin, The application of nanosecond-pulsed laser welding technology in MEMS packaging with a shadow mask, Sens. Actuators A, Phys. 97–98 (2002) 398–404.
[30] H. Yang, M. Wu, W. Fang, Localized induction heating solder bonding for wafer level MEMS packaging, J. Micromech. Microeng. 15 (2005) 394–399.
[31] X. Qiu, J. Wang, Bonding silicon wafers with reactive multilayer foils, Sens. Actuators A 141 (2008) 476–481.
[32] D. Kim, C.C. Lee, Fluxless bonding process in air using Sn–Bi–Au design, Mater. Sci. Eng. A 372 (2004) 261–268.
[33] H. Okamoto, T.B. Massalski (Eds.), Binary Alloy Phase Diagrams, vol. 1, ASM International, Metals Park, OH, 1990, p. 434.
[34] D. Kim, C.C. Lee, Fluxless flip-chip Sn Au solder interconnect on thin Si wafers and Cu laminated polyimide films, Mater. Sci. Eng. A 416 (2006) 74–79.

Chapter 6

Numerical simulation of reflow ovens

Recently, the numerical simulation is getting more and more important, not only in the scientific researches but in the industrial application as well. Generally, the numerical models offers fast, easy, and flexible solution for such technological problems, which are hardly determinable by measurements due to the harsh environment and the usually limited accessibility of process chamber. The numerical simulation of reflow ovens is introduced with vapor phase soldering (VPS) technology, since as it was discussed in Chapter 4, Vapor Phase Reflow Soldering Ovens, this is the most complex method, from the aspect of physical phenomena occurring during soldering. Evaporation and condensation, mass diffusion, and convection take place during the process. Therefore, it is worth to present and build up the topic of numerical simulations with the VPS technology and later apply the presented modeling techniques to the other soldering technologies, which are less complex from the point of physical investigations.

6.1 Numerical simulations of vapor phase soldering ovens

The scaling problem is present in the case of numerical simulation of the VPS system. This means that in the investigated system, the dimensions can differ with orders of magnitudes. Therefore, this topic is distinguished into two levels: the so-called soldering chamber or process zone level and the assembly level. On the level of the process zone, the formation of the vapor space and the formation of the lower pressured environment (during vacuum VPS technology) are investigated. On the level of the assembly, the formation of the condensate layer on the assembly is investigated.

6.1.1 Numerical simulations of vapor space formation

On the level of the process zone, the formation of the vapor space (like evaporation and diffusion of the heat transfer fluid), the effect of the immersed assembly on the vapor space (like condensation of the heat transfer fluid),

Reflow Soldering. DOI: https://doi.org/10.1016/B978-0-12-818505-6.00006-6

and other types of vapor-related topics (like vapor suctioning and dew point formation) are investigated.

6.1.1.1 Model description

After the start of the VPS system, the heater pipes at the bottom of the process zone start to warm up the heat transfer fluid toward its boiling point. The cooler pipes at the opening of the process zone start to cool down the vapor to avoid the vapor loss. The heat generated by the heaters and extracted by the coolers sets the thermal balance of the system, and thermal gradient starts to form in the process zone, which can be described by the following heat equation [1]:

$$\frac{\partial T}{\partial t} = \frac{\lambda}{\rho \cdot C_S} \cdot \left(\frac{\partial^2 T}{\partial x^2} + \frac{\partial^2 T}{\partial y^2} + \frac{\partial^2 T}{\partial z^2} \right) \tag{6.1}$$

where t is the time (s), T is the temperature (K), λ is the specific thermal conductivity (W/m K), ρ is the density (kg/m^3), and C_S is the specific heat capacity (J/kg K). During the condensation, the phase change generates mass transport at the vapor-condensate boundary.

As the boiling point of the heat transfer fluid is reached, it starts to evaporate and the forming vapor fills the process zone. If the hot vapor meets with colder surfaces (like the wall of the process zone, the cooler pipes, or the soldered assembly after the immersion), it will condense on these surfaces. At the present level of the modeling, the condensate layer formation is neglected, the focus is on the extracted amount of vapor by condensation, and on the transferred heat. For the modeling of the vapor space formation, a continuous and static condensate layer is assumed on the surface of the soldered assembly. The heat and mass transport processes can be described separately between the different phases of the system [2] and connect them at the boundary layers [3].

The static layer structure on the surface of the soldered assembly and transport mechanisms at the boundary layers can be seen in Fig. 6.1, where m_{cn} is the condensation mass transport, E_{cn} is the condensation energy transport, $q_{vp\text{-}cn}$ is the heat diffusion at the vapor-condensate boundary, and $q_{cn\text{-}so}$ is the heat diffusion at the condensate-solid boundary. According to the experimental observations, the average thickness of the condensate layer on the top side of the assembly is between 0.15 and 0.3 mm (depends on given substrate parameters, like material, size, and inclination; see later in deeper details). This layer is formed immediately after the immersion of the assembly into the vapor and its thickness remains near constant during the process caused by the balance between the gravity force and the force acting from the condensate surface tension. In the case of static condensate layer, the 0.25 mm thickness is usually a good estimation for the calculations.

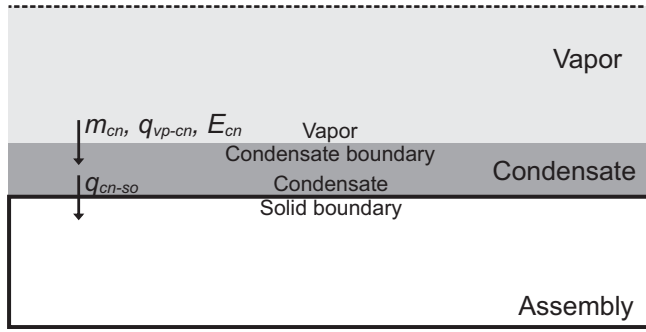

FIGURE 6.1 Layer structure of the condensation model and the transport processes at the boundary layers. *Reproduced with permission from B. Illés, A. Géczy, Investigating the dynamic changes of the vapour concentration in a vapour phase soldering oven by simplified condensation modeling, Appl. Therm. Eng. 59 (2013) 94–100[4].*

The phase change during evaporation as well as during condensation results in mass and energy transport. Both cases can be handled similarly. The transported mass generates energy transport (E), which contains the internal energy and the latent heat of phase changed mass:

$$\frac{\partial E}{\partial t} = (h + C_S \cdot T_b) \cdot \frac{\partial m}{\partial t} \tag{6.2}$$

where h is the latent heat of the heat transfer fluid (J/K), T_b is the given boiling temperature of the heat transfer fluid (K), and m is the phase changed mass (kg). The phase change-induced energy change (Eq. 6.2) has to be proportional with the heat flux into the condensate film (in the case of condensation [3]), or with the additional energy of the boiling heat transfer fluid (in the case of evaporation) [5]:

$$(h + C_S \cdot T_b) \cdot \frac{\partial m}{\partial t} = \lambda \cdot A \cdot \left(\frac{\partial T}{\partial x} + \frac{\partial T}{\partial y} + \frac{\partial T}{\partial z} \right) \tag{6.3}$$

where A is the surface whereon the heat flux is defined (m^2). Reordering Eq. (6.3), we can calculate the phase changed mass:

$$\frac{\partial m}{\partial t} = \frac{\lambda \cdot A}{h + C_S \cdot T_b} \cdot \left(\frac{\partial T}{\partial x} + \frac{\partial T}{\partial y} + \frac{\partial T}{\partial z} \right) \tag{6.4}$$

The phase changes in the system cause vapor concentration gradient, which results in diffusion mass transport in the vapor space. The diffusional mass transport by the Fick law [6]:

$$\frac{\partial \varphi}{\partial t} = D \cdot \nabla^2 \varphi \tag{6.5}$$

where φ is the concentration of the vapor (kg/m^3) and D is the diffusion coefficient of the vapor (m^2/s).

The considerable temperature elevation of the heat transfer fluid causes the thermal expansion of the heat transfer fluid, which can be described with the following expression:

$$\frac{\partial V}{\partial t} = \beta \cdot V \cdot \frac{\partial T}{\partial t} \tag{6.6}$$

where β is the volumetric thermal expansion coefficient of the heat transfer fluid (m^3/m^3 K) and V is the volume (m^3). In a model with fixed geometry, the thermal expansion is easier to be handled by the mass decrease in a given volume and not with the growth of the volume itself:

$$\frac{\partial m}{\partial t} = \rho \cdot \frac{\partial V}{\partial t} = \rho \cdot \beta \cdot V \cdot \frac{\partial T}{\partial t} \tag{6.7}$$

The thermal expansion of the heat transfer fluid results in the "mixing" of itself liquid, typically at the heaters, where the temperature gradient is the largest (this phenomenon decreases the temperature gradient). The mass diffusion in the heat transfer fluid due to the thermal expansion is neglected. The related energy transport can be calculated by the internal energy change of the heat transfer fluid.

The previously defined partial differential equations (PDEs) can be numerically solved by the finite difference method (FDM) [7]. The most simple and compact way for the discretization of the PDEs is the explicit central formula (so-called Forward Time Central Space, FTCS) [8]. Applying the FTCS method, the discretization of first- and second-order PDEs are the following:

$$f'(x) = \frac{f(x+h) - f(x-h)}{2h} \tag{6.8}$$

$$f''(x) = \frac{f(x+h) - 2f(x) + f(x-h)}{h^2} \tag{6.9}$$

where h is the step size.

Eqs. (6.10)–(6.13) show examples for the discretized form of first- and second-order PDEs, which are used. The discretized form of the phase change (pc) induced mass transport (Eq. 6.4, first-order PDE):

$$\Delta m_n^{pc} = \sum_{i=x;y;z} r_i \cdot \left(T_{n+1(i)}(t) - T_{n-1(i)}(t)\right) \tag{6.10}$$

where n is the index of the cells and r is the coefficient of Eq. (6.4):

$$r_x = \frac{\lambda \cdot A}{h + C_S \cdot T_{bl}} \cdot \frac{\Delta t}{2\Delta x}; \quad r_y = \frac{\lambda \cdot A}{h + C_S \cdot T_{bl}} \cdot \frac{\Delta t}{2\Delta y}; \quad r_z = \frac{\lambda \cdot A}{h + C_S \cdot T_{bl}} \cdot \frac{\Delta t}{2\Delta z} \tag{6.11}$$

where Δt is the time step (s) and Δx, Δy, and Δz are the mesh sizes (m). The discretized form of the heat equation (*he*) (Eq. 6.1, second-order PDE) is the following:

$$\Delta T_n^{he} = -2\sum_{i=x;y;z} r_i \cdot T_n(t) + \sum_{i=x;y;z} r_i \cdot \left(T_{n+1(i)}(t) + T_{n-1(i)}(t)\right) \tag{6.12}$$

where r is the coefficient of Eq. (6.1):

$$r_x = \frac{\lambda}{\rho \cdot C_S}\frac{\Delta t}{\Delta x^2}; \quad r_y = \frac{\lambda}{\rho \cdot C_S}\frac{\Delta t}{\Delta y^2}; \quad r_z = \frac{\lambda}{\rho \cdot C_S}\frac{\Delta t}{\Delta z^2} \tag{6.13}$$

(The discretization of the rest of the PDEs can be easily performed according to these examples.) In the case of evaporation (*ev*), the necessary condition of Eq. (6.10) is $\partial T/\partial r > 0$, while the boiling heat transfer fluid has an "energy surplus" for evaporation. In the case of condensation (*co*), the necessary condition of Eq. (6.10) is $\partial T/\partial r < 0$, while the condenser surface has to be colder than the dew point of the vapor and this induces the energy extraction from the vapor. (The dew point calculation of the vapor will be discussed later.)

During the evaporation, if the concentration of the vapor reaches the saturation in a given space, it starts to move toward nonsaturated spaces in the system. This movement is the "saturation movement of the vapor" or "saturation mass transport" [9] and it is several orders of magnitude faster than the diffusion mass transport. Typically, the saturation mass transport is vertical from the bottom to top of the process zone, but the horizontal components are not negligible. This phenomenon can be modeled with simple mass delivery of the excess mass from the saturated cell (the cell, which reaches the maximal mass, m_{max}) to the nonsaturated surrounding cells. The saturation mass transport is weighted according to the directions:

$$\begin{aligned}\Delta m_n^{sat} = &-(m_n(t) - m_{max}) \\ &+ k_{xy} \cdot \sum_{i=x;y} (m_{n+i}(t) - m_{max}) + k_z \cdot \left(m_{n-1(z)}(t) - m_{max}\right)\big|_{m > m_{max}}\end{aligned} \tag{6.14}$$

where k_{xy} and k_z are the weights toward the x, y, and z directions. The exact values of these weights are usually measured by differential pressure measurements (see Chapter 4: Vapor Phase Reflow Soldering Ovens) in the given VPS system, since they depend on the geometry of the process zone as well as the heating device/method of the VPS system. However, the values are usually between $k_{xy} \sim 0.1-0.2$ (toward horizontally) and $k_z \sim 0.5-0.6$ (toward vertically, from to bottom to the top of the process zone) [10]. From the top to the bottom of the process zone, such mass transport is not possible, since the concentration gradient of the vapor always points from bottom to the top of the process zone.

Finally, the mass and energy balances need to be summed for all of the different phases of the system. The mass and energy balances of the vapor (*vp*) are the following (according to Eqs. 6.1, 6.2, 6.4, and 6.5):

$$\Delta m_n^{vp} = \Delta m_n^{ev} - \Delta m_n^{co} + \Delta m_n^{diff} + \Delta m_n^{sat} \tag{6.15}$$

$$\Delta T_n^{vp} = \Delta T_n^{he} + \frac{\Delta m_n^{vp} - \Delta m_n^{co}}{m_n + \Delta m_n^{vp} - \Delta m_n^{co}} \cdot (T_{n+i} - T_n) \tag{6.16}$$

where T_{n+i} is the temperature of the neighboring cells, from where the mass transport arrives. The mass and energy balances of the heat transfer fluid (*liq*) are the following (according to Eqs. 6.1, 6.2, 6.4, 6.6, and 6.7):

$$\Delta m_n^{liq} = \Delta m_n^{co} - \Delta m_n^{ev} + \Delta m_n^{txp} \tag{6.17}$$

$$\Delta T_n^{liq} = \Delta T_n^{he} + \frac{h}{C_n} \cdot \Delta m_n^{co} + \frac{\Delta m_n^{co}}{m_n + \Delta m_n^{co}} \cdot (T_{bl} - T_n) \tag{6.18}$$

where C_n is the heat capacity of the given cell (J/K). The energy balances of the solid (*sol*) structures are the following (according to Eqs. 6.1, 6.2, and 6.6):

$$\Delta T_n^{sol} = \Delta T_n^{he} + \frac{h}{C_n} \cdot \Delta m_n^{co} \tag{6.19}$$

The selection of the appropriate mash, boundary, and initial conditions for the given numerical model is one of the most essential steps of modeling. However, these parameters highly depend on the investigated system. Therefore, in this section, these aspects of numerical modeling are summarized only generally.

First step of the mesh design is to choose the type of the applied mesh. The 2D elements of the mesh are usually quadrat, rhombus, trapeze, or triangle shaped. In a 3D geometry, this will result in hexagonal meshes in the case quadrats, rhombuses, and trapezes, and in tetragonal meshes in the case of triangles. Recently, the application of polygonal meshes—which can contain the mixture of any kind of 2D geometric shape—is also popular. The biggest advantage of the hexagonal and tetragonal meshes is the fixed number and position of neighboring cells in the mesh, which ensures the easy mesh generation and the simple and homogeneous structure of the coefficient matrix of the discretized PDE system. The homogeneous coefficient matrix ensures usually faster calculation speed and easy modification possibilities in the case of any need of such action. However, the biggest disadvantage of the hexagonal and tetragonal meshes is that the mesh generation in the case of "complicated objects" (e.g., different materials with different dimensions or complex shapes) can be unsolvable (in case of rigorous accuracy conditions) or the solution would take long time. Polygonal meshes can describe easily and accurately any kind of structure since they are optimal to generate

inhomogeneous meshes (when the size of the cells can differ even more orders of magnitude if there is a need for such configurations). However, the coefficient matrix of the discretized PDE system in the case of polygonal meshes is usually very inhomogeneous, which results in longer calculation time (compared to the hexagonal and tetragonal meshes).

In the following, we will present a simple hexagonal mesh generation for a batch-type VPS system (which is presented in Chapter 4: Vapor Phase Reflow Soldering Ovens). The mesh contains only cuboid cells. Since equilibrium has to be assumed in all cells, the boundaries of the different materials have to be taken into consideration. The construction of the mesh can be achieved via section planes where the cell boundaries are the section lines of these planes. This method ensures that all neighboring faces of the cells have the same size and all cells can have a maximum of six neighbors. Due to the previous conditions, the coefficient matrix of the PDEs can be generated. Nevertheless, such meshes can be inhomogeneous as well, if the distance of the section planes is varying. The cylindrical and round shaped objects (like heater and cooler pipes) can be meshed with cuboid cells also, which have equivalent volume and surfaces.

Although, the inhomogeneity of the mesh can be increased with the density of the section planes; if there is more than one order of magnitude difference in the dimensions of the different phases/materials in the model, then the previous method could result in the irrational increase of the cell number. The cell number will increase at those parts of the mesh as well where it is not necessary. So, the resulting mesh will have increased calculation requirements. Therefore, in such cases, the application of cosimulation is suggested instead of the application of dense section planes. The embedded mesh structure ensures that the mesh will be refined only at those sections, where it is necessary [4].

In our example, the whole VPS system can be handled with section plane method; also, the soldered assembly can be inserted into the previous description with cosimulation. The horizontal dimension of the soldered assembly (thickness) is one order of magnitude smaller than any other horizontal dimension in the whole oven structure. For the embedded mesh structure, two separated meshes are generated, one for the VPS system and one for the soldered assembly (see Fig. 6.2). As it is visible, the mesh of the soldered assembly is much finer than the mesh of the VPS system. The two different meshes will be used in two different calculations with separated PDEs and numeric solvers. The cosimulation then comprises of the embedding model (in our case, the model of the VPS system) and the embedded model (in our case, the model of the soldered assembly). The models are linked together through the cells of the VPS system in which the soldered assembly is currently located. The models run concurrently and before each calculation step, they change data.

Each calculation step starts with the embedding VPS system model, which defines the actual vapor space parameters (temperature and vapor

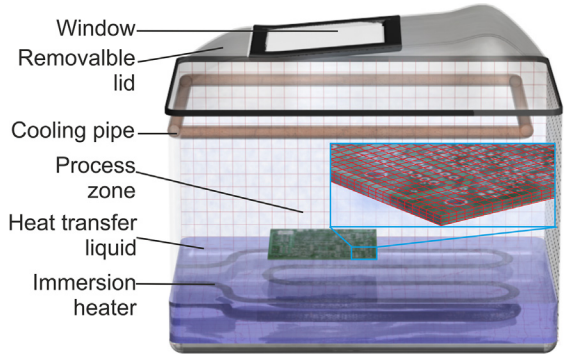

FIGURE 6.2 A batch-type VPS oven with the applied numerical mesh of the process zone and the soldered assembly. *Reproduced with permission from B. Illés, A. Géczy, Numerical simulation of condensate layer formation during vapour phase soldering, Appl. Therm. Eng. 70 (2014) 421–429[11].*

concentration), and gives them to the embedded model. After the embedded model received the actual vapor space parameters, it modifies them according to the condensation on the assembly and gives back the modified vapor space parameters to the embedding model [4]. The biggest advantage of this embedded modeling structure is the reduced complexity (cell number)—compared to the results of simple section plane method—which requires usually much lower calculation capacity.

The applied models contain the following types of simple cells: stainless steel (the wall of the tank and the lid), Galden fluid and vapor, copper (the wall of the cooler pipes). Furthermore, two types of composite cells: the heater pipes as a composite material (wolfram filament in ceramics lining with stainless steel tube) and FR4 substrate cells (glass fiber-reinforced epoxy resin). The physical properties of the composite cells were calculated according to the mass ratio and size ratio of the different composing materials in the cell (the method was presented in Ref. [12]). The applied physical parameters of the materials are presented in Table 6.1.

The initial conditions of the model are the following: the temperature of VPS system is $T_{system}(0) = 25°C$ except the heater and cooler elements. From energetic aspects, the heater and cooler elements are modeled with an infinite source and sink, which have fixed temperatures: $T_{heater}(0) = 238°C$ and $T_{cooler}(0) = 25°C$, respectively. The soldered assembly is immersed into the process zone after 12 minutes preheating of the system, and it has $T_{assembly}(0) = 40°C$ temperature, since the oven structure has some preheating effect on the soldered assembly as well, which is positioned above the lid for immersion. The boundary conditions of the embedded model are the following: the system is adiabatic and hermetic (cannot lose vapor and heat during the operation).

Before the calculations, the last necessary steps are the grid dependency analyses and stability and convergence investigation of the model. The grid

TABLE 6.1 Physical parameters of materials in the model.

Materials	Density (kg/m)	Spec. heat capacity (J/kg K)	Spec. thermal cond. (W/m K)	Latent heat (J/kg)	Diffusion coeff. (cm^2/s)	Thermal exp. coeff. (m^3/m^3 K)
Air	1	1009	0.03	–	–	–
Galden fluid	1820	973	0.77	63,000	10^{-9}	0.1
Galden vapor	19.96[a]	973	0.07	63,000	0.35	–
Stainless steel	8000	500	18	–	–	–
Heater tube	4945	649	22.96	–	–	–
Cooper	8960	390	401	–	–	–
FR4 (PCB)	2100	570	0.25(x, y)[b]; 0.17 (z)	–	–	–

[a] *Saturation vapor concentration.*
[b] *The FR4 has anisotropic heat conduction property.*

dependency means the investigation of the mesh resolution on the calculated results. The execution of the grid dependency analysis is simple: calculations are started with a relatively rougher mesh, which will be refined after each runs, until the numerical results show no significant variation within the confines of reasonable convergence time. When the appropriate mesh resolution is found, the simulations can be performed. Generally, in the case of the VPS system model, an appropriate mesh size is usually between 0.5 and 10 mm, in the case of the assembly model it is between 0.1 and 2 mm. Usually, the modeled systems have some symmetry and this allows us to calculate the model only to the half of the system.

The stability and the convergence criteria of FDM−FTCS method is [13]:

$$r_x + r_y + r_z \leq 0.5 \tag{6.20}$$

where r is the coefficient of the given PDE (see in Eqs. 6.10−6.13) which coefficients depend on the spatial and time steps applied during the calculations. The spatial steps are investigated during the grid dependency analyses; therefore, the last step is to find an appropriate time step for the model. The presented embedded model is stable and the convergence is valid, if the time

step is $\Delta t < 0.26$ seconds in the case of the VPS system model before the assembly would be immersed and $\Delta t < 0.016$ seconds after the immersion of the assembly. The truncation error of FDM−FTCS is O(Δt, Δx^2, Δy^2, Δz^2). Therefore, advantage can be achieved with the decrease of the time step, so in our case, $\Delta t = 0.1$ seconds and $\Delta t = 0.01$ seconds is suggested to be used. Unfortunately, the decrease of the time step increases the number of calculation steps together with the rounding error. The rounding error can be reduced with the application of double words. In order to avoid the large memory demand, the application of sparse vectors is suggested. It means that memory is reserved only for the nonzero elements of the matrix. In addition, the sparse vectors increase the calculation velocity with omitting those calculation steps where they have no elements.

The validation of the vapor phase formation model can be performed via dynamic temperature and pressure measurements. Although the model calculates the concentration of the vapor, the direct concentration measurements are difficult to be performed. However, the comparison of the calculated concentration change and measured pressure change characteristics is possible with the general gas law. The measurement system presented in Chapter 4, Vapor Phase Reflow Soldering Ovens, can be used. For the verification measurements, HT170-type Galden (170°C boiling point) was used. This type of Galden was chosen to achieve relatively faster validation and calculation results since the heating up and cooling down cycles are much shorter than in the case of higher boiling point. (In addition, HT170 is important for soldering with low melting point solder alloys, such as BiSn alloy types.) During the validation of the assembly immersion, an unpopulated FR4 PCB board (with $80 \times 80 \times 1.6$ mm^3 size) was used.

In the first step, the vapor development during the preheating and the saturation of the process zone is validated. Example validation results can be seen in Fig. 6.3; measurements were performed at diagonal location of the process zone: 100 and 150 mm and at three different heights (50, 100, and 150 mm). In the case of the temperature, the measured and calculated results show good agreement, the average relative deviation was 1.71%. Slightly more deviations were observed after the break points of the curves—mainly at the 100 and 150 mm—where increase of the measured values is a bit slower than at the calculated values. This could be probably explained with the fact that adiabatic condition is not an entirely accurate approach between the tank and the environment. There is a small power loss to the outside ambience in this direction.

During the vapor development, a concentration gradient forms in the process zone, which results in a pressure gradient as well. After the temperature saturation at a given height of the process zone, the space below can be considered nearly isothermal (due to the low specific thermal conductivity of the heat vapor). Therefore, the change in the concentration gradient has to be followed by the pressure gradient change with the same characteristics, according to the general gas law.

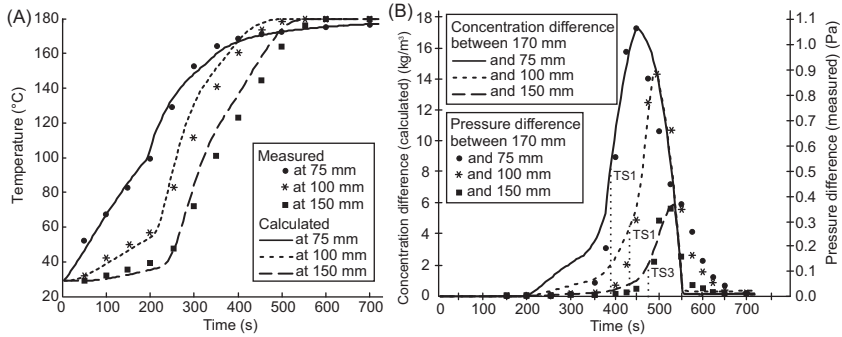

FIGURE 6.3 Comparison of the calculated and measured values: (A) temperature of the vapor space at 100 and 150 mm; (B) calculated concentration and measured pressure differences of the vapor space at 100 and 150 mm. *Reproduced with permission from B. Illés, A. Géczy, Numerical simulation of condensate layer formation during vapour phase soldering, Appl. Therm. Eng. 70 (2014) 421–429.*

The temperature saturation times (over 90%) are marked in Fig. 6.3B with ST1, ST2, and ST3 according to Fig. 6.3A. In the case of the concentration and pressure changes (Fig. 6.3B), we found that the measured and simulated characteristics conformed very well. The measured curves are slightly slower at the inclination and the declination parts than the calculated ones, which effect is caused by the dynamic measurement principle of the differential pressure sensor; it needs a given rate of gas flow for sensing. In our example case study, the best match for the saturation mass transport ratios in Eq. (6.14) was found at $k_{xy} = 0.115$ and $k_z = 0.54$.

In the second step, the vapor space changes are validated after the saturation of the process zone during the immersion of the soldered assembly. The same measurement approach can be applied with one slight modification: the temperature of the assembly is measured instead of the vapor temperature, by embedded thermocouples in the assembly. The thermocouples should be distributed evenly on the surface of the assembly and the average values of the measurements are evaluated (see in more details in Chapter 4: Vapor Phase Reflow Soldering Ovens). Furthermore, the pressure change should be measured below the assembly, to characterize how the oven can reproduce the condensed vapor during the soldering process (since over the assembly, this effect has some delay due to the shadowing effect of the assembly itself; see later in details).

Further aim of these validation measurements can be to determine the dew point model and other parameters of the vapor. According to the definition, if the temperature of a solid subject reaches the dew point, then the condensation stops on its surface. The dew point is always lower than the temperature of the surrounding vapor and it depends highly on the actual

concentration of the vapor. The general approximation of the dew point temperature calculation is the following [14]:

$$T^{dp}(t) = T_{vp}(t) - \frac{1}{k_c}.\left(1 - \frac{m(t)}{m^{st}}\right) \cdot 100 \tag{6.21}$$

where m^{st} is the maximum amount of vapor in a given volume in the case of saturation (kg) (in the case of Galden vapor, it is between 18 and 19.96 kg/m^3) and k_c is a coefficient related to the given material. Unfortunately, there is no available k_c parameter for most of the heat transfer fluids in the literature. The k_c can be determined with the iteration of Eq. (6.21) until the minimum difference between the measured and calculated values is reached [11]. The enthalpy (H (J)) of the Galden vapor is larger than enthalpy of the water vapor, mainly because it has one order of magnitude molecular weight than the water. Therefore, larger entropy change (ΔS (J/K)) is necessary for the phase change to fulfill the Gibbs free energy condition:

$$\Delta G = H - \Delta T \cdot \Delta S < 0 \tag{6.22}$$

Proportionally, the dew point of the Galden vapor is lower than of the water vapor. The k_c value of the water vapor is 1, so the upward iteration can be started from 1. An appropriate value was found at 2.15, see in Ref. [11].

In Fig. 6.4, example validation results can be seen with the following conditions: the pressure changes were measured at the center of the assembly. The immersion velocity of the test board was 50 mm/s, which results in

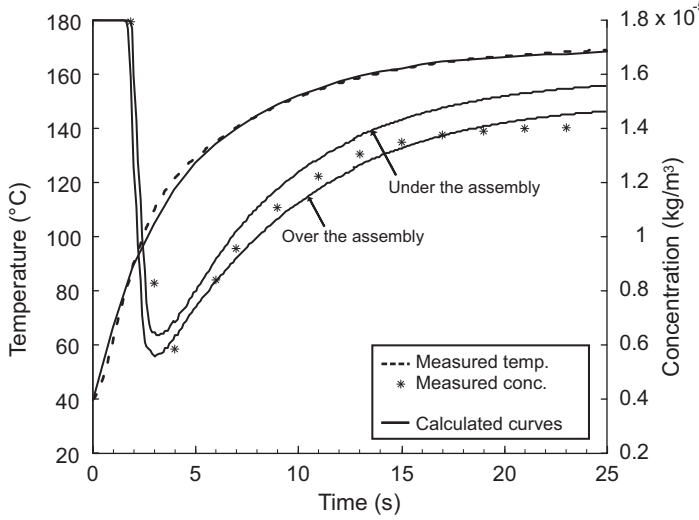

FIGURE 6.4 Change of the vapor space parameters during the immersion of the soldered assembly. *Reproduced with permission from B. Illés, A. Géczy, Numerical simulation of condensate layer formation during vapour phase soldering, Appl. Therm. Eng. 70 (2014) 421–429.*

2-second immersion time until the soldering position (located 70 mm above the bottom of the process zone). With the dew point model ($k_c = 2.15$), the calculated and measured temperature values agree well. In the case of the vapor concentration, the differences are slightly larger. It was probably caused by the low flow rates in the vapor space, which results in measurement failure of the differential pressure sensor (see below). The vapor consumption around the soldered assembly is relatively high 2−3 seconds into the process. The barely visible breaks of the calculated concentration curves indicate that the condensation stops and starts periodically during the process. The "shadowing effect" of the soldered assembly is also visible, which means that vapor reproduction is better under the assembly than over it (as it was expected).

It has to be noted that without the application of dew point model, the vapor would be consumed totally around the assembly in some seconds and it would cause significant calculation errors. Since, the dramatic vapor concentration decrease results in dramatic heat diffusivity decrease of the vapor, this effect limits the heat conduction ability of the vapor (see in details in Ref. [11]). According to the experimental observations, the condensation stops when the soldered assembly reaches the ∼70% of the vapor temperature, and from this moment, the heat conduction from the vapor is dominant in the heating of the assembly. Therefore, the ratio of the heat conduction in the whole heating process can reach even 15%−20%. This is not negligible during any type of calculation in VPS technology.

6.1.1.2 Results of the vapor space formation model

The vapor space formation model can describe the build-up of the vapor space after enabling the heaters. After the saturation of the vapor space, it is able to describe the effect of the immersed assembly on the vapor space as well as the heating up of the assembly. The construction of the given VPS system—like the size and shape of the process zone, the number, positions, and inhomogeneities of the heater and cooler tubes—has considerable effect on the forming vapor space and can delay or even prevent the saturation of the vapor space at given locations.

In the following, we will show an example how the previously presented model can investigate the abilities of a VPS system (from the aspect of vapor space formation). In the first step, temperature and concentration distributions of the vapor space are studied along different section planes from the start of the heating until the saturation of the process zone, in order to find the inhomogeneities of the system. Fig. 6.5 shows the temperature and concentration distributions of the vapor space along the y plane at 150 mm. The top of the Galden fluid is marked by the dark dashed line. The saturation of the vapor concentration began above the inner heater pairs (Fig. 6.5A and B) while the saturation of the vapor temperature started between the heater pairs

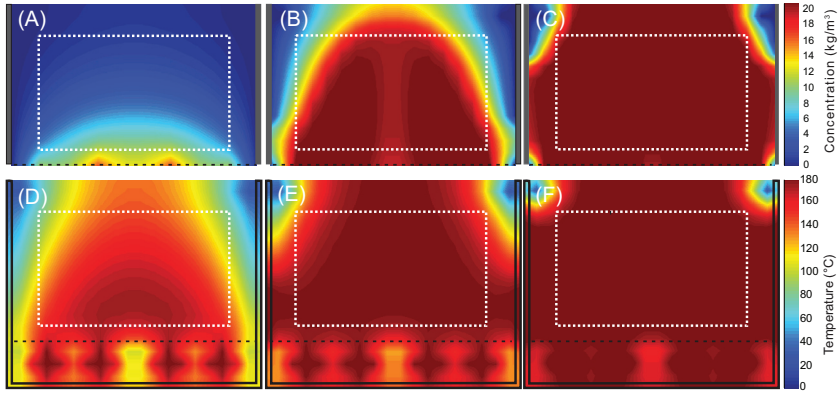

FIGURE 6.5 Temperature and concentration of the vapor along the *y* plane at 150 mm: (A)–(C) vapor concentration at 7, 9, and 12 min; (D)–(F) temperature distributions in the process zone at 7, 9, and 12 min. *Reproduced with permission from B. Illés, A. Géczy, Multi-physics modelling of a vapour phase soldering (VPS) system, Appl. Therm. Eng. 48 (2012) 54–62.*

(Fig. 6.5D and E). It is an interesting result; it would be a straightforward expectation that the temperature of the process zone and vapor concentration saturates together spatially.

This phenomenon can be explained by the following: the evaporation is the most intensive above the closer heater tube pairs due to the higher temperature of the heat transfer fluid in this area while the temperature saturation of the vapor is more rapid in the middle of the process zone due to the cooling effect of the walls. However, it does not cause any problem later, since the phenomenon disappears after a 10 minutes of preheating of the process zone (Fig. 6.5C and F).

According to the obtained results of this simulation, two important parameters can be found. First, the necessary preheating time, which was found to be 12 minutes in the case of the given VPS system. Second, the useful processing volume of the whole process zone where the vapor space is nearly saturated (it is marked by the white dashed rectangles in Fig. 6.5). The cooling system works sufficiently, since at the vicinity of the coolers, the vapor concentration is very low (Fig. 6.5C), so the loss of the vapor has to be very low too.

The investigated VPS oven has an asymmetry in the heater and cooler system along the longer wall (the heater and cooler tube is closer to the right wall as to the left wall, see in Chapter 4: Vapor Phase Reflow Soldering Ovens); therefore, some inhomogeneities of the vapor space can be expected. It has to be the most visible at the middle of the process zone where there is only a short connection between parallel heaters. Fig. 6.6 shows the temperature and concentration distributions of the vapor space along the *x* plane at 100 mm. The top of the Galden fluid is marked by the dark dashed line. The

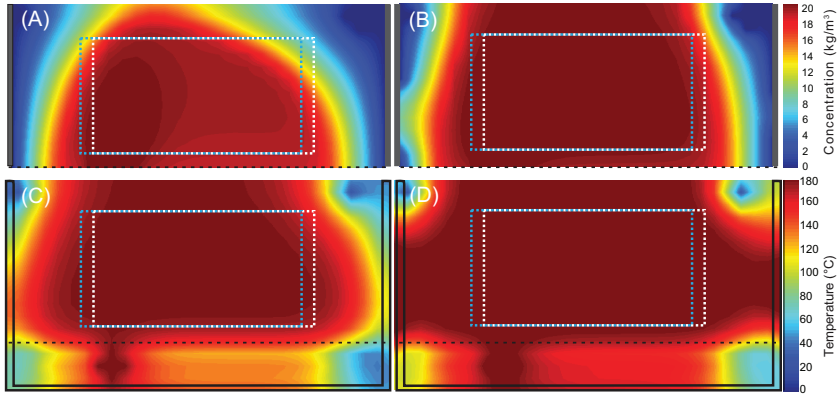

FIGURE 6.6 Temperature and concentration of the vapor along the x plane at 100 mm: (A) and (B) vapor concentration at 7 and 12 min; (C) and (D) temperature distributions in the process zone at 7 and 12 min. *Reproduced with permission from B. Illés, A. Géczy, Multi-physics modelling of a vapour phase soldering (VPS) system, Appl. Therm. Eng. 48 (2012) 54–62.*

asymmetry of the oven causes considerable asymmetry in the saturation of the process zone at the beginning of the preheating process (Fig. 6.6A and C). It almost disappears by the end of the preheating process (Fig. 6.6B and D). Due to the asymmetrical saturation of the process zone, the useful processing volume has to move a bit toward the left walls of the oven (it is marked by the blue dashed rectangles in Fig. 6.6).

After the saturation of the vapor space, the effect of the immersed assembly on the vapor space, and the heating up of the assembly will be investigated along the same section plane, like in the previous cases ($y = 150$ mm and $x = 100$ mm) (Fig. 6.7). The immersion velocity is 50 mm/s. As it was observed during the validation of the model, the immersion of the assembly to be soldered causes a considerable vapor concentration drop, first around itself, later toward the movement of the assembly (Fig. 6.7). It takes 25 seconds until the vapor concentration reaches the 80% level of the saturated velocity state (Fig. 6.7C). The effect of the immersion on the vapor blanket probably depends on the immersion velocity. The results of different immersion velocity can be seen in Fig. 6.8 along the y plane at 150 mm. The change of the vapor blanket is more serious as the immersion speed decreases. This phenomenon can be explained by the following: at slower immersion velocity, the condensation is more inhomogeneous spatially. Most of the condensation takes place at the upper part of the process zone and until the assembly reaches the steady position, the intensity of the condensation decreases. Altogether, a slower immersion perturbs the vapor blanket more than at faster immersion speeds.

It is also an important aspect, how the change of the immersion speed affects the heating of the assembly and the total vapor consumption. The

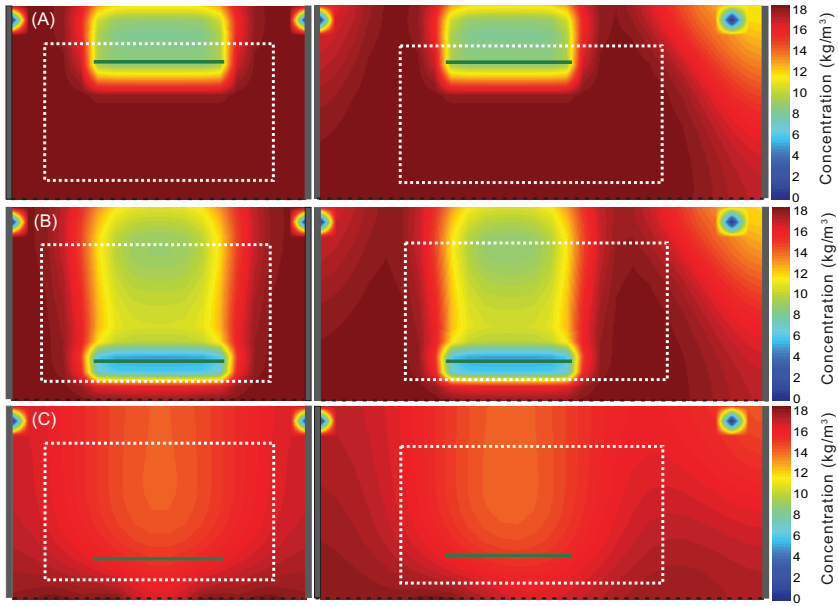

FIGURE 6.7 Vapor concentration along the *y* plane at 150 mm (left) and *x* plane at 100 mm (right) after the immersion: (A) at 1 s; (B) at 3 s; (C) at 25 s [11]. *Reproduced with permission from B. Illés, A. Géczy, Investigating the dynamic changes of the vapour concentration in a vapour phase soldering oven by simplified condensation modeling, Appl. Therm. Eng. 59 (2013) 94–100.*

decrease of the immersion speed decreases the temperature gradient of the assembly at the first 5 seconds of the soldering process and delays the temperature saturation of the assembly (Fig. 6.9). As it was shown in Fig. 6.8, in the case of slower immersion, the vapor concentration decreases more around the assembly and this decreases the heating transfer coefficient. At the soldering steady position of the board, higher concentration delays the temperature saturation.

Since the rapid heating is one of the most serious problems of the VPS process, it can be stated that the decrease of the immersion speed has positive effect on the process, although the differences are not so big. Table 6.2 contains some numerical values about the previous phenomenon, which proves that the thermal profile of the VPS method can be controlled with the immersion speed of the soldered assembly as well and not only with the "heat level" or with "soft vapor" methods (see in Chapter 4: Vapor Phase Reflow Soldering Ovens).

Besides, the total amount of the consumed vapor is also an important aspect, since it influences the processes time via the necessary time to recovery of the system after soldering. Unfortunately, the decrease of the immersion speed increases the total amount of the consumed vapor (Fig. 6.9).

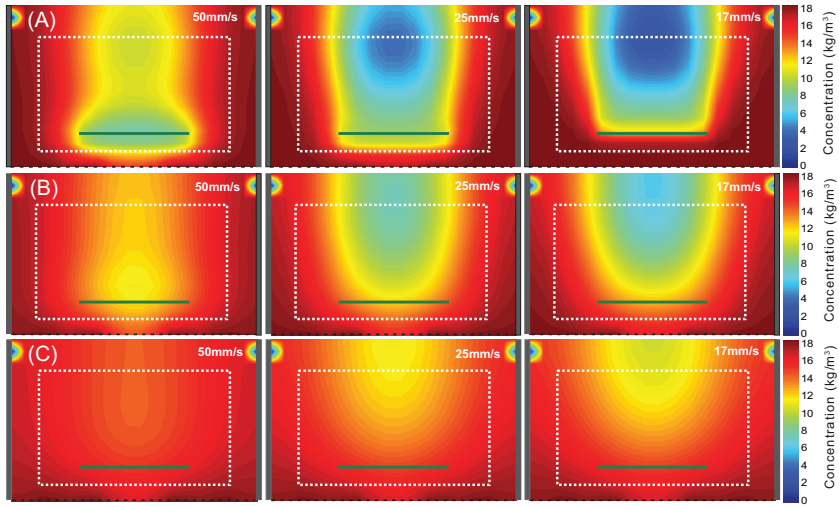

FIGURE 6.8 Vapor concentration along the *y* plane at 150 mm with 50, 25, and 17 mm/s immersion speeds after the immersion: (A) at 1 s; (B) at 3 s; (c) at 25 s. *Reproduced with permission from B. Illés, A. Géczy, Investigating the dynamic changes of the vapour concentration in a vapour phase soldering oven by simplified condensation modeling, Appl. Therm. Eng. 59 (2013) 94–100.*

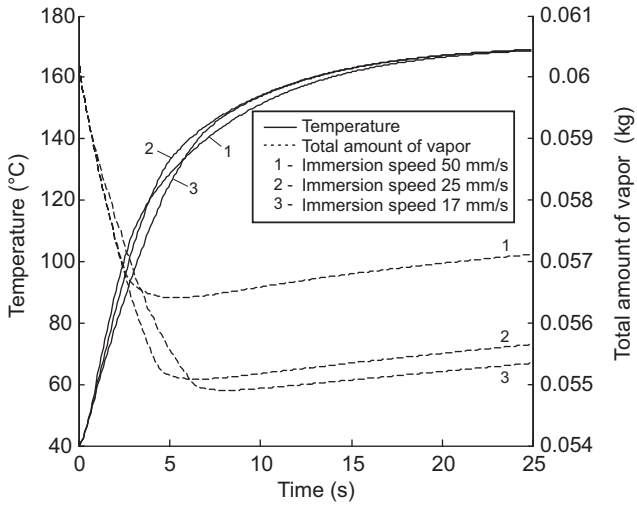

FIGURE 6.9 Temperature profile of the soldered assembly and the consumed amount of vapor during the VPS process in the case of different immersion speeds. *Reproduced with permission from B. Illés, A. Géczy, Investigating the dynamic changes of the vapour concentration in a vapour phase soldering oven by simplified condensation modeling, Appl. Therm. Eng. 59 (2013) 94–100.*

TABLE 6.2 Thermal profile parameters at different immersion speeds of the assembly.

Immersion speed (mm/s)	Gradient of preheating (°C/s)	Saturation starts (°C)
50	22.5	113
25	18.9	130
17	15.2	140

Since in the case of slower immersion, the soldered assembly spends more time at the upper part of the process zone, consequentially, it causes "more efficient" vapor consumption during the movement of the soldered assembly than in the case of faster immersion. Consequently, the slower immersion of the soldered assembly has positive effects on the thermal profile, but unfortunately the process time of soldering will be increased due to the longer recovery time of the system.

6.1.2 Numerical simulation of the condensate layer formation

One major phenomenon was introduced as a simplification in the vapor phase formation model (presented in Section 6.1.1), the static condensate layer. On the level of the process zone, a temperature gradient was not supposed in the assembly; therefore, it was also not necessary to consider the condensate layer to be inhomogeneous and dynamically changing. However, on the level of the assembly, *the dynamic formation of the condensate layer* (condensate layer growth and convectional effects inside the layer); the heat transfer between the condensate layer and the assembly; and any other assembly related questions (like wave formation in the condensate layer, congestion of the condensate layer behind the component) need deeper investigation.

6.1.2.1 Model description

The concept of the condensate layer build-up is the following: after the immersion of the assembly into the process zone, the condensation starts on both sides. Since the position of the assembly during the VPS process is horizontal, the condensation layer will form differently on the top and bottom sides. The area of the components is two orders of magnitude smaller than the area of the substrate; therefore, for the first approximation, the Bejan model for upward facing plate with free edges can be applied on the top side [15]. This model supposes that at the edge of the free surface, nothing holds

the condensate layer and the hydrostatic pressure gradient between the middle and the edges of the free surface initiates the flow of the condensate layer toward the edges. The Bejan model (and it's analytical solution) supposes that the thickness of the condensate layer is zero at the top edges, which results in infinite flow velocity at the edges. During a numerical simulation, such boundary condition is not possible; it is enough if the condensate thickness only tends to zero and the flow velocity only tends to infinite at the edges. For easier understanding, it is assumed that the small SMD components of the assembly are neglected for this time on the top of the assembly PCB.

The condensate flows from the top of the components to the top side and from the top side to the bottom side of the assembly. The dropping of the condensate at the bottom side starts only after the force derived from the surface tension cannot hold the gravity force effects on the condensate layer. The downflowing condensate and later the dropping of the condensate causes the stochastic movements of the condensate layer on the bottom side, which result in such a "wavy structure." The Gerstmann–Griffith model [16] calculated with the phenomena (inc. Taylor instability) at the behavior of the condensate layer on the bottom side of a horizontal plate. The schematic of the dynamic condensate layer model can be seen in Fig. 6.10, according to the aforementioned neglection of the SMD components.

The physics of the condensation process on the surface of the soldered assembly were described in Section 6.1.1.1. The movement of the condensate layer can be described by the continuity equation for incompressible fluids, since in the range of this application, the hydrostatic pressure change has no effect on the density of the heat transfer fluid:

$$\frac{\partial v_x}{\partial x} + \frac{\partial v_y}{\partial y} + \frac{\partial v_z}{\partial z} = 0 \tag{6.23}$$

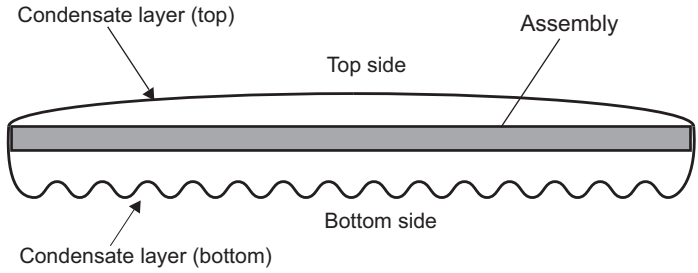

FIGURE 6.10 Dynamic model of the condensate layer formation on the assembly (PCB plate). *Reproduced with permission from B. Illés, A. Géczy, Numerical simulation of condensate layer formation during vapour phase soldering, Appl. Therm. Eng. 70 (2014) 421–429.*

Furthermore, the Navier−Stokes equation for incompressible fluids is necessary to finish the close the governing equations:

$$\frac{\partial v_x}{\partial t} = \sin(\theta)\cdot g_x - \frac{1}{\rho_l}\frac{\partial p_h}{\partial x} + \upsilon\left(\frac{\partial^2 v_x}{\partial x^2} + \frac{\partial^2 v_x}{\partial y^2} + \frac{\partial^2 v_x}{\partial z^2}\right) - \left(v_x\frac{\partial v_x}{\partial x} + v_y\frac{\partial v_x}{\partial y} + v_z\frac{\partial v_x}{\partial z}\right) \tag{6.24}$$

where v is the velocity of the flowing condensate layer (m/s), θ is the inclination angle of the soldered assembly (rad), υ is the kinematic viscosity of the heat transfer fluid (m^2/s), p_h is the hydrostatic pressure of condensate layer (Pa), ρ_l is the density of the heat transfer fluid (kg/m^3), and g is the gravity acceleration (m/s^2). Eq. (6.24) can be expressed for the y and z directions in the same way. Due to the motion of the condensate layer, the basic heat equation (Eq. 6.1 in Section 6.1.1.1) has to supplement with the convective parts:

$$\frac{\partial T}{\partial t} = \frac{\lambda}{\rho_l C_s}\left(\frac{\partial^2 T}{\partial x^2} + \frac{\partial^2 T}{\partial y^2} + \frac{\partial^2 T}{\partial z^2}\right) - \left(v_x\frac{\partial T}{\partial x} + v_y\frac{\partial T}{\partial y} + v_z\frac{\partial T}{\partial z}\right) \tag{6.25}$$

The hydrostatic pressure of the condensate layer, which induces the movement of the condensate layer, is calculated as [15]:

$$p_h = \left(\rho_l - \rho_v\right)\cdot h\cdot g \tag{6.26}$$

where ρ_v is the density of the vapor (kg/m^3) and h is the height of the condensate layer (m). The mass flow (f) of the condensate layer is calculated as:

$$\frac{\partial m_f}{\partial t} = \int_A \rho_l\cdot\overline{v}\cdot \mathrm{d}A \tag{6.27}$$

where A is the surface through which the condensate flows (m^2).

During the VPS process, the temperature difference of the condensate layer can be over 100°C. Therefore, the density and the kinematic viscosity of the heat transfer fluid cannot be constant. These parameters are calculated according to the datasheet of the heat transfer fluid (Galden) [17]:

$$\rho_l(T) = 1820 - 2.133\cdot T \tag{6.28}$$

$$\upsilon(T) = 10^{-6}\cdot\left(0.15 + 5.655\cdot e^{-T/31.67}\right) \tag{6.29}$$

The density depends on the temperature, so height of the condensate layer depends as well:

$$h(T) = \frac{m}{B\cdot\rho_l(T)} \tag{6.30}$$

where B is the base surface (m^2) whereon the condensate height is calculated.

According to the principle of minimum energy [18], the maximum condensate thickness on the bottom side of the assembly—which the surface tension of the heat transfer fluid can hold—is calculated [16] with the following formula:

$$h_{max} = \left(\frac{\sigma}{\cos\theta \cdot g_z \cdot (\rho_l - \rho_v)} \right)^{0.5} \tag{6.31}$$

where σ is the surface tension of the heat transfer fluid (N/m). In the case of zero inclination, h_{max} is $\sim$1.05 mm. This means that the dripping of the condensate layer initiates after reaching this thickness. During the dripping, the condensate layer thrives for the surface with the minimum energy as well; in other words, the condensate layer tends to decrease the spatial hydrostatic pressure differences. Therefore, the condensate layer thickness decrease caused by the dripping (dr) is calculated (with application of Eqs. 6.26 and 6.30):

$$\frac{\partial h_{dr}}{\partial \overline{r}} = \frac{1}{\rho_l \cdot g_z} \cdot \frac{\partial p_h}{\partial \overline{r}} \tag{6.32}$$

where $\overline{r}$ is the local vector. It has to be noted: now the goal is only to approximate the dynamic change of the condensate layer thickness on the bottom side (which is an important factor of the heating) and not to perform a detailed investigation on the dripping phenomenon. Furthermore, the condensate layer and its heating effect on the vertical sides of the substrate are neglected, since the vertical surfaces are two orders of magnitude smaller than the horizontal surfaces.

The last thing which we need to handle is the forming of the condensate on the components. Since the surface of the components is two orders of magnitude smaller than the area of the substrate, the full dynamic approach to calculate the condensate layer flow from the components is not recommended (it would cause considerable increase of calculation time). So, a half-dynamic approach is introduced, which means that only the mass transfer is estimated for approximating the steady-state condensate thicknesses both on the walls and on the top of the components. The steady-state condensate thicknesses (τ) are calculated in each calculation step according to Bejan's approximation [15]:

$$\tau_{max\_top} = \frac{1.28}{\left[\frac{\left(h + 3/8 C_s (T_b - T_l)\right)(\rho_l - \rho_v) g}{\lambda_l (T_b - T_l) \upsilon_l (L/2)^2} \right]^{1/5}} \tag{6.33}$$

$$\tau_{max\_wall} = \left[\frac{\lambda_l (T_b - T_l) \upsilon_l}{\left(h + 3/8 C_s (T_b - T_l)\right)(\rho_l - \rho_v) g} 4z \right]^{1/4} \tag{6.34}$$

where T_l is the temperature of condensate layer (K), L is the characteristic length of the top surface (practically the half width of a surface) (m), and z is the length of the wall (m).

The previously described PDEs can be discretized with the FDM−FTSC method as well (presented in Section 6.1.1.1). Here, only the numerical form of Navier−Stokes equation (Eq. 6.24) and convective heat equation (Eq. 6.25) are presented. They are more complex than the equations in Section 6.1.1.1, from the aspect that they contain first- and second-order derivatives as well. The Navier−Stokes equation (Eq. 6.24) has the following numerical form:

$$\begin{aligned}\Delta v_{x(n)} = g_x - \left[r_{x1}\left(p_{h(n+1)}(t) - p_{h(n-1)}(t)\right)\right] \\ + \sum_{i=x;y;z} -2r_{i,2}\cdot v_{x(n)}(t) + r_{i,2}\left(v_{x(n+1)}(t) + v_{x(n-1)}(t)\right) \\ - \sum_{i=x;y;z} v_{i,(n)}(t)\left[r_{i,3}\left(v_{x(n+1)}(t) - v_{x(n-1)}(t)\right)\right]\end{aligned} \tag{6.35}$$

where the coefficients are the following:

$$r_{x1} = \frac{1}{\rho_l}\frac{\Delta t}{2\Delta x}; \quad r_{x2} = \upsilon\frac{\Delta t}{\Delta x^2}; \quad r_{x3} = \frac{\Delta t}{2\Delta x}; \quad r_{y1} = \frac{1}{\rho_l}\frac{\Delta t}{2\Delta y}\cdots \tag{6.36}$$

The other equations and their coefficients toward the different directions can be written in the same way. The numerical form of the convective heat equation (Eq. 6.25) is the following:

$$\begin{aligned}\Delta T^{he}_{(n)} = \sum_{i=x;y;z} -2r_{i,1}\cdot T_{(n)}(t) + r_{i,1}\left(T_{(n+1),i}(t) + T_{(n-1),i}(t)\right) \\ - \sum_{i=x;y;z} v_{i,(n)}(t)\left[r_{i,2}\left(T_{(n+1),i}(t) - T_{(n-1),i}(t)\right)\right]\end{aligned} \tag{6.37}$$

where the coefficients are the following:

$$r_{x1} = \frac{\lambda}{\rho\cdot C_S}\frac{\Delta t}{\Delta x^2}; \quad r_{x2} = \frac{\Delta t}{2\Delta x}; \quad r_{y1} = \frac{\lambda}{\rho\cdot C_S}\frac{\Delta t}{\Delta y^2}\cdots \tag{6.38}$$

The mass and energy balances of the dynamic condensate layer (*dc*) are the following (according to Eqs. 6.23−6.27, 6.31, and 6.32):

$$\Delta m^{dc}_n = \Delta m^{co}_n + \Delta m^{f}_n - \Delta m^{dr}_n \tag{6.39}$$

$$\Delta T^{dc}_n = \Delta T^{he}_n + \frac{h}{C_n}\cdot\Delta m^{co}_n + \frac{\Delta m^{co}_n}{m_n + \Delta m^{co}_n}\cdot(T_{bl} - T_n) \tag{6.40}$$

The mass transfer estimation of the half-dynamic model is the following: each cell gives the excess amount of the condensate ($\tau_{max} - \tau_n$) to the

neighboring cell(s). The affected neighboring cell(s) are appointed by the direction of the gravitational force field at the given part of the model. The mass transfer is calculated:

$$\Delta m_n = (\tau_{max} - \tau_n)\rho_l x_n y_n \big|_{\tau_{max} > \tau_n} \tag{6.41}$$

where x_n and y_n are the lateral dimensions of the cell (m).

With the the dynamic condensate layer model, we will investigate the following cases: local and spatial formation of the top and bottom condensate layers on horizontal and inclined assemblies local and spatial change of the heat transfer coefficient (HTC) on different substrate materials; and finally the effects of the components on the condensate layer formation. In addition to the concept of inclination: $\theta < 10$ degrees, inclination over 10 degrees is not allowed due to any possible movement of the components to be soldered during the process.

Condensate layer formation is investigated on PCB substrates with $80 \times 80\ mm^2$ areas. Five different substrate materials were studied: FR4, polyimide, Alumina 94% (Al_2O_3), glass-ceramic ($Al_2O_3 + Ca(Si,Al)_4O_8$) and Insulated Metal Substrate (IMS). Alumina is one of the most widely used, general-purpose technical ceramics, for example, substrate material in thick film electronics. Glass-ceramic materials are used as substrate material in Low Temperature Cofired Ceramic (LTCC) electronics. (In both cases, soldering is applied for component joining onto the substrates.) Table 6.3 contains the applied physical parameters of the investigated materials.

In the case of FR4 substrate, the effects of the substrate shape were also investigated. Studied aspect ratios were 1:1 (substrate size was $80 \times 80\ mm^2$), 1:2 (substrate size was $56.5 \times 113.3\ mm^2$), 1:3 (substrate size was $46 \times 139.1\ mm^2$), and 1:4 (substrate size was $40 \times 160\ mm^2$), the area was the same $\sim 6400\ mm^2$ in all cases. During these studies, Galden fluid with 170°C boiling temperature (HT170) was applied.

During the investigation of the component's effects on the condensate layer formation, a 4036 SMD PET capacitor (size: $10 \times 9 \times 5.5\ mm^3$) was used. This component belongs to the family of polymer film capacitors. The base of the component is polyethylene terephthalate (PET—as a dielectric material) with Al electrodes. The components have cap-type metallization prepared from 150 μm thick Al sheets, covered by Sn surface finishing. The structure of the solder pads holds a 17 μm thick copper layer covered by 2 μm thick chemical tin layer (surface dimensions: $9 \times 2.4\ mm^2$). The data were based on component manufacturer datasheets. The thickness of the deposited SAC305 solder paste was considered to be 125 μm, and the parameters of HS230-type Galden (boiling point 230°C) were applied during the calculations. A general soak-type thermal profile was set with three different soak temperatures: 140°C (low), 160°C (normal), and 180°C (high) soak temperatures. This simulation focuses on the further investigation of the soak

TABLE 6.3 Substrate material properties.

Materials	Density (kg/m^3)	Specific heat capacity (J/kg K)	Specific heat conductivity (W/m K)	Volumetric heat capacity (kJ/m^3 K)	Thermal diffusivity (m^2/s)
FR4	2100	570	0.25(x,y); 0.17(z)[a]	1197	2e − 7
					1.4e − 7
Polyimide	1420	1090	0.12	1548	0.8e − 7
Alumina 94%	3690	880	18	3247	55e − 7
IMS[b]	2580	1530	3	3947	7.6e − 7
Glass-ceramic[c]	3100	989	4	3066	13e − 7

[a] *FR4 has different lateral and horizontal thermal conductivity.*
[b] *IMS is composed from 0.15 mm FR4 on 0.85 mm aluminum.*
[c] *DuPont GreenTape 951 material.*

and ramp periods, which are critical for reflowing appropriately the deposited solder paste. The heat conductivity of the solder paste is calculated according to the Maxwell model for colloid suspensions [19]:

$$\lambda_{paste} = \lambda_w \left(1 + \frac{3\left(\lambda_{SAC}/\lambda_w - 1\right) v_f}{\left(\lambda_{SAC}/\lambda_w + 2\right) - \left(\lambda_{SAC}/\lambda_w - 1\right) v_f} \right) \tag{6.42}$$

where λ_w and λ_{SAC} are the specific heat conductivities (W/(m K)) of the carrier fluid (water) and the SAC alloy; and v_f is the volume friction ($\sim$0.5 in this suspension). The applied material properties are collected in Table. 6.4.

During the meshing, the stability and convergence criteria (Eq. 6.20) have to be applied and due to the application of the Navier−Stokes equation, the Courant−Friedrichs−Lewy (CFL) condition has to be taken in to consideration as well [20]. In the case of the investigations on pore substrates, the cell dimensions vary between 0.5 and 2 mm (10,000−15,000 cells) and the time steps between 0.125 and 1 ms (mainly depends on the degree of inclination). When components are also applied, the cell dimensions vary between 1 and 300 μm (70,000−80,000 cells) and the time steps between 0.1 and 0.4 ms. The symmetries of the system (discussed in Section 6.1.1.1) usually allow us to calculate only the quarter or the half of the geometrical model.

Since the dynamical condensate layer is only the extension of the vapor space formation model, all the boundary and initial conditions presented in Section 6.1.1.1 are still valid. Further initial conditions for the dynamic condensate layer are: $v(0) = 0$ m/s, $p_h = 0$ Pa, and $m(0) = 0$ kg (the condensate

TABLE 6.4 Component and solder joint material properties.

Materials	Density (kg/m^3)	Specific heat capacity (J/kg K)	Specific heat conductivity (W/m K)
PET	1400	1200	0.3
Cu	8960	385	385
SAC	4185/7370[a]	2542/2320[a]	2.29/58[a]
Al	2700	900	220

[a]*Paste/liquid state.*

layer is not present before the process) and boundary conditions are: $\lim p_h = 0$; $\lim v = \infty$ (top side) and $v = 0$ (bottom side).

The validation of the dynamic condensate layer formation model cannot be performed with the measurements of layer thicknesses inside the heated oven. However, the change of the condensate layer thickness effects on the thermal diffusivity of the layer, so the change of the condensate layer thickness can be validated with temperature measurements of the soldered assembly. Measurements were performed with K-type thermocouples (TCs) having an absolute measurement accuracy of $\pm 0.5°C$. TCs were embedded into the FR4 substrate at the middle and at one corner of the substrate. The validation results are shown in Fig. 6.11, at the edge and at the middle of the substrate. The results of the static condensate layer are also presented in Fig. 6.11. In the case of the static condensate layer model, no temperature difference is supposed in the substrate. The dynamic condensate layer model shows significant improvement, and the absolute calculation error decreased from 5% to 1% compared to the static condensate layer model.

6.1.2.2 Formation of the condensate layer on horizontal and inclined substrates

First, the condensate layer formation on the top and bottom sides of a horizontal FR4 substrate will be investigated. On the further condensate layer visualizations, the following parameters are presented: the thickness and the temperature of the condensate layer and the $x-y$ projection of the velocity vectors. Different scaling of the z-axis was applied due to the better visualization of the condensate layer thickness; however, it causes a minor visual distortion in the representation. The edges of the surfaces are truncated to better visualization of the velocity vectors. They represent the direction of the flow and the relative velocity differences. (Detailed discussion of the absolute velocity values will be presented later.)

The formation of the condensate layer on the top side of the substrate can be seen in Fig. 6.12. The condensation is very intense after the immersion of

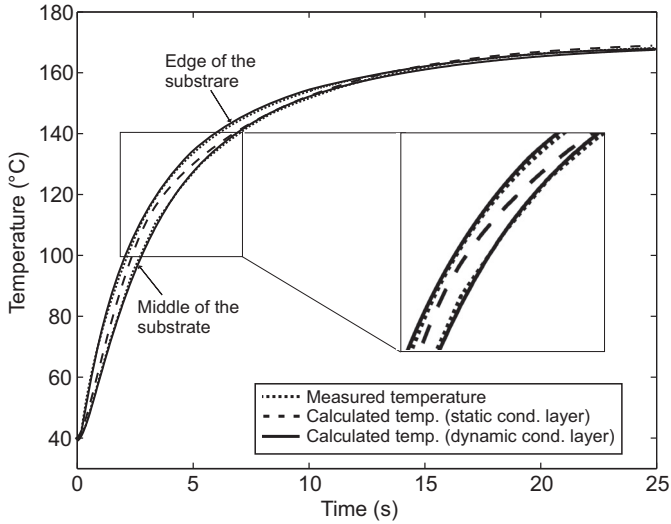

FIGURE 6.11 Validation results of the dynamic condensation layer model. *Reproduced with permission from B. Illés, A. Géczy, Numerical simulation of condensate layer formation during vapour phase soldering, Appl. Therm. Eng. 70 (2014) 421–429.*

the assembly into the vapor space. The thickness of the condensate reaches 100 μm at 0.5 second (Fig. 6.12A). The fast thickness increase results in high hydrostatic pressure gradient in the layer between the middle and the edges, which causes sudden velocity increase of the condensate towards the edges (Fig. 6.12A and B). This results in the fast decrease of the condensate layer thickness at the edges (Fig. 6.12B). During the first second, a slight corner effect (numerical error) is observable both in the temperature and the thickness values. Between 1.5 and 2 seconds, the condensate thickness reaches the maximum value over 200 μm (Fig. 6.12C); then the layer thickness is decreasing, since the condensing mass is less than the mass of the downflowing fluid. However, the decrease of the layer thickness is not as fast as the increase was. Since the flow velocity is decreasing in the decreasing layer due the convective components of the Navier–Stokes equation (Fig. 6.12C). Further condensation can be observed to 4 seconds (Fig. 6.24D) when the temperature reaches the dew point in the whole layer (at the edges, it happens a bit faster).

Considerable temperature gradients (~4°C–8°C) form in the condensate layer between the middle and the edges. During the first 0.5 second, the condensate layer is colder at the edges, since the thinner condensate at the edges has smaller heat capacity and cool down faster as the thicker condensate at the middle. After 0.5 second, this trend reverses due to the heat convection effect (Eq. 6.25). After 2 seconds, the temperature gradients in the condensate layer decrease; however, they remain over zero during the whole

soldering process. These temperature gradients affect the heating of the soldered assembly; therefore, this phenomenon will be investigated later.

Fig. 6.13 presents the condensate layer parameters, where the zero level is at the bottom of the substrate. Besides the intense condensation, the downflowing condensate form the top side also accumulates on the bottom side. These effects results in the even faster thickness increase as on the top side, after 1 second the condensate layer thickness reaches $\sim$200 μm. The continuously downflowing condensate initiates waves on the bottom side (Fig. 6.13) as it was expected by the Gerstmann and Griffith's model and the so-called Taylor instability.

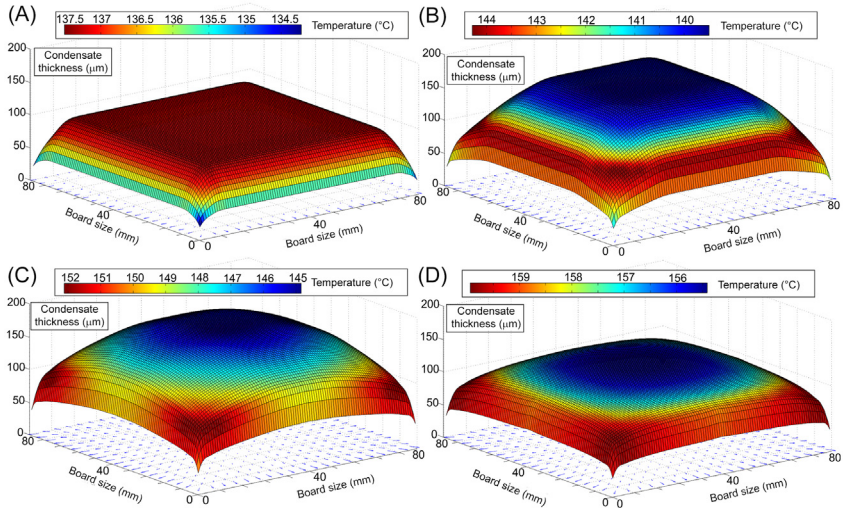

FIGURE 6.12 Condensate layer on the top side: (A) at 0.5 s; (B) at 1 s; (C) at 2 s; (D) at 4 s. *Reproduced with permission from B. Illés, A. Géczy, Numerical simulation of condensate layer formation during vapour phase soldering, Appl. Therm. Eng. 70 (2014) 421–429.*

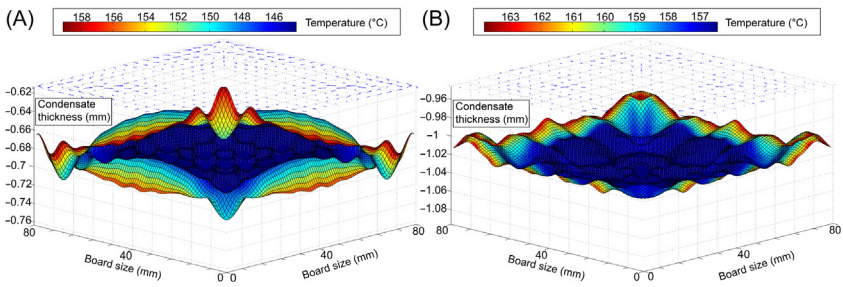

FIGURE 6.13 Condensate layer on the bottom side: (A) at 4 s; (B) at 11 s. *Reproduced with permission from B. Illés, A. Géczy, Numerical simulation of condensate layer formation during vapour phase soldering, Appl. Therm. Eng. 70 (2014) 421–429.*

After 11 seconds at some points, the condensate layer thickness reaches the maximum value ($h_{max} = \sim 1.05$ mm) and the dropping starts (Fig. 6.13B). After this, the increase of the condensate layer thickness stops and equalizes around 1.05 mm level. The downflowing condensate and the dropping results in a disordered flow field on the bottom side without dominant flow direction. Generally, the temperature distribution is more homogeneous on the bottom side than on the top side, except at the edges where the maximum temperature difference reaches 14°C. It is caused by the combined effect of the relatively equalized condensate thickness, by the huge amount of downflowing condensate from the top side and by the temperature difference between the top and bottom sides of the condensate layers. The much thinner condensate layer on the top side is warmer due to its higher heat diffusivity.

In Fig. 6.14, the condensate thicknesses and the absolute flow velocities are analyzed from the middle towards a corner and towards a side of the substrate during the whole period of heating. On the top side the rapid velocity increase between 0 and 1.5 seconds (Fig. 6.14C) results in break points on the condensate thickness increase (Fig. 6.14A). The thickness increase is slowing (sometimes changes to decrease) when the velocity increase starts. The dew point—where the condensation stops—is also visible in Fig. 6.14A; after the dew point, the thickness decrease is even faster. To the end of the process (25 seconds), the condensate layer thickness decreases under 10 μm on the top side. The flow is more intense towards the corners than the sides.

On the bottom side (Fig. 6.14B and D), during the first 11 seconds, the maximum condensate thickness differences are between 10% and 15%; after the start of the dropping, it decreases to 1%−2% (Fig. 6.14B). As it was previously discussed, the flow field is disordered on the bottom side (Fig. 6.14D) and the maximum velocity values are 15 times smaller compared to the top side (Fig. 6.14C). The flow analysis of the bottom side shows that the condensation starts again for a short time after the general dew point at 4 seconds. The same is barely visible on the top side as well, via a minor velocity increase (Fig. 6.14C). As it was shown in Figs. 6.12 and 6.13, considerable temperature gradients can form in the condensate layer, which can cause differences in the heating along the soldered PCB surface during the VPS process. The temperature analyses of the assembly can be seen in Fig. 6.15. Although the temperature gradients in the assembly are smaller (Fig. 6.15A and B) than in the condensate layer (Figs. 6.12 and 6.13), the maximum of difference can reach 7°C between the edges and the middle of the assembly. Therefore, it is suggested to define keep-out zones at the edges of the assembly whereon components are not suggested for placement. From the middle till the 75% of the characteristic length of the assembly, the temperature gradients are under 3°C, which is generally acceptable and considered to be excellent in the case of reflow soldering technologies. But after the 75% of the characteristic length from the center

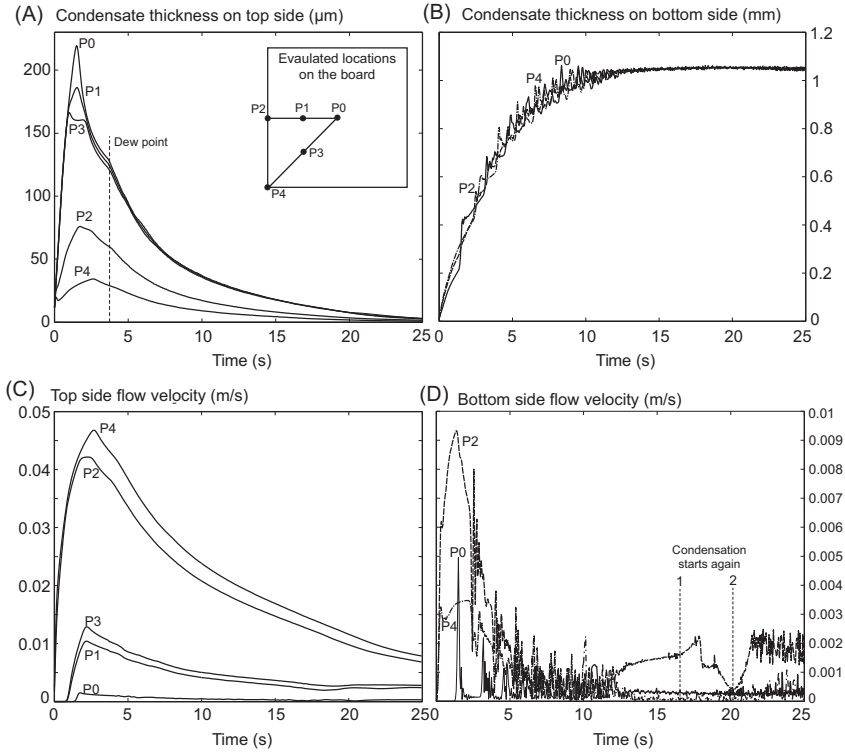

FIGURE 6.14 Condensate layer parameters: (A) condensate thickness on the top side, (B) condensate thickness on the bottom side, (C) top-side flow velocity, (D) bottom-side flow velocity. *Reproduced with permission from B. Illés, A. Géczy, Numerical simulation of condensate layer formation during vapour phase soldering, Appl. Therm. Eng. 70 (2014) 421–429.*

toward the edges, the temperature gradients increase considerably; therefore, the placement of the components onto this area is not suggested.

The thermal profile analyses show (Fig. 6.15C) that the heating of the top side of the assembly is more intensive than the heating of bottom side. This is caused by the $\sim$10 times thinner condensate layer on the top side than on the bottom side, which ensures much efficient heat transfer on the top side than on the bottom side. After 5 seconds of the immersion, the maximum temperature difference can reach even 14°C between the same locations on the top and bottom sides. The relatively high temperate differences between the top and bottom sides do not cause any soldering failures during the VPS process; however, it has to take into consideration during the thermal profile setting/optimization of the VPS process.

In real soldering ovens, it is a constructional goal to ensure that the assembly is in total horizontal position during the VPS process. However,

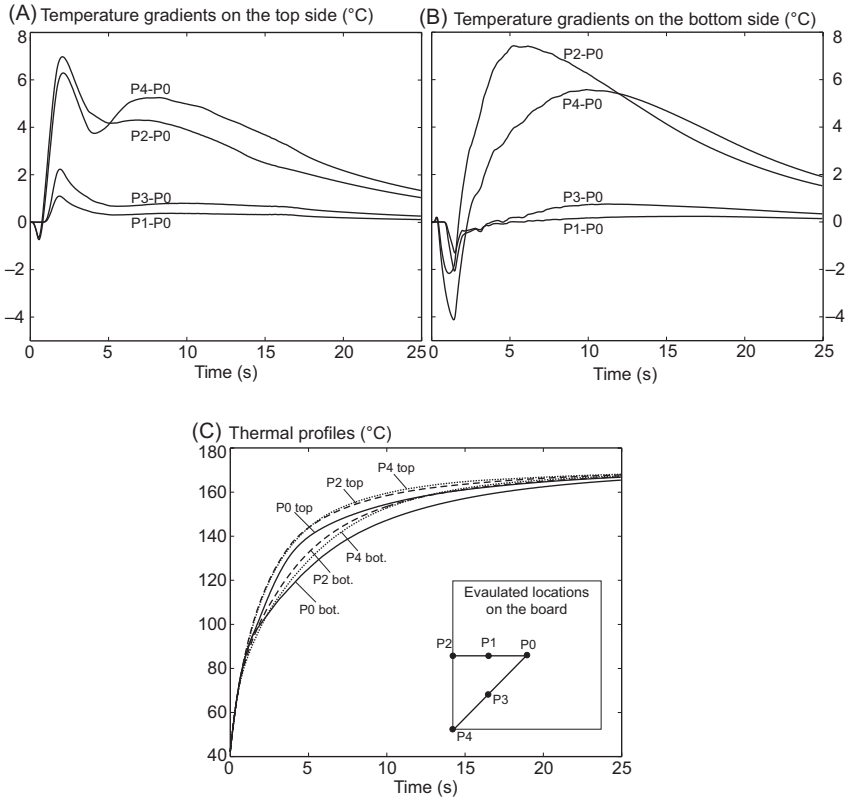

FIGURE 6.15 Temperature analyses of the soldered assembly: (A) temperature gradients on the top side of the assembly, (B) temperature gradients on the bottom side of the assembly, (C) thermal profiles. *Reproduced with permission from B. Illés, A. Géczy, Numerical simulation of condensate layer formation during vapour phase soldering, Appl. Therm. Eng. 70 (2014) 421–429.*

minor inclinations can occur, and these inclinations may have nonnegligible effects on the condensate layer formation and on the heat transfer. Lips and Meyer [21] found that the inclination has considerable effect on the condensate layer thickness and therefore on the heat transfer coefficients. Meyer et al. [22] as well as Lips and Meyer [23] showed that the inclination has an optimal angle from the point of condensate layer formation and heat transfer. Therefore, in the second step, we will investigate how the inclination of the FR4 substrate affects the condensate layer formation via this on the heating of the assembly. It was found during our investigations [11] that thermal cross effects are negligible between the sides of the FR4 substrates since this material has low specific thermal conductivity. In addition, the phenomena on top side are significant from the aspect of soldering. Therefore, in this research, we investigate only on the top side of the PCB. The inertia system

of the inclined substrate can be seen in Fig. 6.16. Furthermore, stationary and saturated boundary conditions will be applied for the vapor space in order to separate the effects of inclination from the effects of the practically possible instationary and nonhomogeneous vapor space conditions (as it was shown in Section 6.1.1).

In Fig. 6.17, the condensate layer parameters on the top side (thickness, temperature, and $x-y$ projection of the relative flow velocity vectors) at 2 seconds are presented at different inclination angles. The 2-second time point was chosen to show the more significant parameter differences of the condensate layer. Fig. 6.17A shows the basic horizontal case; as the inclination angle increases, the condensate layer becomes more and more asymmetric along the x-axis (Fig. 6.17B–H). Maximum condensate thickness with minimum temperature moves from the middle of the substrate toward the lowered y edge (defined in Fig. 6.16). Minimum condensate thickness with maximum temperature is located at the lifted corners. The condensate layer becomes more and more homogeneous with the increase of inclination, since the inclination increases the flow velocity of the condensate layer toward the lowered y edge. This results in the decrease of condensate thickness as well with the decrease of spatial condensate thickness differences. The smaller spatial condensate thickness differences decrease the temperature gradients in the condensate layer, which results in more homogeneous heating of the soldered assembly (see later). Inclination between 0.5 and 2 degrees forms moderate waves in the condensate layer (Fig. 6.17D–F), which disappear over 2 degrees of inclination due to higher flow velocities (Fig. 6.17G and H). This phenomenon does not affect the heat transfer during the VPS process.

Fig. 6.18 shows thickness differences of the condensate layer and the temperature differences of the substrate between the middle and the lowered corners of the substrate. This presentation is useful since there is a strong relation between condensate thickness and heat transfer. Thinner condensate layer has higher heat diffusivity. The increase of inclination decreases the thickness difference of the condensate layer between middle and lowered corners (Fig. 6.18A). This decreases the temperature differences between the given points (Fig. 6.18B). At 10 degrees of inclination, the maximum

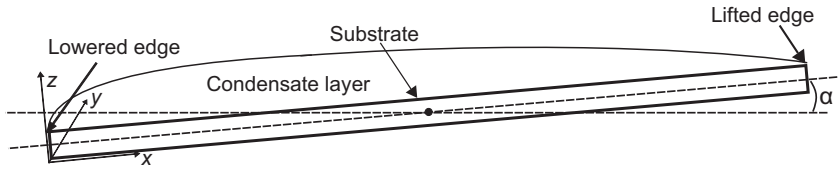

FIGURE 6.16 The inclined substrate. *Reproduced with permission from B. Illés, A. Géczy, Investigating the heat transfer on the top side of inclined printed circuit boards during vapour phase soldering, Appl. Therm. Eng. 103 (2016) 1398–1407[24].*

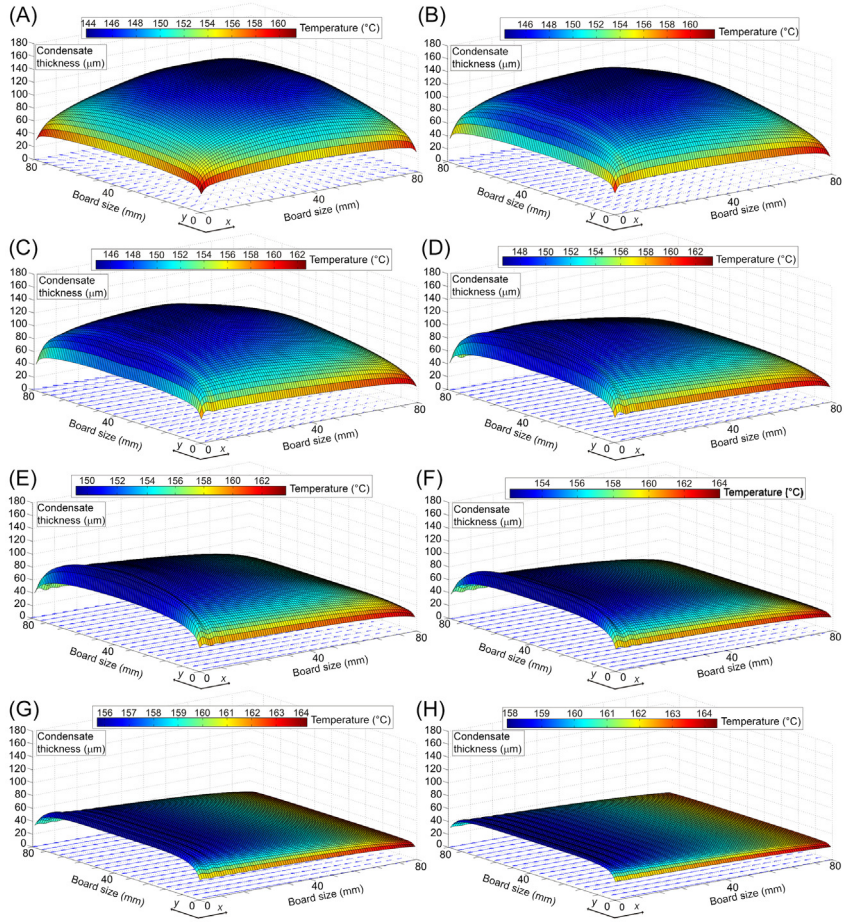

FIGURE 6.17 Condensate layer on the top side at 2 s: (A) inclination angle 0 degree; (B) inclination angle 0.1 degree; (C) inclination angle 0.2 degree; (D) inclination angle 0.5 degree; (E) inclination angle 1 degree; (F) inclination angle 2 degrees; (G) inclination angle 5 degrees; (H) inclination angle 10 degrees. *Reproduced with permission from B. Illés, A. Géczy, Investigating the heat transfer on the top side of inclined printed circuit boards during vapour phase soldering, Appl. Therm. Eng. 103 (2016) 1398–1407.*

thickness difference is only 19 μm with 3°C maximum temperature difference. Between middle and lifted corners, we would see the similar effects of the inclination, however, on a bit moderate way. The thickness difference of the condensate layer decreases only from 0.5-degree inclination and it is less considerable as in the case of the lowered corners. At of 10-degree inclination, the maximum thickness difference remains 35 μm with 6°C maximum temperature difference. The small differences between lowered and lifted corners are caused by the following effect: on the lowered part of the

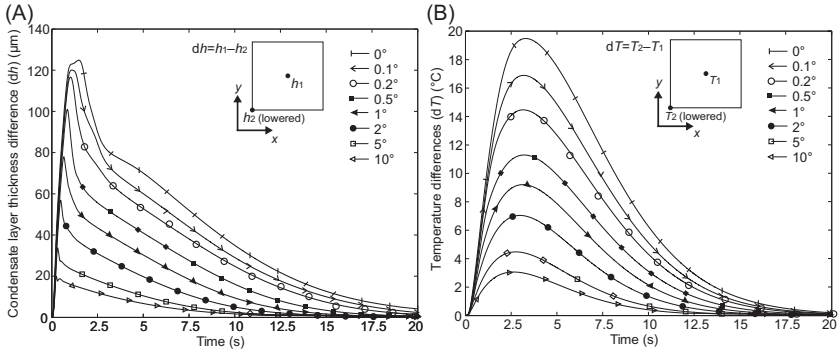

FIGURE 6.18 Differences between the middle and the lowered corner in the case of different inclinations: (A) thickness differences of the condensate layer; (B) temperature differences of the substrate. *Reproduced with permission from B. Illés, A. Géczy, Investigating the heat transfer on the top side of inclined printed circuit boards during vapour phase soldering, Appl. Therm. Eng. 103 (2016) 1398–1407.*

substrate, the flow velocity increase monotonously with the inclination. While on the lifted part of the substrate, first the flow toward the lifted edge slows down and only after a given time, it turns toward the lowered edge. This causes some delay in the decrease of the condensate thickness differences there.

The results between the middle and the edges of the substrate are also very similar to the results between the middle and the corners of the substrate (as in Fig. 6.18). A minor difference is that at the lowered edge, the higher inclinations (between 5 and 10 degrees) cause such a high mass flow increase, which can push the condensate thickness as well as the temperature differences below zero. This means higher condensate thickness with higher temperature at the lowered edge than at the middle of the substrate, as it can be seen in Fig. 6.17. However, this phenomenon is not so serious at 10-degree inclination, the maximum difference is only -15 μm and -2.1°C. At the lifted edge, the smaller inclinations (between 0 and 0.2 degree) show a minor negative effect on the temperature differences, since it increases 2°C, compared to the horizontal case. The effect of inclination turns to positive over 0.5 degree similarly like at the lifted corners.

The inclination has an inevitable negative effect, since it causes condensate thickness and heat transfer differences between opposite parts of the substrate, which differences do not exist at horizontal position. Between the lowered and lifted edges (Fig. 6.19A and B), the thickness of the condensate layer as well as the temperature differences of the substrate increases until 1-degree inclination angle. Maximum differences between the edges are 57 μm and 12°C at 1-degree inclination. From 1 to 10-degree inclination angles, the maximum differences decrease back to 41 μm and 6.5°C at 10-degree inclination. This effect is similar but less significant between the opposite

corners. The maximum differences between the opposite corners are under 20 μm and 6°C at 0.5-degree inclination.

Fig. 6.20A presents the global maximum temperature differences of the substrate during the process (usually referred as ΔT in soldering technology) in the case of different inclinations. As it was discussed in Chapter 1, Introduction to Surface-Mount Technology, the small ΔT value is crucial during reflow soldering since it ensures the homogeneous heating. The low inclination angles (between 0 and 0.2 degree) increases the ΔT a bit; however, over 0.2 degree, the inclination has positive effect. The maximum ΔT is 21°C in the case of horizontal position, while it decreases under $\Delta T = 9$°C in the case of 10-degree inclination. Fig. 6.20B shows the most rapid heating

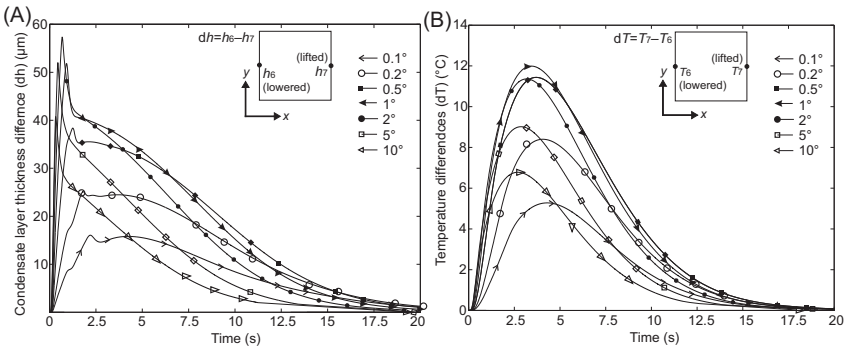

FIGURE 6.19 Differences between the lowered and lifted edges in the case of different inclinations: (A) thickness differences of the condensate layer; (B) temperature differences of the substrate. *Reproduced with permission from B. Illés, A. Géczy, Investigating the heat transfer on the top side of inclined printed circuit boards during vapour phase soldering, Appl. Therm. Eng. 103 (2016) 1398–1407.*

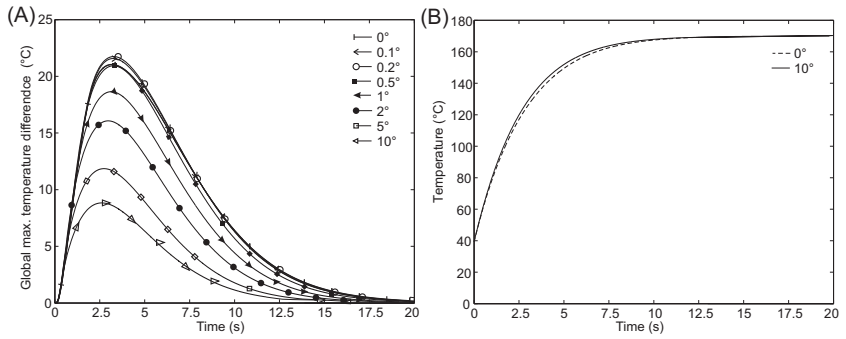

FIGURE 6.20 Global temperature analyses: (A) global maximum temperature differences of the substrate (ΔT); (B) the fastest thermal profiles. *Reproduced with permission from B. Illés, A. Géczy, Investigating the heat transfer on the top side of inclined printed circuit boards during vapour phase soldering, Appl. Therm. Eng. 103 (2016) 1398–1407.*

profiles in the case of the horizontal position and 10-degree inclination. The inclination has only a minor effect on the overall intensity of heat transfer. This is also an important aspect since basic VPS processes have high values of HTCs compared to the conventional reflow technologies.

Consequently, the effect of the very low angle inclination (under 1 degree, which can be caused by practical, but not intended phenomenon, e.g., the nonappropriate fixing of the elevation or sample holding) is negligible. However, a moderate inclination (between 1 and 10 degrees) decreases the spatial thickness differences of the condensate layer, thus improving heat transfer uniformity considerably. Therefore, with the application of an optimal inclination of the substrate during the VPS process, more even heat transfer can be achieved; consequentially, the number of the soldering failures can be reduced, ultimately leading to better overall soldering quality.

During the VPS process, the large components can cause congestion of the flowing condensate layer, resulting in both the accumulation of the heat transfer fluid and the variation of the heat transfer locally. This phenomenon might cause difference in the onset of solder alloy melting at the different leads of the component, which can lead to component displacement failures (see Chapter 1: Introduction to Surface-Mount Technology). Therefore, an examination of condensate layer formation around a large-size SMD PET capacitor component is presented; the possible imbalance in the melting of the solder alloy and prediction of the component alignment failure is calculated.

According to the calculations, significant amount of condensate flows down from the component at the beginning of the VPS process (0.1−1 second) and it has significant effect on the flow field. Between 0 and 0.1 second, the condensate accumulates on the component; still, the force originated from surface tension can hold the condensate on the component. Behind the component, the flow can even turn back toward the middle of the assembly instead to flow toward the edges. After 4 second, the amount of the downflowing condensate from the component decreases considerably, since the surface temperature of the component approaches the vapor temperature and slows down the condensation. This effect makes the flow field near steady.

Fig. 6.21 shows the condensate layer on the FR4 substrate in the case of different component locations at different times (quarter view of the assembly). The component and the substrate are not shown to enable easier examination of the condensate layer. The downflowing condensate from the component causes waves in the condensate layer nearby the component. The degree of condensate layer perturbation depends substantially on the component location on the substrate. The perturbation is smaller when the component is closer to the middle of the substrate (Fig. 6.21E), since the downflowing condensate can leave the substrate easily without reflections at the middle of the substrate. When the component is located closer to the edges (Fig. 6.21A and C), the wave reflections from the middle of the

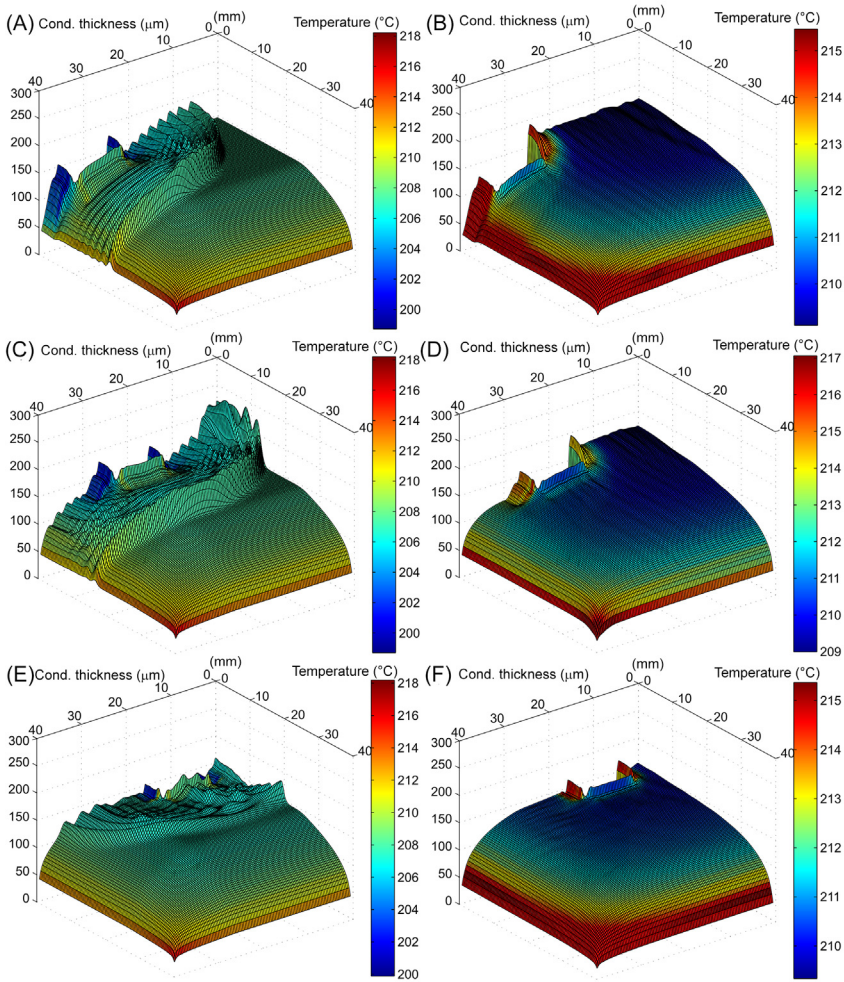

FIGURE 6.21 Condensate layer thickness and temperature distribution: (A) component position 1 at 1 s; (B) component position 1 at 4 s; (C) component position 2 at 1 s (D) component position 2 at 4 s; (E) component position 3 at 1 s; (F) component position 3 at 4 s. *Reproduced with permission from B. Illés, A. Géczy, O. Krammer, K. Dušek, D. Bušek, Numerical investigation on the effect of condensate layer formation around large-size components during vapour phase soldering, Int. J. Heat Mass Transf. 125 (2018) 202–209[25].*

substrate are higher, which causes higher perturbation in the condensate layer. The highest wave can reach ~250 μm, while the average condensate thickness is only 130–150 μm during the whole process. Up to 4 seconds, the effect of the downflowing condensate from the component is barely visible (Fig. 6.21B, D, and F). During the whole process, considerable difference forms between the condensate thicknesses at the opposite leads (solder

joints) of the component. Still, the amount of the downflowing condensate is considerable, the maximum difference can even reach ~100 μm (at 2 seconds), but later the average difference still remains over 22 μm due to the congestion of the condensate behind the component.

After the condensate layer is stabilized (4 seconds), the temperature distribution of the condensate layer has no special characteristic (see Fig. 6.12), the coldest part is at the middle and the warmest part is at the edge of the substrate (Fig. 6.21). The transported heat by the downflowing condensate from the component has considerable effect on the temperature of the condensate layer on the substrate. At the beginning of the soldering process (0−3.5 seconds), the temperature of the condensate flowing down from the component leads is colder than the average temperature of the condensate layer, and this cools down the condensate layer locally at the solder joints (Fig. 6.21A, C, and E). After 3.5 seconds, the temperature of the previous tendency alters (Fig. 6.21B, D, and F). The temperature analyses of the component show that between 0 and 3.5 seconds, the leads of the component are a bit colder than the body the component. This can be explained with the heat removal by the solder paste and by the inside terminals of the capacitor. Up to 4 seconds, the temperature of the leads becomes equal to that of the component body. However, the condensation is much more intensive on the leads than on the other parts of the component body during the whole process, since the heat capacity and heat conductivity of the metal leads are much higher than these parameters of the PET (Table 6.4). Eighty five percent of the downflowing condensate arrives from the leads of the component. Therefore, only the condensate flowing down from leads will have effect on the temperature of the condensate layer (Fig. 6.21).

Since the condensate thickness difference is considerable between the solder joints and the heat transfer of the condensate layer highly depends on its thickness, we examine the heating differences of the opposite solder joints. The temperature distribution of the substrate and the solder joints can be seen in Fig. 6.22A in the case of component location 1 (Fig. 6.21) at 4 seconds. The solder pads and the solder alloy on them are heating up more rapidly than the other part of the substrate. Under the component,—where the condensation is less intense—the temperature of the substrate is even lower. Although it is barely visible, there is already ~2°C difference between the solder pads at 2 seconds (the left one is the warmer pad). On the ramp part of the thermal profiles of the solder pads (Fig. 6.22B), the previous difference is more visible. The difference in the onset of the alloy melting between the opposite leads is 924 ms. The relatively long phase change of the solder alloy (~3.5 seconds)—when the temperature is constant—is also clearly visible in Fig. 6.22B.

Table 6.5 shows the average differences in the condensate thickness between the solder joints and the differences in the onset of melting in the case of different component positions and soak temperatures (see in Chapter 1: Introduction to Surface-Mount Technology). At the middle of the

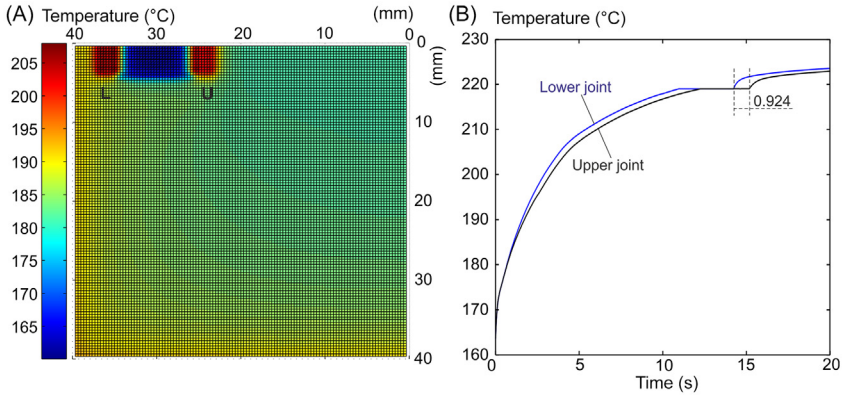

FIGURE 6.22 Temperature of the solder joints in the case of component location 1: (A) temperature distribution of the PCB at 4 s; (B) ramp part of thermal profile of the solder joints. *Reproduced with permission from B. Illés, A. Géczy, O. Krammer, K. Dušek, D. Bušek, Numerical investigation on the effect of condensate layer formation around large-size components during vapour phase soldering, Int. J. Heat Mass Transf. 125 (2018) 202–209.*

TABLE 6.5 The average differences in condensate thickness and in the onset of melting at different component locations and by different soak temperatures [25].

Component position	Soak temperature (°C)	Avg. condensate thickness diff. (μm)	Onset of melting diff. (ms)
1	140	15.1	114
	160	6.1	37
	180	3.2	16
2	140	24.6	***399***
	160	22.4	237
	180	19.5	178
3	140	51.4	***1414***
	160	47.8	***924***
	180	38.5	***625***

Values with bold and italics mean the risky values, where the component movement is possible.

substrate (location 1), the flow of the condensate layer is very slow (compared to that at the edges); therefore, neither considerable difference in the thickness of condensate nor significant difference in the onset of melting could form between the solder joints. Oppositely, at the edges of the substrate (location 3), considerable differences in the thickness of condensate will form, and this will cause difference in onset of melting over 1 second.

According to industrial experiences, if the difference in onset of melting is higher than 250−300 ms, then the possibility of component displacement is considerable. However, this value can vary from case to case according to the solder joint parameters (component size, pad size, lead design, etc. [26,27]). For reducing the possibility of component displacement failures during VPS process, the large-size SMDs has to be located closer to the middle of the substrate, but not farther from the middle than the half of the characteristic length of the substrate. The effect of the soak temperature is also substantial. In the case of higher soak temperature, the difference in the onset of melting of the solder is lower. The application of higher soak temperatures is not problematic in VPS technology, since it utilizes inert atmosphere inherently, which prevents the oxidation of the solder paste.

6.1.2.3 Heat transfer coefficient on different substrate materials

Finally, in the topic of condensate layer formation, we examine the relations between the condensate layer parameters and the HTC, like how the material and the shape of the substrate affect the condensate layer formation and consequentially, the HTC. The spatial HTC of a substrate (*sub*) can be calculated from the Newton's equation of heat transfer and according to the internal energy change of the heated substrate [28]:

$$HTC(\bar{r},t)=\frac{C_{S(sub)}\cdot\rho_{sub}\cdot V_{sub}\cdot(T_{sub}(\bar{r},t+\Delta t)-T_{sub}(\bar{r},t))}{A\cdot(T_{cond}(\bar{r},t)-T_{sub}(\bar{r},t))\cdot\Delta t} \tag{6.43}$$

Like during the investigation of the inclination of the assembly (Section 6.1.2.2), stationary and saturated boundary conditions are applied for the vapor space here as well, in order to separate the effects of different thermal parameters of the different substrates from the effects of the practically possible instationary and nonhomogeneous vapor space conditions.

Fig. 6.23 shows the spatial averages, and maximum and minimum values of HTCs in the different substrate materials during the whole soldering process. It can be concluded that the substrate material has considerable effects on the heat transfer during the VPS process. There are more than one order of magnitude differences between the HTC values on the different substrates. However, the characteristics of the HTC changes are very similar; HTC values decrease significantly within the first 2 seconds, which is followed by a slower increase till the end of the process. The calculated HTC values correlate strongly with the thermal diffusivity of the substrate materials

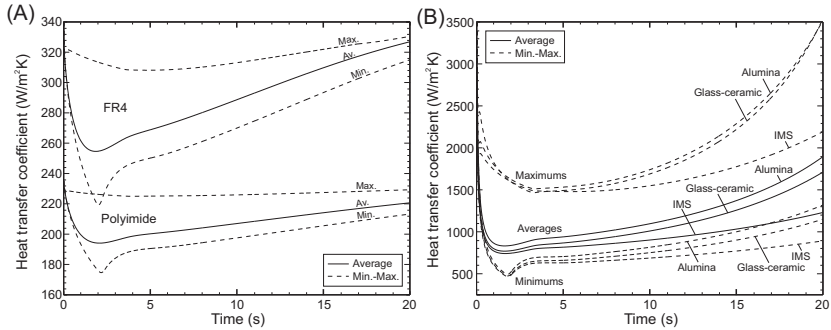

FIGURE 6.23 HTC values (spatial average and min−max values): (A) on the FR4 and polyimide substrate; (B) on the LTCC, alumina, and IMS substrate. *Reproduced with permission from B. Illés, A. Géczy, A. Skwarek, D. Busek, Effects of substrate thermal properties on the heat transfer coefficient of vapour phase soldering, Int. J. Heat Mass Transf. 101 (2016) 69−75.*

(Table 6.3), and larger thermal diffusivity results in larger HTC. A weaker correlation between HTC values and specific thermal conductivity is also visible. However, these correlations are far from linear, since HTC values are determined not only by the thermal parameters of the substrate materials but also by the thermal parameters of the condensate layer. This is proven mostly by the high deviations between the spatial minimum and maximum HTC values, which is obviously caused by spatial differences of the condensate layer thickens (as it was shown previously).

In order to understand HTC changes, we need to study the build-up of the condensate layer on the different substrate materials (Fig. 6.24). The HTC change (Fig. 6.23) correlates strongly with the change of the condensate layer thickness (Fig. 6.24A). The heat transfer is inversely proportional with the thickness of the condensate layer, the thinner condensate layer ensures more effective heat transfer (as we could see in Section 6.1.2.2). The sudden increase of the condensate layer thickness during the first part of the soldering process causes the steep decrease of the HTC values, and later when the condensate thickness start to decrease, the HTC values start to increase. Fig. 6.24B shows the spatial average and spatial minimum and maximum values of the condensate layer thickness on of FR4 substrate (the other substrates show similar results). According to the results, the main influencing factor on the HTC is the condensate layer thicknesses. The minimum condensate layer thickness with the maximum HTC is located at the corners of the substrate, while the maximum condensate layer thickness with the minimum HTC is located at the middle of the substrate.

However, it is still not possible to determine the change of HTC straightforwardly by the condensate layer thickness, since absolute differences between the HTC values are much larger than absolute differences between the condensate layer thicknesses. If we investigate the thermal parameters of

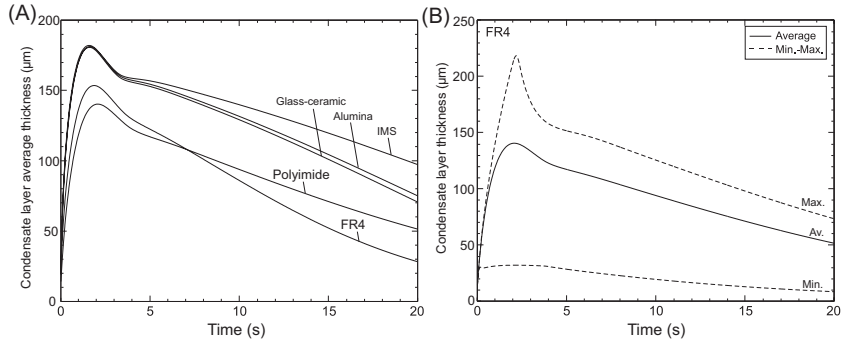

FIGURE 6.24 Spatial condensate layer thicknesses: (A) in the case of the different substrate materials; (B) spatial average and spatial minimum and maximum of the condensate layer thickness on FR4 substrate. *Reproduced with permission from B. Illés, A. Géczy, A. Skwarek, D. Busek, Effects of substrate thermal properties on the heat transfer coefficient of vapour phase soldering, Int. J. Heat Mass Transf. 101 (2016) 69–75.*

the different substrate material, the average condensate thickness correlates only with the volumetric heat capacity (Table 6.3). The larger C_V value results in thicker condensate layer, mainly during the second part of the soldering process, since substrate materials with larger C_V need more energy, and this causes condensation that is more intensive. Interestingly, the effect of the specific thermal conductivity on the condensate layer formation is much less considerable. For this phenomenon, a good example is the case of alumina and the glass-ceramic substrates. There is only 6% difference in volumetric heat capacity between them with 350% difference in specific thermal conductivity (Table 6.3). Nonetheless, they have almost the same condensate layer thickness (Fig. 6.24A).

For deeper understanding of the HTC differences in the case of different substrate materials (Fig. 6.23), the effect of the thermal diffusivity of the substrate materials and the effect of the condensate layer thickness on the different substrates have to be examined together. To prove this with a given example, thermal diffusivity difference between the alumina and glass-ceramic should result in larger difference in HTC values, but the similar condensate layer thicknesses on them limit the HTC difference between them. The lower HTC value of the IMS substrate compared to the glass-ceramic cannot be justified by the thermal diffusivity differences; it is caused by the thicker condensate layer on the IMS.

Fig. 6.25A shows the average thermal profiles of different substrates. After some reorganizing of Eq. (6.41), it is visible that the heating of the substrate depends on the given ratio of the HTC to the volumetric heat capacity. The order of plots in Fig. 6.25 is in accordance with the previous statement. Fig. 6.25B shows minimum and maximum thermal profiles of

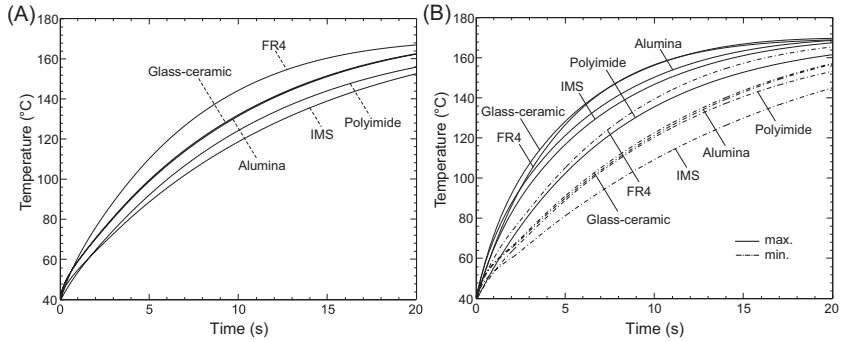

FIGURE 6.25 Thermal profiles of the different substrates: (A) Average thermal profiles; (B) Minimum and maximum thermal profiles. *Reproduced with permission from B. Illés, A. Géczy, A. Skwarek, D. Busek, Effects of substrate thermal properties on the heat transfer coefficient of vapour phase soldering, Int. J. Heat Mass Transf. 101 (2016) 69–75.*

different substrates. Unfortunately, the increase of volumetric heat capacity increases the temperature gradient of the substrates (ΔT), which is an important parameter of soldering technologies (see in Chapter 1: Introduction to Surface-Mount Technology). The aspect ratio of the substrate has also some effect on the thermal behavior of the VPS process. Growth of the aspect ratio increases mass flow toward the narrower sides of the substrate, which results in a global decrease of the condensate thickness increasing HTC and decreasing temperature gradient (ΔT) on the substrate. This enables more consistent, more even temperature distribution.

The previously presented dynamic HTC values can be useful for thermal profile calculations and for optimization steps during industrial application of VPS technology. Growth of the aspect ratio and the consequent consistent temperature distribution on the substrate may have practical use during design of the circuit layout and during manufacturing as well, in order to optimize overall soldering quality.

6.1.3 Numerical simulation of the vacuum vapor phase soldering system

Chapter 4, Vapor Phase Reflow Soldering Ovens, discussed one of the main problems of the VPS technology, the increased void formation in the solder joints. The application of the low-pressured process zone—vacuum VPS technology—can efficiently decrease the void formation after melting of solder on the assemblies, since it helps the removal of the flux gasses from the solder joint. Therefore, it is worth to study the vacuum VPS technology by numerical simulation, in order the investigate the effects of the vapor concentration decrease on heat transport processes during the soldering, and to

investigate whether the possible changes of the setup has any effect on the efficiency of the void separation.

6.1.3.1 Model description

The suctioning of the vapor space from the process zone causes a turbulent gas flow [29], so the numerical simulation is based on the three-dimensional Reynolds Averaged Navier−Stokes (RANS) equations. The RANS equations compute only the average movement in a turbulent flow, which makes this process relatively fast compared to the similar turbulent methods, while the fluctuations are only modeled by the Reynolds stress tensor. The standard $k-\varepsilon$ method has been chosen to handle the Reynolds stress tensor [30]. The vapor suctioning is initialized by a pressure drop generated by a vacuum pump. The Einstein notation is applied during the presentation of the model. For the description of the vapor flow, the transient continuity equation for compressible Newtonian fluids is used since the local pressure change has effect on the density of the vapor:

$$\frac{\partial \overline{\rho}}{\partial t} + \overline{\rho}\frac{\partial \overline{u_i}}{\partial x_i} = 0 \tag{6.44}$$

where u is the velocity of the vapor (m/s). The RANS equation for compressible Newtonian fluids is the following:

$$\frac{\partial \overline{u_i}}{\partial t} + \overline{u_j}\frac{\partial \overline{u_i}}{\partial x_j} = g_i - \frac{1}{\rho}\frac{\partial \overline{p}}{\partial x_i} + \frac{\partial}{\partial x_j}(\upsilon + \upsilon_T)\left(2\overline{S_{ij}} - \frac{2}{3}\frac{\partial \overline{u_j}}{\partial x_j}\delta_{ij}\right) \tag{6.45}$$

where δ_{ij} is the Kronecker delta and the mean rate of strain tensor is:

$$\overline{S_{ij}} = \frac{1}{2}\cdot\left(\frac{\partial \overline{u_i}}{\partial x_j} + \frac{\partial \overline{u_j}}{\partial x_i}\right) \tag{6.46}$$

and the turbulent eddy viscosity is the following:

$$\upsilon_T = C_\mu \frac{k^2}{\varepsilon} \tag{6.47}$$

where k is the turbulent kinetic energy:

$$\begin{aligned}\frac{\partial k}{\partial t} + \overline{u_j}\frac{\partial k}{\partial x_j} = &\left(\upsilon_T\left(2\overline{S_{ij}} - \frac{2}{3}\frac{\partial \overline{u_j}}{\partial x_j}\delta_{ij}\right) - \frac{2}{3}k\delta_{ij}\right)\frac{\partial \overline{u_i}}{\partial x_j} \\ &- \upsilon_T\frac{1}{\overline{\rho}^3}\frac{\partial \overline{\rho}}{\partial x_i}\frac{\partial \overline{p}}{\partial x_i} - \varepsilon + \frac{\partial}{\partial x_j}\left(\upsilon + \frac{\upsilon_T}{\sigma_k}\right)\frac{\partial k}{\partial x_j}\end{aligned} \tag{6.48}$$

and ε is the turbulent dissipation rate:

$$\frac{\partial \varepsilon}{\partial t} + \overline{u_j}\frac{\partial \varepsilon}{\partial x_j} = C_{\varepsilon 1}\frac{\varepsilon}{k}\left(\left(\upsilon_T\left(2\overline{S}_{ij} - \frac{2}{3}\frac{\partial \overline{u_j}}{\partial x_j}\delta_{ij}\right) - \frac{2}{3}k\delta_{ij}\right)\frac{\partial \overline{u_i}}{\partial x_j} - \upsilon_T\frac{1}{\overline{\rho}^3}\frac{\partial \overline{\rho}}{\partial x_i}\frac{\partial \overline{p}}{\partial x_i}\right) - C_{\varepsilon 2}\frac{\varepsilon^2}{k} + \frac{\partial}{\partial x_j}\left(\upsilon + \frac{\upsilon_T}{\sigma_\varepsilon}\right)\frac{\partial \varepsilon}{\partial x_j} \tag{6.49}$$

The applied constants, which are the generally used constants of the standard $k-\varepsilon$ model [30], were the following:

$$C_\mu = 0.09; \quad \sigma_k = 1; \quad \sigma_\varepsilon = 1.3; \quad C_{\varepsilon 1} = 1.44; \quad C_{\varepsilon 2} = 1.92$$

The vapor pressure is calculated by the general gas law:

$$p = \frac{amu_H}{amu_{Galden}} \cdot \rho \cdot R \cdot T \tag{6.50}$$

where amu_H is the average molecular weight of hydrogen, amu_{Galden} is the average molecular weight of Galden, R is the gas constant (8.314 J/(K mol)). The energy transport in the flowing vapor can be described as well by the RANS method:

$$\frac{\partial \overline{T}}{\partial t} + \overline{u_j}\frac{\partial \overline{T}}{\partial x_j} = \frac{\lambda}{\rho C_s}\frac{\partial}{\partial x_j}\frac{\partial \overline{T}}{\partial x_j} \tag{6.51}$$

During the suctioning process, the vapor will condensate on the colder wall of the suction pipe, which can be described by equations presented in Section 6.1.1.1.

During the numerical investigation of the vacuum VPS process, an Asscon VP8000 VPS system is applied. The detailed expression of this system can be seen in Chapter 4, Vapor Phase Reflow Soldering Ovens. Briefly, the working principle of the system is the following: after the melting of solder paste, the vapor is removed from the process zone via a suction pipe. Volume separation-type vacuum pump is used, which means that the pump separates the same volume of vapor out from the process zone in a given time. This results in a constant decrease in the relative pressure between the suction pipe and the vacuum chamber. The vacuum pump reduces the pressure from the ambient 101 to 5 kPa in 5 seconds, and the assembly spends further 15 seconds at this state to give adequate time to the voids to leave the solder joints.

First, the possible effects of the vapor suctioning on the heat transport processes are studied on FR4 substrates assembled with 0603 chip resistors (Al_2O_3 ceramic substrate). Later chip resistors on Polyimide, glass-ceramic, alumina 94%, and IMS substrates with 1 mm thickness were also studied, as well as QFP, TQFP, QFN, TQFN, and BGA components on FR4 substrate with 1 mm thickness. SAC305-type solder alloy was applied in 125 μm

thickness on the 17 μm thick Cu solder pad. The surface of the substrate was $160 \times 160\ mm^2$ and three different thicknesses (0.5, 1, and 2 mm) were examined. LS230-type Galden was used as heat transfer liquid. The structure of the process zone and the assembly can be seen in Fig. 6.26. The physical parameters of the materials, which were not used in the previous sections, can be seen in Table 6.6.

The numerical conversion of the previously defined PDEs can be performed with the FDM−FTCS method, like in Section 6.1.1.1. In the given

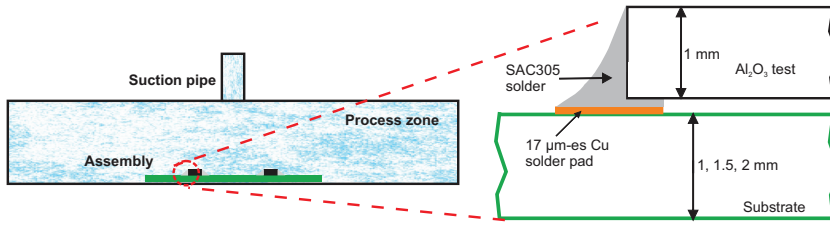

FIGURE 6.26 The structure of the process zone and the assembly. *Reproduced with permission from B. Illés, A. Skwarek, A. Géczy, O. Krammer, D. Bušek, Numerical modelling of the heat and mass transport processes in a vacuum vapour phase soldering system, Int. J. Heat Mass Transf. 114 (2017) 613−620[31].*

TABLE 6.6 Physical properties of the applied materials.

Property/ material	LS230	FR4	Cu	SAC305	Al_2O_3	Silicone rubber
Boiling point (°C)	230	–	–	–	–	–
Density (kg/m^3)	19.96[a]	2100	8960	7370	3690	1420
Dynamic viscosity[b] (Ps s)	2.13×10^{-5}	–	–	–	–	–
Average molecular weight	1010/1085	–	–	–	–	–
Spec. thermal cond. (W/m K)	0.065	0.23	385	58	18	0.35
Spec. heat cap. (J/kg K)	973	570	3850	2320	880	1200
Latent heat (J/kg)	6.3×10^4	–	–	–	–	–

[a] *The saturated vapor concentration of the LS230 Galden.*
[b] *The dynamic viscosity of the LS230 Galden vapor was calculated by the method of Lee et al. in Ref. [32].*

case, the assumed high flow velocities suggest the application of the Courant−Friedrichs−Lewy (CFL) conditions during the meshing of the model [20]. All for the cells of the model have to fulfill:

$$\Delta t\left(\frac{u_x}{\Delta x}+\frac{u_y}{\Delta y}+\frac{u_z}{\Delta z}\right)\leq 1 \tag{6.52}$$

According to the CFL condition, the process zone should be divided to ~48,000 cells while the assembly is divided to ~2000 cells with 10^{-5}-second time steps. The assembly model is embedded into the model of the process zone and they run together as a cosimulation (details can be read in Ref. [11]). Due to the symmetry of the system only a quarter of the whole geometry is calculated.

At the start of the vapor suctioning process, saturated vapor conditions are supposed as an initial conditions, means: $\rho(0) = 19.96$ kg/m^3, $T(0) = 230$°C, and the vapor is not moving before the suctioning, $v(0) = 0$ m/s. The initial condition of the Galden vapor pressure is $p(0) = 101$ kPa. The initial temperature of the assembly is 230°C. Initial condition of the turbulent kinetic energy is the following:

$$k=\frac{3}{2}(U\cdot I)^2 \tag{6.53}$$

where U is the mean flow velocity and I is the turbulence intensity which was chosen to 0.1 since the flow is supposed to be highly turbulent. Initial condition of the turbulent dissipation rate is the following:

$$\varepsilon = C_\mu \cdot \frac{k^{1.5}}{l} \tag{6.54}$$

where l is the turbulent length scale (the possible largest eddy in the given system), which is around ~0.1 m in given case.

During the suctioning process, the process zone suffers a heat loss on the suction pipe, since the hot vapor is condensing on the colder wall of suction pipe. It can be measured by simple thermocouples that the initial temperature of the outer wall of the suction pipe is 60°C, which increases with an average ~1.5°C during each suctioning process. Fig. 6.27 shows the calculated and measured temperatures of the outer wall of the suction pipe during the suctioning process. It has to be noted, that even such a simple measurement can be used as the validation of our model. All of the physical phenomena have some role in the temperature change of the suction pipe, like the amount of the flowing vapor, its condensation on the wall of the suction pipe, and finally, its heat transfer. Boundary conditions of the model are the followings: the walls of the soldering chamber are adiabatic and the flow velocity tends to zero at the walls. The last setting step of the model is to determine the relative pressure decrease generated by the vacuum pump, which ensure that the process zone will reach the 5 kPa in 5 seconds. This

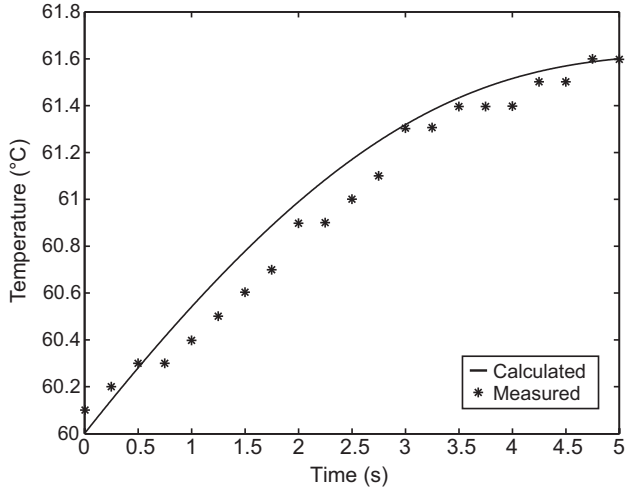

FIGURE 6.27 Calculated and measured temperature of the outer wall of suction pipe during the suctioning process. *Reproduced with permission from B. Illés, A. Skwarek, A. Géczy, O. Krammer, D. Bušek, Numerical modelling of the heat and mass transport processes in a vacuum vapour phase soldering system, Int. J. Heat Mass Transf. 114 (2017) 613–620.*

can be performed with simple approximation from $-0.1\%p$ (p—pressure) toward down. In our case, the $-3.4\%p$ vacuum pump setting is the best (with this setting, the vapor concentration decreases to 1.98 kg/m^3).

6.1.3.2 Results of the vacuum vapor phase soldering model

In the first step, the flow field, and the spatial concentration changes in the process zone during the suctioning are analyzed. Fig. 6.28 shows the average flow velocities in the process zone. The movement of the vapor is highly fluctuating in the process zone at the beginning of the suctioning process, 0–0.075 second. This is the result of the pressure fluctuation of the vacuum pump directly after the switching on. After 0.075 second, the average flow velocities become near constant. At the beginning of the suctioning process (0.01 second), the flow velocity can reach even 28 m/s at the entrance of the suction pipe, and later it is stabilizing around 14 m/s (Fig. 6.28A). Large velocity differences form diagonally in the process zone, the vapor almost stands at the corners and the flow velocity is still only $\sim$2 m/s at the half of the diagonal space (Fig. 6.28A). The velocity differences are smaller vertically (under the suction pipe), the flow velocity is $\sim$9 m/s at the bottom of the soldering chamber (Fig. 6.28B). As a conclusion, the suctioning can remove the vapor in the most effective manner in the middle space of the process zone.

The changes of the vapor concentration are studied during the suctioning process at the bottom, at the middle, and at the top of the process zone

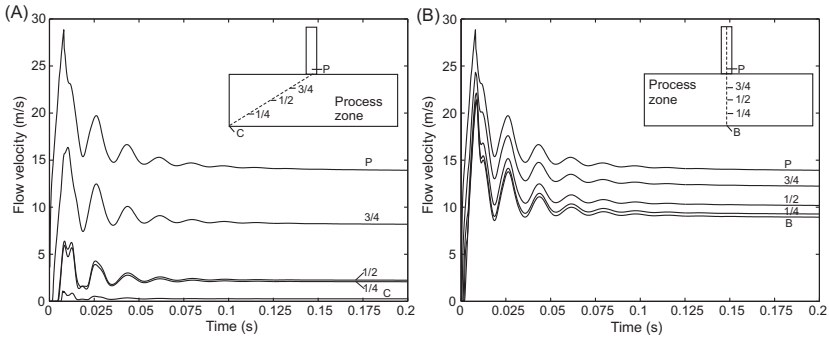

FIGURE 6.28 Average flow velocities in the process zone between 0 and 0.2 s: (A) diagonally; (B) vertically. *Reproduced with permission from B. Illés, A. Skwarek, A. Géczy, O. Krammer, D. Bušek, Numerical modelling of the heat and mass transport processes in a vacuum vapour phase soldering system, Int. J. Heat Mass Transf. 114 (2017) 613–620.*

(Fig. 6.29). At the beginning of the suctioning process (0–0.03 second), the fluctuation of the pressure and the flow velocity changes the distribution of the vapor concentration, mainly under the suction pipe (Fig. 6.29A and B). After 0.1 second, the distribution of the vapor concentration is stabilizing (Fig. 6.29C and D). Considerable concentration gradient forms horizontally, between the suction pipe and the corners of the process zone (Fig. 6.29C). The maximum difference is 2.25 kg/m^3 ($\sim$12%) at the top level of the process zone at 0.1 second. This difference is decreasing until the end of the suctioning process (Fig. 6.29D), when it is only 0.15 kg/m^3 ($\sim$10%). Vertically, the differences of the vapor concentration are smaller, under the suction pipe, between the top and the bottom level of process zone the difference is: 1.5 kg/m^3 ($\sim$8.3%) at 0.1 second and 0.1 kg/m^3 ($\sim$7.1%) at 5 seconds.

The heat loss on the suction pipe causes considerable heat loss in the process zone. Fig. 6.30 shows the temperature changes of the vapor during the whole void removal process (20 seconds). During the suctioning process (0–5 seconds), the vapor temperature can drop to 80°C (Fig. 6.30B). However, the temperature gradient is low in the process zone ($\sim$2°C–4°C). During the second part of the void removal process (between 5 and 20 seconds), the assembly is heating back the vapor nearby the assembly to 130°C–145°C; however, this heating effect on the whole process zone is moderate.

The previously discussed heat loss and the vapor concentration differences affect the heat transport processes of the soldering. It is possible that the solder joints can solidify earlier than the end of the void removal process and the voids cannot leave the solder joints. First, this effect is studied on solder joints placed to the middle and corner of different thick FR4 substrates (with different heat capacities). Fig. 6.31A shows the minimum and

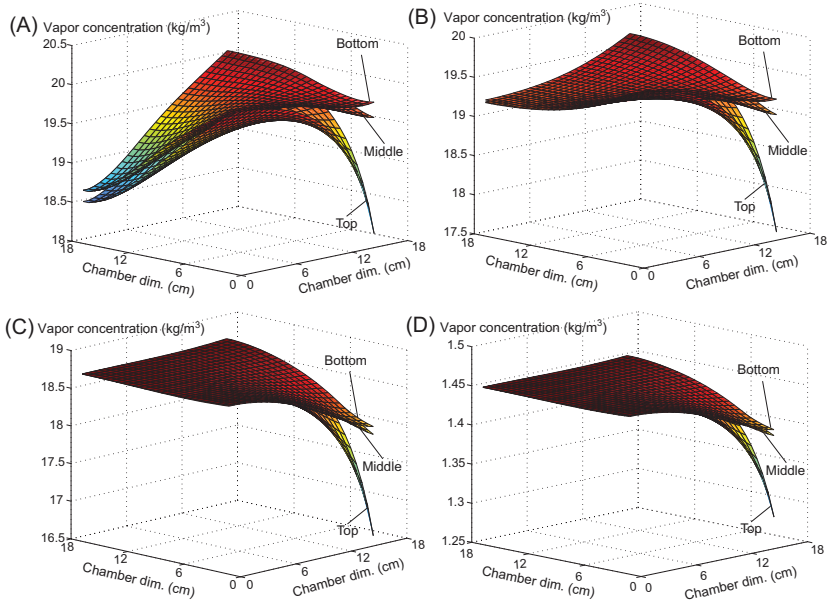

FIGURE 6.29 Vapor concentration at different levels of the soldering chamber (quarter sections): (A) at 0.015 s; (B) at 0.03 s; (C) at 0.1 s; and (D) at 5 s. *Reproduced with permission from B. Illés, A. Skwarek, A. Géczy, O. Krammer, D. Bušek, Numerical modelling of the heat and mass transport processes in a vacuum vapour phase soldering system, Int. J. Heat Mass Transf. 114 (2017) 613–620.*

maximum solder joint temperatures during the whole void removal. During the suctioning, the temperature of the solder joints decreases considerably with 8°C–14°C in the function of the FR4 substrate thickness. The temperature decrease is the most considerable at the middle of the FR4 substrate (point 2) and the heat loss is less toward the corners (point 1). This effect can be explained by the characteristic of the suctioning, namely that the vapor concentration (Fig. 6.29C) as well as the vapor temperature (Fig. 6.30) is the lowest under the suction pipe, where the assembly is usually positioned.

The solidus/liquidus temperatures of the most frequently applied SAC solder alloy are 217°C/219°C. According to the calculations, if the thickness of the FR4 substrate is lower than 1.5 mm, the solder joints can be solidify (or get very close to the solidification) to the end of the vapor suctioning process. During the second part of the void removal process, the temperature of the solder joints increases a bit with ∼2°C, which effect is caused by the heating effect of the assembly. However, the time of the void removal will be still shorter than it has to be according to the reflowing process. If the previous calculation is repeated on different substrate materials with 1 mm thickness, the results shows that, the much higher heat capacity of the

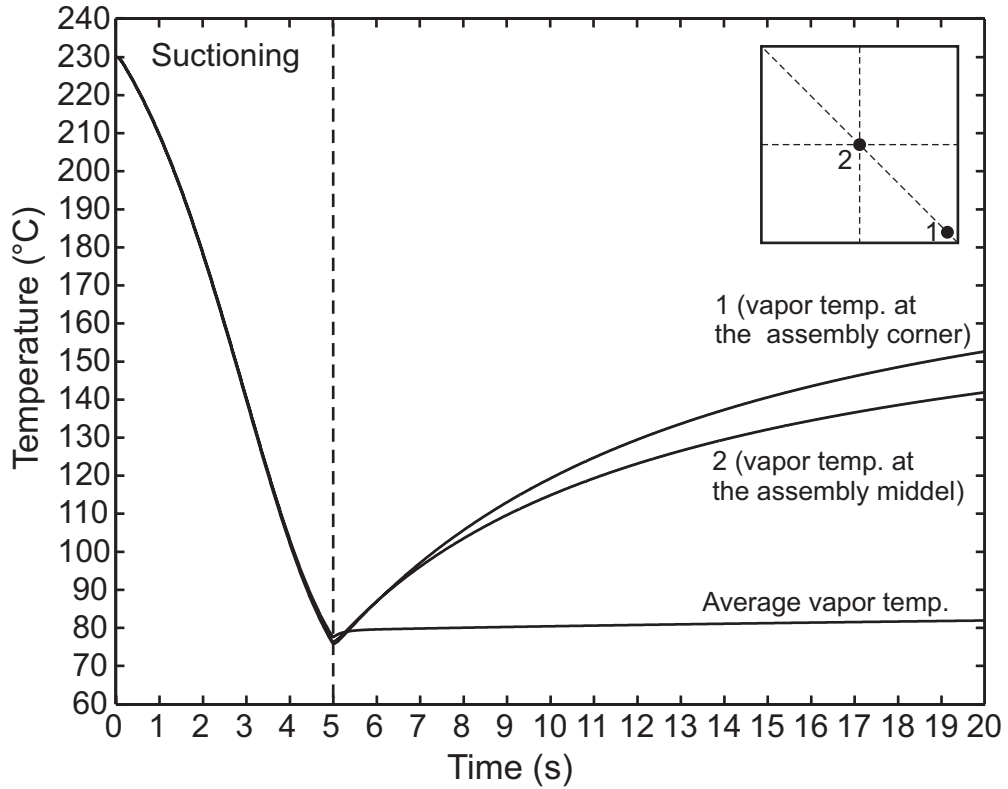

FIGURE 6.30 Temperature change of the vapor during the void removal process (0−20 s). *Reproduced with permission from B. Illéś, A. Skwarek, A. Géczy, O. Krammer, D. Bušek, Numerical modelling of the heat and mass transport processes in a vacuum vapour phase soldering system, Int. J. Heat Mass Transf. 114 (2017) 613−620.*

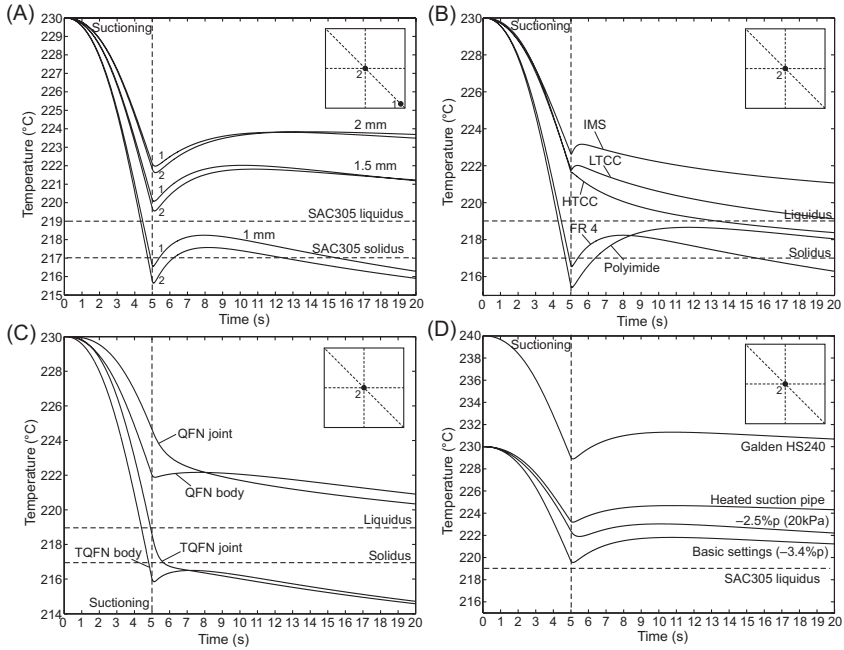

FIGURE 6.31 Solder joint temperature during the void removal process: (A) chip capacitors on FR4 substrates with different thicknesses; (B) chip capacitors on different substrates with 1 mm thicknesses; (C) QFN and TQFN components on FR4 substrate with 1.5 mm thickness; (D) improved settings in the case of an FR4 substrate with 1.5 mm thickness. *Reproduced with permission from B. Illés, A. Skwarek, A. Géczy, O. Krammer, D. Bušek, Numerical modelling of the heat and mass transport processes in a vacuum vapour phase soldering system, Int. J. Heat Mass Transf. 114 (2017) 613–620.*

alumina, glass-ceramic and IMS substrates (compared to the FR4 and Polyimide—see Table 6.3) results in heat loss during the suctioning process (Fig. 6.31B). From the other hand, the back heating effect of these substrates after the suctioning process is also much different and generally lower. The volumetric heat capacities of the alumina, glass-ceramic, and IMS substrates are similar, but the specific thermal conductivity of the alumina is much higher than for the other substrates. This explains why the alumina has the highest heat loss from these types of substrates. After 13.5 seconds, the temperature of the solder joints on the alumina substrate declines below the liquidus of the SAC305 solder alloy. While the solder joints on the IMS, loses the less amount of heat—this substrate material has the highest volumetric heat capacity and the lowest specific thermal conductivity [33].

The temperature decrease of the solder joints is also investigated in the case of frequently used IC packages (see the list in Section 6.1.3.1). The solder joint temperatures of the BGA and TBGA components decreased only by 5°C and 6.3°C, respectively, due to the relatively big amount of solder (in

the bumps). This means that the solidification of these solder joints is not possible before the end of the void removal process [33]. The average solder joint temperatures for QFN and TQFN packages on 1-mm-thick FR4 board can be seen in Fig. 6.31C. The structure of the QFN components is very similar to the BGA, but the lack of the bumps results in much lower amount of solder in their joints. Therefore, the temperature decreases of BGA and QFN component bulk bodies are very similar, but the solder joints' temperatures of QFN-type components decrease much seriously than in the case of BGA-type components. The average solder joint temperature of the QFN component exceeds only with 1.2°C the liquidus of the SAC305 at 20 seconds, while the average solder joint temperature of the TQFN component declines below the solidus of the SAC305 already during the void suctioning and remains there until the end of the void separation process. The QFP-type components behave similarly to the BGA-type components. The relatively large heat capacity of QFP and TQFP leads (as well as the thicker packages) ensures less heat loss of the solder joints during the void reduction process. In the case of these components, the solder joint temperature never drops below 222°C.

Finally, different oven settings are investigated in order to decrease the heat loss during the suctioning process. Fig. 6.31D shows the minimal solder joint temperatures of a chip resistor on the middle of an FR4 substrate with 1.5 mm thickness in the case of different oven settings. The intensity of the vapor suctioning has significant effect on the heat loss since it determines heat convection. If the relative pressure decrease of the vacuum pump is changed to $-2.5\%p$ (instead of $-3.4\%p$), the heat loss is already much lower (Fig. 6.31D), and the minimal temperature of the solder joints remains over 221.5°C. However, this vacuum pump setting ensures only 20 kPa pressure in the process zone after 5-second suctioning, which probably results in less effective void removal than the 5 kPa in the case of $-3.4\%p$ setting. Since the heat loss is happening on the suction pipe, some modification on this part is straightforward. The increase of the wall thickness of the suction pipe may only have a minor effect on the results. However, the elevation of the suction pipe temperature from 60°C to 120°C, would show positive effects. The minimal solder joint's temperature remains over 223°C in this case according to the calculations (Fig. 6.31D) without losing the suction power of the low pressure in the process zone. Nevertheless, the best solution is the increase of the heat transfer fluid boiling temperature; for example, to apply Galden HS240, with boiling point of 240°C. In this case, the minimal temperature of the solder joints remains over 229°C during the whole void removal process (Fig. 6.31D).

As a conclusion, in some component and substrate combinations, the solder joints can solidify during the vapor suctioning process, before the entrapped gas voids could be removed from the solder joints. If the thickness of the FR4 substrate is smaller than 1.5 mm, the risk of the solder joints'

solidification is high. This risk is much lower in the case of alumina, glass-ceramic, and IMS substrates. The risk of early solidification is the highest in the case chip components are the highest, due to the small heat capacity of the component bodies. From the generally used IC packages, only the QFNs are susceptible to the early solidification problem, due to soldering with a lower amount of solder. The efficiency of the void removal can be improved with the suction pipe heating or with the application of a heat transfer fluid with higher boiling point.

6.2 Numerical simulations of other types of reflow ovens

In this chapter, examples are presented about the numerical simulation of convection infrared (IR) and die bonding reflow ovens. Generally, the modeling techniques presented in Section 6.1 are applied and sometimes extended according to the given problems. Therefore, in most of the cases, the previously presented equations and methods are only referred from Section 6.1.

6.2.1 Numerical simulations of convection reflow ovens

The working principle of the convection reflow ovens is presented in detail in Chapter 3, Convection Reflow Ovens. Here, only the crucial points of the operation are repeated: the ovens are built up from heater and cooler zones, which are partially separated and have their own gas circulation system with own temperature management. The gas circulation system controls the gas temperature with heater elements, moving the gas with a ventilator and distributing the gas in the zone with a gas distribution system. The numerical investigations of the convection reflow ovens usually touch upon the following topics: studying the gas flow filled in the heating zones; calculating the temperature distribution in the zones; estimating the HTC; examining the heating/cooling of the assembly. In the next sections, examples are given in the previous topics, which were collected according to the most important parts of the convection reflow soldering technology.

6.2.1.1 Investigation of the gas flow field

Since the heating performance of the convection reflow ovens mainly depends on the gas flow field (see in Chapter 3: Convection Reflow Ovens), the velocity, the direction, and the turbulence of the flow are the mostly investigated parameters of the process zones. An example investigation is presented with a general conveyor-type convection reflow oven, which has seven heater zones (five preheater and two peak zones) and one cooler zone at the end of the oven. The oven applies the nozzle-matrix gas distribution system (see in Chapter 3: Convection Reflow Ovens). The schematic cross-

sectional view of the heater system and the inner arrangement of the oven can be seen in Fig. 6.32.

The main parts of the heater zones are the following: electrical heater modules, which heat the gas, a fan, which moves the gas, and a nozzle-matrix, which distributes the moving gas above the assembly and generates the heater gas streams. The construction of the heating and the cooling system is the same, but the cooling system does not contain electrical heater modules [34]. The nozzle-matrix is 560 mm wide and 415 mm long (toward the moving direction of the assembly). It contains 42 parallel nozzle-lines with 8 nozzles in each line, which are also parallel with the moving direction of the circuit board. The distance of the nozzles in the lines is 50 mm and the distance of the nozzle-lines is 26 mm. The neighboring nozzle-lines are shifted with half raster, so the nozzles are in the vertices of approximately equal triangles. The nozzle diameter is 5.5 mm. The distance between the nozzle-matrix and the PCB can be varied between 20 and 40 mm (the effect of this parameter is investigated during the following simulations). The height of the zones is 60 mm [34].

During the soldering process, the assembly is carried on the conveyor line between the upper and lower nozzle-matrices. A typical 175 mm width was applied for the conveyor line. The investigated reflow oven was designed for double conveyor line; therefore, the position of the single conveyor line is asymmetrical in the oven, the distance from the right and left wall of the oven is 175 and 385 mm, respectively. This conveyor arrangement can affect the gas flow field; therefore, this is also investigated during the simulations [34].

The gas flow field model is based on the following criteria: the vertical gas streams from the nozzle-matrix are laminar and join into a continuous radial flow layer above the board. The radial flow layer has dominant flow directions toward entrance and exit directions of the zones; it can become turbulent due the obstruction points in the zones (like the walls and the assembly). The description of inlet vertical gas streams and the radial flow

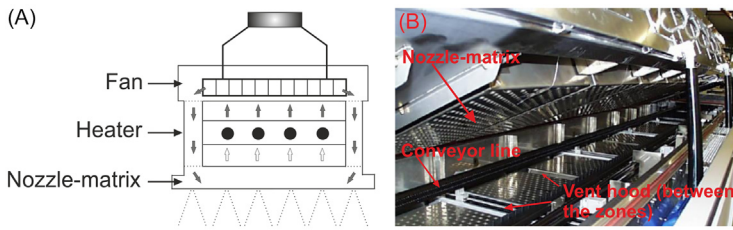

FIGURE 6.32 The investigated convection reflow oven: (A) schematic cross-sectional view of the heater system; (B) inner arrangement (during the operation the oven is closed). *Reproduced with permission from B. Illés, I. Bakó, Numerical study of the gas flow velocity space in convection reflow oven, Int. J. Heat Mass Transf. 70 (2014) 185–191.*

layer can be seen in Chapter 3, Convection Reflow Ovens, and in Ref. [35]. For numerical simulations of the gas flow field, the previously introduced RANS can be applied with the standard $k-\varepsilon$ model (see in Section 6.1.3). The $k-\varepsilon$ model performs well in cases of nonlarge adverse pressure gradients [36] which criteria are valid for convection reflow ovens.

During this investigation, the model was solved by finite volume method (FVM). Since every zone has the same parameters except of the inlet gas temperature, the model of one heater zone was created in 2D and 3D format as well to analyze the abilities and limitations of the different approaches. The following coordinate system was used: x direction is the length of the zone; y direction is the width of the zone; and z direction is the height of the zone. The 2D model applied structured mesh with 0.5 mm uniform mesh size, which resulted in 99,600 cells along the $x-z$ plane and 134,400 cells along the $y-z$ plane. The 3D model needed to use nonstructured and rougher mesh (with 2−5 mm mesh size) due to the increased complexity, which resulted in $\sim$2 million cells [37].

The initial conditions of the inflowing air were the following: temperature 400K (given value in the first preheating zone), density 0.884 kg/m^3, dynamic viscosity 2.289×10^{-5} kg/m s, and velocity 3.7 m/s^2 (it is the given velocity value in the studied oven). The boundary conditions were the following: the nozzles are gas inlets with normal velocity direction, the entrance and the exit of the zone are gas outlets [34]. During the simulation, 10^{-6} convergence criterion was applied. The model can be validated via temperature and HTC measurements by the presented method in Chapter 3, Convection Reflow Ovens.

First, the gas flow field of the zone was calculated without soldered assembly. Fig. 6.33 shows the results of the 2D model along $x-z$ and $y-z$ planes in the middle of the zone. The results show that the gas streams form a lateral flow layer, which is laminar and proceeds toward the entrance and

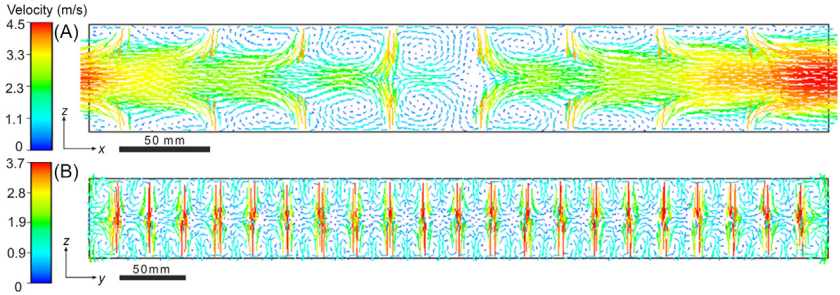

FIGURE 6.33 Gas flow velocities, half view of the zone: (A) 2D results along the $x-z$ plane, (B) 2D results along the $y-z$ plane. *Reproduced with permission from B. Illés, I. Bakó, Numerical study of the gas flow velocity space in convection reflow oven, Int. J. Heat Mass Transf. 70 (2014) 185−191.*

the exit of the zone, as it was expected, according to previous measurements [35]. However, the flow becomes turbulent between the nozzles, under and over the lateral flow layer. The velocity of the lateral flow layer is increasing toward the entrance and exit of the zone. Besides, the gas flow velocity is very low in the center region of the zone. This phenomenon results in that the HTC considerable variations along the length (x direction) of the zone, as well as along the whole oven. An effective processing area of the oven is marked in Fig. 6.33A, which is around 20 mm wide and located at the center of the zones [34]. Therefore, the total thickness of the assembly should not exceed $\sim$20 mm. This parameter can vary in the setup of the different ovens.

The results along the width of the zone ($y-z$ plane) show more homogeneous gas flow field (Fig. 6.33B) than along the length of the zone. Since the gas can leave the zone only toward the x direction, the formation of the lateral flow layer is not possible here. This results in a near homogeneous heat transfer along the width of the zone (y direction), which probably can compensate the inhomogeneity toward the length of the zone (x direction). The velocity increase at the walls indicates that the turbulence is a bit higher at the wall region than between the nozzles, but this region is unused during the reflow soldering. The calculations also showed that the gas flow velocity model can be considered to be stationary and that the buoyancy flux can be neglected due to the relatively high gas flow velocity. These neglections can decrease the calculation time considerably.

To study the effect of the assembly on the gas flow field, an FR4 circuit board (with $175 \times 175 \times 1\ \text{mm}^3$ dimensions) without the components (for simplification) was applied into the zone. During the first investigations, the circuit board was positioned in equal directions from the top and bottom of the zone along the x direction as well as from the right and left walls of the zone along the y direction. Along the x direction, the effect of the circuit board was studied at different points in the zone, simulating the path during the soldering process. The results showed that the symmetrically positioned bare circuit board has got only a negligible effect on the gas flow field.

However, if the circuit board position is asymmetric along the height of the zone, the results change a bit. During the sample study, the circuit board was lowered 10 mm toward the bottom of the zone. Similar arrangements can occur during the real application due to the different height of the oven and the supplying conveyor systems. The asymmetric position of the circuit board increases the lateral gas flow velocity (as well as the HTC value) over the board along the length of the heater zone (x direction, Fig. 6.34A). This can be beneficial in the case of double-sided reflow process where the HTC on the upside of the circuit board must be greater. The change is negligible under the board [34]. Along the width of the zone (y direction, Fig. 6.34B), the gas flow velocity does not change compared to the empty zone (Fig. 6.33B).

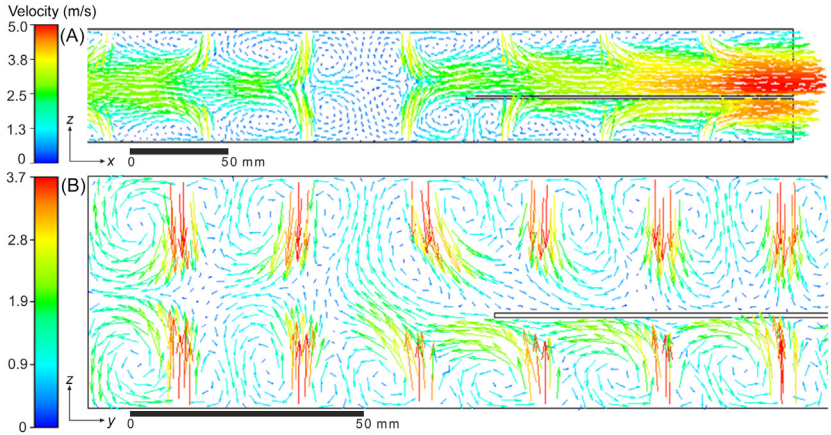

FIGURE 6.34 Effect of the asymmetrical circuit board position in the zone: (A) 2D results along the $x-z$ plane; (B) 2D results along the $y-z$ plane. *Reproduced with permission from B. Illés, I. Bakó, Numerical study of the gas flow velocity space in convection reflow oven, Int. J. Heat Mass Transf. 70 (2014) 185–191.*

The effect of the components on the gas flow field is even more interesting. The results of two different types of components were studied: a columnar type with $8 \times 8 \times 10$ mm^3 size (electrolyte capacitor or TO-2xx package) and a flat type with $15 \times 15 \times 1.5$ mm^3 (QFP package). The results can be seen in Fig. 6.35. Along the length of the zone (x direction), the columnar component perturbs the lateral flow layer (Fig. 6.35A and B), which must step over the component. This results in shadowed area at the sides of the component; there the gas flow becomes turbulent with very low flow velocity. In addition, the size of the shadowed area grows with the velocity of the lateral flow layer. The flow velocity is generally moderate at lower part of the component, where the soldering is taking place [34]. Unfortunately, this can cause inhomogeneous heating of the solder joints at the opposite sides of the component, which can lead to the displacement of the components. In addition, the placement of small size components close to the large-size columnar ones is not practical along length of the zone (x direction). Therefore, the application of tall components can be problematic during the convection reflow soldering.

Along the width of the zone (y direction), the effect of the columnar component is not considerable on the gas flow field. If the component is located between two nozzles (Fig. 6.35C), it attracts the gas streams toward itself, which can increase the heat transfer. Generally, the heat transfer is more homogeneous along the width of the zone (y direction) than along the length of the zone (x direction). The effect of the flat components is negligible along both directions. The results are invariant for the sides of the circuit board [34]. The case of the neighboring columnar components is also

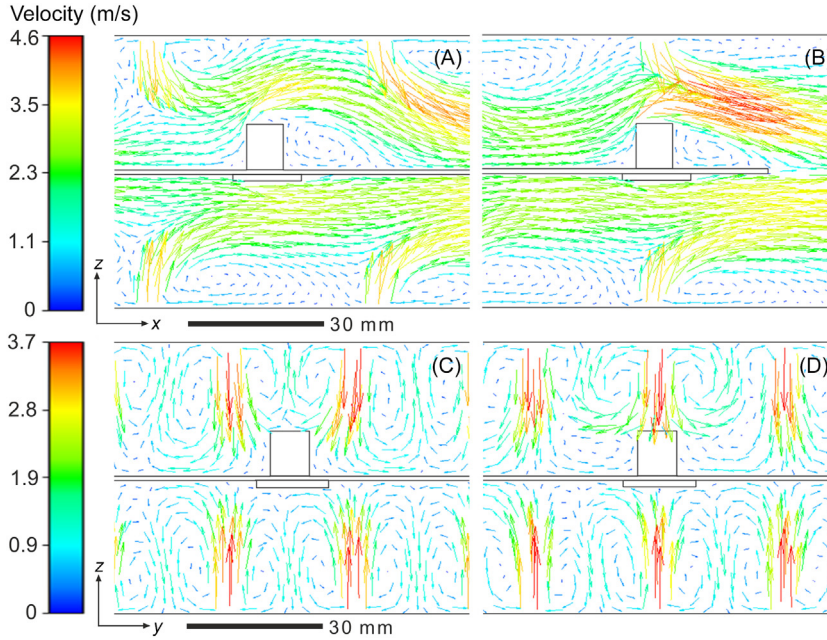

FIGURE 6.35 Effect of the components on the gas flow field: (A) components between the nozzles, $x-z$ plane; (B) components under a nozzle, $x-z$ plane; (C) components between the nozzles, $y-z$ plane; (D) components under a nozzle, $y-z$ plane. *Reproduced with permission from B. Illés, I. Bakó, Numerical study of the gas flow velocity space in convection reflow oven, Int. J. Heat Mass Transf. 70 (2014) 185–191.*

interesting. The studied distances were a quarter, a half, and one nozzle distance along the x direction (12.5, 25, and 50 mm). In the case of a quarter nozzle distance, the gas flow velocity is almost zero between the components, along both directions (Fig. 6.36A and D). In the case of a half nozzle distance, the gas flow velocity is $\sim 1-1.5$ m/s between the components, along both directions (Fig. 6.36B and D), depending on the actual position in the zone. In the case of one nozzle distance, the effect of the neighboring components is negligible (Fig. 6.36C). The results are invariant for the sides of the circuit board. Consequently, the suggested minimum distance between columnar components is at least a half nozzle distance along the length of the zone (x direction). Generally, the assembly design is more critical along the moving direction of the circuit board in the oven than toward the walls of the oven [34].

Finally, it is also interesting to study the effect of model extension to 3D. The results of 2D and 3D model agree in everything expect of the flow velocities of the lateral flow layer on the surface of the circuit board. In the 2D model (Fig. 6.36A), the maximum flow velocities in the lateral flow layers reach even ~ 4.5 m/s, while the 3D model shows much lower values,

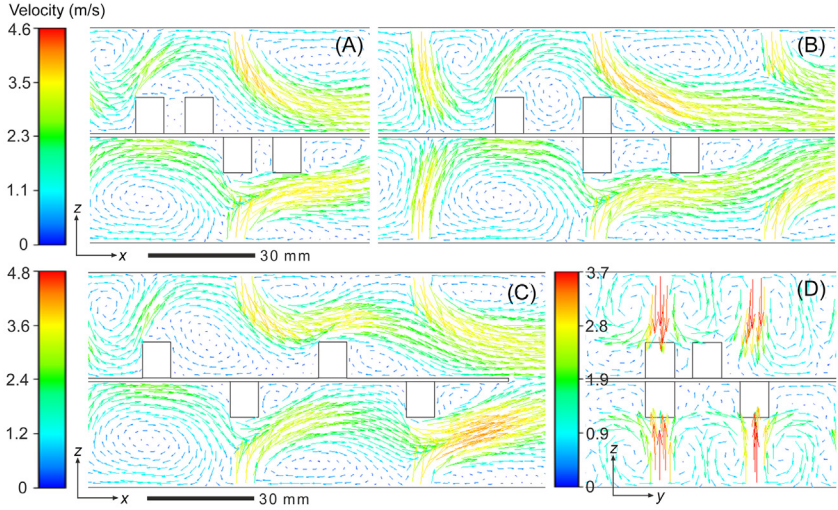

FIGURE 6.36 Effect of neighboring columnar components on the gas flow field: (A) quarter nozzle distance, $x-z$ plane; (B) half nozzle distance, $x-z$ plane; (C) on nozzle distance, $x-z$ plane; (D) quarter and half nozzle distance, $y-z$ plane. *Reproduced with permission from B. Illés, I. Bakó, Numerical study of the gas flow velocity space in convection reflow oven, Int. J. Heat Mass Transf. 70 (2014) 185–191.*

only $\sim$1.4 m/s. In the turbulent region, the differences are much lower, the flow velocities are around 0.9 m/s in both models. It is interesting, but the calculations of both models are correct. The large gas flow velocity differences between the models along the x direction are caused by the different ratio of gas in/outlets. According to the Navier–Stokes equations (Eq. 6.24), mainly the pressure gradients affect the flow velocities. Since the absolute velocities are relatively low, the gas flow can be considered incompressible and the pressure is determined by the ratio of gas in/outlets ($G_{I/O}$). In the 3D model, the $G_{I/O}$ is calculated according to the area of the 328 nozzles (inlets) divided by the double area of the $y-z$ plane (outlets); the obtained result for the parameter is 0.113. In the 2D model, this is calculated from the diameter of the 8 nozzles divided by the double height of the zone, it comes three times higher to 0.366. Therefore, this "virtual" increase of $G_{I/O}$ ratio of the 2D model results in the increase of the gas flow velocity. If the ratio of the $G_{I/O}$ values and the ratio of the maximum flow velocities of the models are compared, it is visible that they are very close [37]:

$$\frac{G_{I/O}(2D)}{G_{I/O}(3D)} = 3.23 \approx \frac{U_{max}(2D)}{U_{max}(3D)} = 3.21 \tag{6.55}$$

The previous results were approved by Lau et al. who investigated the gas flow field in a similar convection reflow oven with nozzle-matrix gas

distribution system [38]. They found that in the case of 3D investigation, the flow velocity on the surface of the circuit board is between 0.5 and 1.5 m/s.

The gas flow field can differ considerably if the reflow oven applies the slot nozzle system (see in Chapter 3: Convection Reflow Ovens). As it was discussed previously, this is a less favorable solution recently, nevertheless, it deserves to be discussed briefly. Ferreira et al. studied the gas flow field with a 3D model in the cooling zone of the reflow oven equipped with slot nozzle system [39]. The velocity of the inflowing gas was 1 m/s. They have found that the gas flow field is much simpler here than in the case of the nozzle-matrix system. This is caused by the rarely positioned slot nozzles compared to the nozzle-matrix system. Without a circuit board in the zone, the laminar streams from the slot nozzles form a lateral flow layer at the bottom of the zone which proceeds toward the entrance and exit of the zone.

Generally, the gas medium moves only nearby the bottom of the zone. The velocity of the gas streams slows down to 0.8 m/s, still the gas streams reach the bottom of the zone, and the average flow velocity of the lateral flow layer is only 0.1 m/s. The appearance of the circuit board in the zones modifies the gas flow field a bit. Large eddies form over the circuit board, the average diameter of the eddies can reach the height of the zone. Consequently, the gas flow field in the case of slot-type nozzles is much simpler than in the case of the nozzle-matrix systems, but it has considerable spatial inhomogeneities as well, which results in inhomogeneous heat transfer in the zone. The heating/cooling performance can be 200%−300% higher under the nozzles than at the other areas of zone.

6.2.1.2 *Investigation of the heat transfer in convection*

As it was discussed in Chapter 3, Convection Reflow Ovens, the heating performance of the convection reflow ovens can be characterized with the HTC which parameter is mainly defined by the previously investigated gas flow field parameters. Lau et al. investigated the average HTC parameter (means the direction independent HTC, see in details in Chapter 3: Convection Reflow Ovens) in a convection reflow oven applies nozzle-matrix-type heater system [38]. They found that at the entrance of the first preheater zone, the initial value of the HTC is already around 15 W/m K, which is the effect of the outflowing gas from the zone. As the whole assembly enters the zone (around 5 seconds), the HTC value reaches 40−45 W/m K at the side of the circuit board, which faces toward the inside of the zone while at the opposite side, it is still only around 20 W/m K. This results in 10°C−15°C temperature gradient in the assembly. At the middle of the zone the HTC distribution becomes more homogeneous on the surface of the assembly, between 45 and 55 W/m K. Until it reaches the end of the zone, the HTC increases to 65−75 W/m K. However, around large-size components the HTC can remain very low ∼25−30 W/m K during the whole process [38],

as it was expected according to the gas flow field analyses (see Section 6.2.1.1).

Generally, less time is necessary to heat up the components, which have low specific heat capacitance compared to the circuit board. Moreover, the transferred heat by the oven is distributing more rapidly throughout the smaller packages. The spatial variations of heat transfer are also affected by the complexity of the given assembly, resulting in a nonuniform temperature distribution during the whole process. However, until the end of the first preheater zone, the temperature gradient decreases to 5°C−11°C. As it was discussed in Chapter 1, Introduction to Surface-Mount Technology, the temperature gradient in the assembly influences on quality and reliability of the solder joints. If the temperature gradient is over a specific level, some components cannot receive enough amount of heat or may receive an uneven amount of heat, resulting in soldering failures [38].

It must be noted, that the complexity of the assembly makes the temperature gradient problem worse. If more components are applied, the number of the cold regions increases. This can also be attributed to the slow and gradual heating of grouped packages as it was expected according to the flow field analyses [38]. Colder regions can appear around the large-size components. This can be explained using the results of the flow field shown in Fig. 6.35. The gas stream from the nozzles faces to the surface of the component, which divides it into three regions, namely, the free-jet, stagnation, and wall-jet regions [38]. At the stagnation region, the direction of the gas stream changes from vertical to horizontal. The sudden decrease in height between the component and the circuit board forms a gap in the flow with a very low velocity (Fig. 6.35) which results in very low HTC value. The other location, where colder region can form, is the component-to-component locations, as it was expected according to Fig. 6.36. The gas flow in the wall-jet region is blocked by the outer component, and this is creating a space between the components where the gas flow velocity is very low [38].

As it was discussed in Chapter 3, Convection Reflow Ovens, the changing the conveyor velocity is a common technique to optimize the thermal profile for a given assembly setting. Lau et al. found that the area of a colder region can be decreased by the decreasing of conveyor velocity. Since, the slower conveyor movement increases the time spent for gas streams touch the surface of the assembly. Temperature gradient can be reduced with 2°C−3°C if the conveyor speed is reduced with 20%−30%. However, a too slow conveyor can result in the overheating of the small size components [38]. According to the industrial experiments the conveyor speed can be varied between 0.8 and 1.8 cm/s.

Deng et al. investigated the heat transfer in a BTU Pyramax-98N convection reflow oven which uses a nozzle-matrix system by CFD method [40]. The detailed construction of the oven can be seen in Chapter 3, Convection Reflow Ovens. The soldering process of a System in Package (SiP) assembly

was simulated. The production of SiPs is challenging due to their small size and high complexity. The modeled structure of the reflow oven and the SiP assembly can be seen in Fig. 6.37.

The applied boundary conditions were the following: entrance and exit sections were pressure outlets. The nozzles were velocity inlets for the top and bottom of the reflow oven. Nitrogen was used as the convection fluid in the reflow process. Temperature and velocity settings in the heater zones were the following: z1 110°C—4 m/s; z2 130°C—4 m/s; z3 155°C—6 m/s; z4 175°C—7 m/s; z5 220°C—8 m/s; z6 250°C—8 m/s; z7 275°C—9 m/s.

The mesh contained more than 8.5 million cells and the minimum orthogonal quality was 0.142. The authors applied the K-epsilon turbulence model with a coupled algorithm which enables the pressure−velocity coupling and a second-order upwind scheme to discretize each control volume for better accuracy [40].

The temperature distribution of the entire reflow oven was investigated. Fig. 6.38 shows the "cross section" of the temperature distribution of zones 1 and 7. The maximum temperature difference of the nitrogen was found to be 6.8°C, in zone 1, while the minimum temperature difference was found to be 0.8°C, in zone 6 [40]. The temperature differences are higher in the zones which are located at entrance and exit of the oven. Since the gas flow is more intense out from the "border zones" to the environment than out from a zone which is in the middle of the oven.

The temperature distribution of the SiP assembly during the soldering can be seen in Fig. 6.39. The maximum temperature difference was found to be within 5°C along the width of the assembly. However, the maximum longitudinal temperature difference was found to be relatively high, 43°C across the entire SiP assembly, when the assembly is entering into zone 5 [40]. This can be explained by the following: the length of the investigated assembly is 239 mm, which is in the same magnitude with the 720 mm length of the zones. Therefore, when the assembly is leaving zone 4 with 175°C set temperature and entering into zone 5 with 220°C set temperature, high temporary temperature difference can form between the front and rear parts of the assembly. However, the size of the discrete circuits on the assembly is more comparable with the width of the assembly, so the relatively high longitudinal temperature difference does not cause any problem during the soldering. It can be problematic only in the case of large-size components.

Deng et al. observed as well, that the cooler area on the assembly usually occurs at those locations where more components are mounted and near the external direction of the reflow oven. Even if the components are relatively small and do not disturb the gas flow, since the components absorbs heat, which reduced the heat flux reaching the substrate [40].

Consequently, it can be concluded that independently from the size of the components if the density of components is high, then a local low temperature zone can form during the application of convection reflow soldering ovens, and this increases the chance of soldering defects.

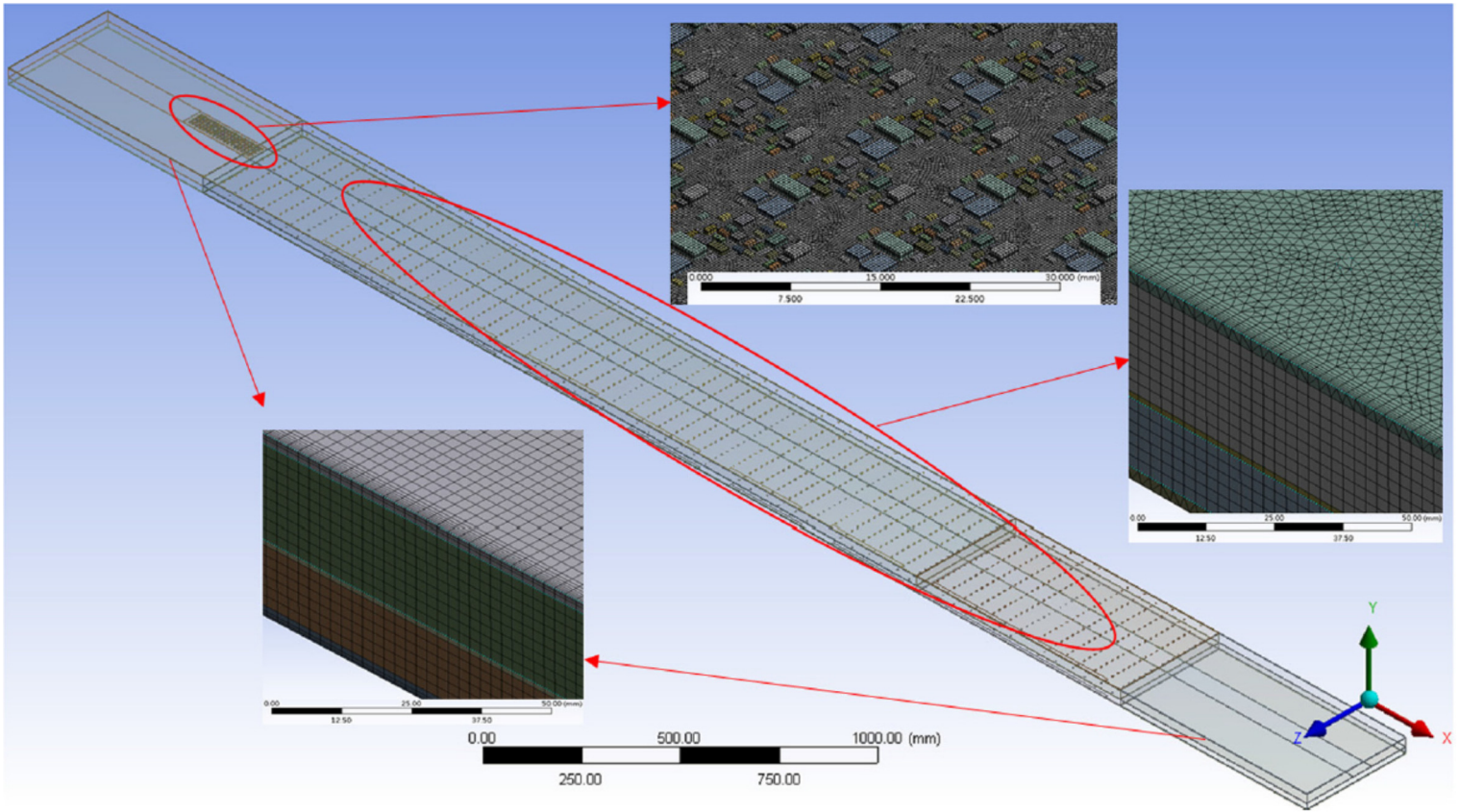

FIGURE 6.37 The geometrical model of the reflow oven and the SiP assembly. *Reproduced with permission from S.-S. Deng, S.-J. Hwang, H.-H. Lee, Temperature prediction for system in package assembly during the reflow soldering process, Int. J. Heat Mass Transf. 98 (2016) 1–9.*

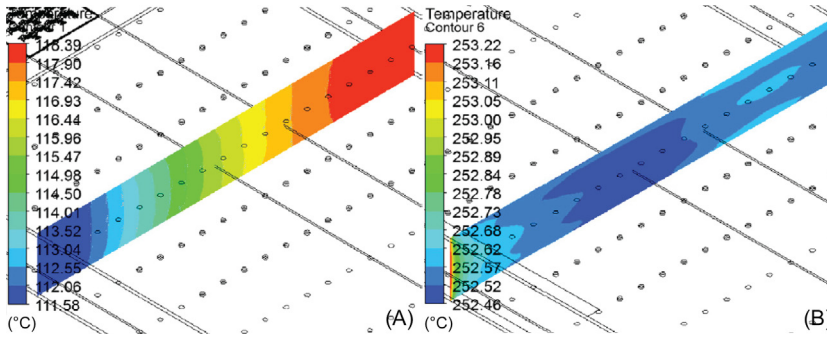

FIGURE 6.38 Temperature distribution in zones 1 and 6 heating zones. *Reproduced with permission from S.-S. Deng, S.-J. Hwang, H.-H. Lee, Temperature prediction for system in package assembly during the reflow soldering process, Int. J. Heat Mass Transf. 98 (2016) 1–9.*

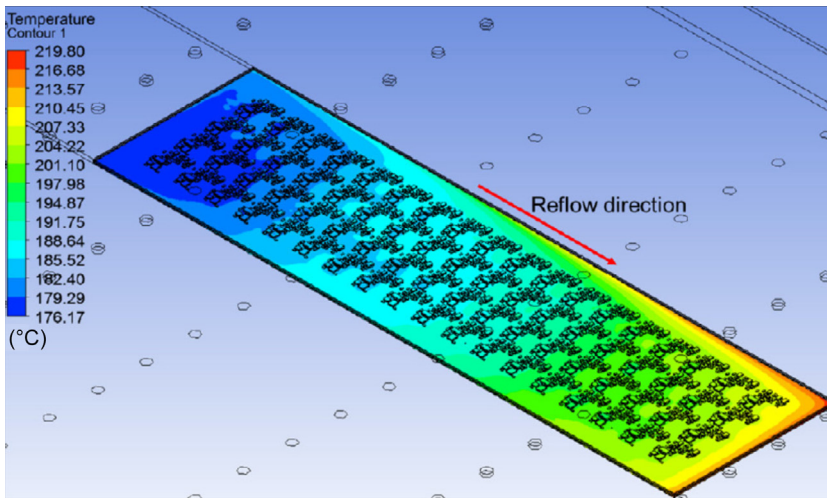

FIGURE 6.39 Temperature distributions along the SiP assembly during entering into zone 5. *Reproduced with permission from S.-S. Deng, S.-J. Hwang, H.-H. Lee, Temperature prediction for system in package assembly during the reflow soldering process, Int. J. Heat Mass Transf. 98 (2016) 1–9.*

In the case of the convection reflow ovens, the investigation of the heat transfer is important not only in the heater zones but in the cooler zones as well, since the too rapid cooling rate can result in cold soldering failure (see in Chapter 1: Introduction to Surface-Mount Technology). During another study, Lau et al. introduced a combined technique (from CFD calculations and gray-based Taguchi method) for optimization of the cooling stage of reflow soldering process [41]. They wanted to decrease the thermal stress in the solder joint of a ball grid array (BGA) package during the cooling stage

of the soldering. Their methodology contains the CFD model of the reflow oven coupled with the structural heating model of the circuit board and the BGA package (Fig. 6.40).

They investigated the effects of various parameters, like assembly density, cooling zone temperature, inlet gas stream velocity, and conveyor speed. It was found that the most influential factor for the multiple performance characteristics is the inlet gas stream velocity [41]. Since this parameter affects the cooling rate the most, the effect of cooling temperature is less considerable. The assembly density and conveyor speed are insignificant to the cooling rate. The optimal setting was found to be the following: assembly density of 0.25, cooling temperature of 373K, inlet gas flow velocity of 0.5 m/s, and conveyor speed of 1.85 cm/s. The application of the previous settings of the cooling zone decreases the thermal stress in the BGA solder joints (Fig. 6.41).

The maximum von-Mises thermal stress is significantly reduced to 60.9%—from 69.96 to 27.38 MPa—when the cooling rate is reduced to 32.6%—from 1.821 to 1.228 K/s. The maximum stress is always located at the neck of the solder bump. In the case of a general cooling zone setting,

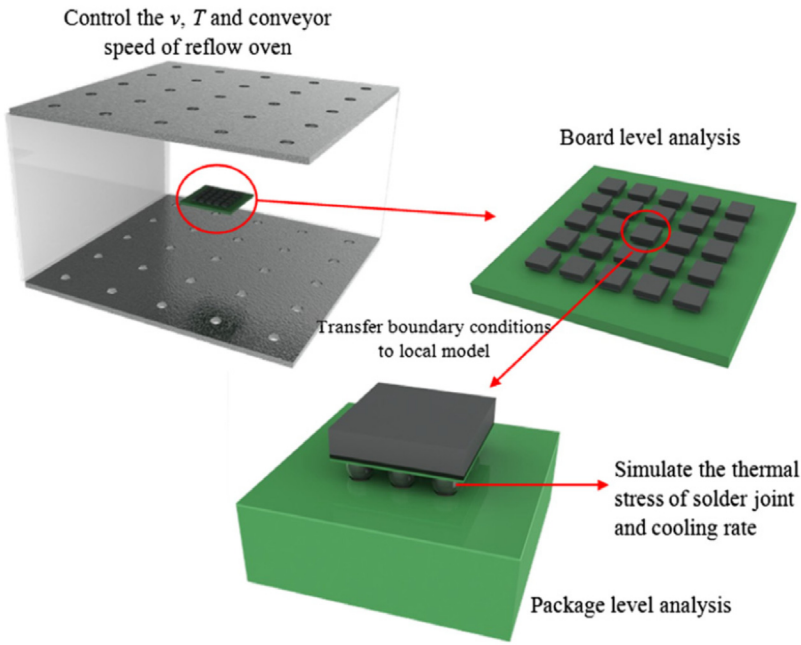

FIGURE 6.40 Combined 3D modeling structure. *Reproduced with permission from C.S. Lau, M.Z. Abdullah, F.C. Ani, Optimization modeling of the cooling stage of reflow soldering process for ball grid array package using the gray-based Taguchi method, Microelectron. Reliab. 52 (2012) 1143–1152.*

the stress can be higher than the tensile strength of the solder joint (~41.5 MPa) [42]. Therefore, the initial crack can occur at the maximum von-Mises stress location and propagates toward the intermetallic layer [41]. However, the implementation of the suggested cooler zone settings above provides significant improvement in reducing the solder cracking.

Finally, an example is presented for the thermal investigations in a reflow oven, which applies slot-type nozzles. Yi et al. performed investigations in the topic [43]. A schematic of half of the oven is shown in Fig. 6.42. Three heating zones are included, with each zone being 4000 mm in length. In zone 1, two types of air inlets (V-nozzles and slots which are located on top platform) are used. In zones 2 and 3, only V-nozzles are used with spacing of 220 mm. There are 50 arrays of the V-nozzles on the top of surface and 54 arrays on the lower plate [43].

The authors of the experiment developed a CFD model. Tetrahedral mesh was applied in fluid domain with different sizes and the cell number was

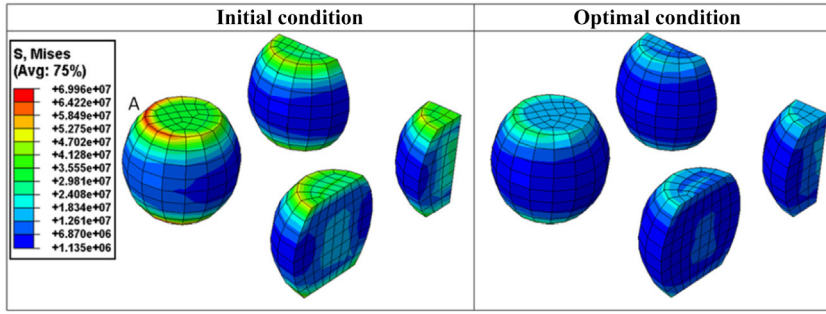

FIGURE 6.41 Comparison of the von-Mises stress between the general and optimal conditions of the cooling zone. *Reproduced with permission from C.S. Lau, M.Z. Abdullah, F.C. Ani, Optimization modeling of the cooling stage of reflow soldering process for ball grid array package using the gray-based Taguchi method, Microelectron. Reliab. 52 (2012) 1143–1152.*

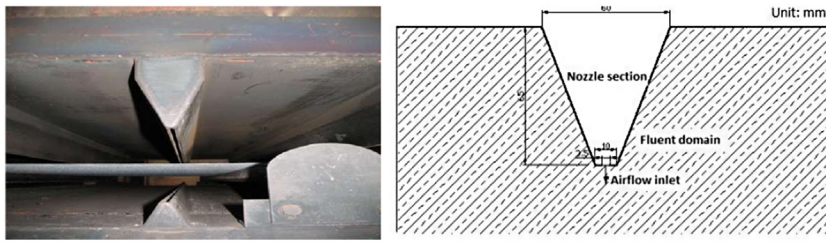

FIGURE 6.42 Schematic diagram of the studied slot-type nozzle system. *Reproduced with permission from Y. Yi, K. Salonitis, P. Tsoutsanis, L. Litos, J. Patsavelas, Improving the curing cycle time through the numerical modeling of air flow in industrial continuous convection ovens, Proc. CIRP 63 (2017) 499–504.*

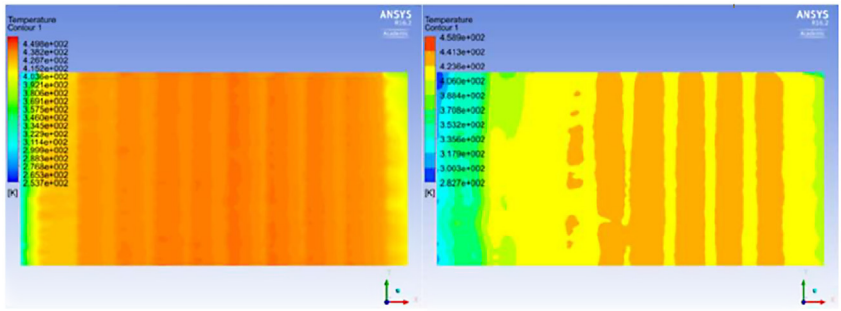

FIGURE 6.43 Temperature distribution in K of the cured substrate under 10 nozzles, in the case of 5 m/s inlet gas flow velocity with 0.15 m/s conveyor velocity (left) and 0.6 m/s conveyor velocity (right). *Reproduced with permission from Y. Yi, K. Salonitis, P. Tsoutsanis, L. Litos, J. Patsavelas, Improving the curing cycle time through the numerical modeling of air flow in industrial continuous convection ovens, Proc. CIRP 63 (2017) 499–504.*

approximately 20 million. For the calculation of the temperature distribution, the one equation turbulence model of Spalart–Allmaras was used, with the compressible density-based solver with explicit formulation; the Flux type was set as Roe-FDS. The Green–Gauss cell-based gradient was applied [43]. Although, they used the oven for curing plasticized (flexible) polyvinyl chloride (PVC-P) material at 170°C, but their results are relevant for the case of soldering as well. It was examined how the conveyor velocity and the inlet gas flow velocity affect the temperature distribution in the heater zones.

Fig. 6.43 shows the temperature distribution of the cured substrate under 10 nozzles, in the case of 5 m/s inlet gas flow velocity and changing conveyor velocity from 0.15 to 0.6 m/s. Two main conclusions can be drawn, according to these results about the slot-type nozzle systems. The temperature distribution along the width of the slot nozzle system can be much more homogenous than along the width of a nozzle-matrix system. However, the longitudinal temperature distribution is more interesting, the maximum temperature difference can reach 15°C–20°C even in the distance of some centimeters. The increase of the conveyor speed—which could increase the productivity of the oven—makes this problem even more serious. They found that at least 5 m/s inlet gas flow velocity is necessary to heat up the product in acceptable time.

6.2.2 Numerical simulations of infrared reflow ovens

Nowadays, the infrared reflow ovens are not so frequently used in mass production. However, they are still useful to produce relatively simple assemblies in small series. For this purpose, the ovens are usually constructed in batch-type (or desktop) format, and they can be equipped with a convection aid system to move the medium inside the oven, which helps to homogenize

the temperature distribution (see in details in Chapter 2: Infrared Reflow Soldering). In this chapter, some examples are presented for the detailed numerical investigation of infrared reflow ovens.

In the infrared reflow ovens, all heat transfer processes (conduction, convection, and radiation) take place; however, the main heat source are the quartz heater tubes (see in details in Chapter 2: Infrared Reflow Soldering); therefore, the previously presented numerical models (Section 6.1) have to be supplemented with the description of radiation heat transfer process. Usually, five different types of radiation models are used: P-1, Rosseland, Surface-to-Surface (S2S), DO, and Discrete Transfer Radiation Model (DTRM). Among these, the DO model describes the best behavior of the quartz heater tubes [44,45]. In the DO model, the equation for the change of radiant intensity (I) in an elementary solid can be written as follows [46,47]:

$$\frac{\partial I}{\partial x_i} = -(\alpha + \sigma_S)\cdot I\left(\vec{r}, \vec{s}\right) + \alpha\cdot\eta^2\frac{\sigma T^4}{\pi} + \frac{\sigma_S}{4\pi}\int_0^{4\pi} I\left(\vec{r}, \vec{s}\right)\cdot\phi\left(\vec{s}, \vec{s}'\right) d\Omega' \tag{6.56}$$

where the right side represents local absorption, local emission, and scattering transport mechanisms for radiation intensity, respectively. Local absorption and scattering by fluid, wall, and solids are solved using these radiative transport equations coupled with the energy equation. The radiation intensity is directionally and spatially dependent and it is determined by the absorption coefficient (α) and the scattering coefficient (σ_S). The intensity decreases due to absorption and out-scattering, and increases due to the surface emission of infrared heater tubes and in-scattering. T is the local absolute temperature of the medium in the oven and σ is the Stefan−Boltzmann constant (5.672×10^{-8} W/m^2 K^4). The scattering coefficient of air is usually assumed to be zero, and absorption coefficient of air is usually set to 5, based on infrared transmittance (95%). The same parameters of other material in a given system can be found on various databases. Eq. (6.54) is usually written in control volumes and is solved sequentially after solving flow and energy equations [47].

Najib et al. studied a desktop infrared reflow oven with convection aid system [47]. They investigated the air flow field in the oven as well as the thermal characteristics during the reflow soldering process by experiments and simulations. Temperature distribution in the oven was studied at various positions, heights, and fan velocities. The main parts of the desktop oven consist of six cylindrical-shaped infrared tubes. Besides, two circulating fans are used to distribute the hot air inside the oven, and outlet holes located at the bottom of the oven to release the air out. During the cooling phase, the infrared heaters are switched off and speed of the fan is increased to force out the hot air from the oven [47].

Fig. 6.44 shows the geometric model and the actual view of the circulating fan. The fans are made of 10 stainless steel plates with thickness of 1.5 mm and the total diameter of 115 mm. Each blade has a shape of 90-degree angles with one side facing to the front of the oven, and the other side perpendicular to it. The workbench area is 350×250 mm^2 [47]. Due to the geometrical symmetry of the oven, only half of the model was calculated during numerical simulation studies. During the reflow soldering process, the assembly is placed on a plane at the height of 46 mm. The distance between the center of infrared tubes and bottom of the assembly is 116 mm [47].

The three-dimensional (3D) oven model was solved by the finite volume solver [34]. Due to large differences in size and attribute between the parts of the oven, the size function of the grid generation was required. The size function was used in the vicinity of all outlet holes, cylindrical-shaped heaters, and fan. The size of the elements in outlet holes and around heaters vicinity was 1 mm only with growth size factor of 1.3. General size of the elements in the process volume of the oven was set to 6 mm. In the case of the fan, the general element size was 1 mm in a radius of 63.5 mm from the center of fan, whereas 6 mm general element size was set for the remaining volume. Almost all elements of the grid were tetrahedrons [47]. As a result of the grid dependency tests, a mesh with 0.93 million cells was set.

The following boundary and initial conditions were used during modeling: the flow features associated with the fans were modeled by multiple reference frames. The multiple reference frames were defined on the blade in the fan cage domain. Rotation with an angular velocity of 150 rad/s was defined on the blades (based on prior measurements). The outlet holes located on the bottom of the oven (Fig. 6.44A) were pressure outlets with atmospheric pressure. Polynomial heat flux profiles were prescribed

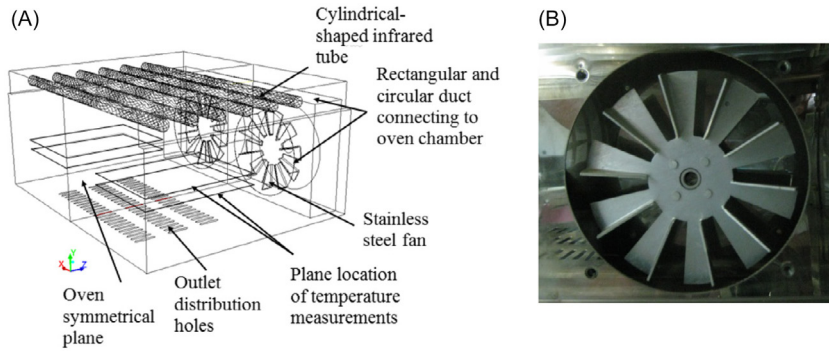

FIGURE 6.44 Geometry model of (A) desktop reflow oven and (B) actual circulating fan. *Reproduced with permission from A.M. Najib, M.Z. Abdullah, C.Y. Khor, A.A. Saad, Experimental and numerical investigation of 3D gas flow temperature field in infrared heating reflow oven with circulating fan, Int. J. Heat Mass Transf. 87 (2015) 49–58.*

uniformly on the outer surface of each heater. Considering the IR lamps as a source of heat to the system, flux is calculated based on the lamp power. The calculated values were supplied for the simulation system via advanced user-defined functions (UDFs). The external wall of the oven was defined by an emissivity value of 0.1 on the wall and 0.9 for the circuit board [47]. The rest of the physical parameters of the applied materials in the model can be found in Section 6.1.

First, the temperature distribution of the oven was investigated. Fig. 6.45A shows the temperature distribution of the oven along the middle cross section. The simulation results showed that higher temperature region is located at back region (closer to the fan). Even with the convection aid, the temperature gradient can reach even 14°C−15°C in 100 mm length, which difference is very high on such a short distance.

The higher temperature region is shifted to the back region (closer to the fan) due to air circulation from the middle side toward the fan cage. The air—close to the bottom wall—recirculates to the back region as well. Partially, the hot air from the front region leaves the oven through the outlet. The high temperature gradients in the oven are mostly due to the outlet design, since the outlet at the front of the oven causes a considerable temperature decrease locally and results in inhomogeneities of temperature distribution in the entire oven [47].

This phenomenon is clearly visible on the flow field analysis in Fig. 6.45B. The air flow field in the oven behaves in the following way: the fans force the air to move parallel to the shaft (it is probably caused by the unique blade design). The air is circulating and moving horizontally into the fan cage, revolving around the blade propeller, and flowing vertically upward out of the fan cage. When the air is heated up at heater tubes

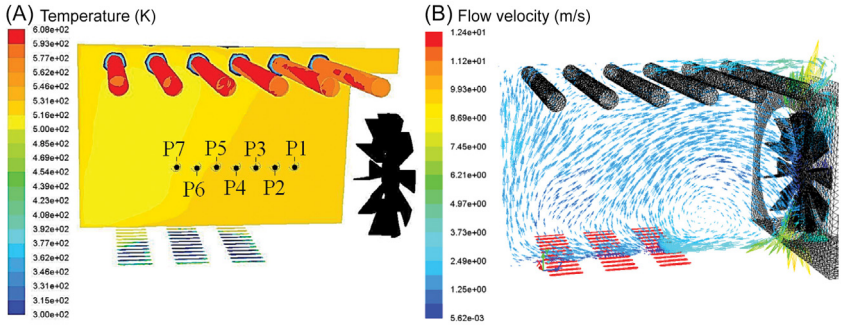

FIGURE 6.45 (A) Temperature distribution in the infrared reflow oven; (B) Air flow field in the oven during the reflow soldering process. *Reproduced with permission from A.M. Najib, M. Z. Abdullah, C.Y. Khor, A.A. Saad, Experimental and numerical investigation of 3D gas flow temperature field in infrared heating reflow oven with circulating fan, Int. J. Heat Mass Transf. 87 (2015) 49−58.*

approximately to the heater tube temperature, then the air is moving downward and back to the fan cage. The continuous flow forms circular motion direct to the fan cage, since the fan creates a continuous suction force toward the fan cage. This flow mechanism enables the air circulation and heat transfer from the infrared heater to the assembly during the reflow soldering process [47].

In the next step, Najib et al. investigated the effect of fan speed on the temperature distribution of the oven. The fan speed was considered at different Reynolds numbers:

$$\mathrm{Re} = \frac{\rho D^2 n}{\mu} \tag{6.57}$$

where D is the fan diameter, n is the RPM of the fan, ρ is the density, and μ is the viscosity of the air. The correlation between the Re number and the average peak temperature of the FR4 circuit board was studied at two different locations in the oven (Fig. 6.46A). At low Re numbers, the PCB1 and PCB2 positions show high surface temperatures, 260°C and 290°C, respectively. The average surface temperature of PCB1 position decreases proportionally from Re numbers 0.35×10^5 until 1.35×10^5. Over Re number 1.35×10^5, the surface temperature remains nearly constant at 235°C. As the Re number increases, the surface temperature at PCB2 position drops gradually to 250°C at 2.75×10^5 Re number. Therefore, it can be concluded that the fan speed is an important parameter in controlling the batch-type infrared

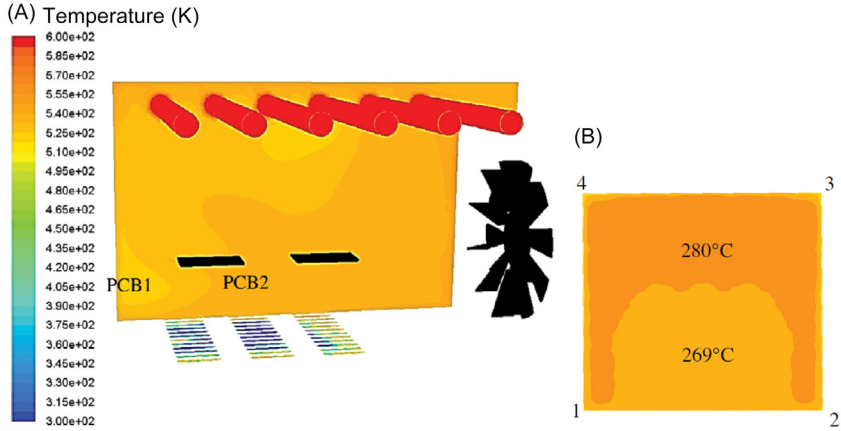

FIGURE 6.46 (A) Temperature distribution of the oven and PCB1 and PCB2 positions; (B) Peak temperature distribution of the circuit board at PCB2 position. *Reproduced with permission from A.M. Najib, M.Z. Abdullah, C.Y. Khor, A.A. Saad, Experimental and numerical investigation of 3D gas flow temperature field in infrared heating reflow oven with circulating fan, Int. J. Heat Mass Transf. 87 (2015) 49–58.*

reflow ovens. Besides, the favorable position of the assembly in the oven is the front region due to the better temperature homogeneity [47].

The PCB2 position reached higher maximum temperature than PCB1. This can be explained with the air flow field shown in Fig. 6.45B. The air leaves the oven at the front region through the outlets, and it causes the lower temperature at this region than at the back region. The results also showed that temperature distribution is less uniform at PCB2 position, since nearly the half of the circuit board reaches the upper limit 280°C, which is 11°C higher compared to the other lower surface area (Fig. 6.46B) [47]. Anyway, these peak temperature values are clearly far beyond the acceptable peak temperature of reflow soldering (~260°C).

Consequently, the better temperature uniformity and targeted thermal profile (peak temperature is between 230°C and 240°C) could be achieved at high Re number (between 1.35 and 2.75×10^5) and when the assembly is in the front region of the oven. However, the result of Najib et al. highlights the more problematic control of infrared reflow ovens compared to the convection ones. Even the application of convection aid in the infrared reflow oven does not guarantee the optimal thermal profiles for soldering.

Lau and Abdullah did investigations with the same infrared reflow oven; they studied the reflow soldering process of BGA components [46]. They applied a fluid/structure thermal coupling method to model the flow field, temperature, and thermal stress response of the BGA assembly during the reflow soldering. A BGA package with the size of $11 \times 11\ mm^2$ on a $48 \times 53\ mm^2$ FR4 board was studied. The structural model contained the FR4 board, silicon die, solder layer, and mold. The silicon die and mold (the body of the component) were considered to be linear isotropic materials, the FR4 board was considered to be linear orthotropic material, and the solder joints were considered to be a temperature-dependent material. The applied thermal properties can be found in Ref. [41]. The geometry mesh was built up from C3D8T hexahedral elements and contained 2910 nodes and 1818 elements [46].

The temperature distribution of the BGA assembly is calculated in a FEM-based structural solver and the fluid dynamics was calculated in an FVM-based solver. The simultaneously running solvers were coupled. Data exchange occurred every 0.1 second, on the following way: the CFD model sends the film temperature and surface heat transfer coefficient to the structural model, which sends the wall temperature to the CFD model. This method is very similar to the cosimulation technique presented in Section 6.1.

The CFD model showed that the average HTC value on the surface of the assembly is 48 W/m^2 K. Considerable inhomogeneities were found during the heating up of the assembly. The edges of the circuit board heat up first and considerable temperature difference forms between the BGA

component and the circuit board. The coolest point is located at the middle of the BGA component, whereas the hottest point is located at corners of circuit board. The highest temperature difference was found to be 29°C during the preheating phase. This can result in that the circuit board suffers a warping damage (see in details in Chapter 1: Introduction to Surface-Mount Technology). The nonuniform temperature distribution causes mechanical stresses in the BGA assembly (von-Mises stress) at the interfaces of different materials because of the differences in coefficient of thermal expansion (CTE). The increasing von-Mises stress can cause bending deformation. The maximum von-Mises stress in the BGA package occurs at the ramp-up phase with 233.7 MPa. The maximum von-Mises stress of solder joints is around 156 MPa. Experiment results showed that the row of solder joints just outside or just underneath the die edge can suffer damage under such stress level [48].

6.2.3 Numerical simulations of die bonding ovens

Among the special reflow ovens (discussed in Chapter 5: Special Reflow Techniques), the numerical simulation of a die (solder) bonding reflow oven is presented. The studied oven is a "Linn"-type fluxless solder bonding oven, which operates between 300°C and 400°C. The oven is used for mounting Si and SiC dies on metal substrates, with 96Pb/4Sn solder alloy at 365°C [49]. For hard soldering purpose, the application of leaded solders is still allowed. The foil-type solder is placed between the Si die and the metal substrate. The soldering foil does not contain flux material; hence, reducing agent (so called "forming gas," which is a mixture of 10 vol.% H_2 and 90 vol.% N_2) was applied to avoid the oxidation of the solder joints. The key parameters of this soldering technology to achieve proper soldering quality are the suitable temperature (340°C−370°C for 13−15 minutes) and the adequate H_2 concentration (8−10 vol.%). The structure of the oven is presented in details in Chapter 5, Special Reflow Techniques; here, only the necessary properties are repeated.

The process area of the oven is 8 m long, 0.24 m wide, and 0.08 m high. The main parts of the oven are the following: entrance vent hood, entrance gas blocks, entrance dilute N_2 intake, heater zone (with four heater panels), forming gas intake, cooling zone, cooling N_2 intake, exit dilute N_2 intake, exit vent hood, and exit gas blocks. The vent hoods contain funnels with 80 mm diameter with controllable throttle valves. The heating zone is a steal duct with ceramic lining to increase the heat capacity. The steel duct is heated at 4 point with electrical heaters. The cooling zone is facilitated by cold water pipes placed on the wall of the cooling zone and by intake of cold N_2 gas [49,50].

In the case of proper operation of the oven, most of the forming gas flows toward the entrance of the oven through the heating zone and the cooling N_2 gas flows toward the exit of the oven. Along the oven, only the gas blocking lamellas and the trapdoors cause considerable flow resistance, they make the oven to be over pressurized. The pressure balance can be controlled by the amount of gas at the intakes and by the vent hoods. The gas flow balance is one of the most important and unfortunately the most sensitive points of the oven. The pressure balance of the oven can easily be ruined by the improper operation of the vent hoods or by a draught in the production hall where the oven is operated [49,50]. Therefore, the aim of the presented simulation study was to characterize the gas flow and thermal circumstances inside the oven in the case of different oven settings.

The applied balances for the simulations can be seen in Fig. 6.47. Since one of the key parameters of this soldering technology is the elimination of the oxygen from the oven and the suitable H_2 concentration (8–10 vol.%) during the solder process, the forming gas cannot be diluted. This condition can be achieved only if a part of the in-taken forming gas (Q_f) flows toward the exit of the oven through the cooling zone, therefore:

$$0 < Q_{back} < Q_f \tag{6.58}$$

In this preferred case, the forming gas in the heater zone is not diluted by the cooling N_2 gas ($Q_{N,c}$). During the proper operation the following equations are valid:

$$Q_{forw} + Q_{back} = Q_f + Q_{N,c} \tag{6.59}$$

$$Q_{forw} + Q_{N,out} = Q_{out} \tag{6.60}$$

$$Q_{back} + Q_{N,in} = Q_{in} \tag{6.61}$$

The gas flow field in the oven can be controlled by the amount of the in-taken gases and by the pressure of the vent hoods; however, it is also influenced by the flow resistances of the gas blocks (ζ_{in} and ζ_{out}). These flow resistances are considered to be concentrated losses, which contain not only the effect of the gas blocks but the effect of the certain tunnel parts and the

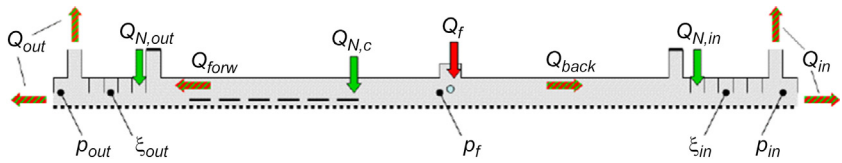

FIGURE 6.47 Normalized volume flows (Q), pressures (p), and flow resistance coefficients (f) in the oven. *Reproduced with permission from B. Illés, G. Kristóf, Gas flow simulations of a fluxless Si solder bonding oven, Microelectron. Eng. 88 (2011) 760–766.*

obstruction effect of the radial gas intakes (see in Chapter 5: Special Reflow Techniques). The pressure balances in the oven can be calculated [49,50]:

$$p_f - p_{in} = \frac{\rho_{in}}{2}\left(\frac{T_{in}}{T_0}\frac{Q_{in}}{A}\right)^2 \zeta_{in} \tag{6.62}$$

$$p_f - p_{out} = \frac{\rho_{out}}{2}\left(\frac{T_{out}}{T_0}\frac{Q_{out}}{A}\right)^2 \zeta_{out} \tag{6.63}$$

where A is the cross-sectional area of the gas blocks; ρ_{in} and ρ_{out} are the normalized density of the gas at the entrance and the exit; T_{in}, T_{out}, and T_0 are the temperatures at the entrance, at the exit and in normal state; Q_{in} and Q_{out} are the normalized volume flows at the entrance and at the exit; p_{in}, p_{out}, and p_f are the pressures in the area before the entrance trapdoor, after the exit trapdoor and at the intake of the forming gas [49,50].

It has to be noted, that the real value of ζ_{in} and ζ_{out} depends on the composition and the temperature of the gas mixture, on the velocity of the gas flow, on the flow resistance of the product carriers, and finally on the position of the trapdoors. However, in the first approach ζ_{in} and ζ_{out} is considered to be constants. Consequently, the operation of the system can be described by five variables: p_f, Q_{forw}, Q_{back}, Q_{out}, and Q_{in}. During the operation of the oven, the front and rear trapdoors are almost always opened. According to preliminary measurements, the pressures at the entrance and exit are almost the same ($p_{in} \approx p_{out}$) in case of opened trapdoors [49,50]. The ratio of Q_{in} and Q_{out} can be approximated from Eqs. (6.59) and (6.60):

$$Q_{in} = Q_{out}\sqrt{\frac{\zeta_{out}\rho_{out}{T_{out}}^2}{\zeta_{in}\rho_{in}{T_{in}}^2}} = Q_{out}\cdot K \tag{6.64}$$

The application of Eq. (6.61) gives the following flow solutions:

$$Q_{forw} = \frac{Q_{N,in} + Q_f + Q_{N,c} - KQ_{N,out}}{K+1} \tag{6.65}$$

$$Q_{back} = \frac{Q_{N,out} + Q_f + Q_{N,c} - K^{-1}Q_{N,in}}{K^{-1}+1} \tag{6.66}$$

Eq. (6.55) can be written in the following form with the application of Eq. (6.62):

$$(K+1)Q_f + Q_{N,in} \geq K\left(Q_f + Q_{N,out} + Q_{N,c}\right) > Q_{N,in} \tag{6.67}$$

Consequently, the operation of the oven can be described if we can determine the value of the K coefficient during the simulations.

A 3D CFD model was constructed to describe the gas flow and the thermal circumstances of the oven. The model contains all parts of the oven which were presented in Chapter 5, Special Reflow Techniques, and in

Fig. 6.47. The model based on the RANS equations with the $k-\varepsilon$ method (which was presented in Section 6.1). The model was solved with a FVM solver. The numerical mesh contains mostly 520,000 cuboid cells (at some parts tetrahedrons were applied). The size of the cells was 5 mm toward the z direction (height), 10−30 mm toward the y direction (along the length of the oven), and 10 mm toward the x direction (along the width of the oven). The time step was 0.2 second [49,50].

The basic gas in-take setting of the oven can be seen in Table 6.7. They acted like initial conditions during the first simulation round. The rest of the necessary initial parameters were measured, like the pressure at the entrance vent hood to be -2.6 Pa, at the exit vent hood to be -0.5 Pa, and $p_{in} = p_{out} = 0$ Pa. The outcoming amount of gas through the funnels of the vent hoods is controlled by the throttle valves. According to the measurements (with the basic throttle valves settings), the loss coefficients of the funnels are approximated with: $\zeta_{f,entrance} = \zeta_{f,exit} = 8$. The heating and cooling in the oven was modeled as an infinite source and sink. In the cooling zone the temperature was fixed to 20°C at the 10 mm surroundings of the walls. In the heating zone the temperature was fixed to 365°C. Adiabatic boundary condition is applied on the walls of the oven.

The simulation results were validated by temperature and H_2 concentration measurements. The detailed measurement methods and possibilities in the oven can be seen in Chapter 5, Special Reflow Techniques. In Fig. 6.48 the measured and simulated parameters are compared. The matching of the measured (discrete points) and simulated (curves) results is quite good. According to the calculated Q_{in} and Q_{out} volume flows, the K coefficient in Eqs. (6.61)−(6.63) is determined to be $K = Q_{in}/Q_{out} = 0.71$.

TABLE 6.7 Basic setting of the gas intakes.

Intake point	Volume flow (Nm^3/h)[a]	Mass flow (kg/s)	Temperature (°C)
Entrance dilute N_2, up	7.11	0.00247	20
Entrance dilute N_2, down	7.08	0.00246	20
Forming gas	11.08	0.00382	280
Cooling N_2	8.47	0.00294	20
Exit dilute N_2, up	10.39	0.00361	20
Exit dilute N_2, down	10.39	0.00361	20

[a] *The volume flows are normalized values.*

The simulation results of the basic oven settings can be seen in Fig. 6.49 along the $x-z$ cross section (length−height) of the oven. The visualization is distorted to 1:5 along the length of the oven. The H_2 concentration is almost 10 vol.% in the heater zone. The N_2 at intake in the cooling zone decreases

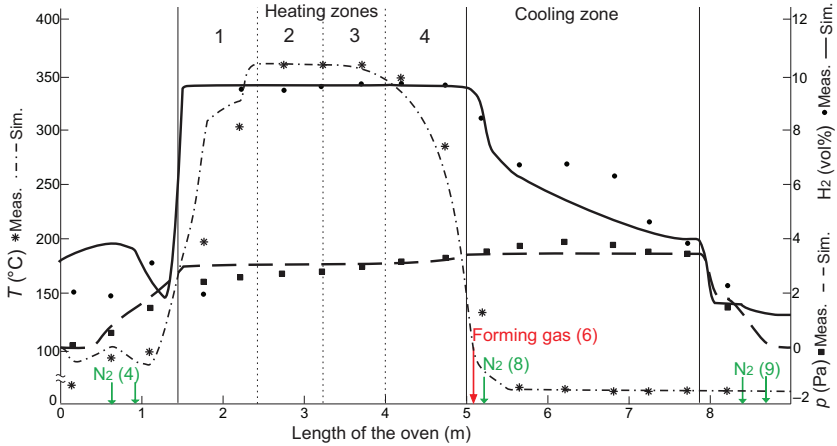

FIGURE 6.48 Comparison of the measured and calculated results. *Reproduced with permission from B. Illés, G. Kristóf, Gas flow simulations of a fluxless Si solder bonding oven, Microelectron. Eng. 88 (2011) 760–766.*

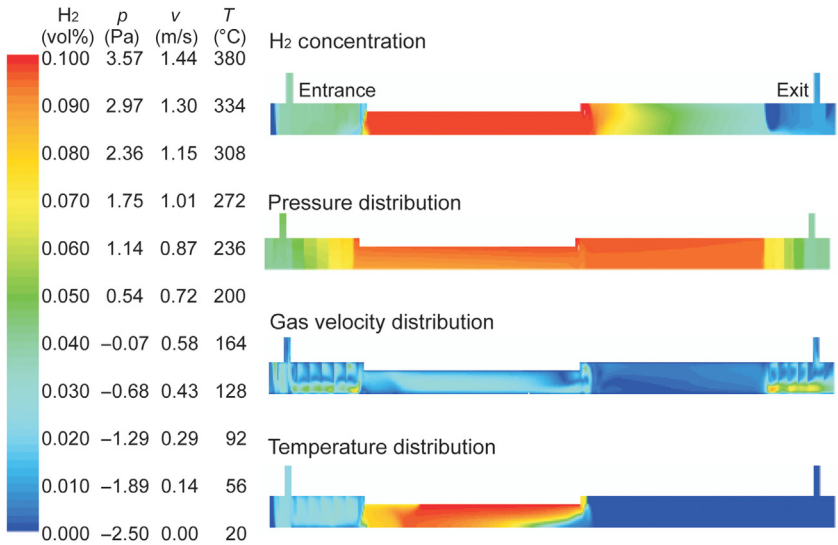

FIGURE 6.49 Simulation results of the basic oven settings. *Reproduced with permission from B. Illés, G. Kristóf, Gas flow simulations of a fluxless Si solder bonding oven, Microelectron. Eng. 88 (2011) 760–766.*

the H_2 concentration to 5 vol.%. The safety dilute intakes at the entrance and exit of the oven causes further concentration decreases below 1 vol.%. The maximum pressure is at the intake of the forming gas and it decreases only moderately in the active areas of the oven (heating and cooling zone), it starts to decrease only at the gas blocks. The gas flow velocity in the cooling zone is much slower ($\sim$0.1 m/s) than in the heater zone ($\sim$0.35 m/s). This effect can be explained with the larger amount of entered gas in the heater zone and with the lower height of the heater zone compared to the cooler zone [49,50].

The temperature is above 350°C in 70% of the heater zone which means more than 20 minutes in soldering time, what is far enough to ensure the appropriate soldering quality. However, the dilute N_2 causes a little backwards flow, which decreases the temperature and H_2 concentration at the end of the heater zone. This effect is considerable only at the level of the conveyor, and below 20 mm from the conveyor.

The quality of the solder joints could be improved by the increase of H_2 concentration (c_{in}) at the entrance gas blocks. The value of c_{in} can be calculated from the H_2 concentration of the forming gas (c_f) and with Eq. (6.58):

$$c_f Q_{back} = c_{in} Q_{in} \tag{6.68}$$

$$\frac{c_{in}}{c_f} = \frac{Q_{back}}{Q_{back} + Q_{N,in}} \tag{6.69}$$

According to Eq. (6.67), the decrease of the H_2 concentration at the entrance gas blocks is caused by the high value of $Q_{N,in}$; therefore, it should be decreased. This decrease can be performed only with the same rate of increase of Q_f, since neither the total amount of gas in-taken and neither $Q_f + Q_{N,in}$ can decrease (according to Eq. 6.64). Consequently, the most promising setting would be to eliminate the dilute N_2 at the entrance and supplement the shortfall at the forming gas intake point (Fig. 6.47). The setting (v1) was: $Q_f^{\text{mod}} = Q_f^{basic} + Q_{N,in}^{basic}$ and $Q_{N,in}^{\text{mod}} = 0$.

In the case of v1 settings, the H_2 concentration increases considerably before the heater zone and high H_2 emission happens at the entrance trapdoor which can be dangerous during the operation of the oven. To prevent this effect, the throttle valve of the entrance vent hood is opened (setting v2), which decreases the loss coefficient of the funnel at the entrance to $\zeta_{f,entrance}^{\text{mod}} = 1$. This reverses the flow direction from outflow to inflow at the entrance trapdoor and results in a lower H_2 concentration at the entrance trapdoor than in the case of setting v1, and also than in the case of the basic setting. The application of v2 setting does not change the H_2 concentration in the other parts of the oven [49,50].

The flow parameters in the case of the different oven settings can be seen in Fig. 6.50. Both setting modifications (mainly v1) increase temperature considerably at the entrance of the oven and shift the thermal profile

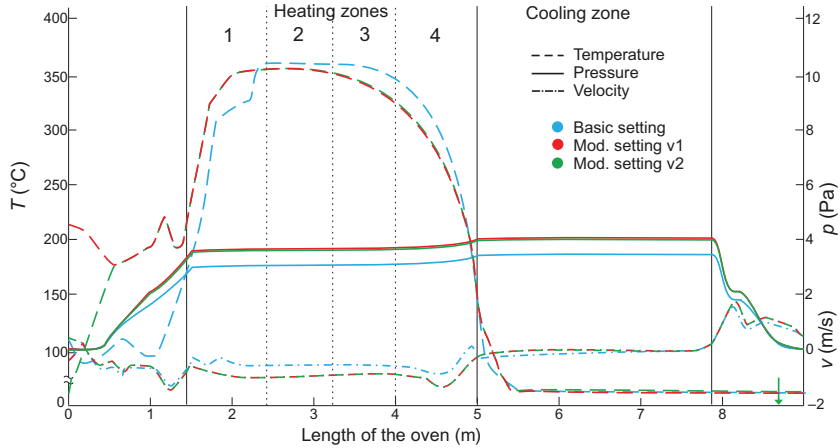

FIGURE 6.50 Flow parameters in the case of the different oven settings. *Reproduced with permission from B. Illés, G. Kristóf, Gas flow simulations of a fluxless Si solder bonding oven, Microelectron. Eng. 88 (2011) 760–766.*

moderately. However, these effects do not cause any problem; moreover, the larger amount of heat at the entrance can be beneficial during the soldering, it helps the preheating of the assemblies.

The pressure and the gas flow velocity are the same in the case of both setting modifications. The pressure increases moderately in the process area (heater and cooling zones) with 0.4 Pa, which supports the over pressurized defense of the oven. Due to the larger amount of forming gas, the velocity of the outflow is increased from the process area (manly from the heater zone) toward the ends of the oven; but this can be neglected [49,50]. Finally, the volume flow balance (Eq. 6.64) must be checked in the case of the modified settings. In order to get the best H_2 utilization in the heater zone, the operating volume flow value of $K\left(Q_f + Q_{N,out} + Q_{N,c}\right)$ must be close to the upper border $(K+1)Q_f + Q_{N,in}$ (defined in Eq. 6.64). The modified settings fulfill this condition.

According to the manufacturer experiments, the application of v2 setting increases the mechanical strength of the solder joints with 19% in average and decreases the void percent with 3%. This shows another example for application of numerical simulations to solve reflow soldering problems.

References

[1] W. Cheng, N. Liu, W. Wu, Studies on thermal properties and thermal control effectiveness of a new shape-stabilized phase change material with high thermal conductivity, Appl. Therm. Eng. 36 (2012) 345–352.

[2] G.H. Tang, H.W. Hu, Z.N. Zhuang, W.Q. Tao, Film condensation heat transfer on a horizontal tube in presence of a noncondensable gas, Appl. Therm. Eng. 36 (2012) 414–425.

[3] T.-B. Chang, Mixed-convection film condensation along outside surface of vertical tube in saturated vapor with forced flow, Appl. Therm. Eng. 28 (2008) 547–555.
[4] B. Illés, A. Géczy, Investigating the dynamic changes of the vapour concentration in a vapour phase soldering oven by simplified condensation modeling, Appl. Therm. Eng. 59 (2013) 94–100.
[5] C.V. Gonçalves, S.R. Carvalho, G. Guimarães, Application of optimization techniques and the enthalpy method to solve a 3D-inverse problem during a TIG welding process, Appl. Therm. Eng. 30 (2010) 2396–2402.
[6] A. Fouda, Z. Melikyan, A simplified model for analysis of heat and mass transfer in a direct evaporative cooler, Appl. Therm. Eng. 31 (2011) 932–936.
[7] K.W. Morton, D.F. Mayers, Numerical Solution of Partial Differential Equations: An Introduction, Cambridge University Press, Cambridge, 2005.
[8] C.-L. Chen, C.-H. Cheng, Numerical simulation of periodic mixed convective heat transfer in a rectangular cavity with a vibrating lid, Appl. Therm. Eng. 29 (2009) 2855–2862.
[9] A. Géczy, Investigations Into the Process of Vapour Phase Soldering (Ph.D. Dissertation), BME, 2014.
[10] B. Illés, A. Géczy, Multi-physics modelling of a vapour phase soldering (VPS) system, Appl. Therm. Eng. 48 (2012) 54–62.
[11] B. Illés, A. Géczy, Numerical simulation of condensate layer formation during vapour phase soldering, Appl. Therm. Eng. 70 (2014) 421–429.
[12] B. Illés, G. Harsányi, 3D thermal model to investigate component displacement phenomenon during reflow soldering, Microelectron. Reliab. 48 (2008) 1062–1068.
[13] M. Li, J. Steiner, S. Tang, Convergence and stability analysis of an explicit finite difference method for 2-dimensional reaction-diffusion equations, J. Aust. Math. Soc. B 36 (1994) 234–241.
[14] A.L. Buck, New equations for computing vapor pressure and enhancement factor, J. Appl. Meteorol. 20 (1981) 1527–1532.
[15] A. Bejan, Film condensation on an upward facing plate with free edges, Int. J. Heat Mass Transf. 34 (2) (1991) 578–582.
[16] J. Gerstmann, P. Griffith, Laminar film condensation on the underside of horizontal and inclined surfaces, Int. J. Heat Mass Transf. 10 (1967) 567–580.
[17] Daitoku Tech, Co., LTD., Manufacturer datasheet of Galden fluid <http://www.daitoku-tech.com/products/galden/data/HT170.pdf>.
[18] O. Krammer, Modelling the self-alignment of passive chip components during reflow soldering, Microelectron. Reliab. 54 (2014) 457–463.
[19] Q.-Z. Xue, Model for effective thermal conductivity of nanofluids, Phys. Lett. A 307 (2003) 313–317.
[20] J. Diaz, M.J. Grote, Multi-level explicit local time-stepping methods for second-order wave equations, Comput. Methods Appl. Mech. Eng. 291 (2015) 240–265.
[21] S. Lips, J.P. Meyer, Experimental study of convective condensation in an inclined smooth tube. Part I: Inclination effect on flow pattern and heat transfer coefficient, Int. J. Heat Mass Transf. 55 (2012) 395–404.
[22] J.P. Meyer, J. Dirker, A.O. Adelaja, Condensation heat transfer in smooth inclined tubes for R134a at different saturation temperatures, Int. J. Heat Mass Transf. 70 (2014) 515–525.
[23] S. Lips, J.P. Meyer, Stratified flow model for convective condensation in an inclined tube, Int. J. Heat Fluid Flow 36 (2012) 83–91.

[24] B. Illés, A. Géczy, Investigating the heat transfer on the top side of inclined printed circuit boards during vapour phase soldering, Appl. Therm. Eng. 103 (2016) 1398–1407.
[25] B. Illés, A. Géczy, O. Krammer, K. Dušek, D. Bušek, Numerical investigation on the effect of condensate layer formation around large-size components during vapour phase soldering, Int. J. Heat Mass Transf. 125 (2018) 202–209.
[26] N.-C. Lee, Reflow Soldering Process and Troubleshooting, first ed., Newnes, Woburn, MA, 2008.
[27] S.M. Ramkumar, R. Ghaffarian, A. Varanasi, Lead-free 0201 manufacturing, assembly and reliability test results, Microelectron. Reliab. 46 (2006) 244–262.
[28] B. Illés, A. Géczy, A. Skwarek, D. Busek, Effects of substrate thermal properties on the heat transfer coefficient of vapour phase soldering, Int. J. Heat Mass Transf. 101 (2016) 69–75.
[29] B. Illés, A. Skwarek, A. Géczy, K. Witek, Numerical study of vapour concentration reduction in a vacuum vapour phase soldering oven, in: Proceedings of 40th International Spring Seminar on Electronics Technology, Sofia, Bulgaria, 2017, <https://doi.org/10.1109/ISSE.2017.8000941>.
[30] Y.-Y. Bae, E.-S. Kim, M. Kim, Assessment of low-Reynolds number $k-\varepsilon$ turbulence models against highly buoyant flows, Int. J. Heat Mass Transf. 108 (Part A) (2017) 529–536.
[31] B. Illés, A. Skwarek, A. Géczy, O. Krammer, D. Bušek, Numerical modelling of the heat and mass transport processes in a vacuum vapour phase soldering system, Int. J. Heat Mass Transf. 114 (2017) 613–620.
[32] A.L. Lee, M.H. Gonzalez, B.E. Eakin, The viscosity of natural gases, J. Petrol. Technol. 18 (8) (1966) 997–1000.
[33] B. Illés, A. Skwarek, A. Géczy, L. Jakab, D. Bušek, K. Dušek, Effect of the vapour concentration decrease on the solder joints temperature in a vacuum vapour phase soldering system, Solder. Surf. Mt. Technol. (2018) 66–73.
[34] B. Illés, I. Bakó, Numerical study of the gas flow velocity space in convection reflow oven, Int. J. Heat Mass Transf. 70 (2014) 185–191.
[35] B. Illés, Distribution of the heat transfer coefficient in convection reflow oven, Appl. Therm. Eng. 30 (2010) 1523–1530.
[36] D.C. Wilcox, Turbulence Modeling for CFD, second ed., DCW Industries, Anaheim, 1998, p. 174.
[37] B. Illés, Comparing 2D and 3D numerical simulation results of gas flow velocity in convection reflow oven, Solder. Surf. Mt. Technol. 26 (4) (2014) 223–230.
[38] C.S. Lau, M.Z. Abdullah, F.C. Ani, Three-dimensional thermal investigations at board level in a reflow oven using thermal-coupling method, Solder. Surf. Mt. Technol. 24 (3) (2012) 167–182.
[39] A.C. Ferreira, S.F.C.F. Teixeira, R.F. Oliveira, N.J. Rodrigues, J.C.F. Teixeira, D. Soares, CFD modeling the cooling stage of reflow soldering process, in: Proceedings of the ASME 2016 International Mechanical Engineering Congress and Exposition IMECE2016, November 11–17, 2016, Phoenix, AZ, 2016, pp. 1–9, IMECE2016-66447.
[40] S.-S. Deng, S.-J. Hwang, H.-H. Lee, Temperature prediction for system in package assembly during the reflow soldering process, Int. J. Heat Mass Transf. 98 (2016) 1–9.
[41] C.S. Lau, M.Z. Abdullah, F.C. Ani, Optimization modeling of the cooling stage of reflow soldering process for ball grid array package using the gray-based Taguchi method, Microelectron. Reliab. 52 (2012) 1143–1152.

[42] J. Zhao, Y. Mutoh, Y. Miyashita, S.L. Mannan, Fatigue crack-growth behavior of Sn−Ag−Cu and Sn−Ag−Cu−Bi lead-free solders, J. Electron. Mater. 31 (8) (2002) 879−886.

[43] Y. Yi, K. Salonitis, P. Tsoutsanis, L. Litos, J. Patsavelas, Improving the curing cycle time through the numerical modeling of air flow in industrial continuous convection ovens, Proc. CIRP 63 (2017) 499−504.

[44] N. Chhanwal, A. Anishaparvin, D. Indrani, K.S.M.S. Raghavarao, C. Anandharamakrishnan, Computational fluid dynamics (CFD) modeling of an electrical heating oven for bread-baking process, J. Food Eng. 100 (2010) 452−460.

[45] S.Y. Wong, W. Zhou, J. Hua, CFD modeling of an industrial continuous bread baking process involving U-movement, J. Food Eng. 78 (2007) 888−896.

[46] C.-S. Lau, M.Z. Abdullah, Simulation investigations on fluid/structure interaction in the reflow soldering process of board-level BGA packaging, Int. J. Comput. Theory Eng. 5 (4) (2013) 645−649.

[47] A.M. Najib, M.Z. Abdullah, C.Y. Khor, A.A. Saad, Experimental and numerical investigation of 3D gas flow temperature field in infrared heating reflow oven with circulating fan, Int. J. Heat Mass Transf. 87 (2015) 49−58.

[48] R. Darveaux, J. Heckman, A. Syed, A. Mawer, Solder joint fatigue life of fine pitch BGAs—impact of design and material choices, Microelectron. Reliab. 40 (2000) 1117−1127.

[49] B. Illés, G. Kristóf, L. Jakab, Thermal and gas flow characterization of a fluxless Si solder bonding oven, Exp. Therm. Fluid Sci. 35 (2011) 29−36.

[50] B. Illés, G. Kristóf, Gas flow simulations of a fluxless Si solder bonding oven, Microelectron. Eng. 88 (2011) 760−766.

Index

Note: Page numbers followed by "*f*" and "*t*" refer to figures and tables, respectively.

E

F

G

H

I

K

L

M

N

O

P

T

V

W

REFLOW SOLDERING

APPARATUS AND HEAT TRANSFER PROCESSES

Authored by Dr. Balázs Illés, Dr. Olivér Krammer, and Dr. Attila Géczy

Reflow Soldering: Apparatus and Heat Transfer Processes investigates the technology of reflow soldering from the aspect of the applied apparatus and the physical foundations. The book introduces the basic concept of surface mount technology. This is followed by the description of infrared ovens, convection ovens, vapour phase soldering (VPS), and special reflow ovens. The chapters include discussion of the physical background, structure and working principles, and characterization of the heating, flow, and work zone medium parameters. Each chapter aims to review the application of the different soldering techniques and typical related quality and reliability issues. The book concludes with a discussion of numerical simulation cases.

This book aims researchers or design engineers within the electronics and manufacturing industries.

Key Features

- Provides an overview and comparison of the existing reflow apparatus, heating methods, and working principles
- Analyzes and compares the different reflow oven types
- Discusses useful tools such as characterization and measurement methods and includes numerical case studies to assist in solving soldering problems and improve quality and reliability
- Discusses vapour phase soldering (VPS) and other alternative soldering technologies

About the Authors

Dr. Balázs Illés

PhD, DSc, Full Professor, Budapest University of Technology and Economics, Budapest, Hungary

Dr. Olivér Krammer

PhD, Associate Professor, Budapest University of Technology and Economics, Budapest, Hungary

Dr. Attila Géczy

PhD, Associate Professor, Budapest University of Technology and Economics, Budapest, Hungary

ISBN 978-0-12-818505-6

9 780128 185056

ELSEVIER elsevier.com/books-and-journals